Max-Born-Institut
für Nichtlineare Optik
und Kurzzeitspektroskopie
im Forschungsverbund Berlin e.V.

Annual Report 2021

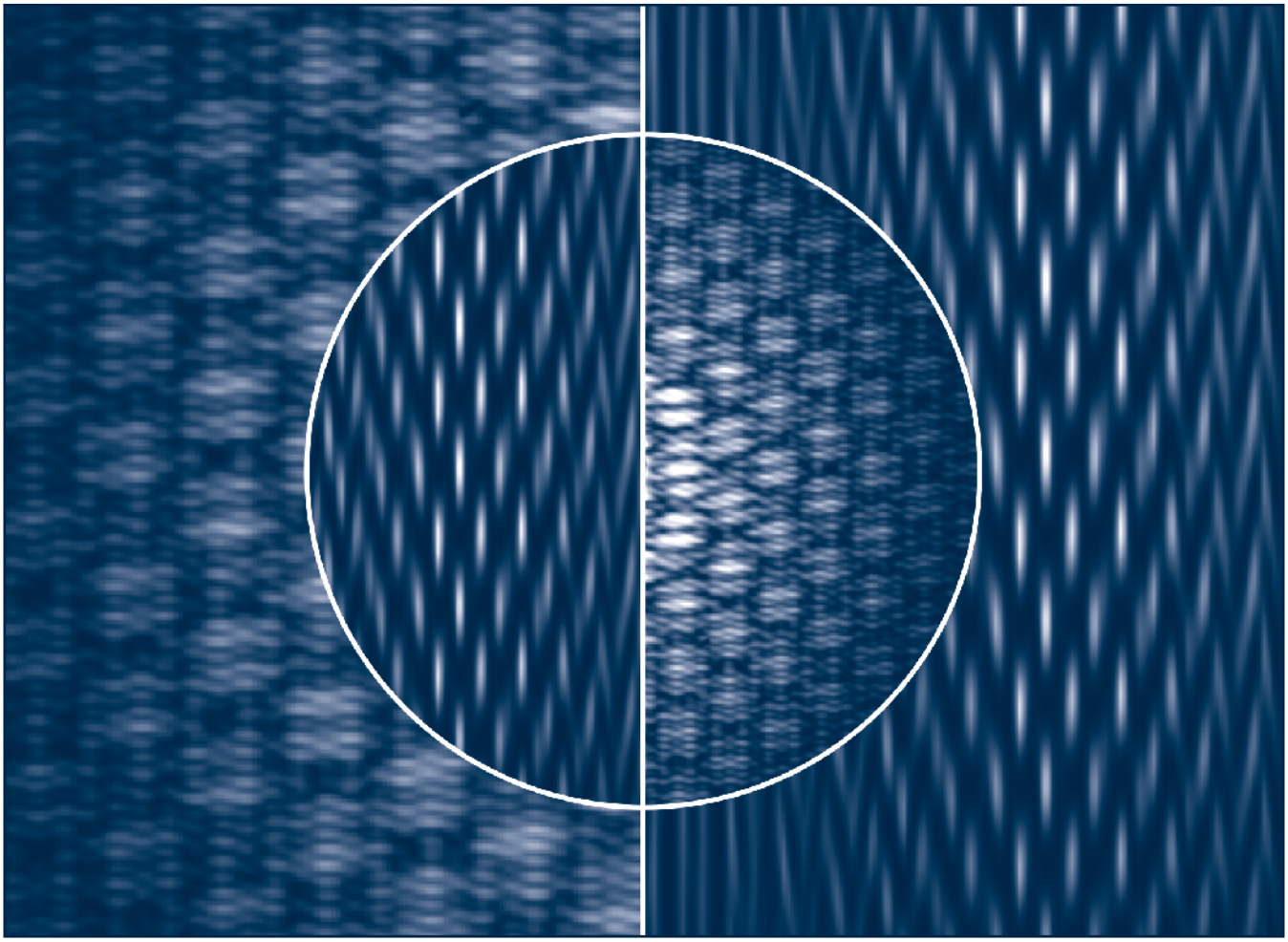

Max-Born-Institut

für Nichtlineare Optik
und Kurzzeitspektroskopie
im Forschungsverbund Berlin e.V.

Annual Report 2021

2021 in Figures

Budget

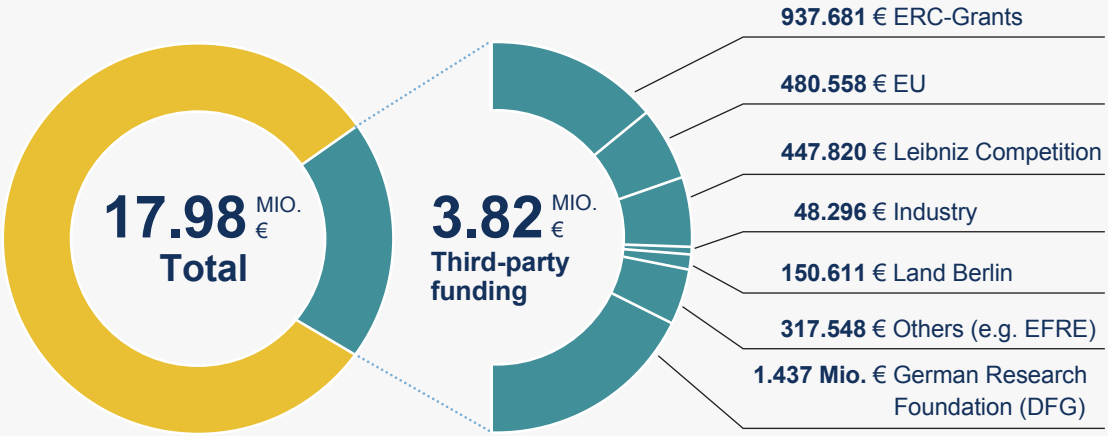

Staff total

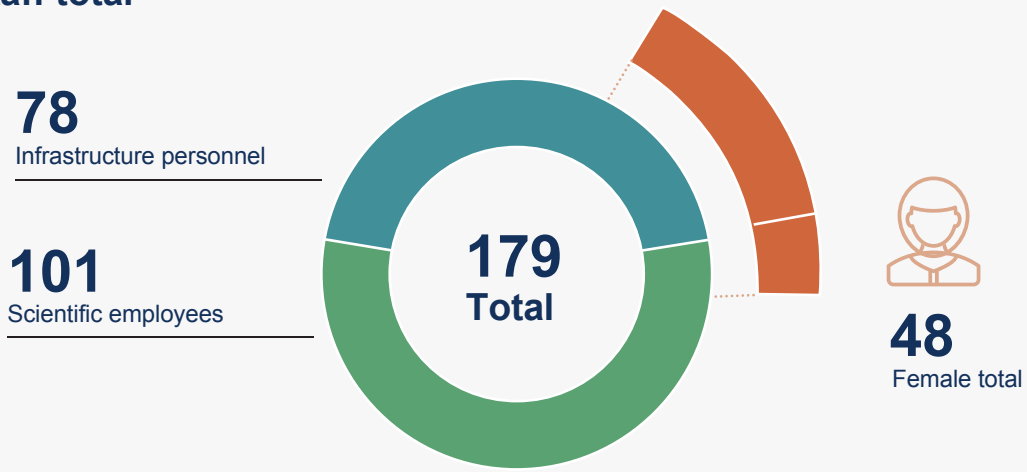

Scientific staff

There are two Junior Research Groups at MBI.

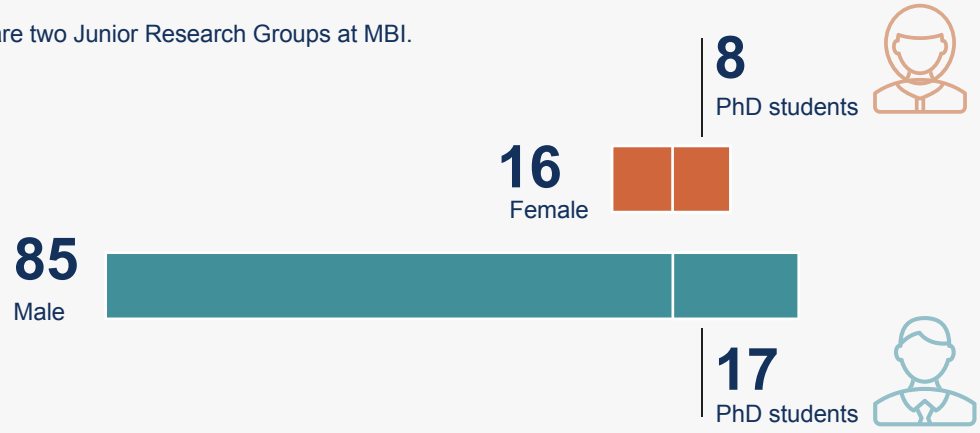

Publications

Scientific communication

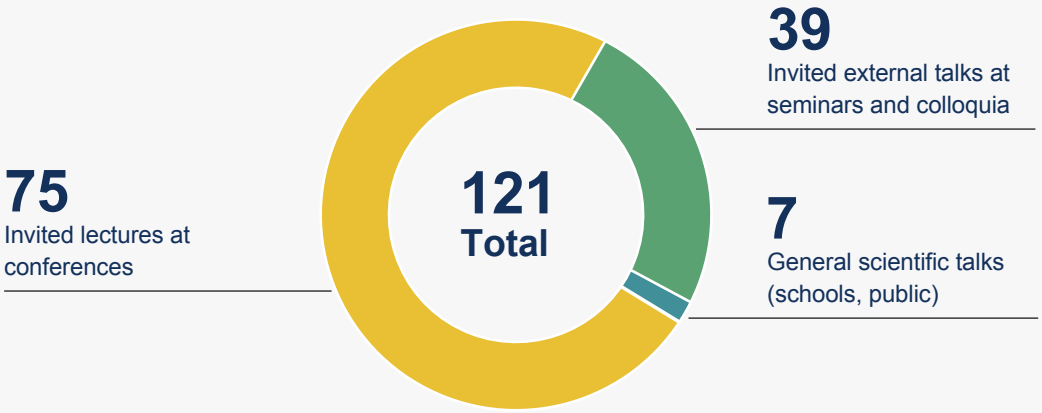

Education and Teaching

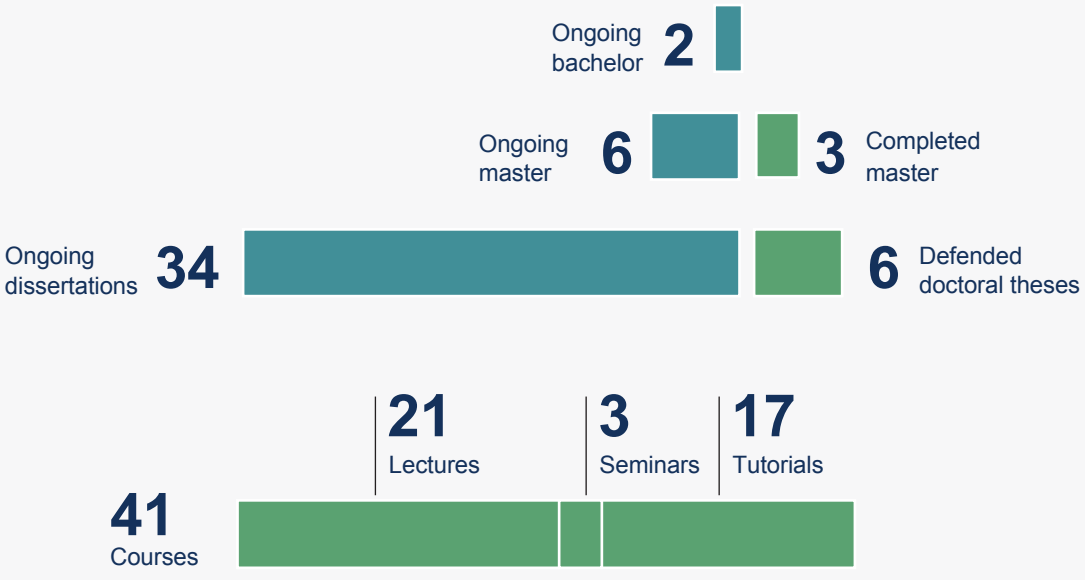

Annual Report 2021

Max-Born-Institut
für Nichtlineare Optik
und Kurzzeitspektroskopie
im Forschungsverbund Berlin e.V.

Max-Born-Straße 2 A
12489 Berlin
Germany
Phone: (++49 30) 63 92 - 15 05
Fax: (++49 30) 63 92 - 15 19
mbi@mbi-berlin.de
www.mbi-berlin.de

Preface

This Annual Report provides an overview of the research pursued at the Max-Born-Institute (MBI) in 2021. A presentation of scientific highlights is followed by progress reports of all projects which are part of the scientific program of the institute. A complete record of publications and invited talks is given in the appendix, together with information on academic teaching and training, guest lectures, activities in scientific organizations, and third-party funding. A new element in the Annual Report are two pages presented under the header “2021 in Figures”, which provide a bird’s eye view on the activities and organizational structure of the institute. We hope that these pages facilitate getting a quick, yet accurate overview of the institute, and motivate a more detailed exploration of the materials that are presented in the remainder of the Annual Report. Further information is available on the MBI website (http://www.mbi-berlin.de).

In 2021, the COVID-19 pandemic continued its severe impact on life at the institute. While the institute managed to organize the presence of its research staff in a manner that allowed most laboratories to remain operational, a significant fraction of the staff had to be asked to work from home, and the social life at the institute was limited by the continued necessity to organize meetings involving a larger number of staff members as online events, with unavoidable negative consequences for the level of scientific discourse. It is with this in mind, that the institute eagerly looks forward to the time, hopefully in the not too distant future, that work at the institute can go back to normal (to the extent that this may be possible, considering currently ongoing geo-political developments …).

The following key results are representative of the extensive scientific output of MBI in 2021:

- A novel compact scheme was developed for achieving high focused extreme ultra-violet (XUV) intensities, rivaling the intensities achieved at free electron lasers. In the scheme, high-harmonic generation (HHG) is performed at a distance of several Rayleigh lengths from a tight focus, leading to a situation where the generated XUV light has a virtual source size of just a few microns. Upon further demagnification of the XUV source using a focusing optic, sub-micron XUV foci were achieved, and 4-photon ionization of Argon (producing Ar^{3+}) was observed, using a standard Ti:Sapphire laser as the driver of the experiment.

- Attosecond science makes use of extreme ultra-violet (XUV) and soft X-ray laser pulses, that are ionizing radiation for any sample that is placed in the beam path. Accordingly, it is expected that attosecond pump-probe experiments are frequently influenced by quantum entanglement between the ion and photoelectron that are produced in an ionization process by the attosecond pulse. In a theoretical study, which meanwhile was also followed by a successful experiment, the role of ion + photoelectron entanglement was demonstrated to be limiting the degree of vibrational coherence in H^{2+} ions formed by attosecond ionization, and it was suggested how the use of phase-locked attosecond pulse sequences can be used to advance studies of attosecond laser-induced charge migration.

- Nonlinear terahertz (THz) spectroscopy has given new insight in the many-body dynamics of electrons in water and alcohols. The relaxation of nonequilibrium electrons in the liquid initiates collective charge oscillations at THz frequencies, which persist for tens of picoseconds. The underlying polaron excitation is a hybrid mode of a mixed electronic-vibrational character and a frequency determined by dipole-dipole interactions and the electron concentration in the liquid. The weak damping points to a longitudinal character of the oscillations. Polaron dynamics are governed by long-range Coulomb interactions involving several thousands of solvent molecules, while local electron solvation geometries play a minor role.

- Nonequilibrium lattice dynamics in few-layer hexagonal boron nitride (hBN), a prototypical quantum material, were studied in collaboration with groups from Montpellier, Nantes, Paris, and Ithaca. Femtosecond mid-infrared experiments and theoretical work demonstrate a 1-ps lifetime of transverse optical (TO) phonons and show that TO phonon excitations within individual layers of hBN couple directly to motions of the layers against each other. For a period of some 20 ps, the anharmonic coupling of the two types of excitation results in a frequency down-shift of TO phonons and their infrared absorption line. This behavior is a genuine property of the quantum material and of interest for applications in high-frequency optoelectronics.

- Resonant soft x-ray scattering is a powerful approach to analyze structural as well as magnetic order down to the approx. 1 nm length scale – so far, however, use of this photon-hungry combination of spectroscopy and scattering was limited to large scale facilities. Targeting picosecond time resolved studies of magnetic order, MBI scientists have set up the first laser-driven plasma source and associated high-efficiency beamline and diffractometer enabling the lab-based use of this method. In a proof of principle experiment, the laser-induced temporal evolution of antiferromagnetic order in conjunction with the superlattice dynamics could be followed in a synthetic antiferromagnet with a temporal resolution of 10 ps. This development fills a temporal gap for time resolved resonant diffraction opening up at synchrotron radiation sources, where the push for diffraction-limited x-ray beams results in >100 ps pulse duration.

- Magnetic skyrmions in thin magnetic films are quasiparticles with a non-trivial topology, the latter determining their dynamics and stability. In the context of potential applications, MBI scientists have systematically explored how magnetic skyrmions can be generated and controlled via femtosecond laser pulses as opposed to the common but much slower current-pulse-based manipulation. Via control of the laser fluence and external magnetic field, the areal density of skyrmions generated from a magnetically saturated state can be precisely controlled. Furthermore, single laser pulses of appropriate fluence can be used to randomize the skyrmion positions at constant skyrmions density, which is of interest for stochastic computing schemes based on magnetic information bits.

- Intense few-cycle light pulses, or multi-color light fields with sub-cycle control over the time-delays between the colors, offer opportunities to excite and control attosecond electron currents and polarization in molecules. In chiral molecules, these currents and polarization can lead to highly enantio-sensitive electronic dynamics. Several novel, highly efficient all-optical schemes for chiral recognition have been proposed theoretically. The schemes are based on using intense laser fields to induce and control attosecond electronic currents in chiral molecules and observing light emitted by these currents, leading to macroscopic enantio-sensitive nonlinear-optical response in the far field.

- Optical inter-site spin transfer (OISTR) is one of the fastest mechanisms for local spin-manipulation which, since its theoretical prediction, has been confirmed experimentally in several ferro-magnets. In original work it was proposed that this mechanism can lead to a transient ferromagnetic state in a material possessing an antiferromagnetic ground state. In the recent joint theory-experimental work, this prediction was confirmed by demonstrating the emergence of such a transient ferro-magnetic state in Co/Mn films. These results prepare the ground for future femtosecond scale laser control over magnetic order, with a view to designing optical switches at the femtoscale.

All in all, 167 articles have been published in peer-reviewed journals and books, including a substantial number of papers in high-impact journals. In this second year of the COVID-19 pandemic, the number of invited talks at international conferences naturally was lower than customary in previous years, due to cancellation of a large number of conferences.

In 2021, MBI scientists received several honors. Among these, Thomas Elsaesser received the 2022 Ahmed Zewail Award of the American Chemical Society (ACS), Lorenz Drescher received the 2021 Carl Ramsauer Award of the Deutsche Physikalische Gesellschaft zu Berlin (PGzB) and Michael Schneider received the 2021 XFEL Young Researcher Award. MBI was twice successful in the annual Leibniz SAW competition, acquiring both a grant within the Leibniz Professorinnenprogramm (Sangeeta Sharma) as well as funding for a project within the Leibniz Cooperative Excellence scheme (Arnaud Rouzée).

Berlin, March 2022

Stefan Eisebitt Thomas Elsaesser Marc Vrakking

Research Structure of the Max-Born-Institut

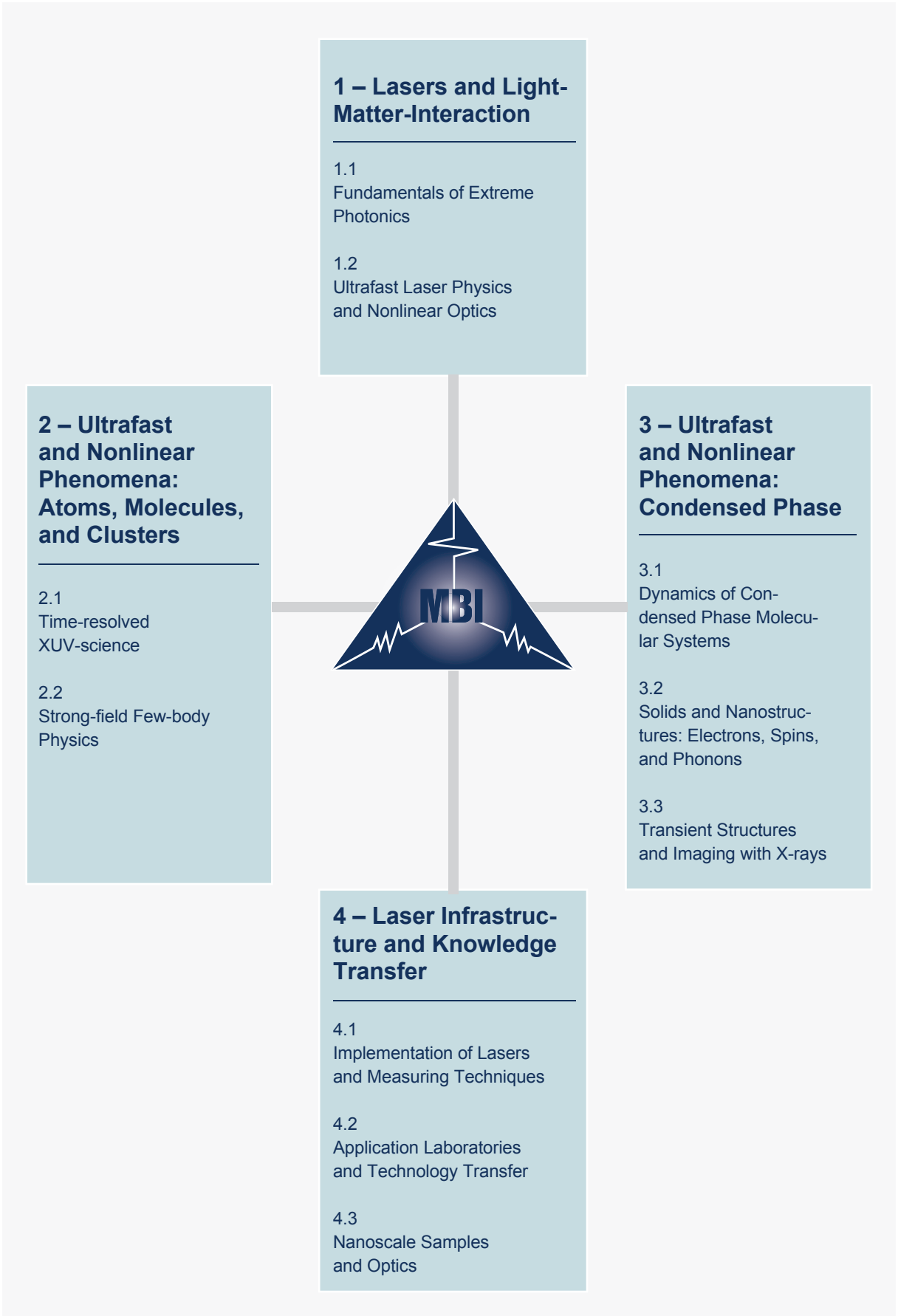

Organizational Structure of the Max-Born-Institut

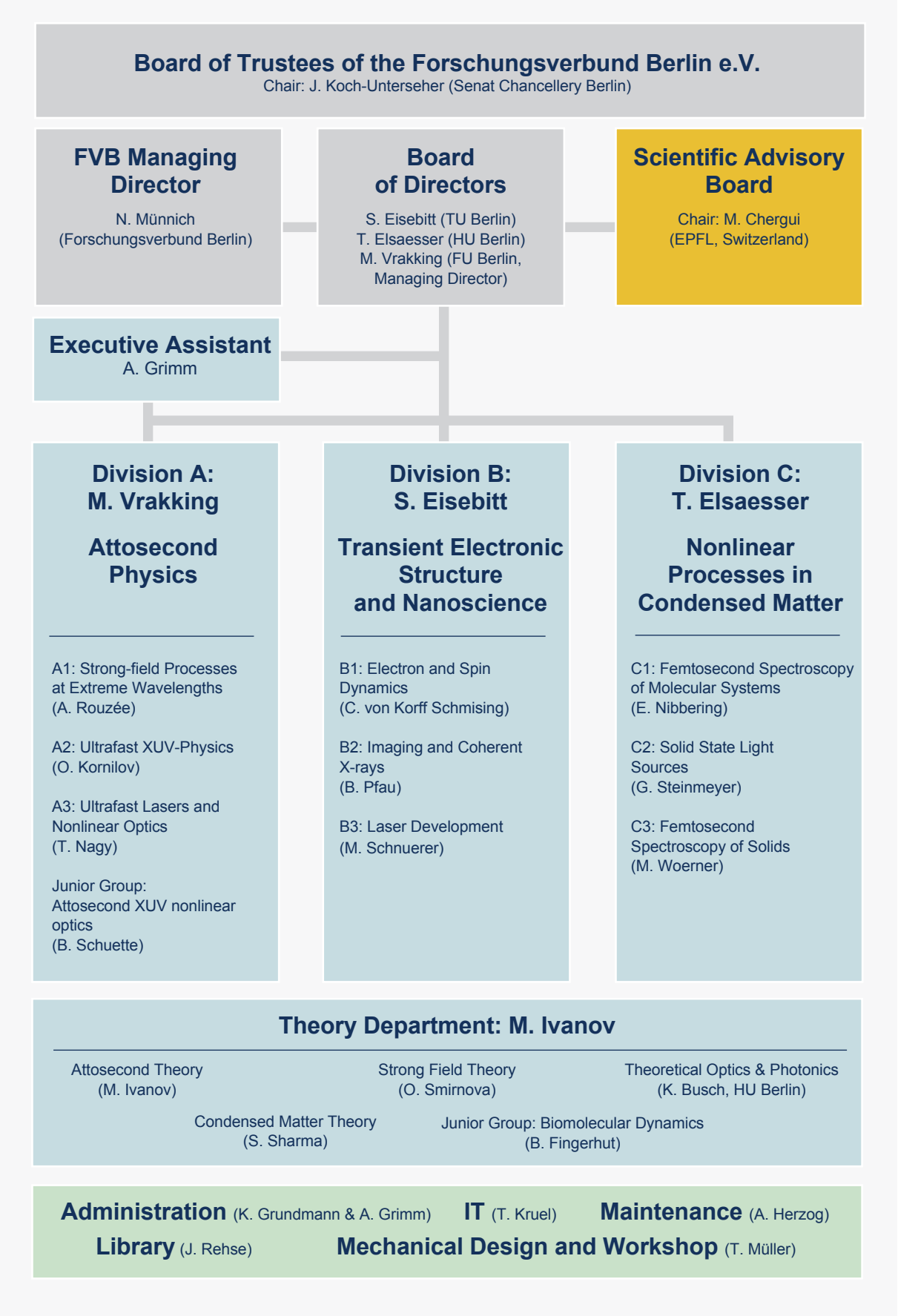

Members of the Scientific Advisory Board

Prof. Dr. Giulio Cerullo
Politecnico de Milano, Dipartimento di Fisica, Italy

Prof. Dr. Majed Chergui (Chair)
École Polytechnique Fédérale de Lausanne (EPFL), Institute of Chemical Sciences and Engineering, Switzerland

Prof. Tony Heinz
Stanford University, Department of Applied Physics, USA

Prof. Dr. Jon Marangos
Imperial College London, Department of Physics, UK

Prof. Dr. Christoph Quitmann
RI Research Instruments GmbH and Lund University, Max IV Laboratory, Sweden

Prof. Dr. Ursula Roethlisberger
École Polytechnique Fédérale de Lausanne (EPFL), Institute of Chemical Sciences and Engineering, Switzerland

Prof. Dr. Regina de Vivie Riedle
Ludwig-Maximilians-Universität München (LMU), Department Chemie, Germany

Prof. Dr. Jan Michael Rost
Max-Planck-Institut für Physik komplexer Systeme, Dresden, Germany

Representatives of the Cooperating Universities

Prof. Dr. Christoph Koch
Humboldt-Universtität zu Berlin, Institut für Physik, Germany

Prof. Dr. Andreas Knorr
Technische Universität Berlin, Institut für Optik und Atomare Physik, Germany

Prof. Dr. Martin Weinelt
Freie Universität Berlin, Fachbereich Physik, Germany

Representatives of the Federal Republic and the State of Berlin

Jan Neitzke
Bundesministerium für Bildung und Forschung, Ref. 711, Bonn, Germany

Dr. Heike Mewis
Senatskanzlei, Wirtschaft und Forschung, Ref. VI D, Berlin, Germany

MBI is a member of the Leibniz Association

Leibniz Association

Scientific Highlights

White turns into (extreme-)ultraviolet

L. Drescher, O. Kornilov, T. Witting, V. Shokeen, M. J. J. Vrakking, and B. Schütte

Light, as emitted by the sun, consists of many different colors and typically appears as white. Sometimes, however, only certain colors reach our eyes, leading to stunning phenomena like an afterglow. For technical or scientific applications that require a specific color, gratings and prisms can be used to extract this color from the white light. However, most of the incoming light is lost during this process, and the light intensity at the exit is very low.

Nonlinear optical techniques have made it possible to change the color of light and modify its spectral bandwidth without compromising the intensity. As illustrated in Fig. 1, this enables the generation of light with a specific color from broadband light (such as white light) or vice versa. These techniques are widely applied in spectroscopy, imaging, and for the generation of ultrashort laser pulses. However, nonlinear optical techniques are not readily available in the extreme-ultraviolet (XUV) region of the electromagnetic spectrum. This region is of increasing interest for various applications, including attosecond science and EUV lithography.

We have recently demonstrated a new concept to generate narrowband laser pulses in the XUV range. Broadband white light in the visible region was combined with light having a broad spectrum in the vacuum-ultraviolet (VUV) region. After both of these light pulses simultaneously propagated through a dense jet of krypton atoms, a new laser pulse in the XUV range was generated. Remarkably, the spectral width of the new XUV pulse was more than hundred times narrower compared to the initial visible and VUV pulses.

The scientists employed a scheme known as four-wave mixing, where one krypton atom absorbs two visible photons and one VUV photon, leading to the emission of one XUV photon. Due to energy conservation, the emitted XUV photon must have a frequency equal to the sum of the frequencies of all three absorbed photons. At the same time, due to momentum conservation, the velocity of the incoming light wave has to match the velocity of the outgoing wave inside the mixing medium. This velocity changes very fast close to an atomic resonance.

To generate the narrowband XUV laser band, we chose a VUV spectral range quite far away from any resonance and a target XUV range between two resonances. In doing so, the velocities of a broad range of incoming wavelengths could be matched to a narrow region of outgoing wavelengths. In Fig. 2, on the left side, absorption in the VUV over a broad spectral range (blue area) is indicated. The red dashed curve indicates the frequency-dependent refractive index, which is a measure of the light velocity. On the right side, a narrow spectral region in the XUV range (violet area) is shown. In these regions, the light travels approximately at the

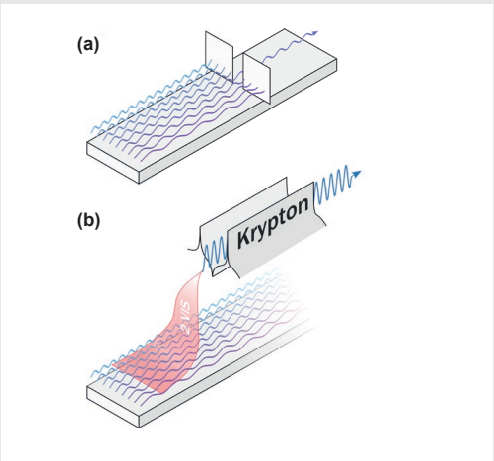

Fig. 1:
(a) A specific color can be selected from a broadband light source using e.g. a prism or a grating. This comes, however, at the expense of losing most of the light. (b) By applying a nonlinear optical technique such as four-wave mixing in krypton, it is possible to generate a specific color using all the available light at different colors.

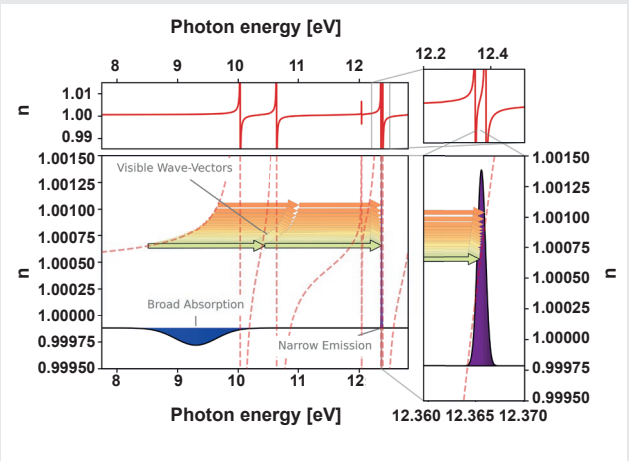

Fig. 2:
XUV spectral compression scheme: The refractive index as a function of the photon energy is shown by the red dashed curve. In the region around 9.2 eV it changes comparably slowly (left side), whereas it changes very fast in the region around 12.365 eV. Therefore, a broadband absorption (blue area) can lead to a narrowband emission (violet area) with the help of two visible photons (shown by the arrows).

same speed, i.e., with a similar refractive index. These velocities can be matched by the near-horizontal arrows indicating the photons in the visible spectrum. The illustration shows that this allows converting a broadband VUV spectrum with a relatively flat wavelength-velocity dependence into a narrowband XUV pulse, where the wavelength-velocity dependence is near vertical.

The generation of narrowband XUV pulses is interesting for applications such as electron spectroscopy, the investigation of resonant transitions, and the coherent diffractive imaging of nanoscale structures. In the future, the new method could also be used in the opposite direction, i.e., to spectrally broaden XUV pulses, which may result in the generation of very short XUV pulses from sources such as free-electron lasers and soft-X-ray lasers.

Publication

DKW21: L. Drescher, O. Kornilov, T. Witting, V. Shokeen, M. J. J. Vrakking, and B. Schütte; Extreme-ultraviolet spectral compression by four-wave mixing; Nat. Photonics **15** (2021) 263-266

Tracking down antiferromagnets

D. Schick, M. Borchert, J. Braenzel, H. Stiel, J. Tümmler, C. von Korff Schmising, B. Pfau, and S. Eisebitt

For a long time, antiferromagnetic (AFM) spin order was only interesting from a theoretical point of view, e.g. as a precursor phase of superconductivity. The absence of a net magnetization seemed to prevent most technological applications. With the recent advances in reading and controlling the AFM spin order e.g. by electrical currents and light, the zero net magnetization has turned into a great advantage compared to ferromagnetic (FM) systems – domain configurations in AFM materials are stable against external magnetic fields, the lack of magnetic stray fields allows for smaller domain sizes to store bits of information, and the intrinsic time scale to manipulate magnetization states is orders of magnitudes faster compared to FM materials. This renders antiferromagnets as promising candidates for faster and more energy-efficient data processing and storage.

Along this way, resonant magnetic scattering in the soft X-ray region – a combination of spectroscopy and scattering experiment – allows for direct insight into the otherwise elusive spin order of antiferromagnets. Towards that end, the probing photon energy must be tuned to an atomic resonance generating a suitable magnetic contrast and the associated wavelength must be smaller than the periodicity of the AFM order. Due to these demanding requirements such experiments could so far exclusively be performed at large-scale facilities, such as synchrotrons and free-electron lasers, which provide sufficient intensity and energy-tunability in the soft X-ray range. Due to the lack of suitable laboratory-scale sources, the availability of this powerful experimental method was severely limited. At the Max Born Institute, it has now been possible for the first time to study spin and lattice dynamics of an antiferromagnetic sample using resonant magnetic scattering at a laser-driven source.

We utilized and optimized an established technique for generating soft X-rays – a laser-driven plasma source. A thin-disk laser system was developed for this and similar applications: it emits high-energy pulses (150 mJ) of 1.5 picosecond duration at a wavelength of 1030 nm. These pulses are focused onto a metal cylinder made of tungsten. In the focus, the extremely high peak intensities lead to the generation of a plasma, which emits light over a very broad spectral range with a sufficiently large soft X-ray flux between 600-1500 eV, covering in particular the transition-metal *L*- and rare-earth *M*-edges, which are of high relevance in magnetism research. Based on our first time-resolved experiments, an upper limit for the duration of these soft X-ray pulses of 10 picoseconds was established. Using a reflection zone plate (RZP), it is possible to collect sufficient soft X-ray flux from the plasma emission and utilize it for resonant magnetic scattering experiments. Here the RZP acts as a single optical element to both focus and disperse the soft X-rays; a suitable bandwidth for a scattering experiment is selected via a slit. Figure 2 show the linear reflectivity spectrum in resonance with the Fe *L*-edges from an antiferromagnetic Fe/Cr superlattice.

To demonstrate the laboratory-based concept of resonant magnetic scattering, we have investigated an artificial antiferromagnet. A Fe/Cr superlattice with alternately layers of pure iron and chromium each only about a nanometer thick was grown by magnetron sputtering.

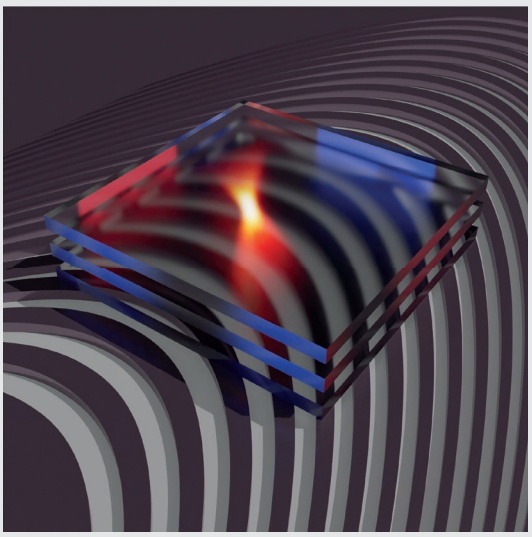

Fig. 1:
Artistic impression of the resonant magnetic scattering experiment. The reddish X-ray spectrum is scattered by an artificial antiferromagnet. The elliptical structure of the reflection zone plate appears in the background. Credit: Moritz Eisebitt.

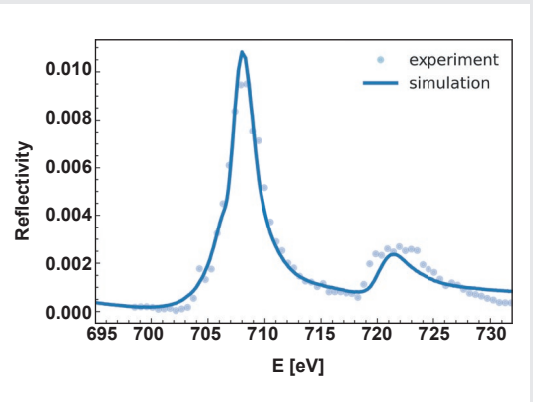

Fig. 2:
Reflectivity spectrum around the Fe L_3 and L_2 absorption edges of the Fe/Cr superlattice, measured at a grazing incidence angle $\vartheta = 10°$. The solid line represents a simulation including magnetic and charge scattering.

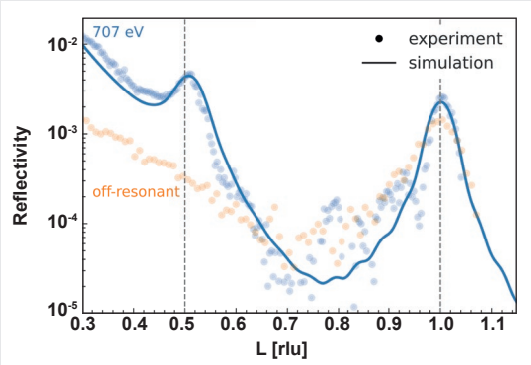

Fig. 3:
Static L-scan of the Fe/Cr superlattice at resonance (E = 707 eV, blue dots) and off resonance (E = 680 eV, orange dots). The blue solid line represents a scattering simulation of the sample structure including magnetic and charge scattering. At L = 1 the structural Bragg peak is present for both photon energies, while the AFM Bragg peak at L = 0.5 only appears on-resonance and is also reproduced by the simulations.

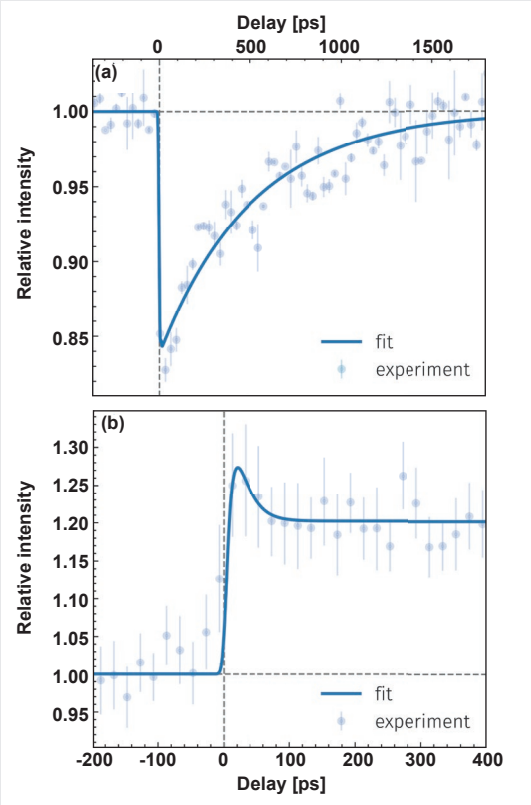

Fig. 4:
(a) Delay scans of the SL0.5 AFM Bragg peak intensity at the Fe L_3 absorption edge. The peak intensity decreases within a few picosecond and recovers over hundreds of picosecond upon photoexcitation, tracing the magnetic response of the sample. (b) Delay scans on the low-angle side of structural SL1.0 peak at L = 0.95. The rapid rise of the signal is due to a Bragg peak shift toward smaller L because of the photoinduced lattice expansion.

The iron layers themselves are ferromagnetic, but they align exactly antiparallel to their next neighbour iron layer, because of the interlayer exchange coupling mediated by the chromium layers in between. The multilayer system thus has a *magnetic* periodicity that is exactly twice as large as the *structural* periodicity, resulting in a so-called antiferromagnetic superstructure. As shown in Fig. 3, both periodicities can be resolved by resonant soft X-ray scattering, where they give rise to well-separated distinct peaks at the corresponding momentum transfer. In this fashion, both the structural order as well as the elusive antiferromagnetic order can be directly followed, e.g. in response to excitation by a laser pulse in time resolved experiments.

In this fashion, we have used this approach in first pump-probe experiments tracking the AFM order parameter as well as the strain-wave induced lattice deformation on a picosecond time scale after photoexcitation. As shown in Fig. 4(a)) the intensity of the AFM Bragg peak at L=0.5 drops upon excitation at delay t=0 picoseconds within a few picoseconds and a slow recovery over more than a nanosecond. These dynamics can be well explained by an ultrafast quenching of FM order in the individual Fe layers due to the excitation of electrons by the intense pump pulses and a subsequent loss of AFM order within the whole superlattice. The photoexcited electrons also couple to the lattice degree of freedom by launching coherent and incoherent phonons, typically resulting in a pronounced shift of the structural Bragg peak. This is shown in Fig. 4(b)) where we plot the scattered intensity at the low-angle slope of the structural SL1 Bragg peak at L=0.95, to translate the peak shift into an intensity modulation of the detected X-ray signal. The recovery of the Bragg peak position happens again on a nanosecond time scale (not shown) and provides important information about heat diffusion within the superlattice with its high density of interfaces.

In the future, a full spatiotemporal map of the correlated spin and lattice dynamics will be accessible via time-resolved reciprocal-space-scans, complemented by scattering simulations allowing to model the underlying microscopic processes. We are convinced that our laboratory-based approach is a powerful alternative to picosecond scattering experiments at synchrotron facilities, which require special operation modes to reach the temporal resolution demonstrated here

Publication

SBB21: D. Schick, M. Borchert, J. Braenzel, H. Stiel, J. Tümmler, D. E. Bürgler, A. Firsov, C. von Korff Schmising, B, Pfau, and S. Eisebitt; Optica **8** (2021) 1237-1242

Ultrafast reshuffling of skyrmions

K. Gerlinger, B. Pfau, and S. Eisebitt

Smaller, faster, more energy-efficient: future requirements to computing and data storage are hard to fulfill and alternative concepts are continuously explored. Small magnetic textures, so-called skyrmions, may become an ingredient in novel memory and logic devices. In order to be considered for technological application, however, fast and energy-efficient control of these nanometer-sized skyrmions is required.

Magnetic skyrmions can exist in thin magnetic films with perpendicular magnetic anisotropy as isolated, particle-like magnetization textures. They appear as spherical bubbles in the magnetic film with a magnetization that continuously reverses from the outside to the inside. In particular, skyrmions are distinguished from other textures by their particular topology of the magnetization vector field. As a result, the creation or annihilation of a skyrmion involves a transition of the magnetic system's topology which is considered to cause a certain topological protection against this transition. This topological stability of skyrmions makes them attractive for data storage and data-processing technologies but also renders their fast creation very difficult.

It is already known that skyrmions can be created and moved by short pulses of spin-polarized electric current. However, recent research has revealed that also ultrashort laser pulses are able to create skyrmions in suitable materials. We have recently discovered that this creation proceeds via a high-temperature state where spin fluctuations lead to the formation of topological skyrmion nuclei on a time scale of approximately 300 ps. Later these nuclei coarsen to their equilibrium room-temperature size and density during cool-down of the magnetic film (see highlight in MBI annual report 2020 and F. Büttner et al., Nat. Mater. 20 (2021) 30).

Here, we investigated in detail how laser-based creation and annihilation of skyrmions can be controlled to promote the application of this process in devices. In particular, we systematically studied the influence of the applied magnetic field and the laser fluence on the creation process in two different ferromagnetic multilayers, a symmetrically stacked Co/Pt multilayer and an asymmetric Pt/CoFeB/MgO multilayer with a resulting sizeable antisymmetric exchange interaction, also known as Dzyaloshinskii-Moriya interaction. We imaged the magnetization textures nucleated from a single femtosecond laser pulse with holography-based soft-X-ray imaging at the PETRA-III synchrotron-radiation source in Hamburg, Germany. To this end, a mobile X-ray holography endstation used in these experiments was equipped with a fiber-laser system for in-situ excitation of the magnetic film, allowing to combine laser excitation with synchrotron-radiation-based probing.

First, we discovered that the density of the skyrmion patterns depends linearly on the magnetic field applied in the film's out-of-plane direction (Fig. 1(a)). We observed this behavior in both materials. The applied field, therefore, provides an easy and direct handle to control the number of skyrmions generated in a certain area. At high fields, it is possible to create a single skyrmion within our field of view of 1.5 µm diameter. Furthermore, such a single skyrmion can be subsequently deleted by an additional single laser pulse after slightly increasing the strength of the external magnetic field. A laser can, therefore, be used to write and erase information encoded by skyrmions.

Second, we found a sharp threshold for the laser fluence required to create skyrmions via a single pulse (Fig. 1(b)). This threshold is material dependent. Above it, the

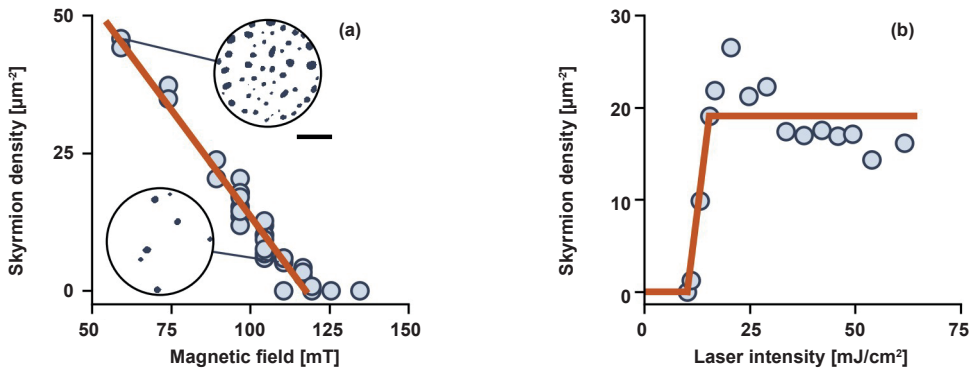

Fig. 1:
Properties of laser-induced skyrmion creation. (a) Linear dependence of the skyrmion density on the applied field. Insets show examples of magnetization images of the laser-nucleated skyrmion patterns within a circular field of view of 1.5 µm. Scale bar is 0.5 µm. (b) Sharp laser intensity threshold for skyrmion creation via a single laser pulse.

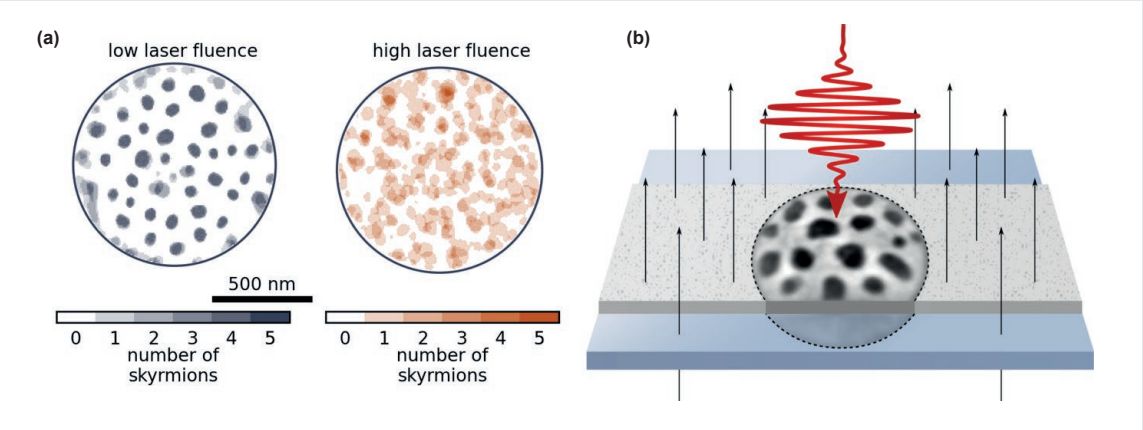

Fig. 2:
Proposal of an ultrafast "skyrmion reshuffler": (a) Probability maps for skyrmion positions after exposing an existing skyrmion pattern (compiled as the sum of 5 skyrmion patterns). At low fluence (above the nucleation threshold), the pattern is reproduced after every pulse. Only at high fluence, the pattern is rewritten and, thus, randomized. (b) Artistic scheme of the "skyrmion reshuffler" device for stochastic computing. The skyrmion density (the probability value) is adjusted by the externally applied magnetic field. The laser pulse creates a random arrangement of skyrmion data bits in the stripline used for storing the data.

skyrmion density created is almost independent of laser fluence for a given external magnetic field. In contrast to current-pulse induced skyrmion nucleation, the skyrmion creation probability is spatially remarkably homogenous. Within the above-threshold illuminated area, skyrmions appear at random positions in the film, if the laser pulse impinges on a fully "erased", magnetically saturated sample. However, when exciting a magnetic film with an existing skyrmion pattern with another laser shot, the skyrmion pattern remains unaltered if the laser fluence is too close to the creation threshold. Only laser pulses of significantly higher fluence (in our case roughly twice as high as the nucleation threshold) are able to completely erase the existing skyrmion pattern and recreate a new one (Fig. 2(a)). In this case, the new skyrmion positions exhibit no correlation with the previous positions.

We proposed, that this skyrmion creation process can be used as a "skyrmion reshuffler" in stochastic computing (Fig. 2(b)). There, numbers are represented as strings of random bits of "0" and "1", with the probability to encounter "1" encoding the number value. Computations can then be carried out via logic operations between individual bits of bit-streams representing different input numbers. While this scheme is inherently very error tolerant, it requires decorrelated gate inputs for correct results of stochastic computing operations. Magnetic skyrmions have been proposed as the physical realization of individual bits in such stochastic computing approaches. As demonstrated in our work, the required randomizing "reshuffling" of skyrmions while retaining the same skyrmion density can be performed optically on a timescale of picoseconds, compatible with state-of-the-art computer clock speed and much faster than in previously proposed concepts based on thermal diffusion operating on the timescale of seconds..

Publication

K. Gerlinger *et al.*; Appl. Phys. Lett. **118** (2021) 192403/1-7

Mono-cycle terahertz pulses from intersubband shift currents in asymmetric semiconductor quantum wells

M. Runge, T. Kang, K. Biermann, K. Reimann, M. Woerner, T. Elsaesser

A time-dependent electric current emits an electromagnetic wave, a basic physical effect exploited in telecom antennas. Transferring this mechanism to the ultrashort length and time scales of the quantum world allows for generating intense picosecond terahertz (THz) pulses in asymmetric semiconductor quantum structures. The THz pulses display a single oscillation of the electric field and can be tailored via the nonlinear generation process.

THz waves are an important analytical tool in science and technology, with applications ranging from materials and tissue characterization to security checks at airports. Ultrashort THz pulses with a duration of a few picoseconds (1 ps = 10^{-12} s) are used in time-domain linear THz spectroscopy and, with high electric-field amplitudes, in nonlinear time-resolved spectroscopy of condensed matter, such as two-dimensional THz (2D-THz) spectroscopy. Moreover, they play a key role in telecommunication at ultrahigh data transmission rates. The strong potential of THz methods and technology calls for the development of efficient and compact THz sources.

Scientists from the THz team of project 3.2 and the Paul-Drude-Institute in Berlin have now demonstrated a novel concept for generating ultrashort THz waveforms by tailoring electronic currents in a highly compact optically driven quantum device [RKB21]. A mid-infrared driving pulse generates a time-dependent electric current in a highly compact semiconductor structure consisting of 20 asymmetric nanometer-thick quantum wells. This current emits THz pulses, which consist of a single THz oscillation cycle with a peak electric field amplitude of up to several kilovolts/cm. The time structure of the THz pulses can be tailored via the excitation conditions of the quantum device.

The basic mechanism of THz generation is illustrated in Figure 1. Electrons are spatially confined in a quasi-two-dimensional potential well, which is asymmetric along the stacking axis (c axis) of the AlxGa1-xAs semiconductor layers. Due to the narrow width of the potential well, electron quantum states 1 and 2 with different (minimum) energies arise, the so-called subbands. The asymmetric shape of the potential along the c axis results in spatially shifted probability distributions of electrons in the two subbands. Upon electron excitation from subband 1 to subband 2 by a femtosecond mid-infrared pulse, the overall electron density experiences a time-dependent spatial shift of several nanometers within the asymmetric well. This transient spatial charge shift is equivalent to a time-dependent current. According to the basic laws of electrodynamics, this so-called shift current emits an electric field. For a femtosecond duration of the driving pulse, the frequency of the emitted field is in the THz range.

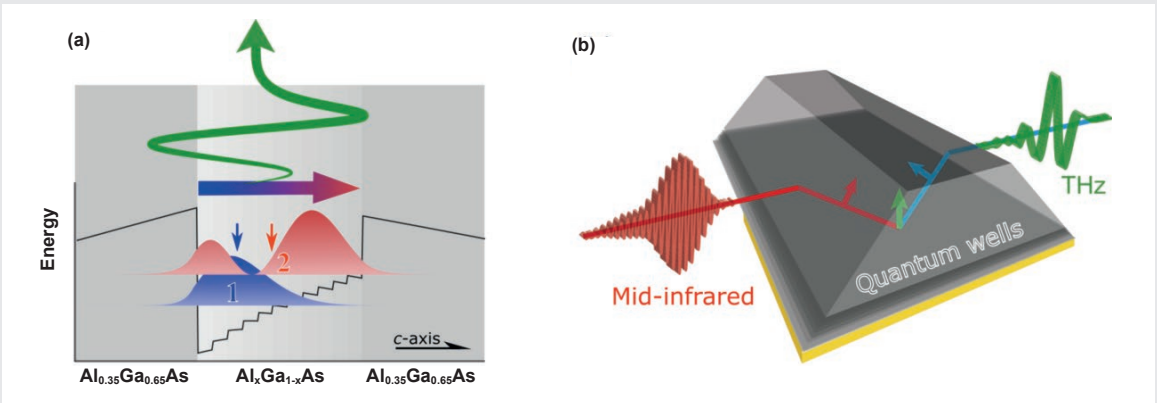

Fig. 1:
Ultrafast shift current generation in asymmetric semiconductor quantum wells and optical geometry. (a) Electrons are confined within a 13-nm wide quantum well made from AlxGa1-xAs. By varying the aluminum content one obtains an asymmetric ('triangular') potential, sandwiched between potential barriers. Quantum confinement leads to the formation of discrete energy levels 1 and 2 of electrons along the c axis. The contours are the spatially shifted probability distributions of electrons in the ground state (blue) and in the first excited state (red). The blue and red arrows mark the centers of gravity of the respective distribution. Electrons are promoted from state 1 to state 2 by an ultrashort mid-infrared pulse, resulting in a time-dependent spatial shift of electron position, which represents a time-dependent electric current. This so-called shift current emits a mono-cycle THz pulse. (b) Optical geometry of the THz source. 20 quantum wells are stacked at the bottom of a prism structure. They are excited by a femtosecond mid-infrared pulse (red transient, left). The THz pulses emitted in forward direction (green transient, right) are analyzed in the experiment. The height of the prism structure is approximately 350 µm.

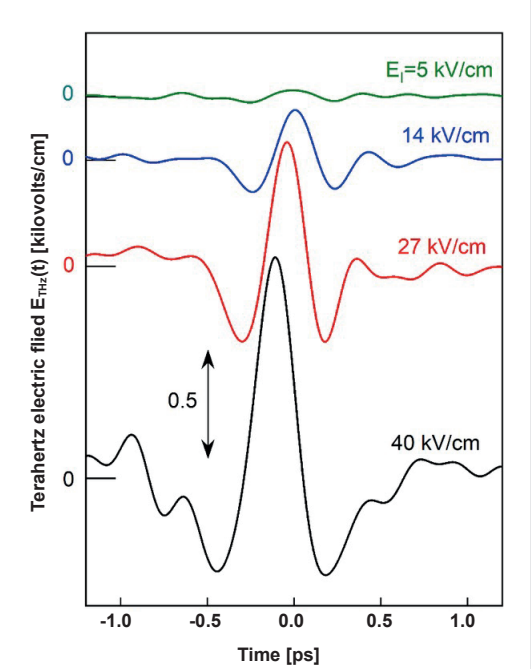

Fig. 2:
(Terahertz waveforms emitted by shift currents in asymmetric quantum wells. The THz electric field ETHz is plotted as a function of time. It displays a single main oscillation. The time structure of the THz transient changes with the electric-field amplitude EI of the driving pulses, as is evident from the time shift of the maximum THz field with EI.

Figure 2 displays the emitted THz electric field as a function of time, as measured for different strengths of the mid-infrared driving pulse. All THz pulses are monocycles, i.e., the THz field oscillates only once during the pulse. The shape of the THz waveforms changes with the strength of the driving pulses, due to the nonlinear character of the generation process. This fact can be exploited to tailor the THz waveforms in a wide parameter range.

On top of the radiating shift-current, difference frequency mixing of spectral components of the mid-infrared driving pulse via the resonantly enhanced second-order nonlinearity of the quantum wells contributes to the overall THz emission. A 2D-THz experiment allows for the separation of the two contributions and demonstrates the prevalence of shift-current emission.

The overall THz generation efficiency of up to several percent of the driving mid-infrared field makes this scheme particularly interesting for generating versatile THz pulses in highly compact optoelectronic sources working at, e.g., gigahertz repetition rates.

Publication

RKB21: M. Runge, T. Kang, K. Biermann, K. Reimann, M. Woerner, and T. Elsaesser; Mono-cycle terahertz pulses from intersubband shift currents in asymmetric semiconductor quantum wells; Optica **8** (2021) 1638-164

Phonon-induced valence-charge relocation in cubic BN observed by ultrafast x-ray diffraction

S. Priyadarshi, I. Gonzalez-Vallejo, C. Hauf, K. Reimann, M. Woerner, and T. Elsaesser

Phonons, the quantized lattice excitations of a crystal, are typically described in the adiabatic limit by introducing a harmonic or anharmonic vibrational potential surface, the shape of which is determined by the charge distribution in the electronic ground state and the resulting interatomic interactions. The adiabatic approximation has been applied widely for interpreting nonlinear phonon dynamics. The adiabatic limit breaks down whenever phonons induce electronic motions such as charge transfer between lattice sites or charge rearrangements in polar covalent bonds. Such phenomena occur in a wide range of materials including polar semiconductors and ferroelectrics. The classical core-shell model introduced by Cochran treats the coupled nuclear and electronic motions by solving the mechanical equations of motion of coupled ions with polarizable electron clouds.

In a recent study [PGH], we experimentally demonstrate the direct impact of nonequilibrium acoustic phonon excitations on the valence charge distribution in the electronic ground state of crystalline matter. Cubic boron nitride (cBN) with the zinc blende crystal structure (Fig. 1(a)) is chosen as a prototypical system, in which the small number of core electrons allows for mapping relocations of valence charge by time-resolved x-ray diffraction. Transverse acoustic (TA) phonons, impulsively excited at the zone edge close to the L point by a second-order Raman process, induce a pronounced transfer of valence charge from the interstitial regions onto the B and N atoms, connected with an increase of diffracted intensity, opposite to a Debye-Waller scenario. This nonadiabatic behavior is caused by the coupling of nuclear and electronic degrees of freedom via local electric fields.

The cBN powder sample (≈100 µm thick) consists of very small crystallites (diameters of 165±50 nm) to ensure that the diffraction experiment is in the kinematic diffraction limit. The experiments at room temperature are based on a femtosecond time-resolved optical-pump–hard-x-ray-probe scheme. Optical pulses centered at 800 nm (E = 1.55 eV), i.e., far below the bandgap of cBN at Eg = 6.36 eV, generate a coherent superposition of phonon states by impulsive second-order Raman scattering within the spectral envelope of the pulses (bandwidth:

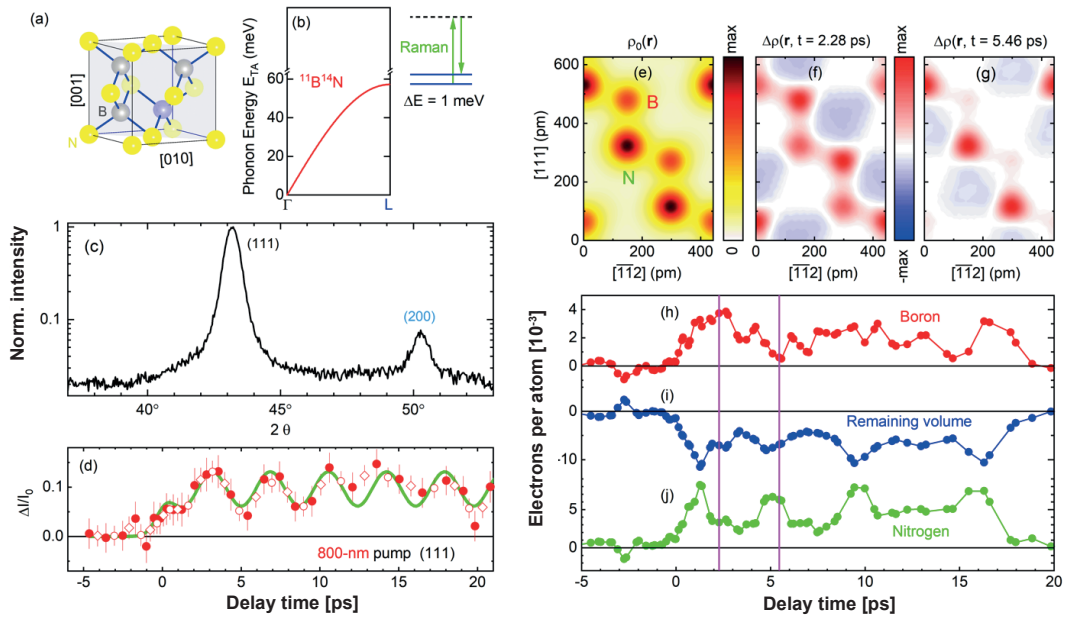

Fig. 1:
(a) Unit cell of cubic BN (cBN) with the (1-10) plane shown in light blue. (b) Transverse acoustic (TA) phonon dispersion along the Γ−L direction in k space for $^{11}B^{14}N$ (red line). The arrows show the Raman transitions. (c) Stationary diffraction intensity of cBN powder, integrated over the Debye-Scherrer rings as a function of 2θ. (d) Transient changes of diffracted intensity of the (111) reflection. (e) Stationary electron density $\rho_0(r)$ of cBN in the (1-10) plane [scale: 0 to 5340 e^-/nm^3]. (f), (g) Transient differential charge-density maps $\Delta\rho(r, t)$ for delay times of t = 2.28 ps (f) and t = 5.46 ps (g) after TA phonon excitation [scale: ±6 e^-/nm^3]. (h)–(j) Spatially integrated charge on the B and N atoms and in the remaining volume as a function of delay time.

ΔEp =50 meV) allowing for impulsive excitation of TA phonons at the L point. The impact of this lattice excitation on the electronic charge distribution is mapped by diffracting 100-fs hard-x-ray probe pulses off the sample.

Both, the optical pump and hard-x-ray probe pulses are derived from a Ti:sapphire laser system (sub-50-fs pulses, energy 5.2 mJ, 1 kHz repetition rate). Hard x-ray probe pulses [Cu Kα: photon energy 8.04 keV] are generated by focusing 4-mJ, 800-nm pulses onto a moving copper tape target (thickness 10 μm). The x-ray probe pulses are collected, monochromatized, and focused to a 100-μm spot size on the sample by a Montel optic. The x-ray photons diffracted from the sample are recorded by a large-area detector, which provides the intensities of multiple Debye-Scherrer rings simultaneously. Integration along Debye-Scherrer rings yields the x-ray intensity *I* as a function of 2θ showing the (111) and (200) reflections (Fig. 1(c)). The differential change in x-ray intensity is given by $\Delta I(t,\theta)/I0(\theta) = [Ipumped(t,\theta) - Iunpumped(\theta)]/Iunpumped(\theta)$. Upon excitation by the optical pump pulse, one observes changes of diffracted intensity on both (111) and (200) reflections, those for (111) are plotted as a function of pump-probe delay in panel (d). One observes a step-like increase of diffracted intensity superimposed by oscillations. Transient differential charge-density maps $\Delta\rho(r,t) = \rho(r,t) - \rho_0(r)$ are derived from the changes of diffracted x-ray intensity ΔI/I0 by analyzing the underlying changes of the x-ray structure factors with the maximum entropy method adapted to the conditions of the femtosecond experiment.

In Fig. 1(f) we show $\rho_0(r)$ in the (1-10) plane of the unit cell [panel (a)], with local maxima of ρ0(r) on the B and N atoms and a low quasi-continuous charge density throughout the (1-10) plane. In Figs. 1(g) and (h), transient differential maps $\Delta\rho(r,t)$ are shown for exemplary delay times of t = 2.28 ps and 5.46 ps, respectively. At t = 2.28 ps, charge density is transferred from the inter-atomic regions of the unit cell almost equally to both boron (B) and nitrogen (N) atoms. At t = 5.46 ps charge transfer towards the N atoms prevails. To illustrate charge dynamics within the cBN unit cell, we integrated the differential electronic charge over spherical volumes around the B and N atoms and in the remaining volume of the unit cell. The transients in Figs. 1(h) to (j) demonstrate an accumulation of charge on the atoms and a depletion in the rest of the unit cell. The interatomic length scale of charge relocations is orders of magnitude larger than the phonon-related nuclear displacements. On top of a step-like kinetics, the charge density displays oscillatory components with opposite signs on the atoms and in the remaining volume. A detailed analysis shows that the 250-GHz oscillations are due to quantum coherences between different zone-edge TA phonons, i.e., acoustic phonons involving $^{10}B^{14}N$ unit cells have a ≈ 2 % higher frequency than those involving $^{11}B^{14}N$ unit cells.

The intensity increase on the (111) and (200) diffraction peaks upon phonon excitation is in clear contrast to a Debye-Waller scenario. In the latter, the change of atomic positions connected with a phonon excitation results in a spatial smearing of electronic charge in the unit cell and a concomitant decrease of diffracted x-ray intensity. The intensity *increase* observed here requires a less broad distribution of valence electron density, which is accomplished by a charge transfer from the interstitial region onto the B and N atoms. Our experiments provide new insights into phonon-induced electronic charge relocations in ionic crystals. Moreover, ultrafast x-ray powder diffraction is a remarkable experimental tool to probe the coherent dynamics of phonons even at the zone boundary.

Publication

PGH: S. Priyadarshi *et al.*; Phonon-induced relocation of valence charge in boron nitride observed by ultrafast x-ray diffraction; Phys. Rev. Lett.

Sub-cycle valleytronics using few-cycle linearly polarized pulses

Á. Jiménez-Galán, R. Silva, O. Smirnova, M. Y. Ivanov

Intense light fields with electric fields shaped at the sub-laser-cycle timescale open unique opportunities for shaping coherent electronic dynamics in atoms, molecules, and solids. In solids, sub-cycle shaped electric fields give rise to the dream of lightwave electronics, aiming at inducing and shaping electron currents at a single femtosecond time-scale, thereby pushing the potential speed of information processing to petahertz rates.

One area where the ideas of lightwave electronics find natural applications is valleytronics. The word "valley" here refers to the local minima – valleys – of a Brillouin zone (BZ) in a dielectric or a semiconductor. For example, a 2D hexagonal gapped graphene-type material, such as the hexagonal Boron Nitride (hBN), has a hexagonal BZ with valleys at K and K' points, shown in the figure.

Valleytronics comprise the study of optical, electric and magnetic ways to generate controlled electronic excitations in dielectrics or semiconductors, with the goal to excite the desired valley in the Brillouin zone, or a coherent superposition of different valleys. The ultimate goal is to write, manipulate and read the valley degree of freedom (or valley pseudospin), employing it as an ultrafast information carrier.

Selective excitation of valleys has been shown by using relatively long circularly polarized drivers, tuned in one-photon resonance with material's band gap. Using circularly polarized pulse allows one to take advantage of the selection rules in one-photon excitation associated with the Berry curvature: the direction of rotation of the circularly polarized driver has to match the sign of the Berry curvature to induce excitation in, say, **K** valley. Changing the handedness of the driver selects the opposite, **K'** valley. To make ultrafast valleytronics feasible, this should be combined with controlled manipulation and reading of the valley excitation. This is difficult with long pulses relying on one-photon resonance, making ultrafast valley switching (e.g. from K to K') challenging.

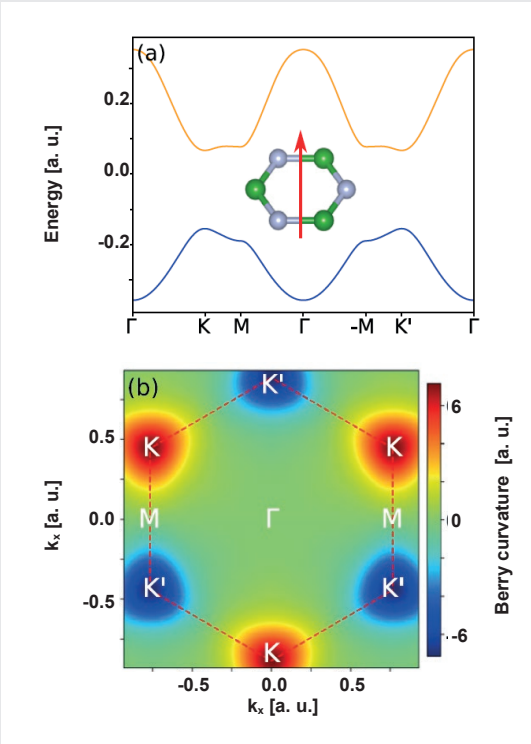

Fig. 1:
(a) Energy and (b) Berry curvature of the first conduction band in hBN. The red dashed lines indicate the FBZ, with the K' and K valleys at its vertices forming two triangular sub-lattices. Red arrow in panel (a) shows polarization of the linearly polarized driven used in this work.

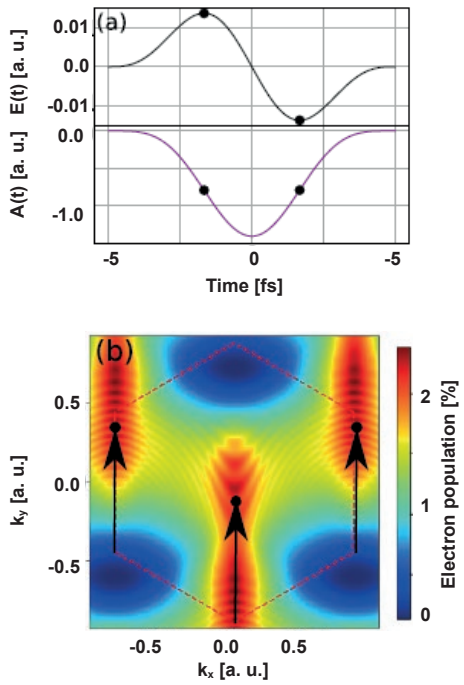

Fig. 2:
a) Electric field (top) and vector potential (bottom) in a linearly polarized single-cycle pulse carried at 3 micron, with the peak field 1.1 V/Å, for a simplified two-band model of hBN. The black dots indicate the times when the electric field peaks and electron injection occurs, corresponding to a non-zero vector potential amplitude $A_L^{inj.}$. (b) Conduction band populations after the vertically polarized pulse in (a). Arrows indicate the streaking. Valley polarization is clear.

What is more, excitation with linearly polarized pulses has never been considered in this context, as linearly polarized pulses they populate equally both **K** and **K'** valleys.

In our paper, we demonstrate that intense, few-cycle, linearly polarized pulses can generate selective electron population in a desired valley and drive excitations between the valleys, inducing a high degree of valley polarization. The mechanism of valley polarization is non-material-specific, independent of the Berry curvature, and can be controlled on a sub-cycle timescale by the controlling the carrier-envelope phase (CEP) of the few-cycle driver. We also show how this valley polarization can be read all-optically, by looking at harmonic emission with a weak probe field, without destroying the valley state.

The main physical idea behind our proposal is illustrated in figure 2, for an extreme case of a single-cycle pulse driver. Electron injection into the valleys takes place at the maxima of the electric field. However, for a very short pulse, the maxima of the laser electric field E(t) do not coincide with the zeroes of the vector potential A(t) (panel a). As a result, the electrons are streaked away from the bottom of the valley where electron injection takes place, generating excitations after the laser pulse not at the crystal momenta $\mathbf{k}_0$=**K**, **K'**, but at the streaked positions $\mathbf{k}_0$-$\mathbf{A}_L^{inj}$, as shown in panel b. As a result, initially identical populations of the two valleys become different, thanks to different streaking from the **K** and **K'** valleys. Adjusting the CEP controls the streaking and changes valley polarization.

Of course, the results presented above use extremely short pulses. However, strong effects are observed even for longer pulses and a standard material such as MoS2, where 22 bands are included in the calculation. The results are shown in figure 3. Panel (a) shows the pulses we used, while panel (b) shows the valley Hall conductivity (VHC), which is proportional to the difference in valley polarizations. The dependence of VHC on the CEP is very clear.

Valley polarization can be measured by looking at even harmonic generation from a probe pulse polarized along the Γ-M direction. Indeed, in the absence of valley polarization, the system has symmetry perpendicular to this direction (i.e in the Γ-K direction). Therefore, no even harmonics polarized along the Γ-K direction will be generated. If, however, valley polarization is present, second harmonic polarized along this direction will be generated. We have confirmed this expectation in our simulations.

In conclusion, we have demonstrated that few-cycle linearly polarized pulses can induce a high degree of valley polarization. The mechanism does not rely on the optical selection rules, and therefore can be used in inversion symmetric materials, such as TMD bilayers or graphene, opening a new way for implementing ultrafast valleytronic devices.

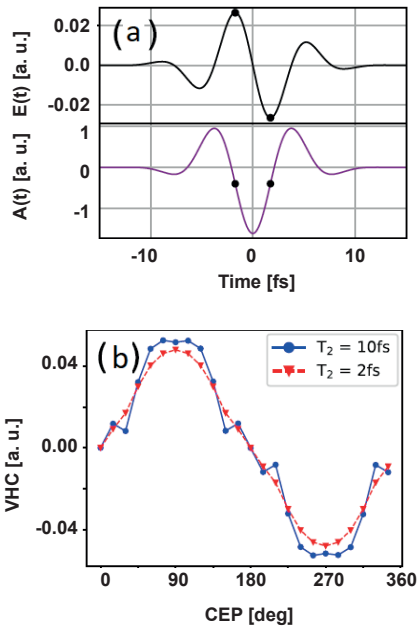

Fig. 3:
(a) Electric field (top) and vector potential (bottom) with carrier wavelength of 3 micron, peak field 1.5 V/Å, for CEP of 90o. (b) CEP control of the valley Hall conductivity for two dephasing times, T2 =10 fs (blue) and 2 fs (red). The valley Hall conductivity is proportional to valley polarization.

Publication

JSS21: Á. Jiménez-Galán *et al.*; *Sub-cycle valleytronics: control of valley polarization using few-cycle linearly polarized pulses*; Optica **8** (2021) 277-280

Short Description of Research Projects

1.1: Fundamentals of Extreme Photonics

O. Smirnova, B. Fingerhut (project coordinators)
and M. Y. Ivanov, K. Busch, M. Klük, A. Perez-Leija, K. Tschernig, D. Reiche, F. Loth, T. Bredtmann, S. Patchkovskii, Á. Jiménez-Galán, S. Carlstroem, W. Becker, D. Milosevic, H. Reiss, F. Morales, I. Babushkin, D. Ayuso, A. Ordonez, Maria Richter, A. Harvey, J. Kaushal, A. Andreev, J. Herrmann, A. Gusakov, M. Osswald, E. Palacino-González, N. Acharyya, R. Ovcharenko, S. Sharma, S. Shallcross, P. Elliott, Q. Li, P. Scheid, S. Solovyev

1. Overview

The main objective of the project 1.1 in 2021 has remained to be the development of analytical and numerical methods for the description of light-matter interactions in extreme conditions. The number of photons in a light field incident on a system can range from zero (vacuum fluctuations), to just a few (quantum electrodynamics and quantum optics regime), to hundreds and thousands of absorbed or emitted photons during the interaction with very intense light fields. When a low number of photons are involved, the quantum properties of matter and light play a very important role in the description of the interaction. At high intensities, the description of light as a classical electromagnetic wave is adequate, but a precise description of the (often highly nonlinear) quantum response of matter is needed. Non-perturbative theoretical models and methods are developed and applied, focusing on adequate description of system's optical properties and geometrical structure, as well as on many-body effects such as electron-electron correlation, coupled electronic and nuclear dynamics, optically induced and controlled spin dynamics, including laser-driven and laser-controlled ultrafast spin and magnetization dynamics in solids, and the role of quantum coherence in these dynamics. The range of material systems involves atoms, molecules, and solids – from dielectrics to semiconductors to magnetic materials, and photonic structures such as waveguides.

2. Topics and collaborations

In 2021 the project was organized around five general directions:

T1: Theory of attosecond and few-femtosecond electron dynamics

T2: Theory of matter in intense laser fields

T3: Theoretical Optics and Photonics in structured media (Joint HU-MBI Group)

T4: Bio-molecular dynamics in condensed phase

T5: Condensed Matter Theory

In-house collaborations with Projects 1.2, 2.1, 2.2, 2.3, 3.1, and 3.2.

External collaborations: IC London (UK), HU Berlin, TU Berlin (Germany), The Weizmann Institute (Israel), CEA Saclay (France), CELIA and University Bordeaux (France), University of Ottawa (Canada), UCLA (USA), RQC Moscow (Russia), UA Madrid (Spain), University Trieste (Italy), XLIM Limoges (France), University Sherbrook (Canada), University of Central Florida (USA), University Sarajevo (Bosnia-Herzegovina), University Geneva (Switzerland), MPI Halle (Germany), Hebrew University of Jerusalem (Israel), Ben-Gurion University of the Negev, Beer-Sheva (Israel), University of Colorado and JILA (USA), University of Zurich (Switzerland).

3. Results in 2021

Representative results are given below for a range of general research direction.

T1: Sub-cycle valleytronics in graphene

The realization of atomically thin monolayer graphene has led to breakthroughs in fundamental and applied sciences. Charge carriers in graphene are described by the massless Dirac equation and exhibit exceptional transport properties, making graphene very attractive for novel electronics applications.

One of the most interesting features of these materials is the electron's extra degree of freedom, the valley pseudospin, associated with populating the local minima located at the **K** and **K'** points of the hexagonal Brillouin zone (BZ). In pristine graphene, there is no bandgap at these energies, and the Berry curvature is equal to zero. In gapped graphene-like materials these **K** and **K'** points correspond to the minimal band-gap, and the valleys have opposite-sign Berry curvatures. The localization of electrons in one or the other valley is labeled by the valley pseudospin that takes the values of **K**, **K'**, or their coherent superposition. This extra degree of freedom has the potential to encode, process, and store quantum information, opening the field of valleytronics development of methods to selectively excite a desired valley in 2D materials has emerged as an important research topic.

In the valleytronics context, pristine graphene has been the most challenging material. Indeed, standard methods of generating valley polarization (selective population of a given valley) rely on taking advantage of the valley selection rules in gapped graphene-type materials: resonant light couples to one or the other valley depending on its helicity with respect to the Berry curvature

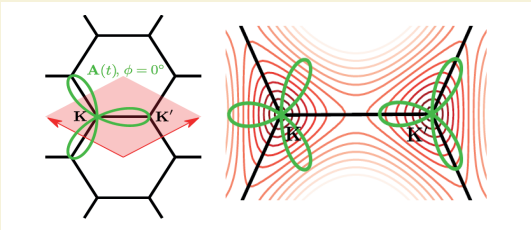

Fig. 1:
Valleytronics with polarization-shaped non-resonant light field in pristine graphene. (Left) The trefoil Lissajous figure generated by the bi-circular field can be oriented relative to the lattice. Its orientation is controlled by the relative two-color phase. (b) Hexagonal structure with two different atoms, e.g. hBN. Changing f rotates the trefoil relative to the crystal structure and selects the valley.

of the valley. As a result, a clockwise-rotating one-photon resonant field would couple to only one valley, while a counter-clockwise rotating field would couple to the other. In pristine graphene with zero bandgap and zero Berry curvature, these selection rules show no preference between the valleys. As a result, it has been commonly accepted that valleytronics in pristine graphene is not possible.

Following the successful work on topological strong field physics on sub-cycle time scale [SJA19] and valleytronics in gapped hexagonal 2D materials [JSS20], we have extended our valleytronics protocol developed in [JSS20] to pristine graphene [MJI21].

Fig. 1 shows (in green) the vector potential of the bicircular field and its orientation with respect to the BZ (i.e. in the momentum space). The orientation of the green trefoil can be controlled by the relative phase between the two colors, the fundamental (ω) and its second harmonic (2ω), both circularly polarized and rotating opposite to each other. The trefoil drives the electrons promoted to the conduction band, as the trajectories in the momentum space are controlled by the vector potential. The right panel shows energy contours in the valleys. It is clear from the right panel that, even though the two valleys are nearly identical at the bottom, their landscapes change as one moves away from the bottom, forming mirror-image shapes. The fit of the light-induced electron velocity into these shapes is not the same, thus suggesting the possibility of valley selectivity.

Our numerical results are summarized in Figure 2. To obtain the total population of the different valleys, we have integrated the momentum-resolved population over the sections shown in Fig. 2(a). To quantify the amount of valley polarization, we used the valley asymmetry parameter defined as

$$\eta = 2\frac{n_c^{K'} - n_c^{K}}{n_c^{K'} + n_c^{K}}$$

Here $n_c^{K'}$ and n_c^{K} are electron populations at the end of the laser pulse in the corresponding valleys. Figure 2(b) shows the asymmetry in the populations of the two valleys as a function of the two-color phase. Substantial contrast between the two valleys is achieved once the excitations leave the bottom of the Dirac cone, with values as high as 36 %. Note that each 180 degree change in the two-color phase results in 120 rotation of the tre-

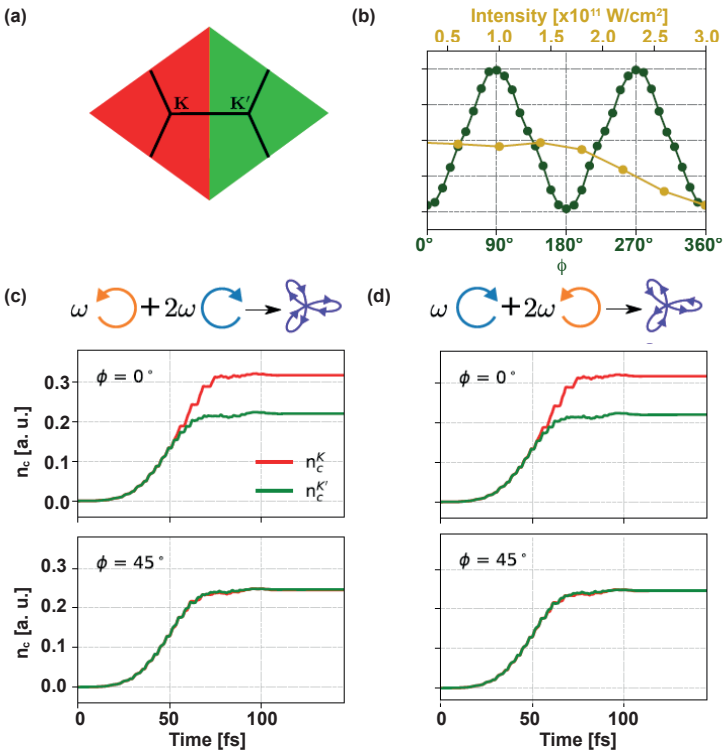

Fig. 2:
Valley asymmetry around two valleys K0 and K. (a) Separation of the Brillouin zone into K0 and K valleys. (b) Green line: Asymmetry in the valley-resolved populations in the conduction band as a function of the two-color phase ϕ for an intensity 3.10^{11} W/cm². Yellow line: valley asymmetry as a function of laser intensity. The laser wavelength is 6 micron (c), (d) Excitation dynamics during the laser pulse for various two-color phases; switching the helicities of both fields simultaneously does not change the outcome (adapted from [MJI21]).

foil, yielding an equivalent configuration. This is the reason for the periodicity of the valley asymmetry presented in Fig. 2(b). The higher-populated valley is the one where the vector potential "fits" better into the shape of the valley. The same results are obtained when simultaneously changing the helicities of both driving fields (Figs. 2(c) and 2(d)). The asymmetry in the valley population is negligible up to an intensity of 210^{11} W/cm^2 and gradually increases with intensity (Fig. 2(b)). The valley asymmetry is observed only when the laser pulse is able to drive the electrons to the anisotropic part of the conduction band.

Thus, valley polarization can be achieved in pristine graphene by tailoring the Lissajous figure of the driving pulse to the symmetry of the graphene lattice. This allows one to both break the inversion symmetry between the adjacent carbon atoms and also exploit the anisotropic regions in the valleys, taking advantage of the fact that the energy landscapes of the valleys are mirror images of each other. Our work opens an avenue for a new regime of valleytronics in pristine graphene and similar materials with zero bandgap and zero Berry curvature, where valley selectivity was generally thought to be impossible before.

T2-T1: Ultrafast optical rotation: imaging molecular chirality with ultrashort and tightly focused laser beams

Chiral molecules exist in pairs of two mirror-reflected versions: the left- and right-handed enantiomers. These "mirror twins" have identical physical and chemical properties, unless they interact with another chiral "object". Light has long served as the preferred tool for chiral recognition. Interestingly, light's chirality is not needed to detect the chirality of matter. It is well known that even linearly polarized light leads to optical activity: when propagating through a chiral medium, its polarization plane rotates, in opposite directions in media of opposite handedness. While this effect relies on weak magnetic interactions, it can produce large rotation angles in optically dense media. Still, detecting the handedness of diluted samples, such as those routinely produced in chemistry labs, can be a difficult task.

The possibility of creating intense laser pulses, of only a few cycles of duration, opened new opportunities for ultrafast spectroscopy. When the electric field amplitude of the laser $E(t) = E_0\, a(t) \cos(\omega t+\varphi_{CEP})$ is strongly modulated by its rapidly varying envelope a(t), the carrier-envelope phase (CEP) φ_{CEP} determines the temporal structure of the wave, and thus the nonlinear response of matter.

We have now shown that sculpting the temporal structure of such few-cycle pulses allows us to image and even control the ultrafast electronic response of chiral matter, with extremely high enantio-sensitivity [AOD21].

We propose to use ultrashort pulses tightly focused into a gas jet of chiral molecules, as depicted in Fig. 3. Commercially available Ti:sapphire lasers allow us to generate coherent CEP-stable pulses of only a few cycles of duration, with broad spectral bandwidths in the frequency domain. By focusing the beam tightly, we can create a strong longitudinal field component, and the field acquires forward ellipticity, or transverse spin. As shown in Fig. 3, the sign of the transverse spin is opposite on the opposite sides of beam's axis, and is locked to the direction of light propagation.

The polarization of the nonlinear response driven by the optical setup of Fig. 3 in isotropic chiral media is highly enantio-sensitive. Figs. 4a and b show the rotation of the polarization ellipse of the harmonic light emitted from randomly oriented left- and right-handed propylene oxide in the far field, as a function of the CEP of the driving field. The chiral medium turns the forward ellipticity of driver into enantio-sensitive polarization in the nonlinear optical response: it records the molecular handedness in the sign on ellipticity and sense of rotation of the polarization ellipses of the emitted harmonic light. Both quantities reach huge values in wide spatial and spectral regions [AOD21]. In particular, the

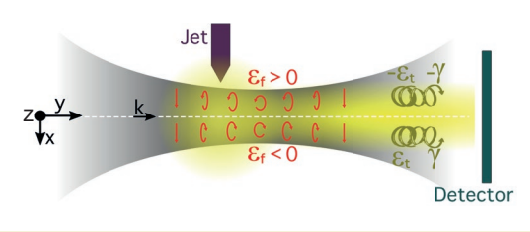

Fig. 3:
Proposed all-optical setup. A few-cycle, linearly polarized, laser beam acquires forward ellipticity (along the propagation direction) upon tight focusing. This forward ellipticity has opposite signs at opposite sides of the beam's axis. The interaction with a sample of randomly oriented chiral molecules, placed before the focus, generates elliptically polarized harmonic light. The ellipticity and rotation angle of the polarization ellipses record the molecular handedness in a molecule-specific manner. Adapted from [AOI21]

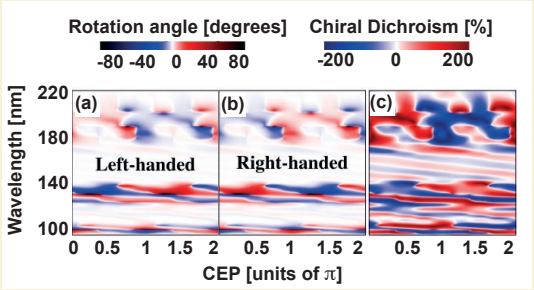

Fig. 4:
Ultrafast optical rotation. (a), (b): Rotation of the polarization ellipse of the light emitted by (L) and (R)-propylene oxide as a function of the driver's CEP and the nonlinear response wavelength. (c): Chiral dichroism, $CD = 2(I_L-I_R)/(I_L+I_R)$, in the harmonic intensity $I_{L/R}$ using a polarizer at 85° relative to input polarization. TDDFT calculations; pulse duration 5 fsec, intensity $6\cdot10^{13}$W·cm^{-2}, λ = 780nm, focal diameter 5μm.

giant enantio-sensitivity observed at nonlinear response wavelengths 195, 130, and 97.5 nm (harmonic numbers 4, 6 and 8) is remarkable.

The highly enantio-sensitive polarization of the emitted harmonic light tan be turned into highly enantio-sensitive intensity by placing a polarizer before the detector. Fig. 4(c) shows that the chiral dichroism, i.e. the normalized difference between the intensity of emission between opposite molecular enantiomers, reaches the ultimate efficiency limits of ±200 %.

This ultrafast optical activity enables highly efficient imaging of chiral matter and ultrafast chiral dynamics at the level of electrons. Furthermore, the polarization of the emitted light can be fully controlled with the driver's CEP in a molecule-specific manner, opening the way to identifying enantio-sensitive molecular markers of attosecond chiral dynamics. This method complements another method we have developed in 2021, based on using chirality-polarized light to induce enantio-sensitive light bending [AOD21].

T2: Spin polarized electrons in strong, circularly polarized, laser fields: generating high-energy spin-polarized electrons in a plasma wakefield accelerator

The role of the magnetic quantum number and spin in strong field ionization of atoms and molecules was mostly ignored until about a decade ago, when we predicted strong selectivity of tunnel ionization to the sign of the magnetic quantum number: optical tunneling of counter rotating electrons in a strong circularly polarized field is preferred [BSm11]. We have shown how the interplay of this sensitivity to the magnetic quantum number and the spin-orbit interaction leads to the generation of spin polarized electrons [BSm13]; this prediction was demonstrated experimentally for Xenon atoms in [HMK16].

Efficient and controlled generation of spin polarized electrons from strong field ionization has many potential applications, as it would allow one to probe magnetic and chiral molecular systems with a sub-femtosecond temporal and sub-Angstrom spatial resolution.

Another application, which also poses an important scientific challenge for the development of plasma-based accelerators for high-energy colliders, is the efficient in-situ generation of high-energy, high-current and low-emittance spin-polarized relativistic electron beams. Current proposed methods cannot generate ultra-short, synchronized on a femtosecond time-scale, spin-polarized electron beams, necessary for injection into plasma-based accelerators. Other proposals require a two-step scheme, where the spin-polarized electrons are generated outside the plasma-based accelerator, limiting its applicability.

In collaboration with the group of Chan Joshi at UCLA, we have proposed a one-step scheme to exploit the generation of spin-polarized electrons via strong field ionization of Xenon atoms using circularly polarized fields, inside a beam-driven plasma wakefield accelerator [NLM21a]. The generated spin-polarized electrons can be then accelerated to multi-GeV energies or higher, without significant depolarization.

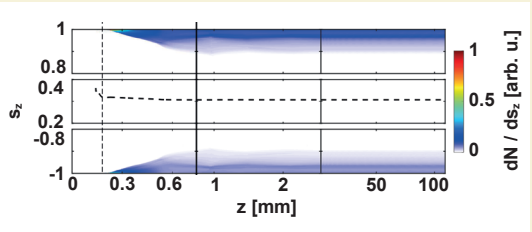

Fig. 5:
Evolution of spin vector in the z direction: s_z. The top box plots the s_z distribution in the range of 0.8 and 1. The central box plots $\langle s_z \rangle$ (net spin polarization) in the range of 0.2 and 0.4. The bottom box plots the sz distribution in the range of −1 and −0.8. The long vertical dashed black line marks the focal position (z = 0.18 mm) of the ionization laser. The long vertical solid black line divides the whole simulation into two stages: the injection and trapping stage (0-0.74 mm) and acceleration stage (0.74-110 mm).

The scheme can be summarized as follows: a relativistic drive electron beam traverses a mixture of Lithium and Xenon gas. The high-current electron beam ionizes Lithium, producing a bubble-like wake cavity containing Li ions and neutral Xe atoms (Li ionizes but Xe does not, due to the different ionization potentials: Ip of Li is 5.4 eV and Ip of Xe is 12.13 eV). Now a delayed circularly polarized laser pulse, co-propagating with the

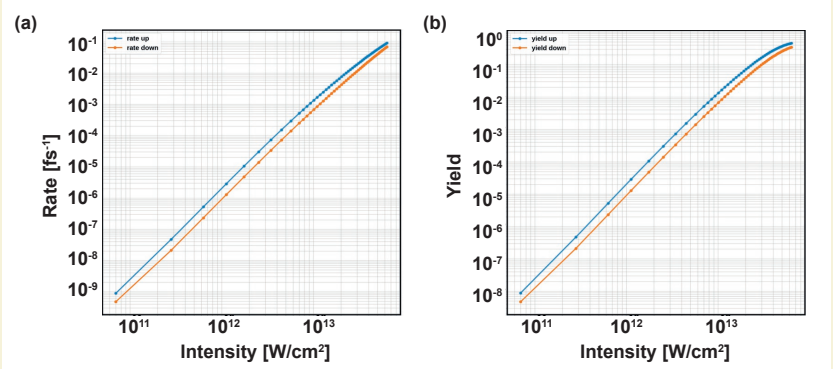

Fig. 6:
TDSE simulations for strong field ionization of Xenon using a circularly polarized laser field. Log-Log plot of the calculated (a) ionization rates and (b) yields of spin-up and spin-down electrons as a function of laser peak intensity of a 260 nm, 10 fs (FWHM), circularly polarized laser.

electron beam will strong field ionize the neutral Xenon atoms, producing spin-polarized electrons close to the center of the first bucket of the wake. These electrons are then trapped by the wake potential, and accelerated to ~2 GeV in ~10 cm without significant depolarization, as it is shown in Fig. 5.

Combining the results of the solution of the Time Dependent Schrödinger Equation, where we have calculated the ionization rate, and the total spin polarization for Xenon atoms, as a function of intensity for a strong, circularly polarized laser field (Fig. 4), together with Particle in a Cell (PIC) simulations, performed in two stages (injection and trapping stage, and acceleration stage), we have demonstrated the feasibility and potential of the scheme. Therefore, we have proposed a solution to the long-standing problem of generating GeV spin-polarized electrons, using plasma wakefield accelerators.

As an outlook, we are currently exploring different pathways to achieve higher levels of total spin-polarization. In particular, we are focusing on an even simpler scheme, using Yb as a plasma photocathode, both for wake formation and ionization injection. Using electrons with a higher angular momentum (*f* in Yb III instead of *p* in Xenon), was predicted to have a higher level of spin-polarization [KSm18].

T3: Topologically protected partially coherent light

In 2021, the research in T3 has been concerned with nonlinear and quantum plasmonics as well as with quantum photonics and few-photon nonlinearities in photonic structures waveguide arrays inscribed in glass. Specifically, with regards to quantum photonics, we have investigated the properties of topologically protected systems with regards to the effects of partial spatial coherence.

Topological physics exploits concepts from geometry and topology to implement systems capable of guiding waves in an unprecedented fashion. These ideas have led to the development of photonic topological insulators, which are optical systems whose eigenspectral topology allows the creation of light states that propagate along the edge of the system without any coupling into the bulk or backscattering even in the presence of disorder. Indeed, topological protection is a fully coherent effect, and it is not clear to what extent topological effects endure when the wave fronts become partially coherent, i.e. the question is to what degree topological protection "survives" the effects of partial spatial coherence. Addressing this question is of considerable importance as all optical fields undergo random fluctuations which may be small, as in many lasers, or large as in light generated by thermal sources.

In order to address this question, we have studied the interplay of topological protection and the degree of spatial coherence of classical light propagating in the archetypal Haldane topological insulator lattice (see Fig. 7). In this context, we are exploiting the formal analogy between the modern theory of polarization (as developed by Emil Wolf and coworkers) and the physics of entanglement for which we have already obtained highly interesting results regarding topological protection [TJC21].

Specifically, we compare the transmittance and fidelity of partially coherent states of light propagating in the Haldane lattice and the topologically trivial regular lattice – both being under the influence of static disorder (see Fig. 7). In general, the eigenspectrum of a topological insulator is composed of two types of eigenstates, the edge and bulk states. The difference between these states is that edge states lie inside an energy bandgap which is energetically separated from the bulk states (see Fig. 7). Under highly coherent conditions, this fundamental property allows one to create topologically protected wave-packets of edge states that are robust against disorder and backscattering.

However, when exciting the system with spatially partial incoherent light, one unavoidably excites all the eigenstates (bulk and edge), as a result, topological protection

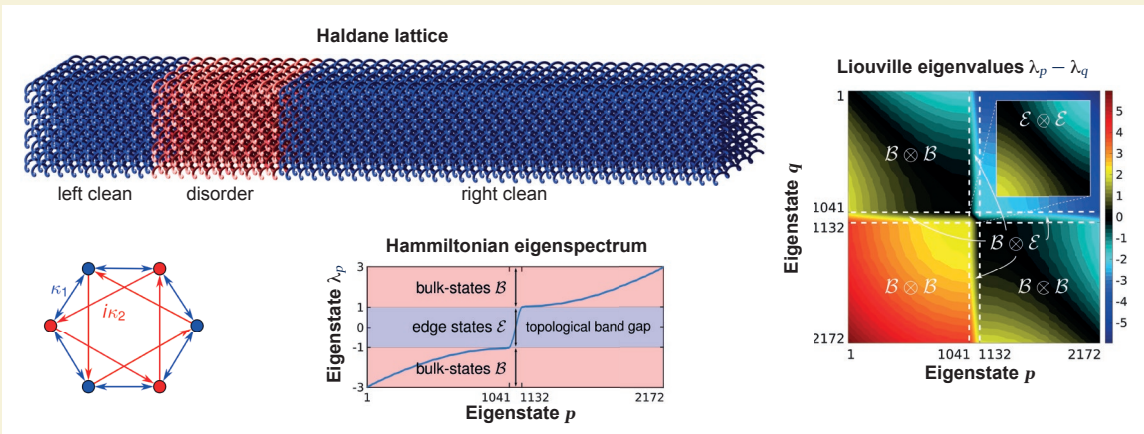

Fig. 7:
The Haldane lattice implemented using a honeycomb lattice of helical waveguides with coupling coefficients as described in the hexagonal cell. For fully coherent light the eigenspectrum exhibits two regions of bulk states and a gap crossed by the edge states. Spatially coherent superpositions of edge states enjoy full topological protection against disorder. In our recent work, we study how topological protection endures under partial spatially coherent excitations.

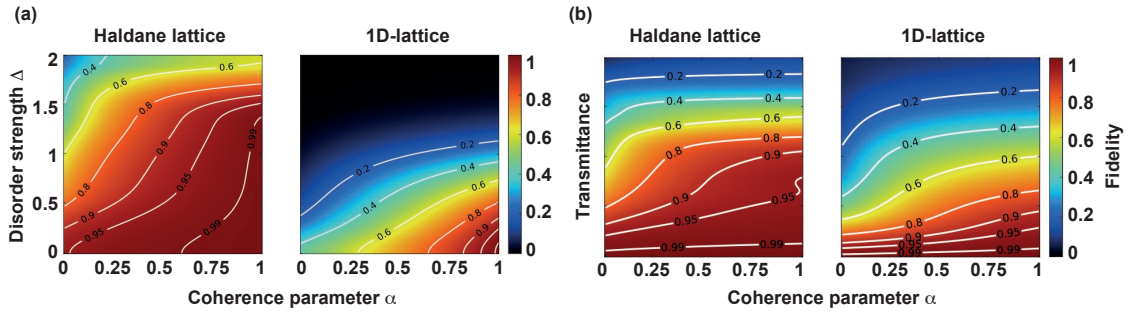

Fig. 8:
The Haldane lattice permits significantly higher (a) transmittance with a higher (b) fidelity than the topologically trivial lattice for the complete parameter range of the strength of the disorder and the degree of spatial coherence of the initial excitation.

cannot occur. Despite this inherent constraint, we have found, via detailed numerical investigations, a window in the eigenspectrum of the system (not in the frequency spectrum of the source) within which partially coherent light is topologically protected. Thus, the requirement of high spatial coherence can be relaxed – not up to any threshold, but a precise one determined by the band gap, disorder strength, spatial width of the initial excitation, and the desired fidelity and transmittance. Overall, we find (see Fig. 8) that the Haldane lattice permits higher transmittance with a higher fidelity than the topologically trivial lattice, for the complete parameter range of the strength of the disorder and the degree of spatial coherence of the initial excitation.

Therefore, our results reveal the existence of a well-defined spectral window in which partially coherent light is topologically protected. These results open up the design space to a wider selection of light sources, possibly yielding smaller, cheaper and more robust devices based on the topological transport of light.

T4: Structure and dynamics of elementary charge carriers in complex environments

The dynamics of quantum systems, like protons and electrons as elementary charge carriers is decisively affected by the interaction with the environment. In particular, the dynamics in liquid and biological environments is of major importance for mechanistic understanding as well as technological applications like fuel cells. In 2021 we have addressed proton solvation structure and dynamics in polar liquid environment [KSP21] and the light absorption induced catalytic electron transfer reaction in the 64-photolyase enzyme environment [OFi21].

Proton solvation in aqueous solutions is paramount for comprehending countless proton transfer reactions and proton transport processes. Our investigations in 2021 revealed the existence of an asymmetric protonated water trimer, $H_7^+O_3$, in acetonitrile. The core $H_7^+O_3$ motif persists in larger protonated water clusters in acetonitrile up to at least 8 water molecules. Quantum mechanics/molecular mechanics (QM/MM) molecular dynamics simulations suggest that irreversible proton transport is promoted by propagating the asymmetric $H_7^+O_3$ structure in solution. The simulations allow for the successful simulation of key spectroscopic observables in the infrared spectral region which reaffirms the assignment of the $H_7^+O_3$ spectra to a hybrid-complex structure: a protonated water dimer strongly hydrogen-bonded to a third water molecule with the proton exchanging between the two possible shared-proton Zundel-like centers.

The $H_7^+O_3$ structure lends itself to promoting irreversible proton transport in presence of even one additional

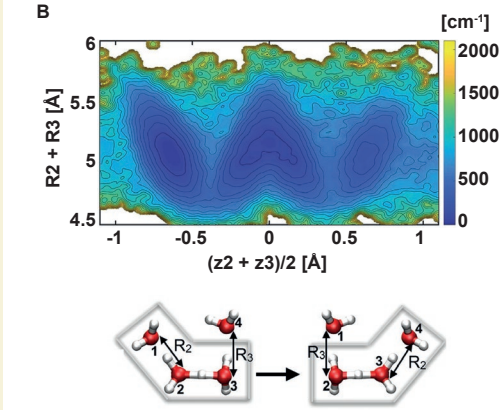

Fig. 9:
Potential of mean force of proton translocation in a molecular chain of four water molecules and an excess proton ($H_9^+O_4$): Panel B shows the rearrangement of hydrogen bond network within $H_9^+O_4$ that drives irreversible proton transport by the translocation of the $H_7^+O_3$ unit to a new site with a different geometry. Reversible proton displacement within the $H_7^+O_3$ unit and irreversible translocation of the $H_7^+O_3$ unit form the elementary steps of the trimer-to-trimer (T-T) proton transport mechanism. z1, z2 and z3 denote proton transfer coordinates between H+ and the oxygen atoms of flanking water molecules and R1, R2 and R3 denote O···O heavy atom distances. The symmetrized proton transfer coordinate (z2 + z3)/2 indicates proton translocation within $H_9^+O_4$ and the sum of hydrogen bond coordinates R2 + R3 characterize structural changes. Adapted from [KSP21].

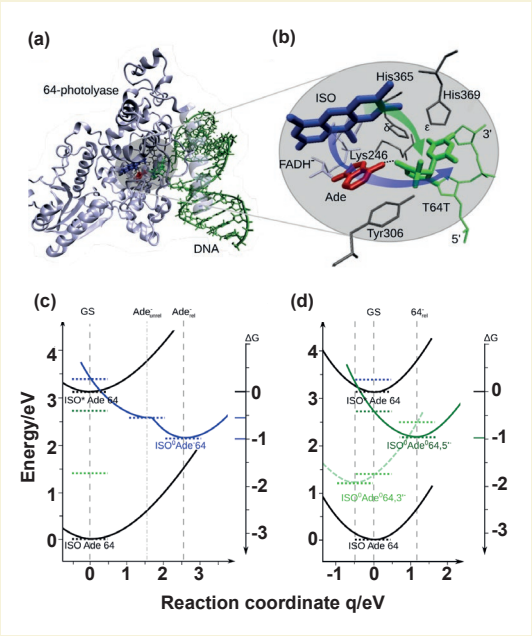

Fig. 10:
(a) Co-crystalized structure of 64-Photolyase (64-PL) of D. melanogaster and double-helical DNA containing a T64T photoproduct (PDB 3CVU). (b) Enlarged view of the active site of 64-PL showing the spatial arrangement of the FADH⁻ cofactor and the (6-4) photoproduct. Selected amino acids in close proximity are His365, His369, Tyr306, and Lys246. Atoms of the FADH⁻ cofactor and T64T photoproduct that are part of the quantum mechanical (QM)-region are indicated in bold color. (c,d) Summary of diabatic states participating in the primary ET reactions ISO → Ade and ISO → T64T,5′ in 64-PL of D. melanogaster. Driving forces ΔG (indicated with the arrow on the right) and reorganization energies λ of ET reactions ISO → Ade and ISO → T64T,5′ were calculated from QM/MM statistical averages, obtained via extensive sampling of reactant and product configuration space.

water molecule (Fig. 9). We demonstrated how continuously evolving $H_7^+O_3$ structures support proton transport within larger water solvates where the translocation of the $H_7^+O_3$ motif is step-wise and allows persistent transport of the proton tightly coupled to ~ps hydrogen-bond angular rearrangements. In this newly suggested scenario of proton transport, the 3-fold hydrogen-bond hierarchy in the protonated water species is preserved with no transient production or destruction of monomeric H_3^+O. Our simulations imply that the transition-state for proton transport in aqueous solutions is associated with the translocation of the $H_7^+O_3$ motif coupled to transient rearrangements of hydrogen-bonds in the trimeric-unit's 1st solvation-shell water molecules in what may be described as streaming $H_7^+O_3$ to $H_7^+O_3$ transitions.

The irradiation of DNA with ultraviolet light induces primary photoreactions that can lead to the formation of (6-4) photoproducts. To avoid mutagenesis and cell death, photolesions have to be efficiently repaired. Photolyases (PLs) are blue-light-activated flavoenzymes with the ability to repair DNA lesions that are widely distributed in almost all domains of life (with the exception of mammals). We have investigated the primary catalytic electron transfer reaction in 64-PL of D. melanogaster for which catalytic electron flow and details of the 64-photolyase repair mechanism are perpetually debated. A characterization of the relative energetics of locally excited and charge separated states in the (6-4) photoproduct enzyme repair complex reveals a charge-separated state involving the adenine moiety of the $FADH^-$ cofactor that facilitates reduction of the photoproduct (Fig.10). Microscopic details of the collective ET reaction coordinate were identified that involve the reorganization of the hydrogen bond network and structural relaxation of the active site. The simulations reveal complex active site relaxation dynamics involving distinguished amino acids (Lys246, His365, and His369), conformational reorganization of the hydroxyl group of the (6-4) photoproduct, and a strengthening of hydrogen bonds with immobilized water molecules.

In particular, rotation of the Lys246 side chain is found to impose a double-well character along the reaction coordinate of the ET reaction. Our findings suggest that the primary ET reactions in the (6-4) photoproduct enzyme repair complex of D. melanogaster are determined by fine-tuned local electrostatics and are governed by complex multi-minima active site relaxation dynamics that potentially precede the equilibration of the protein. ET pathways mediated by the adenine moiety and the 5′ side of the photoproduct were identified to be relevant for triggering the catalytic (6-4) photoproduct reactivation.

T5: Coherent optical control of magnons: ab-initio predictions

Ultrashort laser technology has emerged as a promising tool for manipulating spins on femtosecond timescales, i.e. several orders of magnitude faster than currently available devices. This is an active and rapidly evolving field of research in which several key processes for ultra-fast spin control have emerged-ultrafast demagnetization whereby loss of spin (or magnetic moment) occurs in less than 100 fs when acted upon by an optical laser pulse, all-optical switching in which the spins switch by 180 degrees when excited by the laser, spin transfer from one magnetic sub-lattice to another by charge-excitations induced by the laser, known as Optical Inter-sublattice Spin Transfer (OISTR) etc. Harnessing these techniques to control magnonics would lead to operational times in the femtosecond regime.

In our work we combine magnonics with one of these ultrafast spin control processes [SED21, SED20], namely OISTR, to obtain a three-fold coherent control of magnons using ultrashort laser pulses – we demonstrate, with an example of FeNi alloy, that laser pulses can be tuned to obtain (1) element selective destruction of magnon modes in multi-component magnetic materials, (2) frequency change of selected magnon modes and (3) element selective canting of the magnetic moment i.e. laser induced transient non-collinear state of a ferromagnet by magnon destruction.

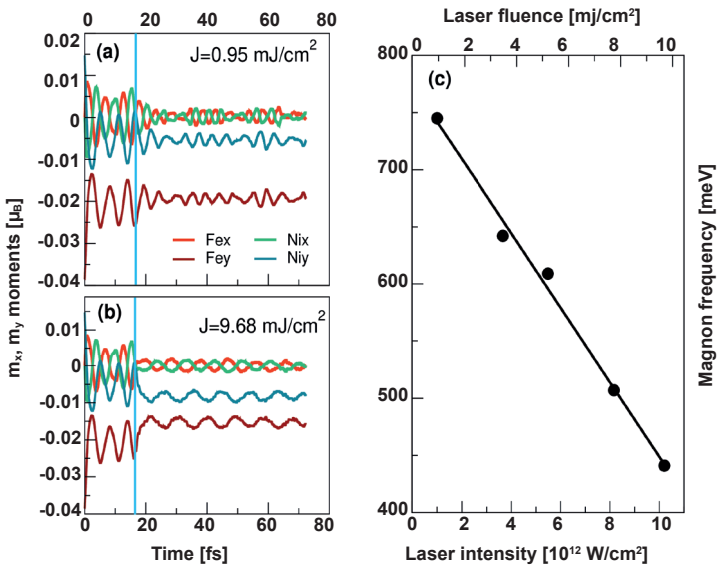

Fig. 11:
The change in magnon frequency in FeNi is shown for two laser pulse of intensities (a) 0.9537 mJ/cm² and (b) 9.680 mJ/cm². (c) The magnon frequency decreases with the increase in intensity of applied laser pulse. The vertical line corresponds to the peak of the laser pulse.

As an example here we show the frequency of the magnon modes can be manipulated by pump-laser pulse. To demonstrate this we excite the optical mode and then look at its dynamics under the influence of pump pulses of differing fluences. The results, for two different laser intensities (0.9537 and 9.68 mJ/cm²) are shown in Fig. 11 (a) and (b) where it is clear that the oscillations are strongly influenced by the laser. Fourier transform of the transverse moment during these oscillations gives the frequency of the magnon mode and this is plotted, as function of laser intensity, in Fig. 11 (c). The main reason behind this change in frequency is the weakened exchange field between the magnetic sub-lattices of Fe and Ni due to two processes, both of which lead to increased screening between the electrons of each atom – (a) excitation of electrons to excited delocalized states and (b) transfer of localized charge from one atom to the other. This implies that the stronger this charge transfer is, the greater the change in the magnon frequency, a fact that is reflected in the linear dependence of the magnon frequency on the pump-pulse fluence (Fig. 11 (c)). Thus optical excitations offer a direct control of frequency of a coupled magnon mode of two sublattices via tuning of the fluence of the laser pulse.

Own Publications 2021 ff

(for full titles and list of authors see appendix 1)

AOD21: D. Ayuso *et al.*; Nat. Commun. **12** (2021) 3951/1-9

AOI21: D. Ayuso *et al.*; Optica **8** (2021) 1243-1246

DSE21: J. K. Dewhurst *et al.*; Phys. Rev. B **104** (2021) 054438/1-5

Fin21: B. P. Fingerhut; Chem. Commun. **57** (2021) 12880-12897

GDC21: M. de Goede *et al.*; Opt. Express **29** (2021) 346-358

GKG21: E. Golias *et al.*; Phys. Rev. Lett. **126** (2021) 107202/1-6

JSS21: Á Jiménez-Galán *et al.*; Optica **8** (2021) 277-280

KSP21: E. Kozari, *et al.*; ChemPhysChem **22** (2021) 053306/1-15

KYS21: A. Kumar *et al.*; Nano Lett. **21** (2021) 7123-7130

LED21: Q. Z. Li *et al.*; Phys. Rev. B **103** (2021) L081102/1-6

MJI21: M. S. Mrudul *et al.*; Optica **8** (2021) 422-427

NLM21a: Z. Nie *et al.*; Phys. Rev. Lett. **126** (2021) 054801/1-6

OFi21: M. Osswald *et al.*; J. Phys. Chem. B. **125** (2021) 8690-8702

SED21: N. Singh *et al.*; Phys. Rev. B **103** (2021) 134402/1-6

SLD: S. Shallcross, *et al.*; Appl. Phys. Lett. **120** (2021) 032403 (in press)

SPR21: T. P. H. Sidiropoulos *et al.*; Phys. Rev. X **11** (2021) 0410601-15

SSM21b: P. Scheid *et al.*; Nano Lett. **21** (2021) 1943-1947

TFG21: S. Theil *et al.*; Phys. Rev. B **104** (2021) 125412/1-12

TJC21: K. Tschernig *et al.*; Nat. Commun. **12** (2021) 1974

ZOP21: Y. Zhou *et al.*; Adv. Theory Simul. **5** (2021) 2100319/1-7

Other Publications

BSm11: I. Barth and O. Smirnova; Phys. Rev. A **84** (2011) 063415

BSm13: I. Barth and O. Smirnova; Phys. Rev. A **88** (2013) 013401

HMK16: A. Hartung *et al.*; Nat. Photonics **10** (2016) 26

JSS20: Á Jiménez-Galán *et al.*; Nat. Photonics **14** (2020) 728/1-7

KSm18: J. Kaushal and O. Smirnova; J. Phys. B **51** (2018) 174003

SJA19: R. E. F. Silva *et al.*; Nat. Photonics **13** (2019) 849-854

SED20: N. Singh *et al.*; phys. status solidi b **257** (2020) 1900654/1-9

Invited Talks at International Conferences
(for full titles see appendix 2)

B. P. Fingerhut; Int. Symposium on Molecular Spectroscopy (ISMS) (Urbana-Champaign, USA, virtual, 2021-06)

Invited External Talks at Seminars and Colloquia
(for full titles see appendix 2)

B. P. Fingerhut; Symposium Physikalische und Theoretische Chemie (Technische Universität München (TUM), virtual, 2021-04)

B. P. Fingerhut; Symposium Theoretische Chemie (Ludwig-Maximilians-Universität München (LMU), virtual, 2021-07)

S. Shallcross and S. Sharma; Int. Psi-K Workshop, Correlated synthetic quantum matter: Theory meets experiment (Bremen Center for Computational Materials Science (BCCMS), Germany, 2021-02)

S. Sharma; 736. WE-Heraeus-Seminar, Magnetism at the Nanoscale: Imaging – Fabrication – Physics (Bad Honnef, Germany, virtual, 2021-01)

S. Sharma; Atto Fridays Seminar Series (UCL, London, UK, virtual, 2021-05)

S. Sharma, On-line SPICE-SPIN+X Seminar (Johannes Gutenberg-Universität Mainz, Germany, virtual, 2021-06)

S. Sharma, Joint School on Spin Physics/SFB/TRR173 (Apolda, Thuringia, Germany, 2021-10)

S. Sharma; 25. Physikerinnentagung (Universität Duisburg-Essen, Germany, 2021-11)

S. Sharma; 13th BESSY@HZB User Meeting (Berlin, Germany, virtual, 2021-12)

S. Sharma, Colloquia (Center for Hybrid, Active, & Responsive Materials, University of Delaware, virtual, 2021-12)

1.2: Ultrafast Laser Physics and Nonlinear Optics

T. Nagy, M. Schnürer, G. Steinmeyer (project coordinators)
and J. R. C. Andrade, A. Boyko, C. Chen, W. Chen, F. Furch, M. Fürtjes, O. Ghafur, L. v. Grafenstein, U. Griebner, R. Grunwald, A. Heilmann, A. Housakou, M. Jasiulek, M. Kretschmar, C. Mei, M. Merö, F. Morales, M. van Mörbeck-Bock, V. Petrov, M. Richter, J. Tümmler, L. Wang, I Will, T. Witting

1. Overview

This project is the home of MBI's research activities in nonlinear optics and laser physics focusing on the development of novel light sources and time-resolved techniques.

Our primary goal is to strengthen MBI's research on ultrafast and nonlinear phenomena in light-matter interaction with state-of-the-art technology from our original research activities. Depending on the planned application of the technology, the focus of the development lies on superior pulse energy, short pulse duration, carrier-envelope phase stability, or high average power and repetition rate. A further goal is to cover a large range of the electromagnetic spectrum from THz to the soft X-rays with few-cycle pulses. Consequently, the project encompasses research on primary laser and parametric sources as well as on compression and wavelength conversion of the primary sources.

2. Topics and collaborations

T1: Primary Sources

Partly supported by DFG (GR2116/5-1), DFG (PE 607/14-1, M-0040), AFOSR/PK (FA8655-20-1-7053). and EU Horizon 2020 (871124 Laserlab-Europe, JRA PRISES)

We extended the operation of our infrared kHz OPCPA systems up to 12 µm wavelength. Furthermore, the architecture of the OPCPA source has been greatly simplified by integrating a new Cr:ZnS laser-based front-end.

A 100 kHz mid-infrared OPA delivering 1.03 µm, 1.5 µm, and 3.2 µm pulses is currently used with two stages for strong-field ionization and low-order harmonic generation in dielectric solids. A 100 kHz near-infrared OPA delivering slightly wavelength-tunable pulses near 800 nm is frequency tripled and drives a photocathode to generate ultrashort electron pulses for electron diffraction experiments.

Furthermore, we achieved Kerr-lens mode locking and sub-50 fs pulse generation in broadband gain media around 2 µm.

T2: Secondary Sources

Partly supported by DFG (NA1102/3-1) and EU Horizon 2020 (871124 Laserlab-Europe, JRA PRISES)

We investigated the efficient generation of elliptically polarized XUV pulses via bi-color high-harmonic generation (HHG) and created few-cycle pulses tuneable across the vacuum ultraviolet (VUV) spectral range via resonant dispersive wave generation along soliton dynamics in hollow waveguides.

Another focus has been on pulse compression: we theoretically investigated the energy scaling potential of multi-mode propagation in hollow waveguides, and compressed pulses to two-cycle duration as well as high-energy ps pulses to sub-100 fs duration at multi-10-W average power in the short-wave infrared spectral range.

Collaboration partners: M. Guina (ORC, Tampere, Finland), A. Demircan, U. Morgner (Leibniz Universität Hannover, Germany), R. Trebino (Georgiatech, Atlanta, GA, USA), S. Carbajo, (UCLA and SLAC, USA), M. Dantus (Michigan State University, East Lansing, MI, USA), B. Hofmann (TU Chemnitz, Germany), Y. Song (Tianjin University, China), T. Feng, (Shandong University, Qingdao, China), U. Wallrabe (IMTEK, University Freiburg, Germany), metrolux GmbH (Göttingen, Germany), J. Jahns (FernUniversity, Hagen, Germany), W. Seeber (Otto Schott Institute, FSU Jena, Germany), E. McGlynn (School of Physics, Dublin City University, Dublin, Ireland), F. Güell (University Barcelona, Spain), HoloEye Photonics AG (Berlin, Germany), X. Mateos (University Tarragona, Spain), P. Fuhrberg (Futonics Laser GmbH, Germany), H. Yu (Shandong University, China), F. Rotermund (Ajou University, Korea), A. Agnesi (Pavia University, Italy), J. Liu (Qingdao University, China), B. Kanngießer (TU Berlin, Germany), V. Pasiskevicius, (KTH, Stockholm, Sweden), P. Schunemann (BAE Systems, Nashua, USA), V. Badikov (HTL, Krasnodar, Russia), K. Kato (Chitose, Japan), I. Buchvarov (Sofia University, Bulgaria), G. Arisholm (FFI, Norway), Z. Heiner (SALSA, HU Berlin, Germany), P. Simon (IFNANO Göttingen, Germany), L. Veisz (Umeå University, Sweden), B. Major (ELI-ALPS, Szeged), V. Tosa (National Institute for Research and Development of Isotopic and Molecular Technologies), T. Metzger (Trumpf Scientific Lasers GmbH, Germany), N. Forget (Fastlite, Antibes, France), Z. Pan (ICM-CAEP, Mianyang, China), Y. Zhao (JSNU, Xuzhou, China), G. Zhang (FJIRSM-CAS, Fuzhou, China), K. Miyata (RIKEN, Wako, Japan), V. Tassev (AFRL, Dayton, USA).

3. Results in 2021

T1: Primary Sources

Midwave- and Longwave-IR OPCPAs at 1 kHz

The first large scale OPCPA system is operating at a central wavelength of 5 µm and emits pulses with 80 fs

duration and 3 mJ energy at a 1 kHz repetition rate [1]. Stable and reliable operation of the OPCPA system was ensured in 2021 leading to the successful application of the system for its main application, serving as a driver for hard x-ray generation (see project 3.3).

The main activities in 2021 were devoted to the extension of our OPCPA systems to the longwave-IR, i.e., emission at wavelengths longer than 10 µm, with few-cycle pulse duration and µJ-level pulse energy. The focus in 2021 was to explore the unique front-end based on a fs Cr:ZnS master oscillator for midwave-IR (MWIR) and longwave-IR (LWIR) OPCPAs. The oscillator spectrum comprises the pump wavelength at 2.0 µm as well as the signal seed at 2.4 µm, which significantly simplifies mid-IR OPCPA architectures because combinations of nonlinear effects such as supercontinuum and difference frequency generation or OPG/OPA are omitted [FGU21].

First of all the performance of our tunable, high-energy MWIR OPCPA was significantly improved. By taking advantage of the broad emission spectrum of the femtosecond Cr:ZnS master oscillator, we are able to directly seed the holmium-based pump around 2 µm. At the same time, the signal pulses for the parametric process are generated via Raman self-frequency shifting of the red end of the spectrum centered at 2.4 µm. Being generated in a fluoride fiber, solitons appear tunable over the wavelength range between 2.8 and 3.2 µm. The optical parametric amplifier operates at a 1 kHz repetition rate, and consists of two stages equipped with $ZnGeP_2$ as nonlinear crystal. Compared to our previous setup, we are now able to phase shape the MWIR pulses up to the fourth order. At the same time, we operate the complete parametric setup as well as the pulse characterization in a practically water free nitrogen atmosphere. With these additional measures, we were able to generate sub-100 fs idler pulses tunable between 5.4 and 6.8 µm with a pulse energy up to 400 µJ [FGM21].

A novel LWIR OPCPA was implemented in 2021. Its setup, designed for two amplification stages equipped with GaSe crystals, is shown in Fig. 1. It contains the already mentioned fs Cr:ZnS oscillator as front-end which seeds the pump and the signal channel directly. The spectrum of the oscillator is split at 2.1 µm by a dichroic mirror where the higher frequency part is used for seeding the pump. The Ho:YLF regenerative amplifier (RA) [FGU21] provides pump pulses at 1 kHz repetition rate up to 13 mJ energy and 3 ps duration. The remaining signal spectrum is centered at 2.4 µm and these pulses have a duration of 46 fs and contain 10 nJ energy. After stretching in bulk material, an acousto-optic programmable dispersive filter enables precise phase shaping of the signal pulses. In the first collinear amplification stage, the signal pulses are amplified to 13 µJ using a 2 mm thick GaSe crystal. The pump intensity amounts to 50 GW/cm². In the GaSe crystal, the process was phase-matched at an internal angle of 11.2° (type-I), The second parametric amplification stage is conducted using a 1 mm thick GaSe crystal, pumped with 3.1 mJ, corresponding to an intensity of 56 GW/cm². An angle of less than 1° is deliberately introduced between the pump and the signal which makes this stage not perfectly collinear due to the need of spatially separating idler, signal, and pump pulses for characterization.

The achieved combined signal and idler energy in the 1 kHz pulse train amounts to 94 µJ. The measured spectra of the signal and idler pulses, are shown in Fig. 2. The central wavelength of the signal pulses appears slightly shifted to 2.44 µm exhibiting a spectral width of 79 nm (FWHM) (Fig. 2(b)). The latter is roughly a factor two smaller than the signal seed spectrum which is related to the limited phase matching bandwidth in our setup. The corresponding idler pulses are centered at 11.8 µm with a FWHM of 1.91 µm (Fig. 2(a)) supporting a sub-100 fs pulse duration. The measured idler pulse energy amounts to 14 µJ. To demonstrate the compressibility of the generated pulses, a Martinez-type compressor based on sapphire prisms is installed for the signal pulses. The measured interferometric autocorrelation trace of the compressed signal pulses is presented in Fig. 2(c). Assuming a $sech^2$-pulse shape a duration of 124 fs is extracted from this trace which is close to the Fourier-limit. The energy throughput of the compressor is ~50 %, mostly limited due to Fresnel

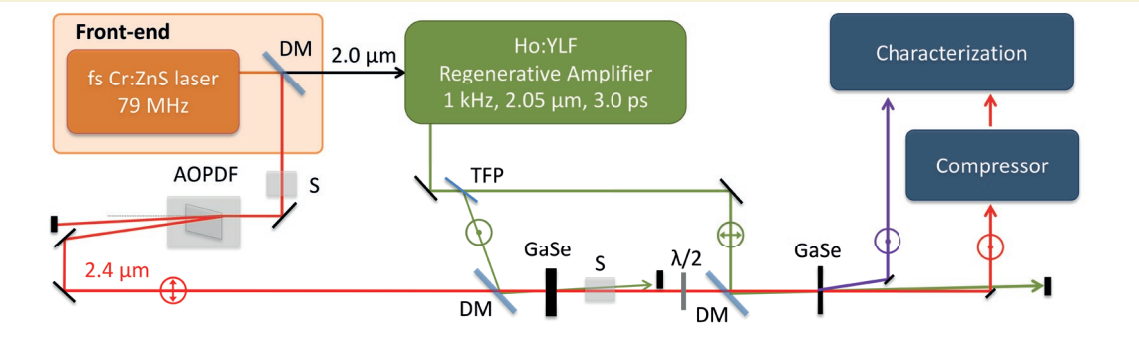

Fig. 1:
Setup LWIR OPCPA with Cr:ZnS based front-end. The main parts are the front-end with the fs Cr:ZnS master oscillator, the Ho:YLF RA as pump, and the two optical parametric amplifier (OPA) stages based on GaSe crystals. AOPDF, acousto-optic programmable dispersive filter; TFP, thin-film polarizer; λ/2, wave plate; S, bulk stretcher; DM, dichroic mirror.

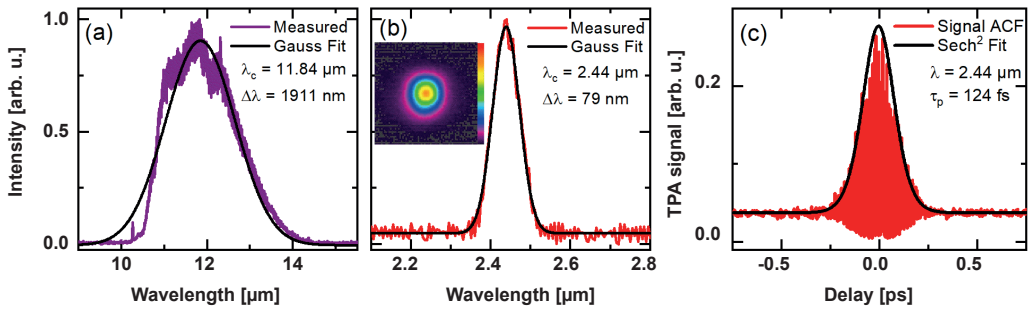

Fig. 2:
Characterization of the GaSe-based OPCPA output performance after the 2nd OPA stage. (a) Idler spectrum, (b) Signal spectrum; Inset: far-field intensity distribution of the signal, (c) ACF of the compressed signal pulse at 2.4 µm.

losses at the uncoated lenses. The output beam profile is nearly Gaussian and shown for the signal beam in the inset of Fig. 2(b).

The generation of high-energy, broadband idler pulses at 12 µm in a two-stage GaSe OPCPA at 1 kHz repetition rate was achieved. The idler energy of 14 µJ surpasses the so far reported values for parametric amplifier systems beyond 10 µm [2,3]. The bandwidth of the idler pulses supports a sub-100 fs duration. Compression was demonstrated for the signal pulses, resulting in nearly Fourier-limited pulses with 124 fs duration.

In 2022, the focus will be on the improvement of the LWIR OPCPA performance, i.e., achieving the few-cycle pulse regime by compression of the idler pulses and further pulse energy scaling.

100 kHz OPAs at 1.5 µm/3.2 µm and 0.800 µm

The home-built mid-infrared OPA system was rebuilt from scratch to avoid long-term laser damage and to add new features (cf. Fig. 3, upper three beam lines). As in 2020, the OPA is pumped by a commercial 30 W, 280 fs Yb fiber laser. The new, simplified architecture is based on supercontinuum generation from 1.03 µm pulses (instead of 0.515 µm pulses), an OPA/DFG stage pumped at 1.03 µm (instead of 0.515 µm pulses) delivering 1.5 µm pulses without passive CEP stability. In addition, the 1.5 µm pulse shaper (MIIPS Box, Biophotonic Solutions, Inc.) and the active pump-seed synchronization system were removed in the upgraded system, while a Pockels cell was added to enable repetition rate tunability down to 50 Hz dictated by experiments on solid-state materials. Over a time period of 24 hours, the root-mean-square (RMS) fluctuations of the 1.5 µm and 3.2 µm pulse trains are at the < 0.2 % level. In 2021, the new mid-infrared OPA system was used in Project 3.2, T2, “Linking HHG in solids to SFI.”

A new near-infrared OPA system was built to provide, after frequency tripling, ≥ 1.0 µJ deep-UV pulses using frequency tripling. These pulses are tunable in the vicinity of 267 nm to drive a copper photocathode-based electron gun (cf. Fig. 3, lower two beam lines). The

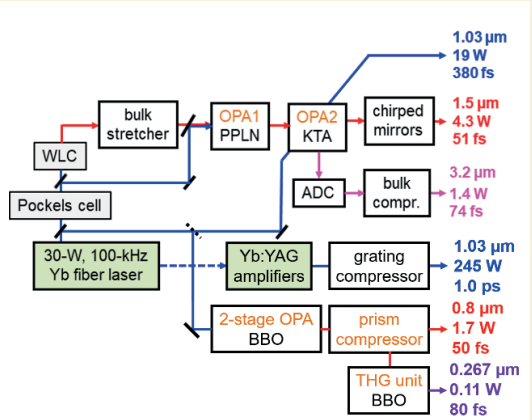

Fig. 3:
Current scheme of 100 kHz optical source including a three-color 1.03/1.5/3.2 µm OPA, a 1.03 µm, ps pump laser branch, and a 0.800/0267 µm photocathode OPA/ frequency-tripler system.

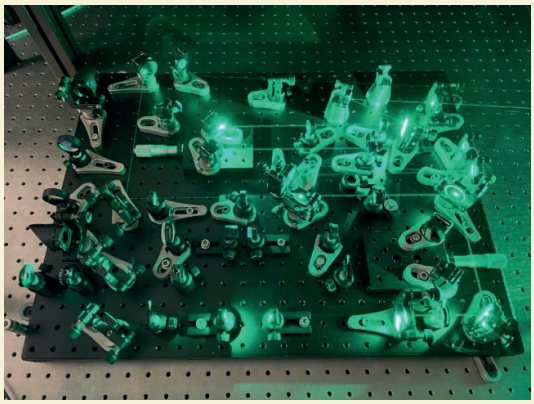

Fig. 4:
Photo of home-built supercontinuum-seeded 100 kHz, 800 nm photocathode-OPA delivering 1.7 W of average power and 48 fs duration after the variable attenuator and prism compressor units.

OPA is driven by 20 W of average power at 100 kHz available from a commercial Yb fiber laser and delivers 1.9 W at 800 nm (Fig. 4). By design, the OPA is tunable in the 780-820 nm range to enable fine-tuning of the deep-UV wavelength to better match the work-function of the photocathode. An average power up to 1.7 W is available at the input of the third-harmonic generation unit, which in turn delivers 110 mW at 267 nm in chirped, 82 fs pulses. The transform limit at 267 nm is 42 fs. The photocathode laser system was used in 2021 in Project 2.1, T4, "Ultrafast electron diffraction."

Kerr-lens mode-locking and sub-50 fs pulses from bulk solid-state lasers in the 2 µm spectral range

For generation of ultimately short pulses near 2 µm we study Tm,Ho-codoped materials exhibiting both intrinsic structural disorder and additional compositional disorder through doping with optically passive ions for extensive inhomogeneous broadening of the active dopant spectral lines, and utilize vibronic interactions and stimulated Raman scattering. The Kerr-effect is investigated as a pulse shortening and mode-locking (ML) mechanism supporting ultimately broad bandwidths but SESAMs and carbon nanostructure saturable absorbers (SAs) are still employed as mode-lockers for hybrid self-starting operation.

Among the rare-earth laser hosts, the cubic (bixbyite structure) sesquioxide crystals and ceramics RE_2O_3, where RE = Lu, Y and Sc, are of particular interest for sub-100 fs, 2 µm solid-state lasers due to their extremely broad and flat gain spectra extending beyond 2.2 µm and emission wavelengths exceeding 2 µm even for singly Tm-doping, where water vapor absorption is negligible. In 2021 we achieved for the first time soft-aperture Kerr-lens mode-locking (KLM) using Tm:$(Lu,Sc)_2O_3$ mixed ceramics (see Fig. 5). Pulses as short as 58 fs were generated at 2083 nm with an average power of 220 mW for a pulse repetition rate of 84.8 MHz [ZWC21b]. Vibronic-assisted long wavelength emission (>2.2 µm) of Tm^{3+} was observed and it was found to be essential for spectral broadening and generating shortest pulses.

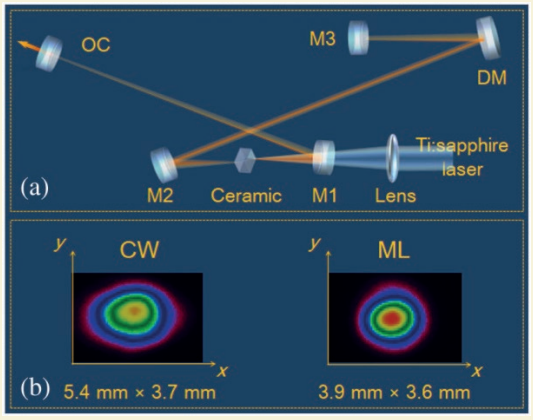

Fig. 5:
Schematic of the KLM Tm:$(Lu,Sc)_2O_3$ ceramic laser (a) and the output beam profiles (b) in the CW and ML regimes.

Power-scaling of the same laser was studied using a SWCNT-SA [WCZ21c]. Using different output couplers at a pulse repetition rate of 82.9 MHz, we obtained average powers of 114 mW at 2076 nm for a pulse duration of 58 fs, 350 mW at 2075 nm for 65 fs, and 486 mW at 2086 nm for 98 fs. The optical efficiency of 22.3 % achieved represents the highest value ever reported for sub-100 fs mode-locked Tm-lasers.

The first sub-50 fs pulse generation from a passively mode-locked Tm,Ho-codoped crystalline laser operating in the 2 µm spectral region was realized in 2021 using a tetragonal Tm,Ho:Ca(Gd,Lu)AlO_4 (CALGLO) mixed crystal with structural disorder [WCZ21b]. Employing a GaSb-based SESAM for ML, this laser delivered pulses as short as 46 fs (~7 optical cycles) at 2033 nm with an average power of 121 mW for a pulse repetition rate of 78 MHz, as shown in Fig 6. To the best of our knowledge, this result represents the shortest pulses ever generated from a Tm and/or Ho based solid-state laser. Polarization switching in this anisotropic (uniaxial)

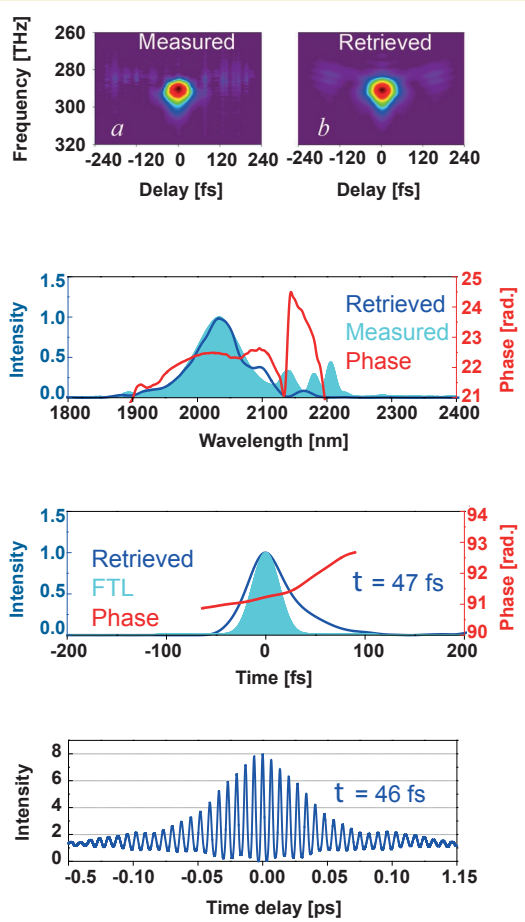

Fig. 6:
SHG-FROG characterization of the shortest pulses from the SESAM ML Tm,Ho:CALGLO laser with a 0.5 % output coupler: Measured and retrieved traces; measured and retrieved optical spectrum and spectral phase; Fourier-transform limited (FTL) and retrieved temporal pulse profile and phase; measured interferometric autocorrelation trace.

gain material was observed for the antireflection-coated a-cut sample at normal incidence without any polarization selective elements. Switching from π (CW) to σ–polarization (ML) was associated with spectral broadening and hence the generation of the shortest pulses. This regime was readily achievable by minimizing the cavity losses and by careful cavity alignment. Note that imposing the σ-polarization simply by the Brewster angle condition for the active medium or taking a c-cut crystal is not practical for this laser because pumping in π-polarization is much more effective.

In 2021 we also investigated some novel disordered garnet type crystals with additional passive ion doping for charge compensation, reduction of vacancies, and additional disorder, such as Tm:CLTGG [WCP21] and Tm,Ho:LCLNGG [PWB21] which showed improved ML performance in terms of achievable shortest pulse durations when mode-locked with SWCNT-SAs.

T2: Secondary Sources

Elliptically polarized High Harmonic Generation

(A. Heilmann – internal MBI young research project)

A relatively new method for the generation of elliptically polarized high harmonics consists in superposing the fundamental driver laser beam with its orthogonally polarized second harmonic. In this way, even and odd order high harmonics of opposite helicity and high ellipticity are generated. In the experiment, we use a BiBO crystal for frequency doubling of the 2 µm driver laser and a BaF2 window for delay adjustment between the two colors (see Fig. 7).

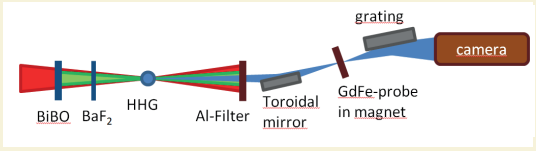

Fig. 7:
Experimental setup for the generation of elliptically polarized high harmonics and their subsequent detection via an XMCD measurement.

Harmonic ellipticity is detected via an X-ray magnetic circular dichroism (XMCD) measurement at the Fe-M-edge. Results are shown in Fig. 8.

For our sample, an XMCD asymmetry of 7 % was predicted. Hence, the measured asymmetry of ~ 3 % indicates a harmonic ellipticity of roughly 0.4. As a next step, we will replace the BaF_2 window by a pair of wedges, so that we can fine-tune the relative phase between the driver laser and its second harmonic. This will allow for an optimization of harmonic yield and ellipticity as well as for a better comparison of our results with theory.

Tunable VUV pulse generation

Few-fs pulses tunable across the UV-VUV spectral range are ideal for time-resolved studies of many biologically or chemically relevant materials. However, the generation of such pulses has been barely possible until recently. Here we follow a recently introduced method based on resonant dispersive wave generation during soliton self-compression in a negatively dispersive hollow waveguide [4]. By varying the gas pressure the overall dispersion of the gas-filled hollow waveguide and thus the phase-matching wavelength of the UV dispersive waves can be comfortably tuned. Numerical simulations predict that the pulse durations of the UV pulses are less than 5 fs throughout the entire tuning range. The schematic of the experimental arrangement is displayed in Fig. 9.

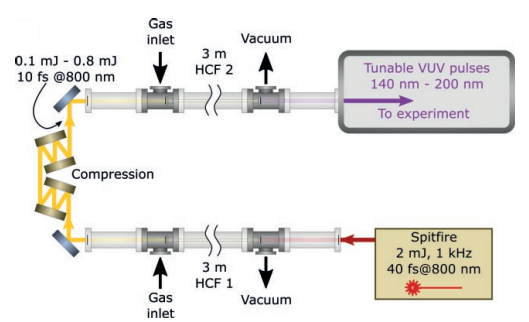

Fig. 9:
Schematics of the tunable VUV pulse apparatus.

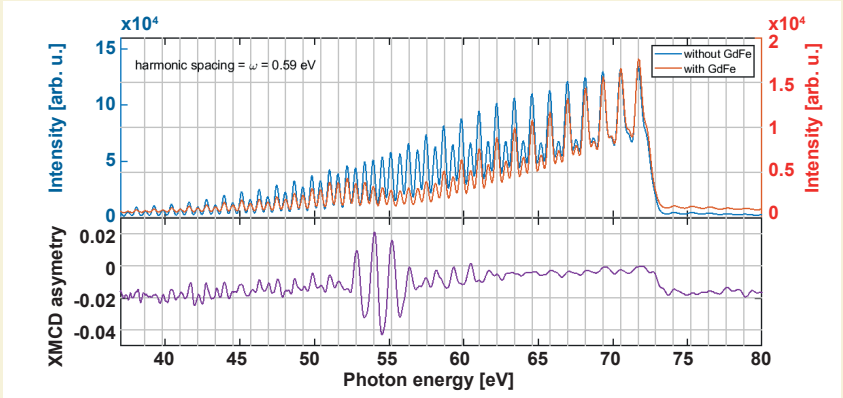

Fig. 8:
Upper panel: Measured harmonic spectra with and without GdFe sample. Lower panel: Calculated XMCD asymmetry from sample absorption in external magnetic fields with different polarisation.

40 fs pulses of a kHz Ti:sapphire CPA system centered at 800 nm are first spectrally broadened in a 3 m long stretched flexible hollow-core fiber (SF-HCF) differentially filled by argon gas and subsequently compressed to 10 fs duration by a chirped mirror compressor. After variable attenuation for optimizing the input pulse energy of the soliton stage between 100 and 800 µJ, the pulses are coupled into a second 3 m long SF-HCF with an inner diameter of 250 µm. Due to the small bore diameter of the fiber, the waveguide exhibits a net negative dispersion necessary for solitonic operation, if filled by gases with low dispersion e.g. helium or neon. The gas at a variable pressure is applied at the front face of the HCF while the output of the waveguide is connected to an evacuated vacuum beamline, where the planned experiments will take place. In this way the self-compressed IR and UV pulses can exit the fiber without passing through a window, which would severely distort the self-compressed temporal shape of the pulses due to its large dispersion. By varying the neon pressure in the HCF we are able to tune the wavelength of the VUV pulses in the range of 140-200 nm, as shown in Fig. 10 (a) and (b). We believe that the tuning range extends below 140 nm; however, our detection system is limited by the transmission window of the MgF_2 cover plate on the CCD chip of the spectrometer.

In 2022 the new light source will be used in Project 3.2 for time-resolved absorption spectroscopy of condensed matter near the absorption edge.

Spatial cage solitons

The hollow fiber compressor currently constitutes the most proven strategy for generating few-cycle pulses with mJ energy. While this method was already first demonstrated 25 years ago [5], scaling efforts only recently pushed peak powers beyond 1 TW [6] and compressed average powers to >300 W [7]. The latter have been demonstrated in collaborative efforts between MBI and researchers in Jena, Göttingen and Szeged, Hungary. One impediment for further upscaling is the lack of an overarching theoretical framework for treating the nonlinear propagation inside the hollow fiber. So far, this propagation problem has mostly been tackled by numerical simulations. Here we followed a different approach [MBN], which is directly based on the seminal calculations of Marcatili and Schmeltzer [8]. The latter calculations indicate the presence of numerous so-called hybrid modes in a hollow fiber with relatively large bore radius. In a completely linear scenario, these various radially symmetric HE_{1n} mode propagate at slightly different phase velocities. Nonlinear optics can compensate for this intermodal dispersion, leading to spatial soliton solutions, which propagate without changes of beam profile, if it were not for increasing losses at higher mode numbers n. Nevertheless, dissipative effects can be considered adiabatic, that is, the emerging spatial solitons reshape accordingly while propagating through the hollow fiber. Following this rationale, we computed pertinent beam profiles for a variety of initial conditions, cf. Fig. 11. These spatial solitons emerge from a balance between nonlinear self-focusing effects and diffraction. The Bessel J_1 radial profile at low powers increasingly flattens at higher powers and eventually transforms into a donut profile at the stability limit of the hollow fiber compressor (blue solution branch in Fig. 11). This branch is stable as dissipation increases the energy content of the fundamental HE_{11} fiber mode. In contrast, one can also find a secondary soliton branch (red curve in Fig. 11), where the higher-order mode contents increases due to dissipation. As higher-order modes see higher losses than the fundamental mode, this solution branch is considered unstable. Additionally, a third solution branch (green) can be found for the hypothetical scenario of a defocusing nonlinearity in a hollow fiber.

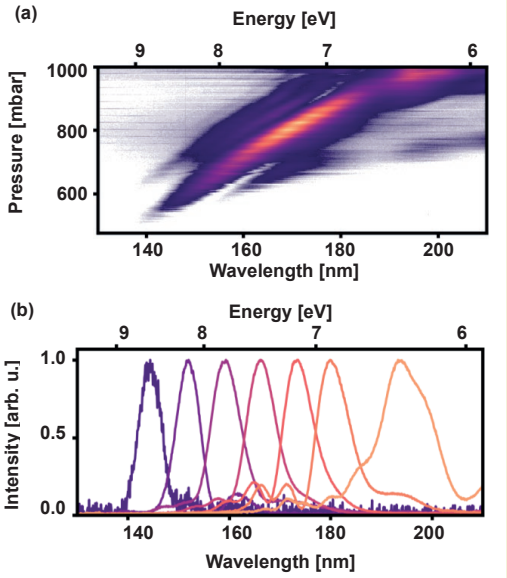

Fig. 10:
(a) A map of output spectra in function of the neon pressure. (b) A series of normalized spectra from the scan shown in a.

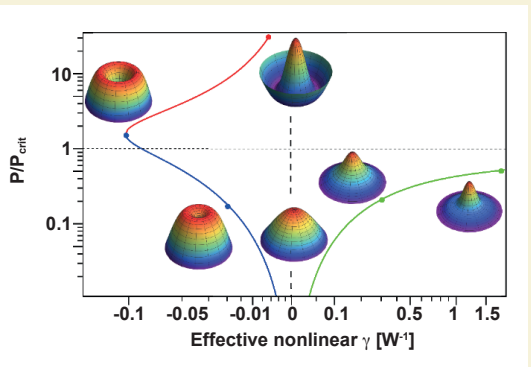

Fig. 11:
Spatial soliton solution branches of the nonlinear transverse wave equation. For normal modal dispersion ($n_{core} > n_{clad}$) or defocusing nonlinearity, a single solution branch exists (green). In hollow fibers with focusing nonlinearity, two branches coexist (blue and red). Powers have been normalized to the critical power of self-focusing P_{cr} in free space. Insets show electric field profiles for parameters indicated by symbols.

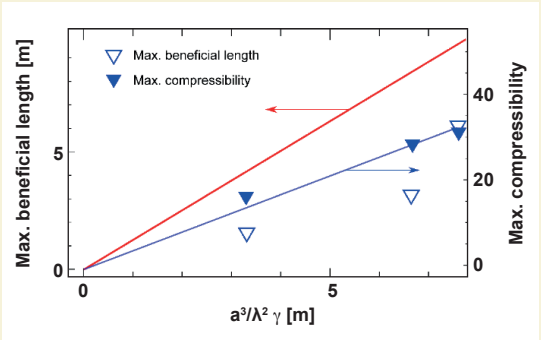

Fig. 12:
Comparison of model results with measured data. Maximum beneficial length (solid curve and hollow triangles) and maximum compressibility (dashed line and solid triangles). This analysis confirms that superior compression can be reached with longer hollow fibers and larger core diameters.

The stable soliton branch (blue) in Fig. 11 now enables a comparison with experimental results, both in terms of the maximum beneficial length of a hollow fiber compressor and expected peak power increase. This analysis indicates that larger compression factors up to 40 can be obtained with longer hollow fibers and larger bore diameters, which fully confirms recently published record-breaking experimental work [6,7], see Fig. 12. At the same time, further up-scaling appears difficult as fiber lengths of more than 5 meters is unpractical in most research or university facilities. It therefore appears necessary to use multi-stage concepts, e.g., for the compression of picosecond pulses to few-cycle pulse duration. Our theoretical investigation also indicates another intriguing possibility towards more efficient hollow fiber compression schemes, and this is the use of metal-coated hollow waveguides. However, as the hybrid HE_{1n} modes do not exist in metallic waveguides, one has to resort to the TE modes of the waveguide. This investigation is currently in progress and appears promising for further up-scaling of hollow-fiber compressors.

Compression of 2 micrometer pulses down to two cycles

(M. van Mörbeck-Bock – internal MBI young research project)

The duration of the driving laser pulses plays an important role in the efficiency of the high harmonic generation (HHG) process; therefore, the pulses should be as short as possible. The project aims on implementing a compact spectral broadening and pulse compression scheme to generate laser pulses of only two optical cycles in the 2 µm wavelength range. First successful attempts were made to spectrally broaden few-cycle optical pulses in so-called chalcogenide glass, arsenic trisulfide. The realized setup is depicted in Fig. 13.

After compression with chirp mirrors pulses energies of 1.9 mJ and pulse durations of 15.5 fs corresponding to a peak power of 120 GW were achieved. Fig.14 shows results of spectral and temporal pulse measurement.

The resulting peak power is slightly higher than without pulse compression scheme, however, due to the shorter pulse duration (involved electric field is higher before the medium is strongly ionized, i.e. gas is ionized past the critical ionization fraction) a significant increase of the harmonic yield (at least by a factor 2) and the cut-off frequency are expected. A possible future plan aims for higher peak powers with an anti-reflection coating. Currently this is a technological challenge because a suitable material with an appropriate surface, or surface treatment has to be identified, which avoids the sputtered AR-layer peeling off. Therefore, ZnSe and ZGP seem to be alternative candidates for spectral broadening in comparison to As_2S_3 glass material.

Compression of high-energy picosecond pulses in the short-wave infrared at multi-10 W average power

In the last decade great progress is achieved in the evolution of high-energy, high-power solid-state lasers operating in the infrared spectral range, most commonly around 1 µm wavelength. In the past years we extended the operation range towards the short-

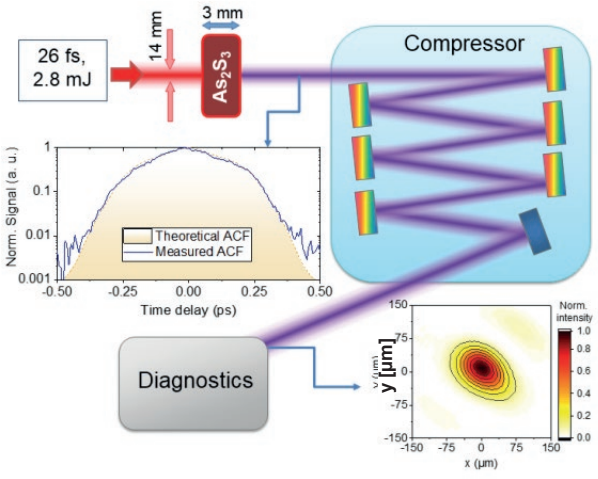

Fig. 13:
Setup of pulse compression scheme. After spectral broadening in arsenic trisulfide the autocorrelation trace (left inset) returns that the pulse duration is about 260 fs. After compression with broadband chirped mirrors the far field beam profile using a 500 mm lens was measured which shows a good beam quality (slightly elliptical).

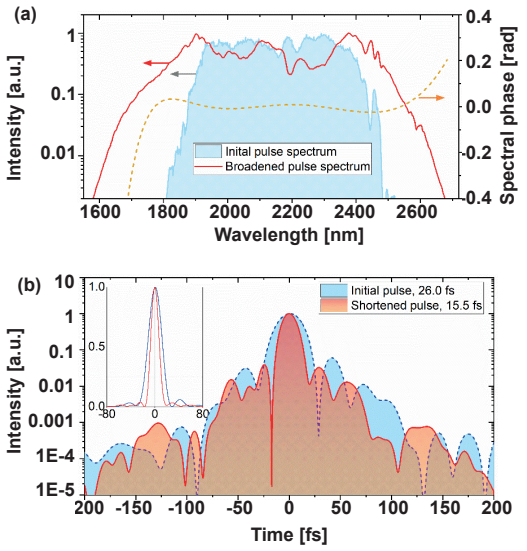

Fig. 14:
(a) Comparison of the spectra before and after spectral broadening (b) Reconstructed pulses of the initial and shortened pulse at 2 micrometer wavelength with pulse energies of 1.9 mJ.

wave infrared (SWIR) at 2 µm by utilizing the Ho:YLF gain medium [9]. Such solid-state systems can typically deliver multi-10 mJ pulses at kHz repetition rates. Given that their usual pulse duration lies in the range of a few picoseconds, these systems are best suited for pumping ultrafast OPCPA systems (see e.g. [1]); however, this duration is too long for directly using them for numerous potential applications. Therefore, it is an appealing yet very challenging option to post-compress the ps pulses to sub-100 fs duration. Here we utilize the powerful stretched flexible hollow-core fiber (SF-HCF) technology (for an overview see [NSV21]) to master the challenges.

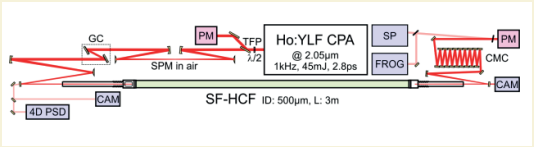

Fig. 15:
Experimental arrangement for the compression of high-energy SWIR pulses (taken from NGU21). CPA: chirped-pulse amplifier, TFP: thin-film polarizer, PM: power meter, SPM: self-phase modulation, GC: grating compressor, 4D PSD: 4-dimensional position-sensitive detector, CAM: CCD camera, SF-HCF: stretched flexible hollow-core fiber, ID: inner diameter, CMC: chirped-mirror compressor, SP: spectrometer, FROG: frequency-resolved optical gating device.

In our study we compressed 45 mJ, 2.8 ps long SWIR pulses at 1 kHz repetition rate. The experimental arrangement is displayed in Fig. 15. In order to increase the compression ratio, the pulses were first pre-compressed by applying moderate self-phase modulation induced by loose focusing into ambient air, which approximately doubled the original spectral width. Subsequently, the induced chirp was compensated by a pair of dielectric gratings. In this way the pulses got shortened to 1.4 ps and then entered a 3 m long SF-HCF of 500 µm bore diameter. The HCF was operated in pressure gradient mode, whereas the back side of the fiber was filled up to 1.6 bar by krypton gas flowing through the hollow waveguide towards the evacuated front side.

The spectrally broadened pulses were then compressed by a set of broadband chirped mirrors and characterized by second harmonic generation frequency-resolved optical gating (SHG-FROG). We achieved 86 fs pulses carrying 20.8 mJ energy at 20.8 W average power (see Fig. 16) setting a new record for such lasers [NGU21].

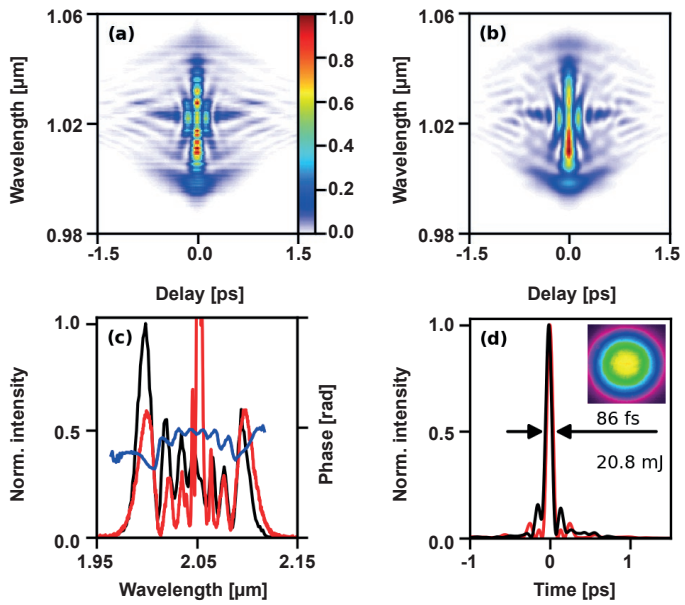

Fig. 16:
SHG-FROG measurement of the compressed pulses (taken from NGU21).
(a) and (b) measured and retrieved traces, respectively.
(c) Measured (red) and retrieved spectrum (black) with the retrieved spectral phase.
(d) Retrieved pulse shape (black) together with the transform-limited shape (red). The inset shows the beam profile behind the SF-HCF.

Own Publications in 2021 ff
(for full titles and list of authors see appendix 1)

APL21b: A. Alles *et al.*; Opt. Mater. Express **11** (2021) 2938-2951

BBA21: L. Beichert *et al.*; Opt. Express **29** (2021) 31499-31507

BLJ21: L. Basyrova *et al.*; J. Lumin. **240** (2021) 118373/1-11

BLM21: L. Basyrova *et al.*; Ceram. Int. **47** (2021) 6633-6642

CNK21: H. Cao *et al.*; Opt. Express **29** (2021) 5915-5922

EDS21: E. Escoto *et al.*; IEEE J. Quantum Electron. **57** (2021) 1300106/1-6

EMV21: U. Elu *et al.*; Nat. Photon. **15** (2021) 277-281

FGU21: P. Fuertjes *et al.*; Opt. Lett. **46** (2021) 1704-1707

HPM21: Z. Heiner *et al.*; SPIE Proc. **11670** (2021) 116700W/1-8

Jas21: M. Jasiulek; Phys. Rev. E **103** (2021) 053306/1-15

JLB21: W. Jing *et al.*; Opt. Mater. **117** (2021) 111128/1-7

KBM21: K. Kato *et al.*; Appl. Opt. **60** (2021) 6600-6603

KLR21: E. Kifle *et al.*; Opt. Lett. **46** (2021) 122-125

KMP21: K. Kato *et al.*; Appl. Opt. **60** (2021) 805-808

KPM21: K. Kato *et al.*; SPIE Proc. **11670** (2021) 116701K-5

KSZ21: M. Kowalczyk *et al.*; Laser Photon. Rev. **15** (2021) 2000441/1-10

KVS21: M. Kretschmar *et al.*; J. Phys. B **54** (2021) 20LT01/1-6

LDW21: J. Liu *et al.*; Opt. Lett. **46** (2021) 4454-4457

LKG21: P. Loiko *et al.*; J. Opt. Soc. Am. B **38** (2021) 482-495

LPS21: P. Loiko *et al.*; J. Lumin. **231** (2021) 117793/1-10

LTB21: M. Liebmann *et al.*; SPIE Proc. **11701** (2021) 11701V/1-7

LZZ21: Z.-L. Lin *et al.*; Opt. Express **29** (2021) 42837-42843

MFH21: M. van Mörbeck-Bock *et al.*; SPIE Proc. **11777** (2021) https://doi.org/10.1117/12.2591309

MGK21: Major *et al.*; Optica **8** (2021) 960-965

MSt21: C. Mei *et al.*; Phys. Rev. Res. **3** (2021) 013259/1-12

NGU21: T. Nagy *et al.*; Opt. Lett. **46** (2021) 3033-3036

NSV21: T. Nagy *et al.*: Adv. Phys. X **6** (2021) 1845795/1-41

PBB21: V. Petrov *et al.*; J. Opt. Soc. Am. B **38** (2021) B46-B58

PKa21: V. Pajer *et al.*; Laser Phys. Lett. **18** (2021) 065401/1-6

PLW21: Z. Pan *et al.*; J. Alloy. Compd. **853** (2021) 157100/1-15

PWB21: Z. Pan *et al.*; Opt. Express **29** (2021) 40323-40332

RVW21: P. Rueda *et al.*; Opt. Express **29** (2021) 27004-27013

SBE21: J. Stamm *et al.*; Opt. Express **29** (2021) 14314-14325

SKM21: G. P. Szekeres *et al.*; Phys. Chem. Chem. Phys. **23** (2021) 13389-13395

TAC21: J. Teichert *et al.*; Phys. Rev. Accel. Beams **24** (2021) 033401/1-16

TJP21: R. Trebino *et al.*; Handbook of Laser Technology and Applications CRC Press (2021) 487-535

VDL21: A. Volokitina *et al.*; J. Lumin. **231** (2021) 117811/1-12

WCP21: L. Wang *et al.*; Opt. Express **29** (2021) 31137-31144

WCS21: L. Wang *et al.*; Opt. Lett. **46** (2021) 332-335

WCZ21a: L. Wang *et al.*; SPIE Proc. **11670** (2021) 11670/1-6

WCZ21b: L. Wang *et al.*; Opt. Lett. **46** (2021) 2642-2645

WCZ21c: L. Wang *et al.*; High Power Laser Sci. Eng. **9** (2021) e50/1-5

ZLL21: H. Zeng *et al.*; Opt. Express **29** (2021) 13496-13503

ZLX21a: H.-J. Zeng *et al.*; Appl. Sci. **11** (2021) 9464/1-8

ZLX21b: H.-J. Zeng *et al.*; Opt. Express **29** (2021) 43820-43826

ZWC21a: Y. Zhao *et al.*; Photon. Res. **9** (2021) 357-363

ZWC21b: Y. Zhao *et al.*; Opt. Lett. **46** (2021) 3428-3431

In press

FGM: P. Fuertjes, L. von Grafenstein, C. Mei, M. Bock, U. Griebner, and T. Elsaesser; Cr:ZnS-based soliton self-frequency shifted signal generation for a tunable sub-100 fs MWIR OPCPA, Opt. Express

MBN: C. Mei, I. Babushkin, T. Nagy, and G. Steinmeyer, "Spatial cage solitons — taming light bullets," Photonics Res.

Other publications

[1] L. von Grafenstein, M. Bock, D. Ueberschaer, A. Koç, E. Escoto, K. Zawilski, P. Schunemann, U. Griebner, and T. Elsaesser, "Multi-millijoule few-cycle 5 µm OPCPA at 1 kHz repetition rate", Opt. Lett. **45** (2020) 5998

[2] K. Tian, L. He, X. Yang, and H. Liang, "Mid-infrared few-cycle pulse generation and amplification", Photonics **8** (2021) 290

[3] K. Liu, H. Liang, L. Wang, S. Qu, T. Lang, H. Li, Q. J. Wang, and Y. Zhang, "Multimicrojoule GaSe-based midinfrared optical parametric amplifier with an ultrabroad idler spectrum covering 4.2-16 µm", Opt. Lett. **44** (2019) 1003

[4] J. C. Travers, T. F. Grigorova, C. Brahms, and F. Belli, "High-energy pulse self-compression and ultraviolet generation through soliton dynamics in hollow capillary fibres", Nature Photonics **13** (2019) 547–554

[5] M. Nisoli, S. De Silvestri, and O. Svelto, "Generation of high energy 10 fs pulses by a new pulse compression technique", Appl. Phys. Lett. **68** (1996) 2793–2795

[6] T. Nagy, S. Hädrich, P. Simon, A. Blumenstein, N. Walther, R. Klas, J. Buldt, H. Stark, S. Breitkopf, P. Jójárt, I. Seres, Z. Várallyay, T. Eidam, and J. Limpert, "Generation of three-cycle multi-millijoule laser pulses at 318 W average power", Optica **6** (2019) 1423-1424

[7] T. Nagy, M. Kretschmar, M. J. J. Vrakking, and A. Rouzée, "Generation of above-terawatt 1.5-cycle visible pulses at 1 kHz by post-compression in a hollow fiber", Opt. Lett. **45** (2020) 3313–3316

[8] E. Marcatili and R. Schmeltzer, "Hollow metallic and dielectric wave-guides for long distance optical transmission and lasers", Bell Syst. Tech. J. **43** (1964) 1783-1809

[9] L. von Grafenstein, M. Bock, D. Ueberschaer, A. Koç, U. Griebner and T. Elsaesser, „2.05 µm chirped pulse amplification system at a 1 kHz repetition rate 2.4 ps pulses with 17 GW peak power", Opt. Lett. **45** (2020) 3836

Invited Talks at International Conferences

(for full titles see appendix 2)

U. Griebner *together with* L. von Grafenstein, M. Bock, T. Nagy, and T. Elsaesser; Photonics Days Berlin Brandenburg 2021 (Berlin, Adlershof, Germany, 2021-10)

V. Petrov together with Z. Heiner, and M. Mero; Photonics West'21: LASE 2021 (San Francisco, USA, virtual, 2021-03)

V. Petrov together with Z. Heiner, S. Krekic, and M. Mero; CLEO'21, (virtual, 2021-05)

Y. Zhao together L. Wang, W. Chen, Z. Pan, Y. Wang, U. Griebner, and V. Petrov; Laser Technology and Optoelectronics, LTO 2021 (Shanghai, China, 2021-06): Research progress of 2-micron ultrafast solid-state lasers

V. Petrov *together with* U. Elu, L. Maidment, L. Vamos, F. Tani, D. Novoa, M. H. Frosz, V. Badikov, D. Badikov, P. St. J. Russell, and J. Biegert; 2021 IEEE Photonics Conference, (virtual, 2021-10)

L. Wang *together with* W. Chen, and V. Petrov; 28th Annual Int. Conference on Advanced Laser Technologies, ALT'21, (Moscow, Russia, virtual, 2021-09)

V. Petrov *together with* M. Kowalczyk, Ł. Sterczewski, X. Zhang, Z. Wang, and J. Sotor; 28th Annual Int. Conference on Advanced Laser Technologies, ALT'21, (Moscow, Russia, virtual, 2021-09)

V. Petrov *together with* A. Sennaroglu, Y. Morova, E. N. Kamun, and M. Tonelli; 28th Annual Int. Conference on Advanced Laser Technologies, ALT'21, (Moscow, Russia, virtual, 2021-09)

2.1: Time-resolved XUV-science

A. Rouzée, S. Patchkovskii (project coordinators)
and K. Amini, U. Bengs, F. Branchi, F. Furch, O. Ghafur, M. O. S. Guzman, C. A. Granados Buidago, E. Ikonnikov, M. Ivanov, A. Jiménez Galàn, A. Husakov, L.-M. Koll, O. Kornilov, M. Kretschmar, N. Mayer, J. Mikosch, M. Mero, F. Morales Moreno, T. Nagy, M. Osolodkov, M. Richter, F. Rodriguez Diaz, F. Schell, C. P. Schulz, B. Schütte, A. Sen, B. Senfftleben, O. Smirnova, E. Svirplyz, M. T. Talluri, M. J. J. Vrakking, T. Witting, Z.-Y. Zhang

1. Overview

The main goal of project 2.1 is to visualize, understand, and steer electron and atomic motion during transformation of finite quantum systems, starting from few-body systems to isolated nanoparticles. The project has both experimental and theoretical components. Experimentally, we are developing a framework of closely interconnected time-resolved methods, unified by the application of novel XUV/X-ray light sources, both table-top, such as obtained by high harmonic generation (HHG), as well as free electron laser facilities. These novel light sources allow us to combine the ultimate temporal resolution (attoseconds) with atomic-scale spatial resolution. Using photoionization as a probe step in a pump-probe configuration, we investigate attosecond electron motion in atoms, molecules and nanoparticles as well as coupling of the electron motion to the nuclear motion. Our experimental framework is complemented by an advanced theory program aiming at (i) tracking and resolving correlated multi-electron dynamics on the attosecond time scale, and (ii) understanding the impact of coherently excited attosecond multi-electron dynamics on the longer, femtosecond-scale nuclear motion. Our common goal is to push atomic and molecular science beyond the present state-of-the-art by looking at the new time scale in chemical and physical processes.

2. Topics and collaborations

Presently, the project is organized in four topics:

T1: Attosecond electronic dynamics in strongly driven systems

T2: Strongly-coupled electronic and nuclear dynamics in photoexcited neutral molecules

T3: Ultrafast electronic decay and fragmentation dynamics at XUV and X-ray wavelengths

T4: Collective and correlated electron dynamics at the nanoscale

Collaborations with: A. Rudenko, D. Rolles (Kansas State University, USA); J. Küpper (Center For Free-Electron Laser, Hamburg); H. Stapelfeldt (Aarhus University, Denmark); A. Vilesov (UCLA, USA), F. Calegari (CFEL, Hamburg); F. Lépine (Institut Lumière et Matière, France); D. Holland (Science and Technology Facility Council, UK); Th. Pfeiffer (Max Planck Institute for Nuclear Physics, Germany); K. Varju (University of Szeged, Hungary); L. Banares (Universidad Compulense de Madrid, Spain); K.H. Meiwes-Broer, I. Barke (Universität Rostock); B. v. Issendorff (Universität Freiburg); P. Piseri (Università di Milano, Italy); P. Hommelhoff (FAU Erlangen); T. Brabec (University of Ottawa, Canada); G.G. Paulus (University Jena); C. Menoni (Colorado State University, USA), A. Orr-Ewing, M. Ashfold (University of Bristol, UK), F. Stienkemier (University of Freiburg), J. Osterhoff (DESY), A. Emmanoulidou (University College London), B. Major (ELI-ALPS), V. Tosa (National Institute for Research and Development of Isotopic and Molecular Technologies, Romania); J. Luiten (Technical University of Eindhoven); B. Siwick (McGill University), F. Martin (Universidad Autonoma de Madrid).

In-house collaborations with projects 1.1, 1.2, 2.2, 3.1, 3,2, 4.1 and 4.3.

3. Results in 2021

T1: Attosecond electronic dynamics in strongly driven systems

Measuring photoionization time delays in molecules is presently one of the hot topics in attosecond science. A typical technique for such measurement is called RABBITT (reconstruction of attosecond beating by interference of two-photon transitions), where the kinetic energy of the photoelectron from a target molecule is registered as a function of the delay between an XUV pulse train and an IR pulse.

In the reporting period, we have measured RABBITT signal from the nitrogen ion (N_2^+) in its C state. This state is the lowest one in the N_2^+, which undergoes predissociation with a lifetime of about 5 ns and can be filtered out by coincidences between N^+ ions and photoelectrons in our reaction microscope (REMI). To determine the ionization time delays one usually needs a reference measurement from a well-known ionization process e.g. in rare gases. In our measurements, we used gas mixtures of N_2 with Argon and Helium, respectively. Hence, by applying N^+-e^- and e.g. Ar^+-e^- coincidences we were able to measure both RABBITT signals simultaneously under the same experimental conditions. Fig. 1 shows the kinetic energy spectrum of N_2^+ C state (a) and Ar^+ (b) as a function of the XUV-IR delay. For the measurement our 100 kHz OPCPA laser system was used, which delivers few-cycle IR pulses of 7 fs duration and consequently short XUV pulse trains via high harmonic generation.

By applying a Fourier transform along the delay axis, the phase corresponding to the sideband oscillations with frequency 2ω has been determined as a function of kinetic energy. Fig. 2 shows the retrieved phases for N_2^+

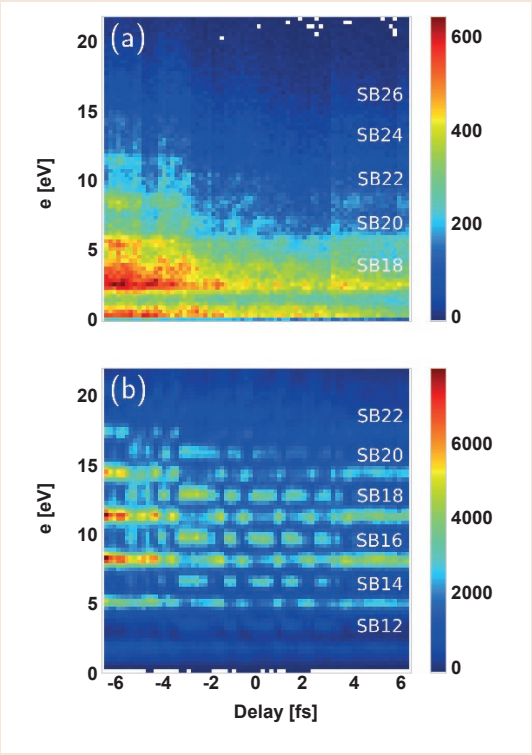

Fig. 1:
shows the kinetic energy spectra of photoelectrons vs. XUV-IR delay correlated with (a) the N_2^+ C state and (b) Ar^+. SB denotes the order of the harmonic sideband.

and Ar^+. The dominant characteristic in the behaviour of the extracted phase is the so-called attochirp, leading to an increase of the phase with higher electron energies. For a deeper understanding of the observed phases we presently collaborate with the theory group of Fernando Martin (Universidad Autónoma de Madrid).

In the reporting period, we have measured RABBITT signal from the nitrogen ion (N_2^+) in its C state. This state is the lowest one in the N_2^+, which undergoes predissociation with a lifetime of about 5 ns and can be filtered out by coincidences between N^+ ions and photoelectrons in our reaction microscope (REMI). To determine the ionization time delays one usually needs a reference measurement from a well-known ionization process e.g. in rare gases. In our measurements, we used gas mixtures of N_2 with Argon and Helium, respectively. Hence, by applying N^+-e^- and e.g. Ar^+-e^- coincidences we were able to measure both RABBITT signals simultaneously under the same experimental conditions. Fig. 1 shows the kinetic energy spectrum of N_2^+ C state (a) and Ar^+ (b) as a function of the XUV-IR delay. For the measurement our 100 kHz OPCPA laser system was used, which delivers few-cycle IR pulses of 7 fs duration and consequently short XUV pulse trains via high harmonic generation.

In a different set of experiments, we have achieved post-compression of the 7 fs pulses from the OPCPA system to durations of 3.5 fs, which is approximately 1.5 optical cycles at 800 nm. These near-single cycle pulses with pulse energies of up to 100 µJ have been successfully used to generate isolated attosecond pulses with a flux of more than 10^6 photons per laser shot on target. The attosecond pulses have been carefully characterized using the attosecond streaking method [WOS]. This new 100 kHz isolated attosecond pulse capability will now be used for experiments with our reaction microscope.

Attosecond dynamics in atoms and molecules

In a recent study [DWK], we combined the RABBITT technique with tunable femtosecond NIR pulses to unveil the phase of two-photon matrix elements for resonant and antiresonant two-color ionization of helium in the vicinity of the **1snp $^1P_1$ (n=3,4,5)** Rydberg series. The technique allowed us to observe characteristic rapid changes of the phase (see Fig. 3), which were well reproduced by simulations of the time-dependent Schrödinger equation in the single-active-electron approximation.

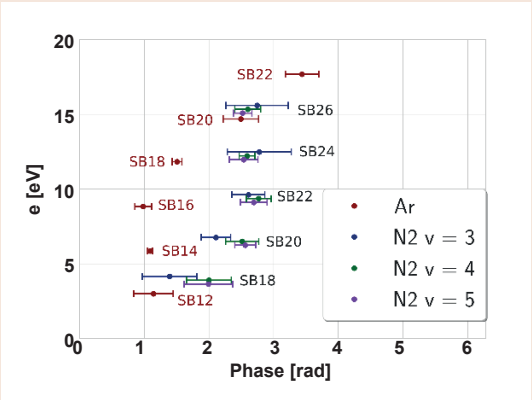

Fig. 2:
Retrieved phases for Ar^+ and N_2^+ C $^2\Sigma_u^+$. v denotes different vibrational states in the N_2^+ C state. The overall decrease of the phase with increasing electron energies is attributed to the so-called attochirp originating from the high harmonic generation process.

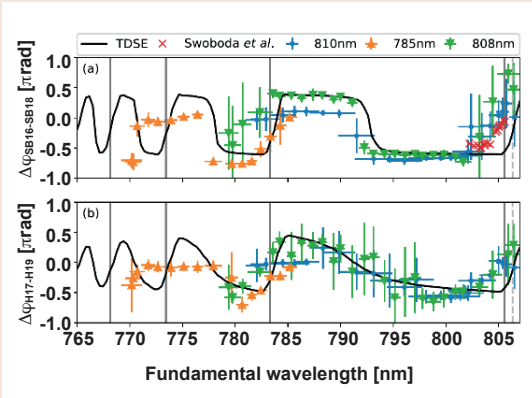

Fig. 3:
Calculated and experimentally determined wavelength dependence of the phase differences of sideband 16 and 18 (a), and the phases between harmonic 17 and 19 (b).

In addition, using new technology developed in house at MBI, phase-locked pairs of XUV attosecond pulses combined with a few-cycle NIR pulse were used to control and probe the entanglement created in the photoionization of H_2 molecules [Vra21, KMD]. By setting the time-delay between the two XUV pulses we controlled the degree of entanglement between the photoelectron and the parent H_2^+ ion (see Fig. 4). The experiment provided direct evidence that in attosecond pump-probe experiments involving ionization, entanglement between the ion and the photoelectron that are produced by ionization by the XUV pulse, constrains the coherence that can be observed when the probe laser interacts with the ion or photoelectron.

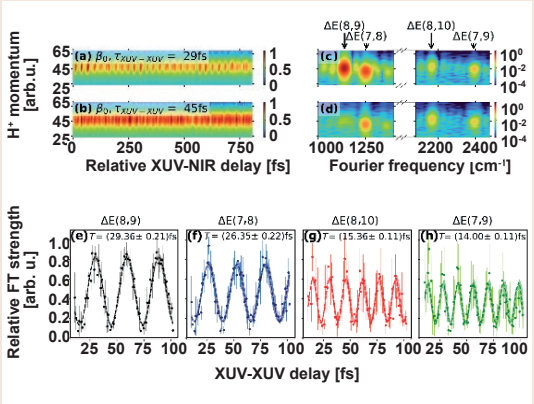

Fig. 4:
(a) Observed wavepacket motion of the H_2^+ ion after ionization by an XUV pulse pair with a delay of 29 fs. (b) Setting the XUV delay to 45 fs results in a high degree of entanglement visible by the lack of coherent fringes. (c) and (d) show the Fourier transform power spectra (FTPS). (e) to (h) show the strength of the quantum beat peaks in the FTPS as a function of XUV-XUV delay.

T2: Strongly coupled electronic and nuclear dynamics in photoexcited neutral molecules

We have accomplished first measurements of the strong field ionization dynamics of molecular nitrogen probed with femtosecond soft X-ray absorption spectroscopy at the nitrogen K-edge. Pioneering experiments performed by Leone and co-workers and Itatani and co-workers at the C- and N K-edges [ABP17, SSI19], respectively, have shown the promising potential of this technique to probe ultrafast molecular dynamics in isolated molecules, with element-selectivity and state-dependent sensitivity.

In our measurements, we use the newly developed high harmonic source that provides soft x-ray pulses in the photon energy range covering 250-450 eV [KEW21] to probe the population distribution dynamics of the first three ionic states of single-ionized molecular nitrogen cations formed by strong field ionization with femtosecond time resolution. We show that the transient A-state population remains small while the ground and second excited states of the molecular cation are equally populated (see Fig. 5). Our experiment suggests that direct electronic population inversion can be achieved by the strong ionizing laser field. Additional experiments are required to vibrationally resolve the population distribution of the molecular ion with sub-cycle time-resolution that would allow to fully decipher the underlying physical mechanisms responsible for the observed high population of the second excited state of the nitrogen molecular ion.

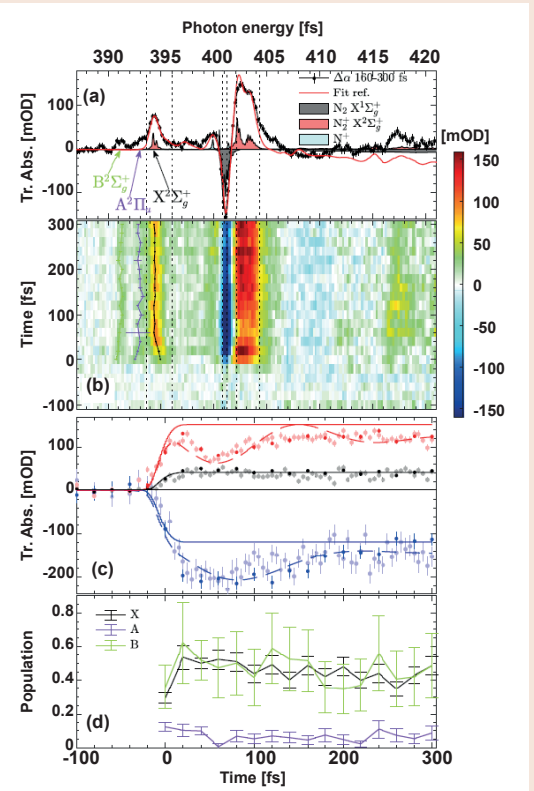

Fig. 5:
(a) Time-integrated transient absorption spectrum recorded at the N K-edge in N_2 ionized by a strong 800 nm laser pulse. (b) Time-resolved soft X-ray absorption spectrum of strongly ionized molecular nitrogen. For each time delay, the spectrum recorded at t = -100 fs was subtracted. (c) Time evolution of the X-ray absorption spectrum at the N_2 $1\sigma_u$-$1\sigma_u$ (blue dotted line), N_2^+ $1\sigma_u$-$3\pi_g$ (black dotted line) and N_2^+ $1\sigma_u$-1π (red dotted line) resonances. The dashed lines correspond to the result of simulations of the ionization dynamics based on the ADK model, including rotational coherences. (d) Time-dependent state population distribution of the three first states of the molecular ion.

T3: Ultrafast electronic decay and fragmentation dynamics at XUV and x-ray wavelengths

Towards attosecond pump-probe inner-shell spectroscopy

Recently, we have demonstrated that complex multiphoton ionization pathways induced by intense XUV pulses (in a photon energy range 16-34 eV) can be identified using a pair of intense attosecond pulse trains [KHM21].

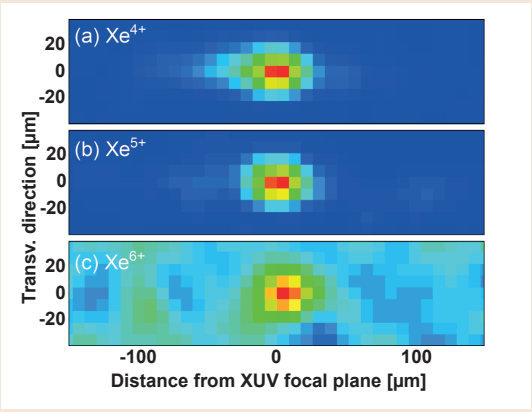

Fig. 6:
Generation of (a) Xe^{4+}, (b) Xe^{5+} and (c) Xe^{6+} ions following nonlinear inner-shell ionization of xenon using an intense APT at 90-100 eV. The estimated number of absorbed XUV photons by a single atom is (a) 2, (b) 2-3 and (c) 3-4.

These experiments were performed using a high harmonic source pumped by the output of an OPCPA system providing up to 30 mJ, sub-10 fs, 800 nm pulses at 100 Hz repetition rate, which allowed us to generate XUV pulses with intensities above 10^{14} W/cm^2, which is substantially higher than anticipated. These first investigations demonstrated that, although extremely challenging, it is possible to perform attosecond-pump attosecond-probe spectroscopy with intense XUV pulses obtained from a high harmonic source.

We are currently aiming at implementing the first attosecond-pump attosecond-probe inner-shell spectroscopy experiments using a photon energy range around 100 eV. To do so, we performed first experiments to investigate the multiphoton ionization dynamics of Xenon induced by intense XUV pulses generated at a central photon energy of 95 eV. Using a single XUV pulse, we could observe the creation of charge states up to Xe^{6+} (see Fig. 6), which require up to four XUV photons to be absorbed by a single atom. Following these first investigations, pump-probe experiments are currently being performed aiming at temporally resolving the complex Auger processes leading to the formation of the Xe^{6+} ions. While for a single Auger process, Auger channels and lifetimes can often be resolved using steady-state spectroscopic methods, this is typically not possible for complex (e.g. double and cascaded) Auger processes. In our experiments, a single- or a double-core vacancy will be generated by an attosecond pump pulse and probed using a second attosecond probe pulse at a different photon energy to temporally resolve double Auger and Auger cascade mechanisms. The successful implementation of this experiment will offer exciting opportunities for the study of inner-shell processes in molecules and in condensed matter at attosecond timescales.

Relaxation dynamics in electronically excited molecular cations

The XUV time-delay-compensating monochromator (TDSM) beamline developed in this project (in collaboration with project 3.1) offers unique opportunities to investigate XUV-induced molecular dynamics in time domain. A particular class of problems targeted within the project 2.1 is relaxation dynamics in electronically excited molecular cations. In 2021 investigation of two systems was completed and results were published supported by theoretical calculations. The first study concerned XUV+IR induced photodynamics in methyl iodide. In collaboration with the groups of L. Banares (Madrid) and F. Martin (Madrid) and with the support of LaserLab Europe, relaxation of methyl iodide cations upon ionization with wavelength-selected XUV pulses was shown to be accompanied by vibrational wavepacket dynamics in the excited state of the cation (see Fig. 7). Ab initio calculations revealed the role of the IR pulse in coupling the exicted cation to dissociative relaxation channels [MRP21]. The second system investigated at the TDSM beamline in tandem with experiments at the attosecond beamline (T1) are the highly excited naphthalene cations. Observation of the fragments related to the hot ground state in combination with model hamiltonian calculations revealed ultrafast intramolecular vibrational energy redistribution on the ground state potential energy surface [RPD21].

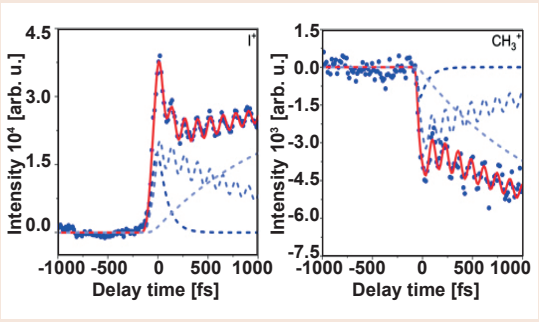

Fig. 7:
Vibrational wavepacket dynamics in the $^2A_1$ excited state of CH_3I^+.

T4: Collective and correlated electron dynamics and nuclear motion at the nanoscale

Ultrafast electron diffraction (UED) has emerged as a powerful method to investigate femtosecond dynamics in isolated molecules and in condensed phase matter. Current state-of-the-art keV non-relativistic [XWC20] and MeV relativistic [SNY19, YZN19] UED set-ups typically provide ~10^4 electrons per pulse and allow performing time-resolved measurements with a typical temporal resolution of 150-fs (FWHM), at a maximum repetition rate of 5 kHz, which limit the possible applications to the investigation of relatively slow dynamical processes.

We have recently designed and implemented the first-of-its-kind high-repetition rate, high brightness 100-keV non-relativistic ultrafast electron diffraction (UED) set-up (see Fig. 8a) driven by the output of a home-built 100-kHz OPA laser system. First electron beam signal and electron diffraction of 11-nm gold (100) crystalline film obtained using the experimental apparatus are shown in Figs. 8b and 8c, respectively. Thanks to the high repetition rate, we expect to perform measurements with

significantly fewer electrons per pulse compared to the previous keV and MeV experiments, while still achieving the same average beam current. According to simulations, reducing the bunch charge should allow for significant decrease in the compressed electron pulse duration to <70-fs, that is beyond the current capabilities of the state-of-the-art keV and MeV UED.

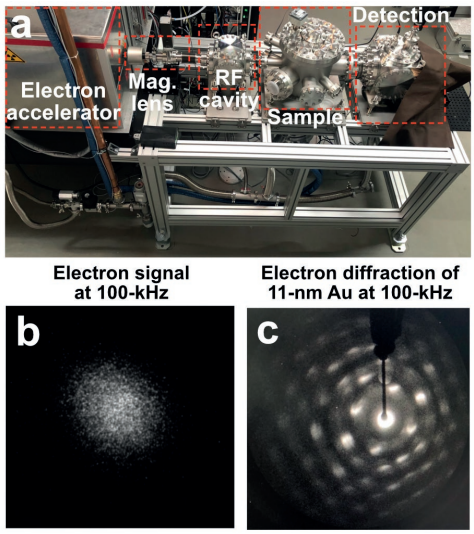

Fig. 8:
a) Schematic of the newly built 100-kHz UED set-up at the MBI. It consists of: (i) an electron accelerator chamber that accelerates electrons to ~100-keV, (ii) a magnetic lens (ML) to focus the electron beam, (iii) a radiofrequency (RF) compression chamber for temporal compression, (iv) a sample chamber, and (v) the detection chamber consisting of a microchannel plate, phosphor screen, CCD camera assembly. The electron beam direction is shown in green. The first measured signals of the electron beam (b) and electron diffraction of gold crystalline (100) 11-nm thin film (c) recorded at 100-kHz with this set-up is shown.

We are currently characterizing and optimizing our electron beam whilst also preparing for the first time-resolved optical-pump UED-probe measurements of solid-state dynamics. Initially, we will use an uncompressed electron pulse to perform first time-resolved UED measurements with an expected temporal resolution of 1-2 ps. We will then improve our instrument's temporal resolution to sub-100-fs by (i) installing a radiofrequency compression cavity to temporally compress our electron beam to sub-100-fs in collaboration with Prof. Jom Luiten (Technical University of Eindhoven) and the company Doctor X Works, and (ii) implementing an active synchronization system to correct the RF-laser timing jitter to sub-20-fs through an existing collaboration with Prof. Brad Siwick (McGill University). The UED set-up will then be used to perform time-resolved gas-phase measurements of molecular dynamics evolving on sub-500 fs timescale.

Own Publications 2021 ff

(for full titles and list of authors see appendix 1)

AAA21: F. Allum *et al.*; Time-resolved diffraction: general discussion; Faraday Discuss. **228** (2021) 161-190

ACC21: F. Allum *et al.*; Ultrafast X-ray science: general discussion; Faraday Discuss. **228** (2021) 597-621

ACF21: M. Ashfold *et al.*; Time-resolved ultrafast spectroscopy: general discussion; Faraday Discuss. **228** (2021) 329-348

BCD21: J. Biegert *et al.*; Attosecond technology(ies) and science; J. Phys. B **54** (2021) 070201/1-14

DKW21: L. Drescher *et al.*; Extreme-ultraviolet spectral compression by four-wave mixing; Nat. Photonics **15** (2021) 263-266

GRB21: P. Grychtol *et al.*; Timing and x-ray pulse characterization at the Small Quantum Systems instrument of the European X-ray Free Electron Laser; Opt. Express **29** (2021) 37429-37442

KAB21: M. Kuster *et al.*; The 1-Megapixel pnCCD detector for the Small Quantum Systems Instrument at the European XFEL: system and operation aspects; J. Synchrot. Radiat. **28** (2021) 576-587

KEW21: C. Kleine, *et al.*; Highly efficient soft x-ray spectrometer for transient absorption spectroscopy with broadband table-top high harmonic sources; Struct. Dyn. **8** (2021) 034302/1-6

Kor21: O. Kornilov; A quantum vortex made of atoms; Science **373** (2021) 1084-1084

KVS21: M. Kretschmar *et al.*; Intense XUV pulses from a compact HHG setup using a single harmonic; J. Phys. B **54** (2021) 20LT01

MGK21: B. Major *et al.*; Compact intense extreme-ultraviolet source; Optica 8 (2021) 960-965

MRP21: M. L. Murillo-Sanchez *et al.*; Femtosecond XUV-IR induced photodynamics in the methyl iodide cation; New J. Phys. 23 (2021) 073023/1-12

RPD21: G. Reitsma *et al.*; Vibrational relaxation of XUV-induced hot ground state cations of naphthalene; J. Phys. Chem. A 125 (2021) 8549-8556

Vra21: M. J. J. Vrakking; Control of attosecond entanglement and coherence; Phys. Rev. Lett. **126** (2021) 113203/1-5

Own Publications in press

DWK: L. Drescher *et al.*; Phase dependence of resonant and antiresonant two-photon excitations; Phys. Rev. A

KLA: H. Köckert *et al.*; UV-induced dissociation of CH_2BrI probed by intense femtosecond XUV pulses; J. Phys. B

KMD: L.-M. Koll *et al.*; Experimental control of quantum-mechanical entanglement in an attosecond pump-probe experiment; Phys. Rev. Lett.

WOS: T. Witting *et al.*; Generation and characterisation of isolated attosecond pulses at 100 kHz repetition rate; Optica

Submitted

KHM: M. Kretschmar *et al.*; Attosecond multi-photon multi-electron dynamics; arXiv:210813383

Other Publications

ABP17: A. R. Attar, A. Bhattacherjee, C. D. Pemmaraju, K. Schnorr, K. D. Closser, D. Prendergast, and S. R. Leone, Femtosecond x-ray spectroscopy of an electrocyclic ring-opening reaction; Science **356** (2017) 54

SNY19: X. Shen, J. P. F. Nunes, J. Yang, R. K. Jobe, R. K. Li, M.-F. Lin, B. Moore, M. Niebuhr, S. P. Weathersby, T. J. A. Wolf, C. Yoneda, M. Guehr, M. Centurion, and X. J. Wang, High-resolution movies of molecular rotational dynamics captured with ultrafast electron diffraction; Phys. Rev. Research **2** (2020) 043064

SSI19: N. Saito, H. Sannohe, N. Ishii, T. Kanai, N. Kosugi, Y. Wu, A. Chew, S. Han, Z. Chang, and J. Itatani, Real time observation of electronic, vibrational, and rotational dynamics in nitric oxide with attosecond soft X-ray pulses at 400 eV; Optica **6** (2019) 1542

XWC20: Y. Xiong, K. J. Wilkin, M. Centurion, High-resolution movies of molecular rotational dynamics captured with ultrafast electron diffraction; Phys. Rev. Research **2** (2020) 043064

YZN19: J. Yang, X. Zhu, J. P. F. Nunes, J. K. Yu, R. M. Parrish, T. J. A. Wolf, M. Centurion, M. Gühr, R. Li1, Y. Liu, B. Moore, M. Niebuhr, S. Park, X. Shen, S. Weathersby, T. Weinacht, T. J. Martinez, X. Wang, Femtosecond gas-phase mega-electron-volt ultrafast electron diffraction; Struc. Dyn. **6** (2019) 054305

Invited Talks at International Conferences
(for full titles see appendix 2)

O. Kornilov, Laserlab Europe user training workshop on data analysis in time-resolved imaging and spectroscopy (Int. Laser Centre, Slovak Centre of Scientific and Technical Information, Slovakia, virtual, 2021-05)

J. Mikosch; Technische Universität Graz, Institute for Experimental Physics (Graz, Austria, 2021-07)

B. Schütte; Seminar (Max-Planck-Institut für Quantenoptik, Garching, virtual, 2021-07)

B. Schütte; DPG Spring Meeting 2021 (virtual, 2021-09)

B. Schütte; Seminar (ELI Beamlines, Prague, Czech Republic, virtual, 2021-11)

M. J. J. Vrakking; Virtual colloquium at Imperial College “Frontiers of Ultrafast Measurement” network (2021-02)

M. J. J. Vrakking; Virtual colloquium at AMOLF (Amsterdam, Netherlands, 2021-06)

2.2: Strong-field Few-body Physics

F. Morales Moreno, J. Mikosch (project coordinators)
and D. Ayuso, W. Becker, U. Bengs, F. Branchi, U. Eichmann, M. Ivanov, Á. Jiménez, T. Kalousdian, M. Merö, D. B. Milošević, A. Ordoñez, S. Patchkovskii, H. R. Reiss, M. Richter, A. Rouzée, F. Schell, O. Smirnova, P. Stammer, M. T. Talluri, N. Zhavoronkov

1. Overview

On a sub-femtosecond temporal and Ångström spatial scale the project aims at

- understanding strong field induced dynamics in atoms and molecules,
- employing strong field processes as a tool for imaging and comprehending atomic and molecular electron dynamics and molecular structural changes,
- using tailored light pulses to manipulate electronic motion, generate high-order harmonics with specific polarization characteristics and investigate chiral phenomena.

We put specific focus on the fundamental aspects of strong field induced multi-electron dynamics, on the excitation of neutrals, on the forces exerted on these neutrals, on the role played by molecular structure and dynamics and on manipulating electronic dynamics. The strong field regime of interaction of light with matter is typically entered at light intensities beyond 10^{13} Watt/cm^2 in the infrared spectral range. There, the electric field of the light wave starts to become comparable with the intra-atomic/intra-molecular field experienced by the valence electrons.

2. Topics and collaborations

We address our objectives via experiment and closely linked theory focusing on these topics:

T1: Recollision physics and dynamic imaging in intense laser fields

T2: Strong-field processes in few-body systems

T3: Strong field excitation and HHG in tailored fields

T4: Coulomb Explosion Imaging of Photochemical Dynamics

Collaboration partners: S. P. Goreslavski, S. V. Popruzhenko (National Research Nuclear University (MEPhi), Moscow, Russia), A. Saenz (HU Berlin, Germany), Y. Mairesse (CELIA, Université Bordeaux, Bordeaux, France), N. Dudovich (Weizmann Institute, Rehovot, Israel), J. Marangos (Imperial College, London, UK), X. J. Liu (Chinese Academy of Sciences, Wuhan, China), J. Chen (Beijing University, Beijing, China), T. Marchenko (Université Pierre et Marie Curie, Paris, France), J. M. Bakker, G. Berden, B. Redlich (FOM-Institute for Plasma Physics, Rijnhuizen, The Netherlands), A. Stolow, A. E. Boguslavskiy (National Research Council of Canada, Ottawa, Canada and University of Ottawa), F. Martín (Universidad Autónoma de Madrid, Madrid, Spain), H. Stapelfeldt (Aarhus University, Aarhus, Denmark), J. Küpper, A. Rubio (Center for Free Electron Laser, University Hamburg, Germany), T. Fennel (University Rostock, Germany), A. I. Kuleff (University Heidelberg, Germany), M. Krikunova (TU Berlin, Germany), V. R. Bhardwaj (University of Ottawa, Canada), R. Cireasa (Institut des Sciences Moléculaires d'Orsay, France), F. Legare (ALLS Montreal, Canada), H. Köppel (University Heidelberg, Germany), V. S. Makhija, (University of Mary Washington, USA), J. P. Wolf (University Geneva, Switzerland), M. Kleber (TU Munich, Germany), R. Forbes (Stanford, USA), M. Spanner (National Research Council, Ottawa, Canada)

In-house collaborations with Projects 1.1, 2.1 and 4.1.

3. Results in 2021

T1: Recollision physics and dynamic imaging in intense laser fields

Laser-induced field-free alignment of indole

Imaging the structure and dynamics of isolated molecules often requires to orient and align the molecular axes along specific direction in the laboratory frame, which can be achieved through laser-induced alignment techniques. In moderately intense laser field, the interaction of the molecular polarizability with the pulse can lead to the population of a coherent rotational wavepacket that rephases periodically after the laser pulse has ended, leading to a transient alignment of the molecular axis along the polarization axis at specific times given by the rotational period of the molecule. A number of studies have investigated the alignment dynamics induced in linear, symmetric and near-asymmetric top molecules containing a heavy (typically halogen) atomic element. The alignment dynamics of more, generic, asymmetric top molecules is generally complicated, and it is often difficult to achieve a high-degree of molecular alignment in such molecular systems. We have recently demonstrated three-dimensional (3D) field-free alignment of the prototypical asymmetric top molecule indole (C_8H_7N) using elliptically polarized, shaped, off-resonant laser pulses [MKW]. We show that using a combined adiabatic-impulsive field design in which the laser pulse is composed of a long adiabatic ramp followed by a kick allows to reach an unprecedented degree of field-free three-dimensional alignment. In our work, the degree of alignment achieved experimentally was fully determined by measuring ion velocity maps of H^+ and C^{2+} fragments resulting from strong-field ionization and Coulomb explo

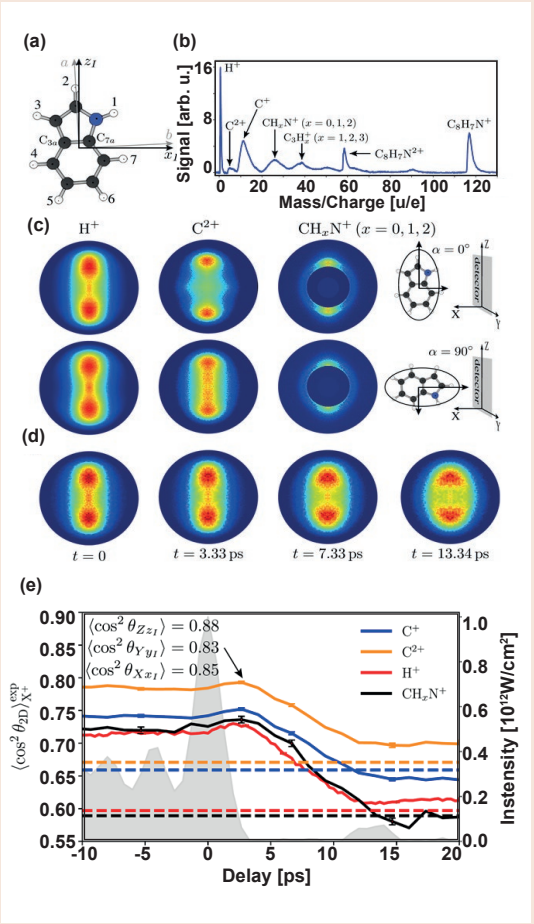

Fig. 1:
(a) Structure of indole; (b) Time-of-flight mass spectrum of indole obtained by strong field ionization of the molecule by intense, 800 nm laser pulses; (c) Ion velocity maps of H^+, C^{2+} and CH_xN^+ when the most polarizable axis of the molecule is aligned parallel or perpendicular to the detector plan; (d) Ion velocity H^+ fragments for different time delays between the alignment laser pulse and the ionizing laser pulse; (e) Extracted expectation values $<\cos^2\theta_{i,j}>$, with i=X,Y,Z the laboratory axes and $j=x_I, y_I, z_I$ the molecular axes from the recorded velocity map fragment distributions.

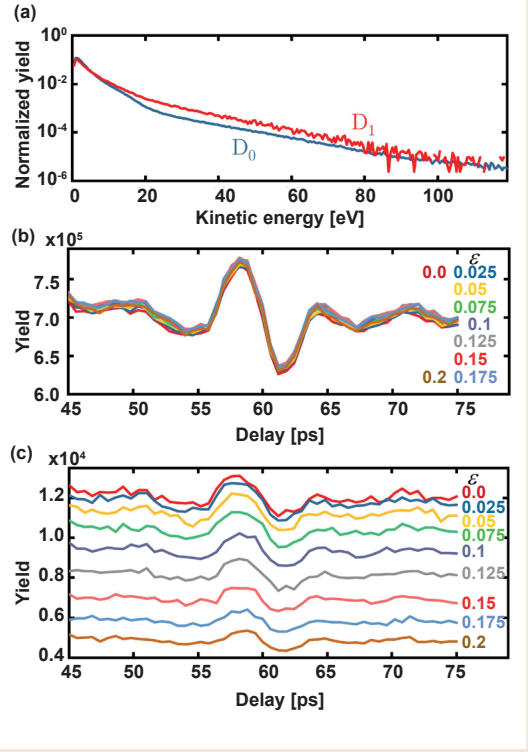

Fig. 2:
(a) Experimentally measured photoelectron kinetic energy spectrum resulting from strong-field ionization of 1,3-butadiene molecules, resolved into the D_0 and D_1 continuum channels by means of a coincidence measurement. (b) Yield of strong-field ionization associated with the D_0 channel, as a function of delay following a preceeding non-adiabatic alignment laser pulse – for ellipticities between 0 and 0.2. Panel (c) shows the respective yield of electrons in the rescattering tail.

sion of the aligned molecules by a time-delayed intense femtosecond laser pulse (see Fig. 1). Our work opens new prospects for imaging ultrafast chemical dynamics in arbitrary (bio)-molecules in the molecular frame.

Ionization channel resolved rescattering in molecules: Evidence for long quantum orbits

Quantum orbits are best known from high-order harmonic generation, where the so-called "long trajectory" and the "short trajectory" contribute, in principle, to any given harmonic, with their relative importance depending on the focusing conditions. In addition, there are the "longer trajectories", which refers to orbits that travel for a longer time between ionization and recombination than the former two. One of the first unambiguous experimental evidences of the longer orbits has been published in 2013 by a team including MBI's Wilhelm Becker [LWC13]. These authors concluded that elliptical polarization favors long quantum orbits in rare gas atoms, resulting in them playing a significant role in the recollision process under such conditions.

In the last few years, we have established experimental studies which separate different channels in strong field ionization and electron rescattering. Features associated with rescattering can be studied for different continuum wavepackets under otherwise identical conditions in a single experiment. At the same time we performed experiments on laser-aligned molecules to extract molecular frame information.

Fig. 2 shows the results of a two-dimensional experiment performed for 1,3-butadiene molecules, in which both the delay between an alignment and a strong-field ionization pulse has been varied around the first half-revival as well as the ellipticity of the mid-IR strong-field ionization driver at 1.5 µm wavelength. Panel (b) displays the strong-field ionization yield for the D_0 channel, while panel (c) displays the respective rescattering yield, i.e. the yield of electrons that appear in the tail of the photoelectron spectrum shown in panel (a). Fig. 3 (a) displays the relative rescattering yield, i.e. the ratio

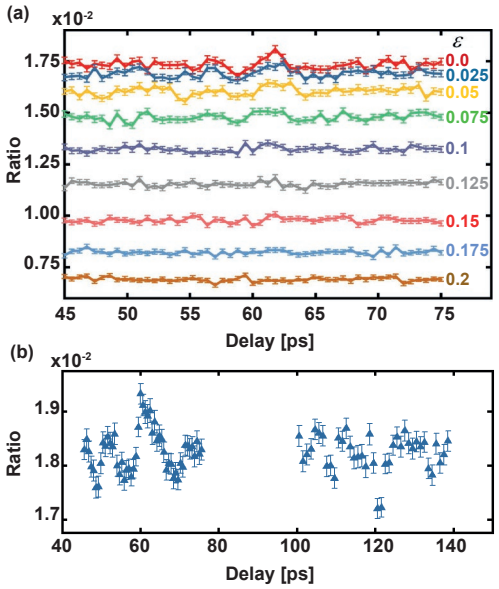

Fig. 3:
(a) Relative yield of rescattering as a function of delay and ellipticity, determined from measured yields shown in Fig. 2 (b), (c).
(b) Same result for a higher statistics measurement for zero ellipticity.

of Fig. 2 (b) and (c) as a function of delay and ellipticity. As can been seen, the weak but significant modulation around 60 ps delay for linear polarization and low ellipticity, which is displayed in Fig. 3 (b) for a higher statistics measurement with linear polarization, rapidly disappears for increasing ellipticity.

The non-adiabatic alignment pulse (~500 fs duration) creates rotational wavepackets. The observed modulation of the relative rescattering yield (Fig. 3 (b)) is a consequence of driving rescattering in a molecular ensemble with a time-dependent alignment distribution. The appearance of minimum rescattering probability at the delay corresponding to maximum alignment and maximum rescattering probability at the delay corresponding to maximum anti-alignment is consistent with the results of our earlier work on channel- and angle-resolved strong-field ionization and rescattering in 1,3-butadiene [SBS18]. The observation on the other hand that the relative rescattering probability becomes unmodulated for increasing ellipticity is stunning at first.

The laser-induced tunnel filter produces a continuum wavepacket with a transverse velocity distribution that depends on the molecular frame – and hence the delay between alignment and strong-field ionization pulse. Our observation implies that for increasing ellipticity the probability of rescattering does not depend on the transverse velocity distribution. This could indicate that longer quantum orbits, which are governed by the isotropic Coulomb interaction rather than alignment-dependent molecular effects, dominate under such conditions.

To further substantiate this interpretation, we have experimentally measured the relative rescattering yield as a function of ellipticity separately for the D_0 and the D_1 channel (see Fig.4). We find a decrease of the relative rescattering yield with increasing ellipticity, which can be fitted by a Gaussian function (see panel (a)). We have determined the width of the Gaussian distribution for different energy intervals in the recollision tail, for driver wavelengths of 800 nm (panel (b)), 1280 nm (panel (c)), and 1510 nm (panel (d)). As can be seen, there are significant differences between the two channels at 800 nm wavelength, with significantly wider distributions for the D_0 channel. This observation is a consequence of the higher transverse velocities of the D_0 continuum wavepacket as compared to D_1, resulting from two nodes in the D_0 Dyson orbital as compared to one node in the D_1 Dyson orbital. The higher transverse velocities

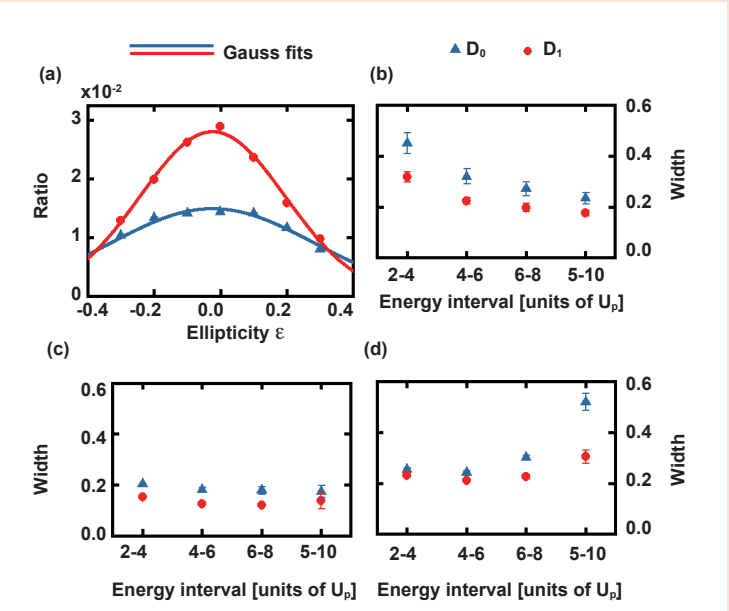

Fig. 4:
(a) Decreasing rescattering yield as a function of ellipticity, measured separately for the D0 and the D1 channel. The solid lines are the result of a Gaussian fit. (b)-(d) Width of the Gaussian distribution for driver wavelengths of 800 nm (b), 1280 nm (c), and 1510 nm (d), for different energy intervals in the recollision tail of the photoelectron spectrum.

for D_0 drives the continuum wavepacket away from the ion core, requiring higher ellipticities to compensate for the drift. However, we find a regime for mid-IR driver wavelength and lower energies in the rescattering tail, where the difference between the D_0 and the D_1 channel largely disappears (see panel (d) for 2-4 U_p and 4-6 U_p energy). This observation is consistent with the interpretation offered above, i.e. that a regime exists for increasing ellipticity in which the dynamics is dominated by longer quantum orbits that are largely governed by the Coulomb interaction and not by molecular effects.

We have started a collaboration with Wilhelm Becker and Dejan Milošević who will perform Coulomb-corrected Strong-Field Approximation (SFA) simulations to shed more light on the observed effects.

T2: Strong-field processes in few-body systems

Dissociation dynamics of state-selected (H_2^+) molecules

We explore the ultrafast dynamics of highly excited states ($np^1\Sigma_u$ & $^1\Pi^u$, n>3) of the hydrogen molecule, lying in the vicinity of the first ionization threshold (15.43 eV). The coherent excitation of the highly excited electronic states of H_2 was achieved by a tunable XUV pulse with a bandwidth of 100 meV, generated by high harmonic generation in a Kr gas cell. The resulting ultrafast wavepacket dynamics was then probed by single photon ionization with a weak infrared ultrashort probe pulse and mapped onto the energy-, angle- and time-resolved photoelectron spectrum (TRPES).

In our measurements, quantum beats are clearly observed in the time-resolved photoelectron spectrum. After energy and angle-resolved Fourier analysis, these beatings can be assigned to two-path interferences involving pairs of electronic and vibrational states populated by the XUV pulse (see Fig. 5). Surprisingly, a beating between the 5pσ(v=2, J=1) and 4pπ(v=3, J=1) states at a frequency of 192 cm^{-1} is observed. This beating is forbidden by photoionization symmetry rules in the Hund's case b. The fact that we have observed such a beating strongly indicates a departure from Hund's case b, which, in this case, it is due to weak couplings between closely lying states of σ and π symmetries. Our experiment shows that TRPES is particularly sensible to study weak nonadiabatic and spin-orbit couplings of highly excited states of molecules.

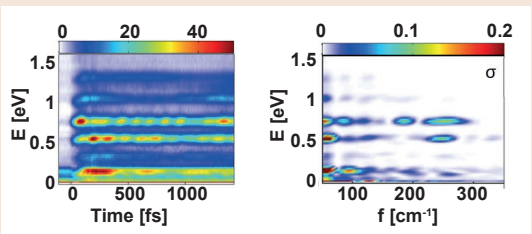

Fig. 5:
Time-dependent angle-integrated kinetic energy spectrum following XUV + NIR photoionization of H_2 molecules, and its corresponding Fourier transform.

T3: Strong field excitation and HHG in tailored fields

All-optical Stückelberg spectroscopy of strongly driven Rydberg states

The formation of electronically highly-excited states (both transient, existing only in the presence of the strong electromagnetic field, and long-lived) is a key process underlying much of atomic and molecular strong-field physics. An important aspect of the field interaction are the multi-photon resonances mediated by the ubiquitous Rydberg states, dubbed "Freeman resonances", later re-emerging as "frustrated tunnelling" in infrared fields [CWC14]. Such resonances are inevitable as the field-dressed Rydberg states experience the AC Stark shift, which mostly follows the ponderomotive potential (Up) of the laser field and exceeds the laser photon energy in strong laser fields, generally leading to resonances on the rising and the falling edges of the laser pulse (Fig. 6 (a)). As the resonance occurs twice, the two pathways must interfere, leading to intensity-dependent oscillations in the population of excited states and ion yield known as the Stückelberg oscillations. They were first predicted for atomic collisions nearly a century ago [Stu32] and arise whenever a transient resonance condition reappears after a well-defined time interval. They have been observed in a variety of contexts, from microwave ionization of Rydberg atoms to Ramsey-type interference in three-photon ionization of Na [Jon95], to one photon ionization by X-ray fields.

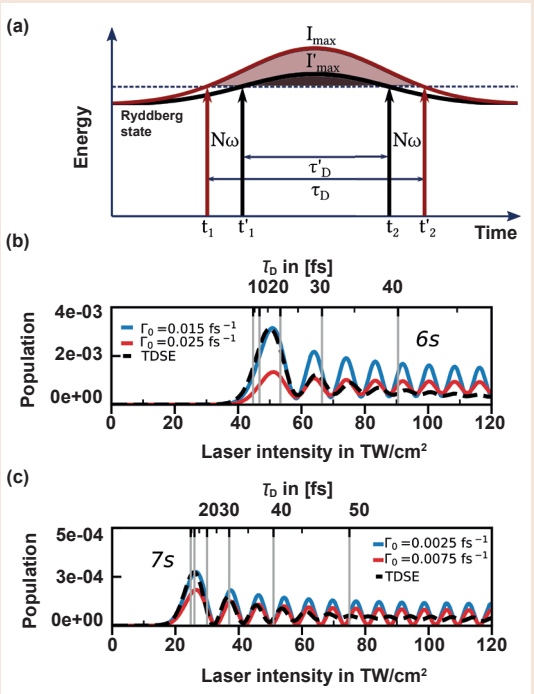

Fig. 6:
a) Origin of the Stückelberger oscillations. Energy of the Rydberg state follows the instantaneous field intensity I(t); (b), (c) populations of the 6 s and 7 s states in Argon as a function of laser intensity in the TDSE calculation and the simplified two-level model. The upper axis shows the time delay between two resonance events (see panel a).

Yet, the Stückelberg oscillations have never been observed for the simplest and ubiquitous strong-field atomic process: the multiphoton Rydberg-state excitation.

We show that an all-optical measurement of the free-induction decay (FID) emission is a sensitive all-optical probe of the coherent, long-lived population of Rydberg states prepared by an intense laser pulse, and that the all-optical setup allows one to control the volume averaging effects and reveal the Stückelberg oscillations hidden underneath. We propose using this Ramsey-type Stückelberg interferometer as a delicate probe of the dynamics and decay of strongly-driven Rydberg states inside the driving laser pulse. We confirm our experimental observations and our spectroscopic proposal through accurate numerical simulations.

Our key idea is detailed in Fig.6(a). It relies on observing the Stückelberg oscillations by changing the peak laser intensity. A laser-dressed Rydberg state passes through a multi-photon resonance with the ground state on the leading (instant t_1) and falling (instant t_2) edges of the pulse. For a symmetric laser pulse and negligible ground-state depletion, the two excitation amplitudes are identical. Their interference yields Rydberg-state population $w(t_{pulse})$ at the end of the laser pulse which is dependent on I_{max} – the intensity of the laser pulse. The depth of the oscillations of $w(I_{max})$ records the population loss from the Rydberg state between t_1 and t_2, as illustrated in Fig.6 (b, c). Thus, following the Stückelberg oscillations vs I_{max}, which controls the delay $D=t_2 - t_1$ between the resonances, allows one to measure the ionization lifetimes of strongly driven Rydberg states. Since the Stückelberg oscillations are mapped onto the final population of the Rydberg states, they can be observed via the intensity of the characteristic free induction decay lines, which are proportional to these populations. Thus, observation of the free induction decay after the laser pulse enables all-optical Stückelberg oscillations spectroscopy of strongly driven Rydberg states during the laser pulse.

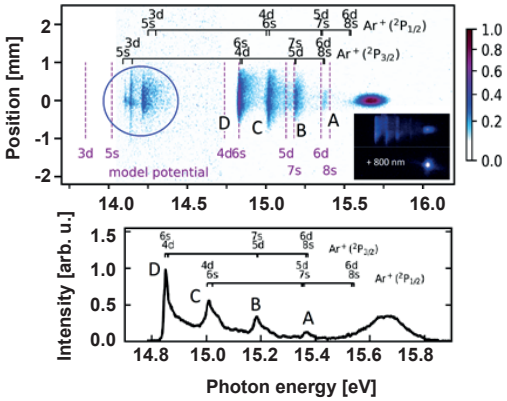

Fig. 7:
Spectrum generated at a peak intensity of 80 TW/cm². The broad peak centred around 15.65 eV corresponds to the 5th harmonic, while the four narrow lines (A-D) originate from FID of excited states associated with spin-orbit components of the Ar+ ion (2P1/2 and 2P3/2). The FID lines from 3 d, 5 s states (inside the blue circle) become prominent at higher intensities (100-120 TW). The FID lines vanish if a weak 800 nm probe pulse spatially overlaps with the 400 nm pump beam, as shown in inset of the upper panel.

We have implemented this idea experimentally [BPI]. In the experiment, we used a 1 kHz Ti:Sapphire laser system, which delivered 35 fs pulses (FWHM) centred around 795 nm with pulse energies up to 4 mJ. A laser beam attenuator at the system output enabled high resolution intensity control without change in the beam propagation direction. The radiation was further frequency-doubled in a type-I-barium-borate (BBO) crystal yielding radiation centred at 397 nm, and further focused with f/100 mirror down to 30 µm (at $1=e^2$) into a 1.0 mm long gas-cell filled with argon at a pressure of 3 mbar. The resulting XUV-radiation was analysed by a XUV spectrometer consisting of a toroidal mirror and a gold-coated grating. The distances between the spectrometer parts were carefully adjusted to obtain a 1:1 image of the interaction area. A microchannel-plate together with a phosphorus screen was placed in the image plane, converting the XUV-radiation into the visible range, which was recorded with a (CMOS) camera.

To observe the dynamics of the FID lines in detail, we spatially separate each line with a slit placed in Fourier plane close to the MCP detector. Fig. 8 shows the intensity of each of the FID lines as a function of the laser intensity. The FID radiation only appears once the AC Stark shift is sufficient to lift the corresponding state up into resonance. After prompt rise, the FID signal decreases and exhibits clear damped oscillations at higher laser intensities. Observing the oscillations confirms that the population excited on the raising edge of the pulse survives through the field maximum until the second resonance on the falling edge.

To model these experimental results, we began with the single-atom simulations. As expected, (Fig. 6), the population of the excited states increases with intensity, starting with the highest (8 s) state and progressing to the lowest (4 d), and oscillates rapidly as a function of the peak intensity for each state. Almost complete destructive interference occurs in the case of 4 d (60 TW/cm²) and 7 s (31 TW/cm²) states, whereas the depth of the oscillation in the 5 d state is rather moderate. High contrast of the Stückelberg oscillations for the 4 d, 5 d, 6 d and 8 s Rydberg states demonstrates that hardly any ionization occurs from these states even at the intensities $I=10^{14}$ W/cm², with 4 d-6 d and 8 s being the most striking examples, providing direct signature of atomic stabilization in Rydberg states.

The two-level model agrees well with the TDSE results, see Fig. 6 (b), (c), allowing us to extract the lifetime. For example, for the 6 s state, which shows rapidly decreasing oscillation contrast with the laser intensity, we find quite long lifetimes of T≈15 fs for I=40-60 TW/cm² decreasing to 10 fs at 60-70 TW/m². The d-states remain extremely stable even at high intensities, with lifetimes exceeding the pulse duration.

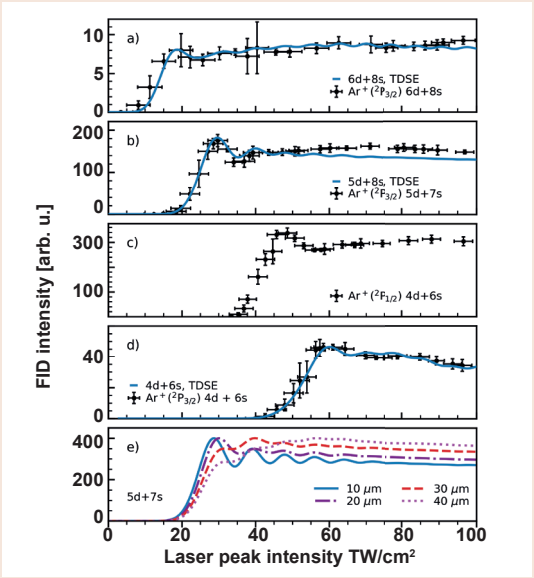

Fig. 8:
Intensity of radiation emitted from FID as a function of laser intensity obtained in the experiment (circles with the vertical and horizontal lines presenting the double standard deviations) together with results of the volume-averaged simulations (solid lines) with 17 μm in the center of the beam. The panel (e) shows the calculated FID intensities of the radiation composed of 5 d+7 s states for various slit sizes as parameter.

The Stückelberg oscillations were initially judged to be completely obscured by the focal averaging. Their observation in the few-photon regime [Jon95] required an ingenious experimental setup mapping the beam position (and thus the peak intensity) onto the detector arrival time. The crucial aspect of the experimental setup which enables observation of the Stückelberg oscillations is the combination of the toroidal mirror and planar grating used at grazing incidence in the spectrometer. This setup excludes a significant part of the divergent FID beam in the horizontal plane and effectively introduces a spatial filter placed in the object or the image plane. Without such an effective aperture, the spatial averaging would have suppressed the oscillations. The effects of the aperture on the simulated FID emission are illustrated in Fig. 8 (e). The interference is barely discernible if the whole target volume is allowed to contribute (pink dotted line). Moreover, in that case the intensity of the FID radiation increases monotonously with laser intensity for all states (data not shown). By decreasing the diameter of the aperture to values smaller than the beam waist at the focus ($2w_0$=60 μm) the interference becomes ever more visible.

To summarize, the Stückelberg oscillations in the Freeman resonances arising during strong-field ionization have been observed for the first time using free induction decay, in an all-optical setup. The aperture introduced by the setup allows one to keep the volume averaging effects under control and is the key for the success of this measurement. Our work shows that Stückelberg interference can be used as a sensitive spectroscopic tool to analyse the behaviour of Rydberg states in strong laser fields. Good agreement of the experiment with both simple two-level model and accurate numerical simulations confirms the feasibility of Ramsey-type “Stückelberg spectroscopy” of strongly driven Rydberg states via their free induction decay.

Probing the ponderomotive force on strong-field excited atoms on a picosecond time scale

Excitation of neutral atoms in strong laser fields accompanied by their acceleration in a focused laser beam as a result of the ponderomotive force has been studied by us for femtosecond long laser pulses both theoretically and experimentally. In the current investigation we explore the limits of excitation and acceleration of He atoms for laser pulse duration in the picosecond time regime. In the experiments we use a thin-disk laser developed at MBI which is able to provide sufficient pulse energy in 1.8 ps (1.3 ps) long pulses at wavelengths of 1030 nm (515 nm) to reach focused laser intensities in the vicinity of the saturation intensity of the He atom. We measure the deflection of He atoms strong-field excited in a well collimated atomic beam after a fixed distance from the laser focus to a position-sensitive detector located downstream from the atomic beam direction. In Fig. 9 we show He atoms excited with a laser field at a wavelength of 515 nm and laser intensities around the saturation intensity.

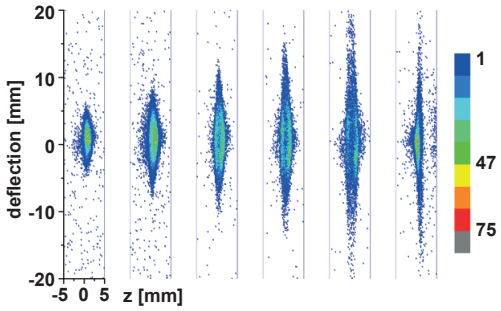

Fig. 9:
Deflected strong-field excited He atoms in a focused 515 nm laser field with a beam radius 11 um. The laser pulse energies, which are 2, 3, 4, 5, 8, and 12 mJ from left to right, respectively, covering the laser intensity range from below to above saturation. z is the laser beam direction. The atomic beam is limited in size in the z direction from z=-1 mm to 2.5 mm.

According to our laser laser parameters we investigate strong-field excitation in a regime, where the magnetic part of the Lorentz force substantially contributes to the electron dynamics. Unfortunately, quantum mechanical ab initio calculations providing information on excitation and acceleration for such long pulses are out of reach. Comparison with full semiclassical Monte-Carlo simulations is the alternative way to gain insight into the dynamics. The simulations show that some of the launched electron trajectories end in a bound excited Rydberg state after the laser field has turned off, as it is shown for a typical trajectory in Fig. 10.

A further analysis of the theoretical data reveal that about one percent of the launched trajectories, depending strongly on the position in the laser beam, survive the laser field in an excited state and are accelerated according to the ponderomotive force. This is particularly true for laser intensities, where saturation of the ionized atoms is not yet reached. The observed final velocity distribution is in accord with a situation where electrons tunneled at the maximum intensity of the laser pulse and then effectively accelerated correspondingly by the second half of the laser pulse. Taking into account the laser intensity distribution in the focal plane, we are able to model the full velocity distribution of atoms via the deflection. In Fig. 11 we show a comparison of the final transverse velocities of He atoms extracted from measured data using the laser beam at 1030 nm.

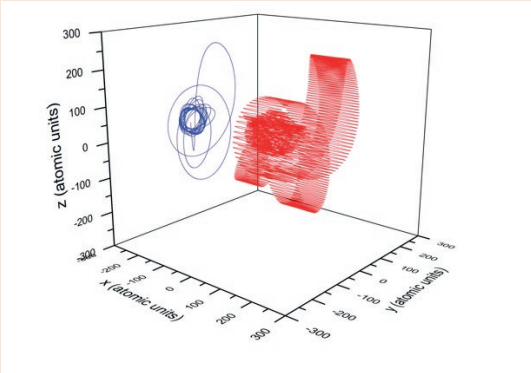

Fig. 10:
Typical bound Rydberg orbit calculated with a laser field of 2000 cycles at 515 nm at a laser intensity of close to saturation.

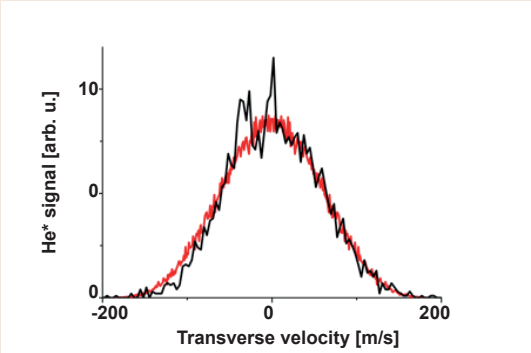

Fig. 11:
Comparison of the transverse velocity deduced for atoms originally located in the focal plane (black line) with the respective calculated velocity distribution (red line) using a focused laser field at 1030 nm close to the saturation laser intensity.

We note that while the width of the laser focus at this wavelength has been measured to be twice the size of the focus at 515 nm, the final velocity is much larger due to the fact that the deflection (velocity) is inversely proportional to the beam radius but inversely proportional to the laser frequency squared and, additionally, the laser pulse duration is longer. At laser intensities above saturation electrons are liberated early in the laser pulse which, in turn, exposes them for a longer period of time to the ponderomotive force and would thus result in larger deflections. In the experiment, however, this is not observed. Preliminary theoretical analysis of the Monte-Carlo simulations shows that atoms located slightly below the maximum gradient more likely survive in an excited state if the active electron tunnels out late in the pulse, thus thwarting the expected larger deflection. Further analysis of the data will concentrate on establishing a clearer picture of this effect. Moreover, an analysis of the final distribution of n, l and m quantum numbers, where n is the principal, l is the angular momentum and m is the magnetic quantum number, is expected to give a quantitative understanding on how the magnetic part of the Lorentz force influences the strong-field excitation process.

Own Publications 2021 ff
(for full titles and list of authors see appendix 1)

AAD21: K. Acheson *et al.*; Strong-field physics: general discussion; Faraday Discuss. **228** (2021) 470-487

KYP21: E. T. Karamatskos *et al.*; Time-resolving the UV-initiated photodissociation dynamics of OCS; Faraday Discuss. **228** (2021) 413-431

Own Publications submitted
(for full titles and list of authors see appendix 1)

BPI: U. Bengs, S. Patchkovskii, M. Ivanov, and N. Zhavoronkov; All-optical Stückelberg spectroscopy of strongly driven Rydberg states; Phys. Rev. Lett.

MKW: T. Mullins et al.; Picosecond pulse shaping for strong three-dimensional field-free alignment of generic asymmetric top molecules; Nat. Commun.

Other Publications

Stu32: E. C. G. Stückelberg; Helv. Phys. Acta **5** (1932) 369

Jon95: R. R. Jones; Phys. Rev. Lett. **74** (1995) 1091

LWC13: X. Y. Lai, C. L. Wang, Y. J. Chen, Z. L. Hu, W. Quan, X. J. Liu, J. Chen, Y. Cheng, Z. Z. Xu, and W. Becker; Phys. Rev. Lett. **110** (2013) 043002

CWC14: M. Chini, X. Wang, Y. Cheng, H. Wang, Y.Wu, E. Cunningham, P.-C. Li, J. Heslar, D. A. Telnov, S.-I. Chu, and Z. Chang; Nat. Photonics **8** (2014) 437

SBS18: F. Schell, T. Bredtmann, C. P. Schulz, S. Patchkovskii, M. J. J. Vrakking, and J. Mikosch; Sci. Adv. **4** (2018) eaap8148

3.1: Dynamics of Condensed Phase Molecular Systems

E. T. J. Nibbering, O. Kornilov (project coordinators)
and M.-A. Codescu, B. P. Fingerhut, C. Granados, P. Han, C. Kleine, A. Kundu, M. Oßwald, R. Ovcharenko, D. Rana, H.-H. Ritze, J. Schauss, M.-O. Winghart, J. Zhang

1. Overview

This project aims at a real-time observation of ultrafast molecular processes in the condensed phase, addressing the dynamics of elementary excitations, photoinduced chemical reactions and ultrafast changes of the electronic and/or chemical structure of molecular systems. The project makes use of a broad range of experimental techniques including all-optical pump-probe spectroscopy in a range from the soft-X-ray to mid-infrared, infrared photon-echo and multidimensional vibrational spectroscopies, and photoelectron spectroscopy using ultrashort VUV, XUV, and soft-X-ray pulses.

2. Topics and collaborations

Research in this project has been structured into four major topical directions:

T1: Dynamics and interactions in hydrated biomimetic and biomolecular systems

Collaboration partners: J. T. Hynes (University of Colorado, Boulder, USA), D. Laage (École Normale Supérieure, Paris, France), E. Pines (Ben Gurion University of the Negev, Beer-Sheva, Israel).

T2: Water-mediated proton transport dynamics between acids and bases

Collaboration partners: Collaboration partners: M. Odelius (Stockholm University, Sweden), Ph. Wernet (Uppsala University, Sweden), N. Huse (University of Hamburg, Germany), E. Pines (Ben Gurion University of the Negev, Beer-Sheva, Israel). D. Sebastiani (Martin-Luther-University Halle-Wittenberg, Germany).

T3: Electron transport dynamics in donor-acceptor molecular systems

Collaboration partner: V. S. Batista (Yale University, New Haven, CT, USA)

T4: Electronic excited state dynamics in molecular model systems

Collaboration partners: O. Rader (Helmholtz-Zentrum Berlin, Germany), L. Banares (Compulensa University, Madrid, Spain). R. Mitrić (Universität Würzburg, Germany), S. Haacke (University of Strasbourg, France), M. Olivucci (University of Sienna, Italy), S. Gozem (State University of Georgia, USA), H. Fielding and G. Worth (University College London, UK), P. Slavicek (University of Prague, Czech), B. Feringa (University of Groningen, The Netherlands), B. Winter (Fritz Haber Institute, Berlin, Germany).

Internal collaborations with Projects 1.1, 2.1 and 3.3 have been established.

3. Results in 2021

T1: Dynamics and interactions in hydrated biomimetic and biomolecular systems
(ERC-2018-ADG-BIOVIB, ERC-2018-STG-NONABVD)

Biomimetic and biomolecular systems and their interactions with water and ions are studied to unravel the couplings between the different molecular entities and the fluctuating water shells in the electronic ground state. Hydration dynamics of RNA and DNA oligomers in water solution, native salmon DNA in thin films and solution, and dimethylphosphate ions in water [as DNA and RNA model systems are the main topics in recent years [FSK21, ESK21]. The investigations on model RNA and DNA oligomers were successfully extended to the complex folded RNA structures of the key biomolecule transfer RNA (tRNA) [SKF21]. Most recently, electric field probing at the surface of DNA and RNA [ESK21] as well as quantitative testing of theoretical predictions from Poisson-Boltzmann theory [FSK21] were pursued.

Electric interactions have a strong impact on the structure and dynamics of biomolecules in their native water environment. Given the variety of water arrangements in hydration shells and the femto- to subnanosecond time range of structural fluctuations, there is a strong quest for sensitive noninvasive probes of local electric fields. We have demonstrated that the stretching vibrations of phosphate groups, in particular the asymmetric $(PO_2)^-$ stretching vibration $\nu_{AS}(PO_2)^-$, allow for a quantitative mapping of dynamic electric fields in aqueous environments via a field-induced redshift of their transition frequencies and concomitant changes of vibrational line shapes [ESK21]. In a systematic study on molecular systems of increasing complexity, including dimethyl phosphate (DMP), short DNA and RNA duplex structures, and tRNA in water quantitative insight in electric-field tuning rates of vibrational frequencies, electric field and fluctuation amplitudes, and molecular interaction geometries was obtained.

It was shown that the asymmetric $(PO_2)^-$ stretching vibration $\nu_{AS}(PO_2)^-$ represents a sensitive probe of local electric fields originating from a fluctuating water shell. Its pronounced frequency redshift with electric field strength is roughly linear for electric fields between 0 and some

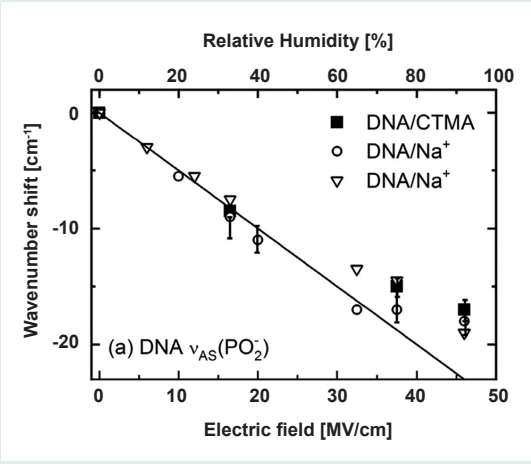

Fig. 1:
Frequency position of the $\nu_{AS}(PO_2)^-$ band as a function of the electric field acting on the $(PO_2)^-$ group: measured shift $\Delta\nu = \nu_{AS}(R.H.) - \nu_{AS}(R.H.= 0\ \%)$ of the $\nu_{AS}(PO_2)^-$ frequency position of different DNA samples (symbols) as a function of relative humidity (R.H., upper abscissa scale). The electric field scale on the bottom abscissa and the solid line were calculated with a frequency tuning rate of −0.5 cm⁻¹/(MV/cm) assuming a zero electric field at 0 % R.H. Figure from [ESK21].

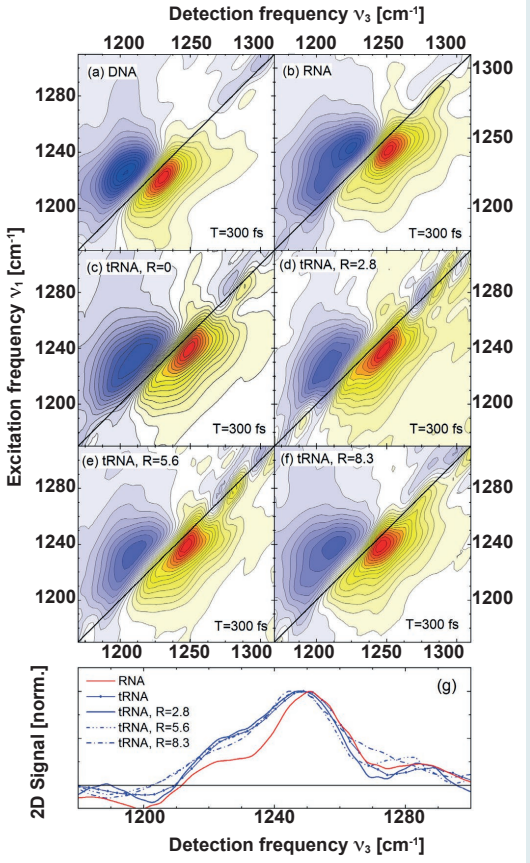

Fig. 2:
Two-dimensional infrared (2D-IR) spectra of $\nu_{AS}(PO_2)^-$ vibrations of (a) double-stranded DNA oligomers with alternating A-T base pairs and (b) double-stranded RNA oligomers with alternating A-U base pairs in water. The absorptive 2D signal is plotted as a function of the excitation frequency ν_1 and the detection frequency ν_3. Yellow-red contours represent signals on the fundamental (v=0−1) transition, blue contours on the v=1−2 transition. The signal change between neighboring contour lines is 7.5 %. The black solid line is the frequency diagonal $\nu_1=\nu_3$. (c−f) The 2D-IR spectra of E.c. tRNA in water for different excess concentrations of Mg^{2+} ions. The quantity $R=c(Mg^{2+})/c(tRNA)$ is the ratio of Mg^{2+} to tRNA concentration. (g) Cuts of the 2D-IR spectra of RNA and tRNA along a diagonal line through (ν_1, ν_3) = (1242, 1250) cm⁻¹ (RNA) and (1240, 1250) cm⁻¹ (E.c. tRNA). Figure from [ESK21].

60 MV/cm (Fig. 1), resulting in a Stark tuning rate on the order of −0.5 cm⁻¹/(MV/cm) in a large class of molecular systems, including DMP, DNA, and different types of RNA. The combination of 2D-IR spectroscopy with MD simulations gives quantitative insight in ultrafast electric field fluctuations with amplitudes between 20 and 35 MV/cm. Beyond probing electrostatic interactions, the $\nu_{AS}(PO_2)^-$ transition frequency was found to be sensitive to repulsive, that is, exchange interactions which come into play in contact pairs of ions with the $(PO_2)^-$ group. Repulsive interactions induce an upshift of the $\nu_{AS}(PO_2)^-$ frequency by up to 30 cm⁻¹, generating a distinct vibrational band that can be isolated in 2D-IR spectra and be applied as a quantitative probe of the concentration of contact pairs (Fig. 2).

The attractive interaction of phosphate groups in the RNA backbone with ions in the water environment leads to the accumulation of positively charged ions in the first few hydration layers around RNA. Electrostatics of this ion atmosphere and the resulting ion concentration profiles are frequently described by solutions of the nonlinear Poisson-Boltzmann (PB) equation and atomistic molecular dynamics (MD) simulations. Much less is known on contact pairs of RNA phosphate groups with ions at the RNA surface, regarding their abundance, molecular geometry, and role in defining RNA structure. We performed a combined theoretical and experimental study of interactions of a short RNA duplex with magnesium (Mg^{2+}) ions [FSK21]. MD simulations covering a microsecond time range provided detailed hydration geometries as well as electrostatics and spatial arrangements of phosphate-Mg^{2+} pairs, including both pairs in direct contact and separated by a single water layer (Fig. 3). The theoretical predictions were benchmarked by linear infrared absorption and nonlinear two-dimensional infrared spectra of the asymmetric phosphate stretch vibration which probes both local interaction geometries and electric fields. In short double-helical RNA, contact pairs of phosphate groups and Mg^{2+} ions were identified via clear spectroscopic signatures reflecting the high sensitivity of noninvasive infrared spectroscopy of phosphate backbone reporter modes. Contact ion pair (CIP) formation is quantified via the systematic increase of infrared absorption around 1278 cm⁻¹ for increasing Mg^{2+} concentration which allows to derive a number of

2–5 CIPs per RNA duplex for a Mg^{2+}/RNA concentration ratio of R=20–30. The quantitative analysis of infrared spectra for a range of Mg^{2+}-excess concentrations and comparison with fluorescence titration measurements thus shows that on average 20–30 % of the Mg^{2+} ions interacting with the RNA duplex form contact pairs.

The MD simulations provide a most detailed view of hydration geometries and show the coexistence of CIP and solvent separated ion pair hydration structures of Mg^{2+} ions and PO_2 groups (Fig. 3, 4). Electrostatic stabilization of helical RNA via the intergroove coordination of Mg^{2+} ions by two PO_2 groups was identified to lead to structural correlations of the sugar-phosphate backbone and ions which are absent in PB approaches. The results clearly revealed the limited reliability of PB approaches in the description of interfacial properties. Deficiencies were identified for local ion arrangements, the molecular electrostatic potential and local electric field strengths, determining peak positions in infrared absorption experiments. The work established the relevant interactions and solvation geometries for modeling of the ionic properties at the biological relevant phosphate-water interface. The findings underscore the importance of balanced molecular level descriptions of ionic interactions, the desolvation of ions and phosphate groups, coupled to structural relaxation of the RNA helix. The results underline the importance of local electric field mapping and molecular-level simulations to correctly account for the electrostatics at the RNA-water interface.

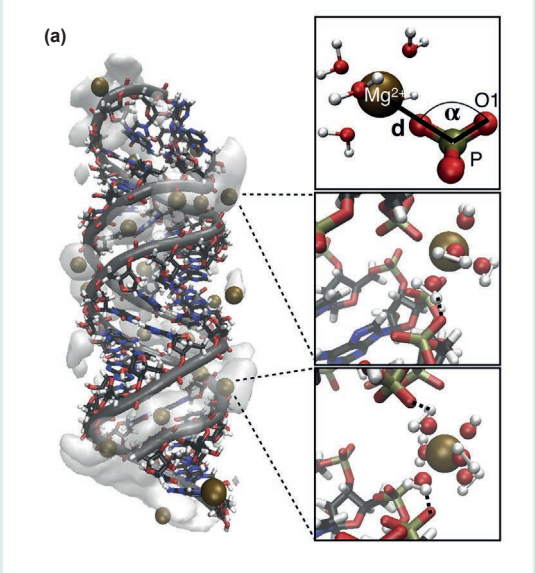

Fig. 3:
(a) Molecular structure of $(A\text{-}U)_{23}$ duplex RNA after 0.6 ms. Mg^{2+} ion positions are shown in ochre, oxygen atoms in red, nitrogen atoms in blue, carbon atoms in black, hydrogen atoms in white, and phosphorus atoms in yellow; gray contours represent the density of Mg^{2+} ions (isovalue 0.02 $Å^{-3}$). The inlays show the internal coordinates d and a (top), a CIP (middle), and an SSIP (bottom) of phosphate groups and Mg^{2+} ions together with water molecules in the first solvation shell of the Mg^{2+} ion, hydrogen bonds of H_2O with the PO_2 group are indicated with dashed lines. Adapted from [FSK21].

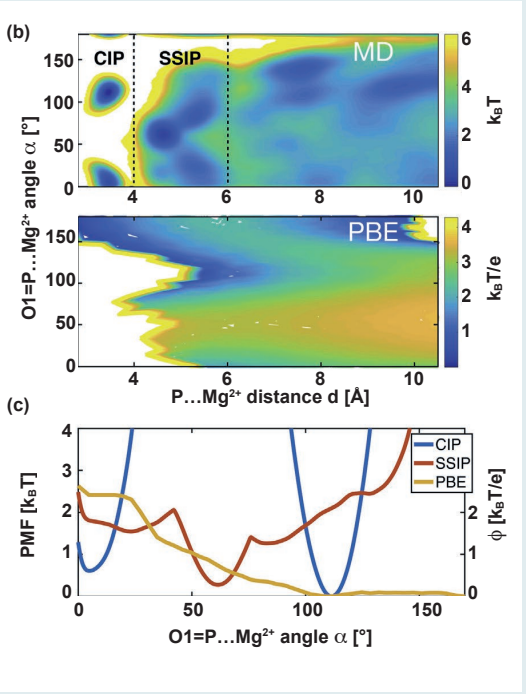

Fig. 4:
(b) PMF (top) and electrostatic potential ϕ (bottom) in the plane of PO_2 groups as experienced by Mg^{2+} ions. (c) Cuts of the PMF for CIPs and SSIPs. The PMF is compared with the electrostatic potential ϕ of angular ion translation evaluated with the nonlinear PB equation, the latter not accounting properly for CIPs and SSIPs. Adapted from [FSK21].

T2: Water-mediated proton transport dynamics between acids and bases
(DFG NI 492/13-1; ERC-2017-ADG-XRayProton)

Aqueous acid-base neutralization predominantly proceeds in a sequential way via water bridging acid and base molecules. This line of research builds on previous ultrafast studies of aqueous proton transfer using photoacids. Experimental techniques include transient UV/IR and UV/soft-X-ray absorption spectroscopies. Mid-IR absorption spectroscopy probes vibrational marker modes of particular species generated during proton transport between acid and base, as well as locally monitors hydrogen bond interactions of these species. X-ray absorption spectroscopy (XAS) probes transitions from inner-shell levels to unoccupied molecular orbitals, making it a tool to monitor electronic structure with chemical element specificity [EWK]. Ultrafast UV/IR spectroscopy enables the elucidation of proton transfer pathways and the associated time scales for individual proton transfer steps [CWB21]. Much effort has been devoted in recent years to develop steady-state and time-resolved soft-x-ray spectroscopy of acids and bases in water-poor and water-rich solutions [EKL, EWK]. Here novel liquid flatjet technology is utilized with soft-X-ray sources at synchrotrons [EKL,

EWK], free-electron lasers [EEM21] as well as table-top laser-based high-order harmonic systems [KEW21], to elucidate the electronic structural evolution of proton transfer pathways.

The COVID-19 pandemic had put the activities on steady-state and ultrafast soft-X-ray spectroscopy at large scale facilities “on hold” in 2020. Fortunately in 2021 beamtimes at HZB-BESSYII and at LCLS enabled further progress in probing transient electronic structure of ultrafast acid-base reaction dynamics.

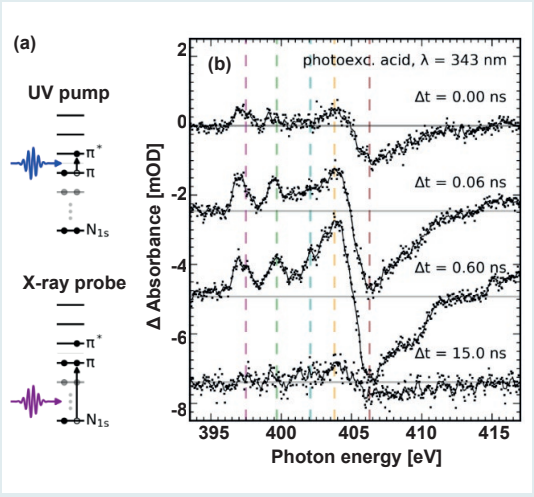

Fig. 5:
Accessing the Förster cycle of APTS through UV pump – X-ray absorption probe spectroscopy. (a) The S_1 state, characterized by a dominant π → π transition, is populated by a photo-excitation of the HOMO → LUMO ($S_0 \rightarrow S_1$) transition. Consecutive absorbance changes in the nitrogen K-edge spectral range probing the transient population kinetics of the π* and other electronic states monitor the dynamics of APTS along the Förster cycle. Transient X-ray absorption spectra of the APTS photo-exci-ted in its photoacid (b) form measured for specific pulse delays, and the time dependence of the transient changes as recorded at specific probe energies enable us to monitor both the deprotonation process, as well as the transient population of the orbitals involved in the excitation.*

Photoacids show a strong increase in acidity in the first electronic excited state, enabling real-time studies of proton transfer in acid-base reactions, proton transport in energy storage devices and biomolecular sensor protein systems. Several explanations have been proposed for what determines photoacidity, ranging from variations in solvation free energy to changes in electronic structure occurring along the four stages of the Förster cycle. We have used picosecond nitrogen K-edge spectroscopy to monitor the electronic structure changes of the proton donating group in a protonated aromatic amine photoacid, 8-aminopyrene-1,3,6-trisulfonate (APTS), in aqueous solution in solution upon photoexcitation and subsequent proton transfer dynamics [SWK]. Probing core-to-valence transitions locally at the amine functional group and with orbital specificity, we clearly reveal pronounced electronic structure, dipole moment and energetic changes on the conjugate photobase side. This result paves the way for a detailed electronic structural characterization of the photoacidity phenomenon.

We have further explored the proton transport mechanism between the proton donating OH-group and the proton accepting quinoline unit of the bifunctional photoacid 7-hydroxyquinoline (7HQ). In previous years proton transfer dynamics of 7HQ in water/methanol mixtures has been investigated. Current activities have focused on the role of bases added to the solution, with which a possible change in reaction pathways can be imposed onto 7HQ [CWB21]. Results on the 7HQ-formate reaction pair in methanol have shown that the outcome of the proton transfer dynamics can be quantitatively changed for high base concentrations (2.0 – 4.0 M). Whereas proton exchange from the proton accepting quinoline unit towards the proton donating OH-group of 7HQ occurs through a proton vacancy methoxide transfer hopping mechanism along a methanol solvent bridge (with 7HQ following the neutral N* → cationic C* → zwitterionic tautomer Z* pathway), the added formate anion accelerates the first proton transfer to take place from the 7HQ OH-group (thus facilitating that 7HQ converts as neutral N* → anionic A* → zwitterionic tautomer Z*). We have continued to explore the proton transport mediating function of imidazole as added base.

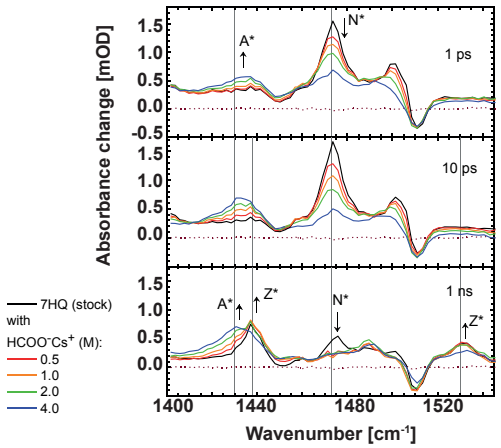

Fig. 6:
Comparison of transient UV/IR pump-probe spectra of 7HQ in CD_3OD measured at 1 ps, 10 ps and 1 ns pulse delay times for different $HCOO^-Cs^+$ base concentrations. Dotted lines are reference lines denoting the frequency positions of N (1473 cm^{-1}), Z* (1437 cm^{-1}) and A* (1430 cm^{-1}) 7HQ-species.*

T3: Electron transport dynamics in donor-acceptor molecular systems
(ERC-2017-ADG-XRayProton, SMART-X)

In this topical area, elementary charge transport dynamics in solution are investigated from the viewpoint of their functional role in biochemical processes. The objective is to elucidate the underlying mechanisms

for electron transfer, proton transfer as well as proton-coupled electron transfer in donor-acceptor molecular systems. This line of research builds on previous ultrafast studies of photoinduced electron transfer processes in donor-acceptor complexes. Experimental techniques include, besides ultrafast UV/IR spectroscopy, ultrafast UV/soft-X-ray measurement methods using laboratory-based table-top laser systems and large-scale facilities (storage rings, free electron lasers).

For the table-top approach we have recorded ultrafast soft-x-ray absorption spectra in transmission mode at the N K-edge of molecular systems in the gas and solution phases. This set-up has been implemented with a new X-ray spectrometer, equipped with a reflective zone plate as diffractive element for the extreme high-order harmonic (HHG) pulses covering 200-450 eV and an X-ray CCD detector to detect the extreme HHG pulses with a frequency resolution sufficient to distinguish pre-edge and main-edge spectral features typical for mid-sized organic molecules in solution [KEW21]. First results on strong field ionization of molecular nitrogen in the gas phase have been achieved (see project 2.1). Current activities involve further developments towards ultrafast soft-X-ray spectroscopic measurements of molecular systems in the gas-phase (in collaboration with project 2.1) and ultimately in liquid solution.

.

T4: Electronic excited state dynamics in molecular model systems
(DFG KO 4920/1-1; DFG FI 2043/1-1)

Photoelectron spectroscopy is one of the most powerful analytical tools for studies of molecular electronic structure. In particular, time-resolved photoelectron spectroscopy (TRPES) is considered to be one of the most viable methods to track dynamics at conical intersections. In this topical area T4 TRPES methods have recently been extended to the liquid phase employing an XUV time delay compensating monochromator beamline based on a high-order harmonic generation source. The setup provides wavelength-selected XUV radiation for the probe pulses in the traditional pump-probe configuration of time-resolved experiments. The beamline is coupled to a microliquid jet endstation, which allows for studies of molecules in solutions. An NIR/vis pump pulse is used to excite organic solute molecules, which are ionized by the probe XUV pulses. The photoelectrons are detected using the magnetic bottle time-of-flight spectrometer. The first application of the technique was demonstrated in 2018 in investigation of intramolecular proton transfer in Quinoline Yellow molecules. In 2019/2020 the work continued and was extended to studies of aminoacids, Quinoline Yellow in solvents with different pH values and to dynamics of proton transfer in pyranine in collaboration with the topical area T2.

One of the particular challenges for the photoelectron spectroscopy experiments is the ab initio theory, which can support the interpretation of photoelectron spectra. This task requires calculation of time-resolved photoelectron spectra for molecules of substantial size surrounded by a solvent. In 2019 a collaboration with one of the leading theory groups in this field, the group of Prof. Roland Mitrić (Uni Wuerzburg) was established. In 2021 the first joined publication on ultrafast relaxation of aminoazobenzenes demonstrated that the TRPES method is sensitive enough to allow choosing a DFT functional most suitable for the description of molecular dynamics.

The development of the method of liquid phase TRPES opens exciting prospects for analytical experiments in molecular dynamics. The main focus of the future applications of the methods are biomimetic photoactuators: molecular switches and motors, which can be used in biological environments. In 2021 a broad collaboration network on this topic has been established. In addition to the existing collaborations with R. Mitrić (Wuerzburg) S. Haacke (Strasbourg) and M. Olivucci (Sienna), joint scientific projects have been initiated with the leading experimental, theoretical and organic chemistry groups in this research area, namely the groups of H. Fielding and G. Worth (London), P. Slavicek (Prague), B. Feringa (Groningen) and B. Winter (Berlin).

Photoelectron spectroscopy is not only a great analytical tool for studies of electronic structure, but was shown to have very high signal contrasts in studies of chiral signals, which opens access to a wide class of phenomena related to molecular chirality. With the topical area T4 circularly polarized UV light pulses and photoelectron detection are used to implement the promising method of circular dichroism photoelectron spectroscopy. In 2020 and 2021 the method was applied to fenchone molecules. The study is funded by a DFG project.

Further activities in the topical area T4 include collaboration with the Leibniz Institute for Zoo- and Wildlife Research (IZW) and the Immunology institute of Free University of Berlin. The topic of collaboration is the investigation of non-linear interaction of laser radiation with living organisms, such as cells or common worm parasites. In 2019 a femtosecond laser laboratory was temporarily established at IZW. In 2021 a PhD student has joined the project and the first results have been obtained demonstrating statistically significant difference in response of ascaris suum eggs to femtosecond pulses as compared to cw radiation. Interpretation of the results is under way.

Own Publications 2021 ff

(for full titles and list of authors see appendix 1)

CWB21: M.-A. Codescu *et al.*; Switching between proton vacancy and excess proton transfer pathways in the reaction between 7-hydroxyquinoline and formate; J. Phys. Chem. A **125** (2021) 1845-1859

EEM21: R. Y. Engel *et al.;* Shot noise limited soft x-ray absorption spectroscopy in solution at a SASE-FEL

using a transmission grating beam splitter; Struct. Dyn. **8** (2021) 014303 /1-10

ESK21: T. Elsaesser *et al.*; Phosphate vibrations probe electric fields in hydrated biomolecules: spectroscopy, dynamics, and interactions; J. Phys. Chem. B **125** (2021) 3899-3908

FSK21: B. P. Fingerhut *et al.*; Contact pairs of RNA with magnesium ions-electrostatics beyond the Poisson-Boltzmann equation; Biophys. J. **120** (2021) 5322-5332

KEW21: C. Kleine *et al.*; Highly efficient soft x-ray spectrometer for transient absorption spectroscopy with broadband table-top high harmonic sources; Struct. Dyn. **8** (2021) 034302/1-6

SKF21: J. Schauss *et al.*; Magnesium contact ions stabilize the tertiary structure of transfer RNA: electrostatics mapped by two-dimensional infrared spectra and theoretical simulations; J. Phys. Chem. B **125** (2021) 740-747

THI21: E. Titov *et al.*; Electronic relaxation of aqueous aminoazobenzenes studied by time-resolved photoelectron spectroscopy and surface hopping TDDFT dynamics calculations; Faraday Discus. **228** (2021) 226-241

Own Publications submitted

EKL: M. Ekimova *et al.*; Covalent nature and hydration of the Zundel cation in solution; Angew. Chem. Int. Edit.

EWK: S. Eckert *et al.*; Revealing the transient electronic structure changes along the photoacid Förster cycle with picosecond nitrogen K-edge x-ray absorption spectroscopy; Angew. Chem. Int. Edit.

Invited Talks at International Conferences
(for full titles see appendix 2)

T. Elsaesser; Max Water Workshop on “Hydration” (Max-Planck-Institute for Polymer Research, Mainz, Germany (virtual, 2021-01)

T. Elsaesser; International Conference on Time-Resolved Vibrational Spectroscopy (TRVS 2021) (virtual, 2021-06)

T. Elsaesser; Vibrational Dynamics Workshop (Telluride, CO, USA (virtual, 2021-07)

T. Elsaesser; Summer School 2021 for the International Max Planck Research School for Many Particle Systems in Structured Environments (Dresden, Germany, 2021-09)

T. Elsaesser; CECAM Workshop “Nonequilibrium dynamical solvent effects on excited states: From spectroscopy to photoreactivity” (Nancy, France virtual, 2021-06)

T. Elsaesser *together with* J. Schauss, A. Kundu, and B. P. Fingerhut; Pacifichem 2021 (virtual, 2021-12)

B. P. Fingerhut; Int. Symposium on Molecular Spectroscopy (ISMS) (Urbana-Champaign, USA (virtual, 2021-06)

E. T. J. Nibbering *together with* M.-A. Codescu, M. Weiß, M. Brehm, O. Kornilov, and D. Sebastiani; Int. Conference on Time-Resolved Vibrational Spectroscopy (TRVS 2021) (virtual, 2021-06)

E. T. J. Nibbering *together with* S. Eckert, M.-O. Winghart, A. Banerjee, C. Kleine, J. Ludwig, M. Ekimova, J. Harrich, R. Mitzner, E. Pines, N. Huse, Ph. Wernet, and M. Odelius; Int. Conference on Photochemistry - 30th Edition ICP2021 (virtual, 2021-07)

E. T. J. Nibbering *together with* S. Eckert, M.-O. Winghart, M. Ekimova, C. Kleine, J. Ludwig, M. Ochmann, T. A. E. Agrenius, A. Banerjee, E. Kozari, J. Harich, R. Mitzner, E. Pines, N. Huse, Ph. Wernet, and M. Odelius; Ultrafast Dynamic Imaging of Matter 2021 (UFDIM 21) (Potsdam, Germany (virtual, 2021-09)

E. T. J. Nibbering; Solid State Proton Conductors SSPC-21 (virtual, 2021-09)

E. T. J. Nibbering *together with* M. Ekimova, C. Kleine, J. Ludwig, M.-A. Codescu, S. Eckert, M.-O. Winghart, F. Hoffmann, G. Bekçioğlu-Neff, M. Weiß, M. Ochmann, A. Rafferty, A. Banerjee, T. E. G. Agrenius, E. Kozari, J. Harich, M. Brehm, O. Kornilov, R. Mitzner, E. Pines, N. Huse, Ph. Wernet, M. Odelius, and D. Sebastiani; 7th Theme Meeting on Ultrafast Science – 2021 (UFS-2021) (virtual, 2021-11)

M.-O. Winghart *together with* C. Kleine, Z.-Y. Zhang, M. Ekimova, S. Eckert, M. J. J. Vrakking, E. T. J. Nibbering, and A. Rouzée; 2nd Annual Workshop of the COST Action AttoChem (virtual, 2021-10)

3.2: Solids and Nanostructures: Electrons, Spins, and Phonons

C. von Korff Schmising, S. Sharma and M. Woerner (project coordinators)
and V. Bender, M. Borchert, K. Busch, J. R. Cardoso de Andrade, V. DeMichele, P. Elliot, A. Ghalgaoui, R. Grunwald, M. Hennecke, S. Jana, P. Jürgens, T. Kang, Q. Li, A. Mermillod-Blondin, T. Noll, A. Perez-Leija, B. Pfau, L. Rammelt, K. Reimann, M. Runge, P. Scheid, D. Schick, S. Shallcross, T. Sidiropoulos, N. Singh, P. Singh, R. Smith, F. Steinbach, N. Stetzuhn, J. W. Tomm, K. Tschernig, K. Yao

1. Overview

This project addresses ultrafast and nonlinear phenomena in solids and nanostructures. In correlated condensed-matter systems, interaction of electrons, phonons and spins lead to a broad range of novel and unusual phenomena, which are interesting from the point of view of both fundamental research and practical applications. To gain new insight into microscopic phenomena in this thriving field of research, experiments are performed with ultrafast time resolution and in a very wide spectral range extending from terahertz to X-ray frequencies. The work includes studies in the regime of nonperturbative light-matter interactions.

Our basic research is complemented by studies of light-matter interactions in materials processing with ultrashort optical pulses and by work on optoelectronic devices. The project includes five topics.

2. Topics and collaborations

Research in this project has been structured into five major topical directions:

T1: Nonlinear THz and mid-infrared spectroscopy
(DFG WO 558/14-1)

Cooperation partners: K. Biermann (Paul-Drude-Institut, Berlin, Germany), C. Flytzanis, (Ècole Normale Supérieure, Paris, France), A. Tkatchenko (University of Luxembourg), G. Cassabois and B. Gil (Université de Montpellier, France), M. Lazzeri (Sorbonne, Paris, France), G. Fugallo (Université de Nantes, France), M. Fiebig (ETH Zurich, Switzerland).

T2: Material modification with femtosecond laser pulses
(DFG ME 4427/1-2, SAW LAPTON, DFG-ANR NA 1102/3-1.)

Collaborations: T. Fennel (University of Rostock, Germany), J. Schwietering (Fraunhofer IZM, Berlin, Germany), J.P. Colombier (LabHC, Saint-Etienne, France).

T3: Optoelectronic devices

Semiconductor-based optoelectronic devices and materials are the subject of investigations in this topic. This includes diode lasers, light emitting diodes (LED), and semiconductor gain materials such as ZnSe:$Cr^{2+}Fe^{2+}$. Such crystals can be considered as potential active elements in solid-state lasers emitting in the 2-5 µm spectral region. Spectroscopic analyses of GaN-based optoelectronic devices were done with J. Jimenez of the University of Valladolid, Spain, and together with scientists from the Ferdinand-Braun-Institut GmbH, Leibniz-Institut für Höchstfrequenztechnik such as S. Einfeld, C. Netzel and J. Ruschel. This includes carrier kinetics in the materials themselves as well as in Al-rich short-wavelength diode lasers and LEDs. Work on Silicon-based infrared emitting devices is being done with F. Yue of East China Normal University in Shanghai, China.

T4: Magnetism and transient electronic structure

Cooperation partners are various principal investigators within the Collaborative Research Center TRR 227 “Ultrafast Spin Dynamics” (MBI projects: A02, A04), M. Ramsteiner and J. M. J. Lopes, Paul-Drude-Institut, Berlin, J. Lüning, HZB, Berlin, S. Bonetti, Stockholm University, Uppsala University, Sweden, Christian Gutt, University Siegen, M. Albrecht, Augsburg University, E. K. U. Gross, MPI Halle, M. Schultze MPQ Garching, M. Münzenberg, Greifswald University.

T5: Joint HU-MBI Group on Theoretical Optics

Projects: within the DFG-SPP-1839 “Tailored Disorder”, project Bu 1107/10-1, Bu 1107/10-2 “Light-path engineering in disordered waveguiding systems” and Bu 1107/12-2 “Non-Markovian continuoustime quantum random walks of multiple interacting particles”.

Cooperation partners: W. Pernice, University of Münster, A. Szameit, University of Rostock, N. A. Mortensen, University of Southern Denmark, R. de Jesus Leon-Mortiel, Universidad Nacional Autónoma de México, and S. Linden, University of Bonn.

3. Results in 2021

T1: Nonlinear THz and mid-infrared spectroscopy

Two-dimensional terahertz (2D-THz) spectroscopy is our key experimental concept for studying the nonlinear response of condensed matter in the spectral range between 300 GHz and 30 THz. In one of the highlights of this annual report, a study of mono-cycle terahertz pulses from intersubband shift currents in asymmetric semiconductor quantum wells using 2D-THz spectroscopy was presented [RKB21].

In another experiment, we investigated in detail ultrafast and coupled – atomic vibrations in the quantum material boron nitride [KZK21].

Materials consisting of a few atomic layers display properties which are governed by quantum physics and can be tailored in a wide parameter range. In a stack of such layers, vibrations of the atoms can be triggered by infrared light. New experimental and theoretical work shows that atomic vibrations within the layers of hexagonal boron nitride, the transverse optical (TO) phonons, couple directly to motions of the layers against each other. For a period of some 20 ps, the coupling results in a frequency down-shift of the optical phonons and their optical resonance. This behavior is a genuine property of the quantum material, i.e., absent in the bulk material, and of interest for applications in high-frequency optoelectronics.

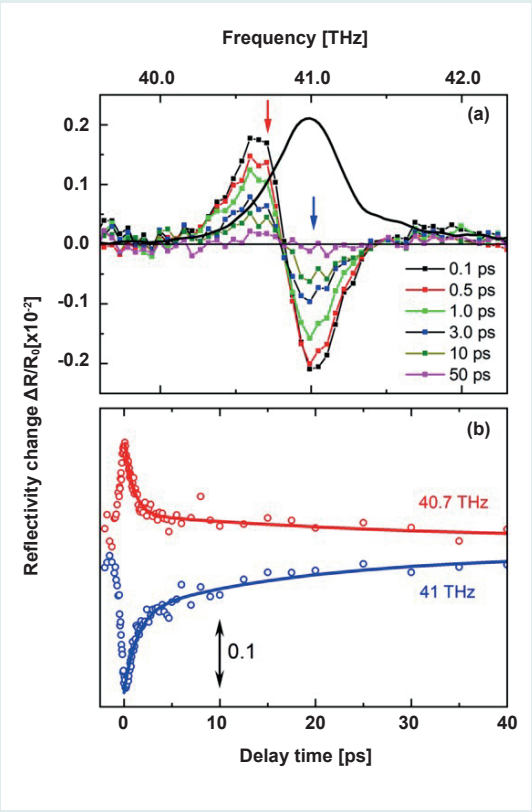

Fig. 1:
(a) Stationary reflectivity spectrum (thick black line) of a stack of 8 to 9 hexagonal boron nitride layers in the range of the TO phonon resonance. The reflectivity is plotted as a function of frequency. The symbols display the change of reflectivity $\Delta R=(R-R_0)/R_0$ observed after femtosecond excitation of the sample at the delay times given in the inset (R, R_0: reflectivity with and without excitation). At delay times longer than 3 ps, the increase of reflectivity at low frequency and its decrease at high frequency correspond to a down-shift of the TO phonon resonance, induced by excitation of shear and breathing modes. (b) Change of reflectivity at 40.7 THz (red arrow in panel (a)) and at 41 THz (blue arrow in panel (a)) as a function of the delay time between pump and probe pulses (in picoseconds). The transients exhibit a fast decay with a time constant of 1.2 ps, the TO phonon lifetime, and a slow decay with 22 ps, the lifetime of shear and breathing modes.

Hexagonal boron nitride consist of layers in which covalently bonded boron and nitrogen atoms form a regular array of six-rings. Neighboring layers are coupled via the much weaker van der Waals interaction. TO phonon excitations are connected with a displacement of boron and nitrogen atoms in the layer and show an oscillation frequency on the order of 40 THz (1378 cm^{-1}). This frequency is ten to hundred times higher than that of shear and breathing motions of the layers relative to each other. So far, there was nearly no insight into the lifetime of such motions after optical excitation and into their coupling.

The THz team of project 3.2 together with scientists from Berlin, Montpellier, Nantes, Paris and Ithaca (USA) studied the nonlinear phonon response of a stack of 8 to 9 boron nitride layers in temporally and spectrally resolved pump-probe experiments with femtosecond mid-infrared pulses. TO phonons display a lifetime of 1.2 ps (1 ps =10^{-12} s), while shear and breathing modes show a decay time of 22 ps (Fig. 1(b)). Such lifetimes are in very good agreement with values derived from a theoretical analysis of the phonon decay channels.

Excitations of shear and breathing modes induce a characteristic spectral down-shift of the TO phonon resonance in the optical spectra (Fig. 1(a)). This shift of approximately 10 cm^{-1} is due to the anharmonic coupling of TO phonons to shear and breathing modes which are excited via a Raman process within the spectral bandwidth of the pump pulses. Theoretical calculations give the coupling energy between the different modes of the layer stack and show that the corresponding coupling is negligibly small in a bulk boron nitride crystal consisting of many layers. Thus, the observed coupled vibrational dynamics represent a genuine property of the quantum material.

The spectral shift of the TO phonon resonance in the optical spectra is a nonlinear optical effect which can be induced by light of moderate power. This is of interest for applications in optoelectronics and holds potential for optical modulators and switches in the giga- to terahertz frequency range.

T2: Material modification with femtosecond laser pulses

The interaction of intense ultrashort laser pulses with transparent solids potentially leads to permanent refractive index changes in the irradiated region, forming the basis for a wide variety of applications from data storage to the direct laser writing of photonic integrated circuits. The laser-induced refractive index changes are triggered by the formation of an electron-hole plasma, i.e. the promotion of valence band electrons into the conduction band. The main excitation mechanisms in solids, strong-field (SFI) and electron-impact ionization (IMP), are well established. However, their relative importance generally remains obscure.

In a recent collaboration with the University of Rostock (AG Fennel), we have demonstrated that the low-order, two-color wave-mixing signal at near-threshold

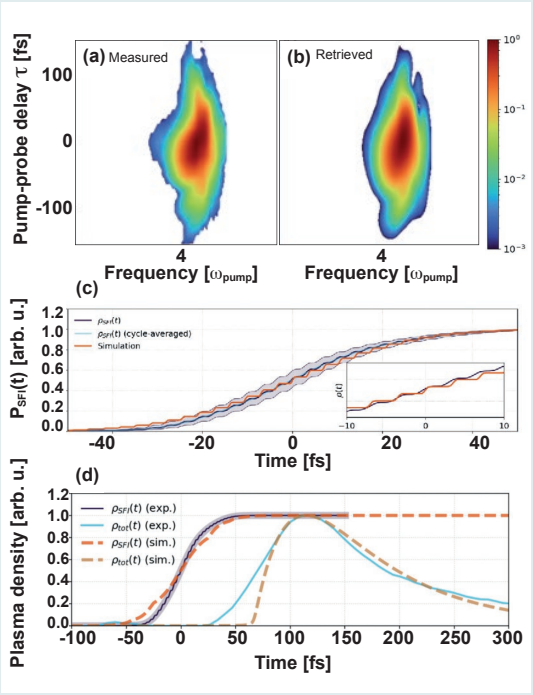

Fig. 2:
Reconstruction of the strong-field-induced plasma formation from a time-resolved measurement of injection harmonics. (a) Measured time-frequency map of the two-color wave-mixing signal at a near threshold pump laser intensity. (b) Retrieved spectrogram using time-domain ptychography. (c) Strong-field-induced plasma formation retrieved from the time-resolved measurement of the two-color wave-mixing signal compared to numerical simulations. (d) Comparison between the SFI-induced plasma formation and the total plasma dynamics obtained from a time-resolved absorption measurement.

pump laser intensities in fused silica is dominated by a previously overlooked mechanism that is directly linked to the interband transition of electrons from the valence into the conduction band (i.e. the injection current).

By combining the time-resolved measurement of the two-color wave-mixing signal with an iterative phase-retrieval algorithm (e.g. time-domain ptychography) we are able to extract the plasma formation solely induced by SFI. An exemplary experimental result of the ptychographic iterative engine obtained at a peak intensity of 13 TW/cm² of the pump laser pulse is shown in Fig. 2(a), (b). The iterative algorithm is able to reconstruct the temporal and spectral features of the measured signal with high accuracy down to the noise level of the experiment. We obtain the strong-field-induced conductivity as a direct result of the phase-retrieval that contains all necessary information to compute the plasma formation due to SFI (see Fig. 2(c)). A nearly stepwise increase of the plasma density with twice the frequency of the excitation field is observed that shows an excellent agreement to the results of our numerical model.

A simultaneous measurement of the time-resolved absorption of a weak probe laser pulse by the electron-hole plasma provides access to the total plasma density dynamics. Comparing the strong-field-induced plasma formation obtained from the iterative phase-retrieval and the total plasma density enables to determine the relative importance of SFI and IMP. As illustrated in Fig. 2(d) the plasma density induced by SFI is already close to its maximum when the total plasma density leads to a measurable increase of absorption. Hence, we can conclude that the formation of the electron-hole plasma under our experimental conditions is clearly dominated by IMP while SFI only provides the necessary seed electrons to efficiently launch the subsequent collisional ionization process.

Possible extensions of our experiment include the implementation of a carrier-envelope phase stabilized laser source to improve the subcycle accuracy of our iterative retrieval, while the exact shape of the steps could be decoded by including higher wave-mixing orders with a well-characterized relative phase.

In conclusion, we have demonstrated the possibility to reconstruct the plasma formation induced by SFI from a time-resolved measurement of injection harmonics. As a first application, we have investigated the relative importance of SFI and IMP in strongly excited fused silica. Our findings provide a simple, all-optical method for real-time monitoring of the carrier dynamics in transparent solids including semiconductors, which will result in advanced control and optimization of the irradiation conditions for femtosecond laser processing.

T3: Optoelectronic devices

The transfer of electronic excitations from Cr^{2+} to Fe^{2+} ions in co-doped ZnSe has been studied by time-resolved photoluminescence (PL) spectroscopy; see Fig. 3 [FTG]. Upon excitation of Cr^{2+} ions by a picosecond pulse at 2.05 µm wavelength, PL from Fe^{2+} ions displays a delayed onset and a retarded decay in comparison to Fe^{2+} PL resonantly excited at 3.24 µm; see blue and black curves in Fig. 3(b). The measured rise time of 60 ns reflects the fastest excitation transfer steps, while the retarded decay is due to a more delayed Fe^{2+} excitation by slower transfer processes up to ~3 µs. The experimental results are analyzed by a model based on the Förster mechanism of radiationless resonant energy transfer. The 60-ns rise time of energy transfer corresponds to a Cr^{2+}-Fe^{2+} distance of 0.95 nm. This value is close to the length of the space diagonal of the ZnSe unit cell. This result demonstrates a significant density of spatially correlated Cr^{2+}-Fe^{2+} ion pairs at short distance, in parallel to ions with a random distribution at a larger mutual separation. Thus, the overall kinetics of Fe^{2+} PL generated by excitation transfer represent the sum of many individual transfer events in a broad range of transfer times. Our results demonstrate that transfer models employing a single average Cr^{2+}-Fe^{2+} distance, e.g., derived from the doping concentration or ion density, fail to account for the complex transfer kinetics in the ion ensemble. In the present samples, the overall transfer efficiency is limited to 3.6 %. Higher doping concentrations and/or doping methods providing a high fraction Cr^{2+}-Fe^{2+} pairs within individual ZnSe unit cells should result in a higher transfer yield and, thus, facili-

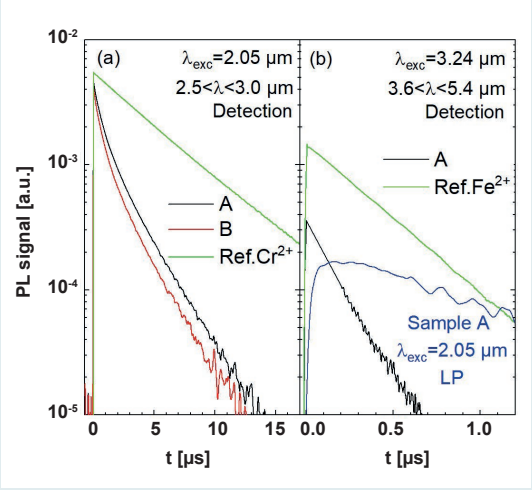

Fig. 3:
PL transients of two co-doped ZnSe:Cr^{2+},Fe^{2+} (A,B) and two singly doped reference samples (Ref.) recorded after (a) excitation of Cr^{2+}-ions with a 2.05-µm laser and detection in the 2.5<λ<3.0 µm channel sensitive to Cr^{2+}-emission. (b) Transients of Fe^{2+} PL after excitation with a 3.24-µm laser and detection in the 3.6<λ<5.4 µm channel. The blue transient was recorded after excitation at λ=2.05 µm.

tate the application of excitation transfer in solid-state lasers for the mid-infrared.

As part of our work on optoelectronic devices, we have analyzed both the thermal behavior of diode lasers [SKT21] and their degradation characteristics [HDJ21]. The latter work was a continuation of earlier work on catastrophic optical damage in GaN-based diode lasers, which was completed with a review article [HDJ21]. Work on gradual degradation of GaN-based LEDs revealed for the first time the contribution of defect-induced carrier lifetime reduction in quantum wells of LEDs, to the overall balance of degradation [TRG21]. In addition, we have demonstrated electrically pumped stimulated emission at 1.54 µm from Er/O-doped planar silicon LEDs. These were fabricated using a novel annealing technology and achieved record-high efficiencies [HWH21].

T4: Magnetism and transient electronic structure

In recent years, research in femto-magnetism has started to focus on more complex, multi-component magnetic systems, where functionality emerges through the interaction of elements with distinct properties. Prominent examples include all-optical switching in rare-earth/transition metal alloys or multilayers, i.e., the deterministic reversal of the magnetization direction upon short-pulse excitation. For the exploration and further development of such new material properties that arise via a non-equilibrium, transient state of matter, a thorough understanding of the microscopic processes is essential. To this end, we have continued to apply and to develop magnetic circular dichroism (MCD) in the extreme ultraviolet (XUV) spectral range as well as all-optical Kerr and Faraday microscopy to probe transient magnetization on an ultrafast time scale. Our experiments are guided by state-of-the-art time-dependent density functional theory.

All-optical switching

Observation of all-optical switching (AOS) relies on Faraday or Kerr microscopy, yielding magneto-optical images of the different magnetization direction. In Fig. 4(a), we show a sketch of our experimental realization that allows measurements of spatially and temporally resolved magnetization dynamics in reflection (Kerr) or transmission (Faraday) geometry. However, access to absolute Faraday or Kerr angles, θ, of the sample, i.e. extracting *quantitative* information of the evolving magnetization, generally requires performing analyzer scans at each time delay, leading to long measurement times and demanding requirements for data processing. This is easily appreciated by inspection of Fig. 4(b), where we show the non-linear dependence of the Faraday angle, θ, as a function of the detected intensity for different analyzer angles α. As the magnetization changes upon laser excitation, the measured Faraday angles follow a $\pm\sqrt{I}$ behavior, such that only for an appropriately chosen value of α, a unique transfer function, $\theta(I)$, can be defined (red line in Fig. 4(b)). Once the transfer function for the sample is found, the 2D magneto-optical images can be easily calibrated across the entire field of view to reflect absolute magnetization changes, as shown in Fig. 4(c) for 1 ps and 1700 ps after optical excitation.

As the pump laser pulse exhibits a known spatial intensity profile, we can now use a single time series of spatially resolved magneto-optical images with a total measurement time of only 3 minutes to extract a fluence-delay map as shown in Fig. 4(d) for a GdFe sample. Only in a narrow fluence range between 4.2 mJ/cm² and 4.6 mJ/cm² GdFe exhibits AOS. [SSK21, SSN21].

The success of AOS for future data devices ultimately depends on the maximum repetition rates of optically induced write/erase cycles. Hence, in a second step we investigated two strategies to minimize the temporal separation of two consecutive femtosecond laser pulses to toggle the out-of-plane direction of the magnetization of ferrimagnetic rare-earth transition metal alloys. First, by systematically changing the heat transfer rates using either amorphous glass, crystalline silicon or polycrystalline diamond substrates, we showed that efficient cooling rates of the magnetic system present a prerequisite to accelerate the sequence of double pulse toggle switching. Secondly, we demonstrate that replacing the transition metal iron by cobalt leads to a significantly faster recovery of the magnetization after optical excitation. The comparison of the ultrafast magnetization dynamics of a GdFe and GdCo alloy after single pulse excitation is shown in Fig. 5(a). While the initial demagnetization is very similar, the relaxation rate to a reversed magnetic state is vastly different. While GdCo reverses its magnetization to -0.6 within 5 ps, in GdFe the same value is reached only after approximately 200 ps. We rationalize this observation by the stronger Co-Co vs. Fe-Fe exchange interaction leading to a faster magnetic ordering of the transition metal sublattice. In Fig. 5(b) and (c), we show the final state magneto-optical images after

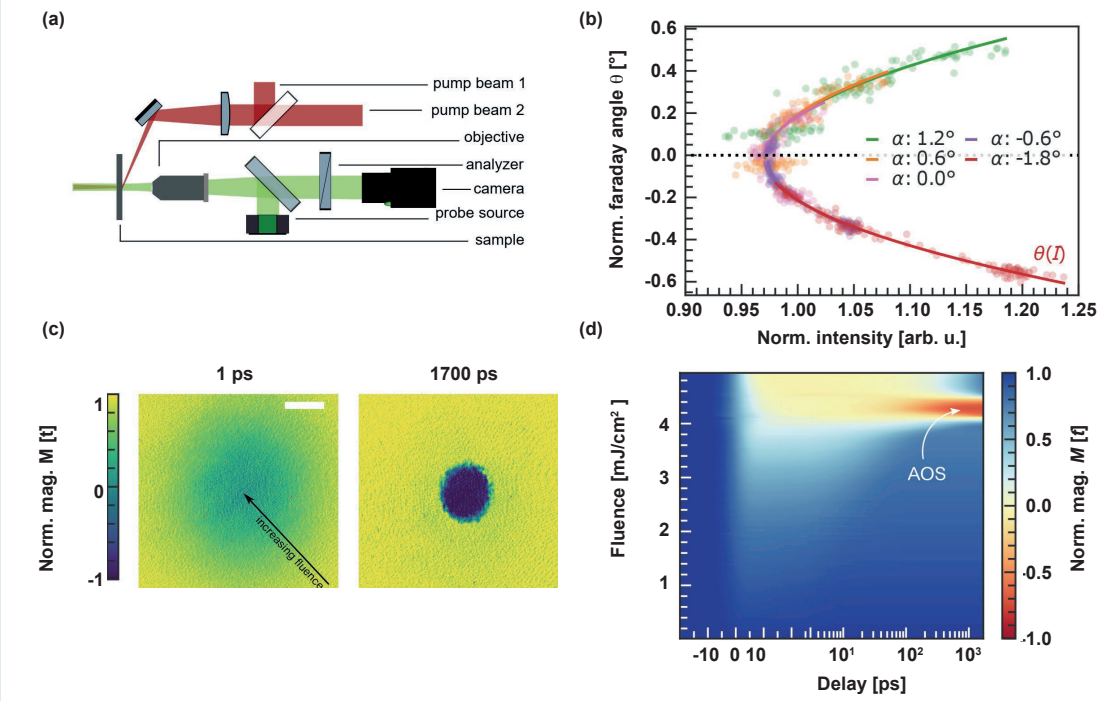

Fig. 4:
(a) Schematic depiction of the Faraday/Kerr microscope to investigate all-optical switching dynamics. (b) Faraday angle as a function of detected intensity on the camera for different times after optical excitation, i.e. as the sample reverses its magnetization. We show measurements for different analyzer angles, α. One observes a non-linear functional dependence, such that only for larger values of α, a meaningful transfer function θ(I) can be defined. (c) Spatially revolved magnetization dynamics 1 ps and 1700 ps after laser excitation. Scale bar corresponds to 15 µm. Yellow and blue correspond to two opposite, out-of-plane magnetization directions. (d) Fluence-delay map of AOS extracted from the spatially revolved images. Adpapted after [SSK21].

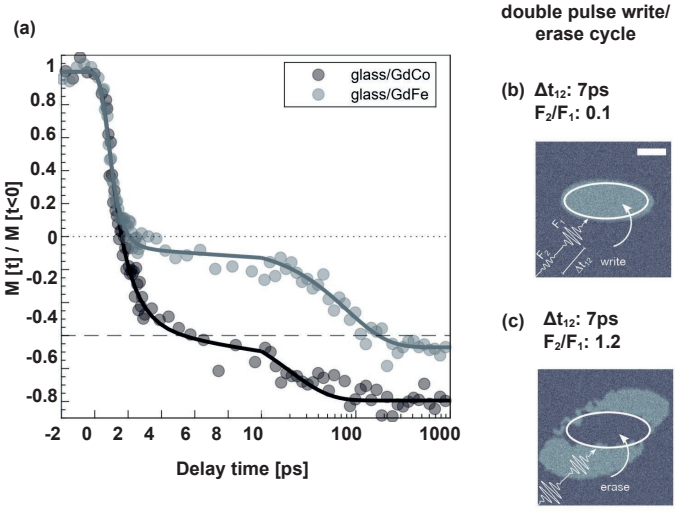

Fig. 5:
(a) Ultrafast switching dynamics of a GdFe and GdCo alloy. The relaxation to a reversed magnetic state is greatly accelerated in GdCo, where after 5 ps the magnetization has already recovered to M(5ps)/M(t<0) ~ - 0.6. To reach the same value takes ~ 200 ps in GdFe. (b) and (c) Final state magneto-optical images after double-pulse excitation with a pulse-to-pulse separation of Δt_{12} = 7ps. For low fluences of the second pulse the magnetic state written by the first pulse remains unaltered, for higher fluence of the second pulse the magnetic bit is erased. This presents the fastest write/erase cycle for magnetic information reported in literature. The scale bar corresponds to 10 µm. Adapted after [SSE].

double pulse excitation for a pulse-to-pulse separation of Δt_{12}=7ps: in (a) the fluence of the second pulse, F_2, is insufficient to influence the magnetization set by the first pulse. In (b) F_2 is increased and the magnetization is successfully switched back to its initial state. To the best of our knowledge, this presents the fastest magnetization reversal to date, approaching terahertz repetition rates for write/erase cycles of magnetic bits [SSE].

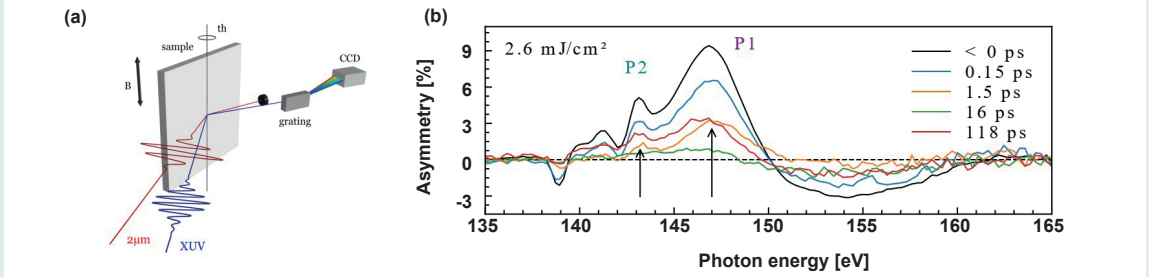

Fig. 6:
(a) Schematic illustration of the θ–2θ spectroscopy setup used for the angle- and time-resolved experiments. The reflected soft x-ray pulses around 150 eV are detected by a spectrometer placed at 2θ consisting of a variable line spacing (VLS) grating which horizontally disperses and focuses the soft x-ray spectrum on a CCD camera. (b) Magnetic asymmetry for different time delays after optical excitation. One observes a time dependent spectral reshaping, which can be related to an ultrafast evolution of a depth-dependent magnetization profile within the magnetic nanostructure.

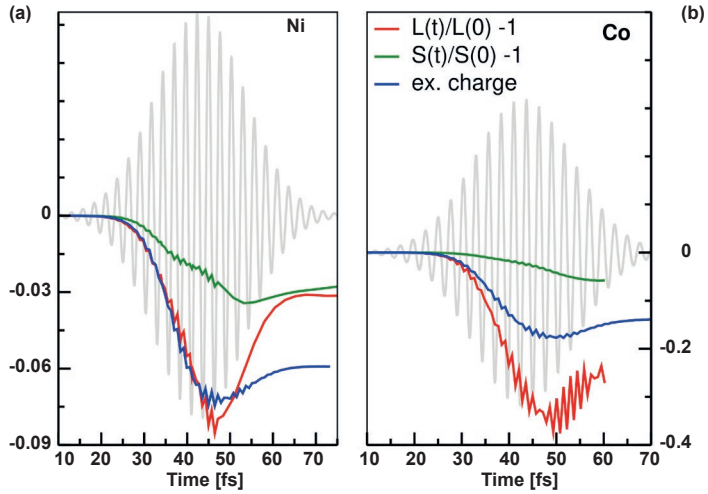

Fig. 7:
Dynamics of L and S for a laser pulse with a full width half maximum (FWHM) of 25 fs, a central frequency of 1.55 eV and an incident fluence of 3.55 mJ/cm². Shown are the normalized orbital angular momentum, $L_z(t)/L_z(0)$-1, and spin angular momentum (instead of moment), $S_z(t)/S_z(0)$-1 for (a) Ni and (b) Co. We also show the negative value of the excited charge and the A-field of the pump pulse. The excited charge is calculated by integrating the transient occupied state density above the ground-state Fermi energy.

Soft X-ray spectroscopy

Functionality of complex, multi-component magnetic alloys or multilayers rely on the interplay of its constituent elements, making element-specific experimental probes key to understand the underlying microscopic processes. This is particularly important to understand the microscopic origin of AOS. However, time resolved access to the magnetic properties of rare-earth elements in table top, laser driven high harmonic setups has not been demonstrated before. In collaboration with project 4.1 in the *Application Laboratory NanoMovie* (see project 4.2), we were able to successfully record high resolution spectra of the magnetic asymmetry around the Gd $N_{4,5}$ edge around 150 eV in a θ-2θ spectroscopy setup (Fig. 6(a)) [HSS]. In addition to element-specific information, the strong variation of the absorption coefficient around the gadolinium resonance allows to correlate depth-dependent transient magnetization profiles to ultrafast spectral reshaping. In Fig. 6(b) we show the asymmetry spectra for different time delays of a 10 nm thick GdFe sample. Careful inspection of the data reveals a transient reshaping of the spectra: the two main peaks, P1 and P2, first shift to higher photon energies within approximately 1.5 ps before they shift back to smaller photon energies on much longer time scales. Together with detailed calculations, this allows for the first time to experimentally determine the ultrafast evolution of depth-dependent magnetization gradients on a nanometer length scale. This is highly relevant for investigations of transport processes in magnetic nanostructures, as well as processes driven by interface effects, like the spin Hall or spin Seebeck Effect.

Spin and Orbital Spin Angular Momentum

We address the femtosecond dynamics of orbital (L) and spin (S) angular momentum, and in particular, the long-standing fundamental question of the flow of S into L and into the lattice at ultrashort time scales via ab-initio calculations. We find that in elemental magnets the dynamics of L is dominated by optical excitations, while that of S by spin-orbit induced spin flips, endowing these momenta with distinct time scales. By employing ultrashort pulses and by enhancing spin-orbit coupling, which can be achieved in magnetic thin films, we show

that these time scales can be separated, and thus temporal disentanglement of the dynamics of L and S can be experimentally observed. Our results demonstrate conclusively (see Fig. 7) that the predominant mechanism by which spin angular momentum transfers to the lattice is through orbital angular momentum of the electronic system: after an initial decrease of L due to the excitation of the electron system L increases. In complex alloys, the dynamics of S and L will include possible optical inter-site spin transfer (OISTR) physics of rearrangement of local spin and orbital moments due to inter-site charge transfer. Our findings of transfer of S to the lattice via L, i.e. transfer of momentum involving only the electron system, suggest that this will also be the case in these materials for very early times [DSE21].

T5: Joint HU-MBI Group on Theoretical Optics

In 2021, research in T5 has been concerned with the implementation and testing of the Landau-Lifshitz-Gilbert equations for modeling micro-magnetic systems, and the continued development of optimization techniques for the design of complex nanophotonic structures.

Specifically, with regards to the development of optimization techniques and their applications, we have utilized our Bayesian framework in order to design a dielectric metasurface for enhanced Faraday rotation consisting of shape-optimized scatterers. Our design features a figure-of-merit (FOM) which is roughly double than the previous record design by the Khanikaev-group from 2018 (Optics Letters **43** (2018) 1838.

Our basic design comprises a (thin) metasurface that consists of a quadratic lattice decorated with a unit cell in which a disk-like scatterer with adjustable shape is

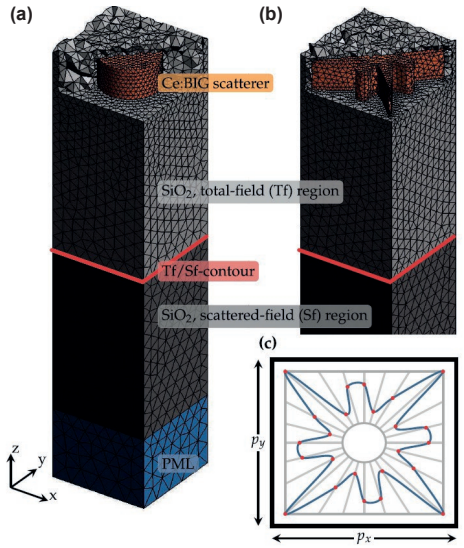

Fig. 8:
Shape design using adjustable surfaces; Panel (a): Lower part of the final mesh for a cylindrical disk-scatterer with adjustable radius (final radius R = 250 nm), the total structure is mirror-symmetric respect to a horizontal plane through the middle of the disk; Panel (b): Final mesh for the best scatterer shape found by the Bayesian optimization algorithm by adjusting the surface control point in panel (c), the total structure is mirror symmetric with respect to a horizontal plane through the middle of the star-shap disk; Panel (c): Two-dimensional scatterer cross-section within the unit-cell (periods px and py) created via spline-interpolation through control points (red), gray lines mark the allowed control-point positions. Adapted from [KVB21].

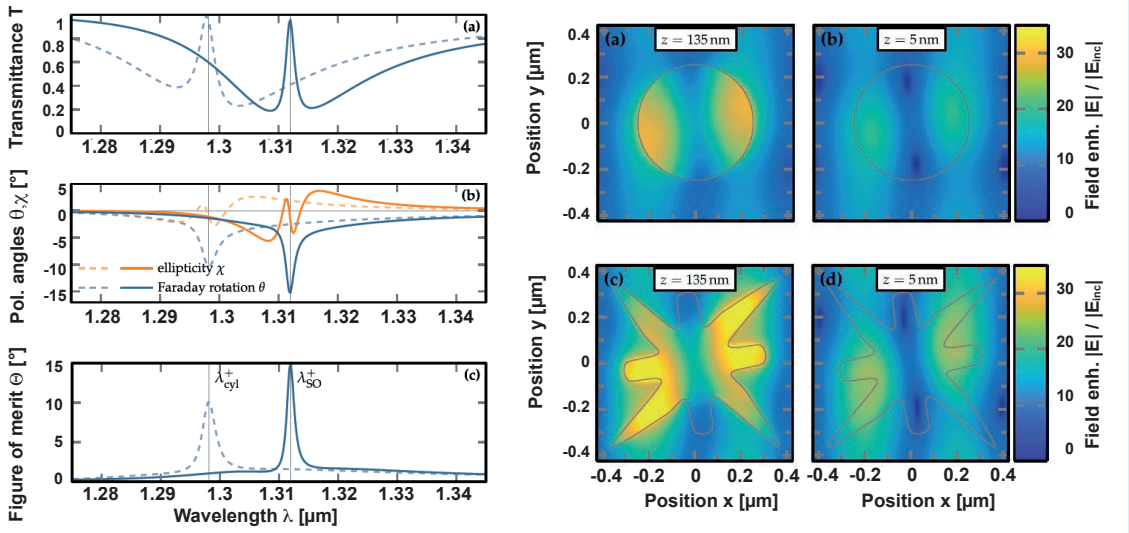

Fig. 9:
Left panel: Spectra for optimized cylindrical (dashed) and shape-modified (disks (sold), sub-panel (a) displays the transmittance, sub-panel (b) depicts the (Faraday-) rotation angle and resulting ellipticity, and sub-panel (c) shows the resulting FOM; Right panel: Electric field enhancement (normalized to the incoming field strength) on top (sub-panels (a) and (c)) and in the center (sub-panels (b) and (d)) of the cylindrical (sub-panels (a) and (b)) and shape-modifed (sub-panels (c) and (d)) disk systems at the corresponding resonance wavelengths (shown in the left panel). Adapted from [KVB21].

placed. In order to have a pure Faraday rotation (as opposed to asymmetric transmittance), it is mandatory that the metasurface be mirror-symmetric with regards to a plane through the middle of the disk. The scatterer itself is made of a magneto-optic material such as cerium-doped bismuth iron garnet and is packed into a silica matrix and a static magnetic field is applied perpendicular to the metasurface.

Using periodic boundary conditions on the unit cell, we compute via our in-house Discontinuous Galerkin Time-Domain (DGTD) finite-element-based Maxwell solver the transmittance and reflectance from the metasurface as well as the angle by which the incoming linearly polarized radiation is rotated in transmittance. This degree of rotation multiplied by the square root of the transmittance generally defines the FOM associated with a given structure. The shape of the scatterer within the unit cell can be modified in a number of ways. One simple way is to let the scatterer have the shape of a cylindrical disk with adjustable radius *R*. A considerably more advanced shape-design proceeds by allowing a number of control points to slide in- or outward in radial direction. These points are then connected with periodic centripetal Catmull-Rom spline – this type of spline is required in order to avoid self-intersection effects in the surface generation (see Fig. 8).

From a careful inspection of the field structures at resonance (see Fig. 9), we conclude that although the cylindrical disk provides a generic shape within which the magnetic and electric dipole resonance can be engineered to occur at (almost) the same frequency (thus satisfying the Kerker condition for near unity transmittance) to form a rotated field, the star-like shape of the optimized scatterers better supports the resulting field distribution.

Apparently, the optimization ensures that the best structure delicately balances the combination of three main factors for the enhanced Faraday rotation, namely, the enhancement and spectral overlap of the electric and magnetic dipole resonances, as well as an efficient coupling to the incident field. Specifically, the resulting shape-modified disks ensure a high metasurface transmittance combined with a large Faraday rotation angle, due to the strong confinement of the electromagnetic field in the scattering layer. The 260 nm thick optimized metasurface provides a 15° polarization rotation in conjunction with near-unity transmittance.

These results highlight the utility of employing our Bayesion shape optimization algorithm for designing optimized nanophotonic structures in general, and metasurfaces in particular.

Own Publications 2021 ff

(for full titles and list of authors see appendix 1)

AHR21: R. M. Abrudan *et al.*; Phys. Status Solidi-R online (2021) 1-15

ASU21: L. Alber *et al.*; Comput. Phys. Commun. **265** (2021) 107990/1-7

CHJ21: V. Chardonne *et al.*; Struct. Dyn. **8** (2021) 034305/1-10

DSE21: J.K. Dewhurst *et al.*; Phys. Rev. B **104** (2021) 054438/1-5

GFR21: A. Ghalgaoui *et al.*; Phys. Rev. Lett. **126** (2021) 097401/1-5

GKG21: E. Golias *et al.*; Phys. Rev. Lett. **126** (2021) 107202/1-6

HDJ21: M. Hempel *et al.*; Phys. Status Solidi-R **2100527** (2021) 2100527/1-12

HWH21: J. Hong *et al.*; Photonics Res. **9** (2021) 714-721

KZK21: T. Kang *et al.*; Phys. Rev. B **104** (2021) L140302/1-6

KKK21: M. Kliem *et al.*; Advanced Photonics Research **2** (2021)

LED21: Q. Z. Li *et al.*; Phys. Rev. B **103** (2021) L081102/1-6

LMJ21: X. Liu *et al.*; Opt. Express **29** (2021) 32388-32403

LOP21: J. Lloyd-Hughes *et al.*; J. Phys.-Condens. Mat. online (2021) 1-15

PSY21: S. Pal *et al.*; Phys. Rev. X **11** (2021) 021023/1-13

RWE21: K. Reimann *et al.*; J. Chem. Phys. **154** (2021) 120901/1-14

RZB21: M. Rothammer *et al.*; Adv. Opt. Mater. **9** (2021) 2100787/1-18

RKB21: M. Runge *et al.*; Optica **8** (2021) 1638-1641

SSM21: P. Scheid *et al.*; Nano Lett. online (2021) 1-5

Sch21: D. Schick; Comput. Phys. Commun. **266** (2021)

SSN21: D. Schick *et al.*; Meas. Sci. Technol. **32** (2021) 025901/1-7

SMR21: T. S. Seifert *et al.*; Adv. Mater. **33** (2021) 2007398/1-10

SPR21: T. P. H. Sidiropoulos *et al.*; Phys. Rev. X **11** (2021) 0410601-15

SBK21: E. Spreafico *et al.*; Molecules **26** (2021) 6244/1-8

SKT21: M. Szymański *et al.*; Energies **14**, 21 (2021) 7006/1-14

SSK21: F. Steinbach *et al.*; J. Appl. Phys. **130** (2021) 083905/1-9

TRG21: J. Tomm *et al.;* SPIE Proc. **11705** (2021) 117050E/1-6

WGR21: M. Woerner *et al.*; J. Chem. Phys. **154** (2021) 154203/1-9

ZJW21: D. Zahn *et al.;* Phys. Rev. Res. **3** (2021) 023032/1-14

In press

JLK: P. Juergens *et al.;* ACS Photonics

Submitted

WFE: M. Woerner *et al.;* J. Phys. Chem. B

SSE: F. Steinbach *et al.;* Appl. Phys. Lett.

HSS: M. Hennecke *et al.;* Phys. Rev. Lett.

FTG: P. Fürtjes *et al.;* Opt. Lett.

Invited Talks at International Conferences
(for full titles see appendix 2)

D. Schick; Optica, Advanced Solid State Lasers Conference - Laser Applications Conference (virtual, 2021-10)

S. Shallcross; International Psi-K Workshop, Correlated synthetic quantum matter: theory meets experiment (Bremen, Germany, 2021-02)

S. Sharma; 736. WE-Heraeus-Seminar, Magnetism at the Nanoscale: Imaging - Fabrication – Physics (Bad Honnef, Germany, virtual, 2021-01)

3.3: Transient Structures and Imaging with X-rays

M. Woerner, B. Pfau (project coordinators)
and M. Borchert, J. Braenzel, D. Engel, K. Gerlinger, I. González Vallejo, L.-M. Kern, C. Klose, A. Koç, C. von Korff Schmising, T. Noll, S. Priyadarshi, D. Schick, M. Schneider, H. Stiel, J. Tümmler, S. Wittrock

1. Overview

The aim of project is the development and application of XUV and X-ray sources for structure analysis and imaging with high spatial and temporal resolution down to atomic length scales and femtosecond timescale. The current applications focus on ultrafast optically induced structural dynamics as, e.g., strain waves, phase transitions, as well as transient charge and spin densities investigated with time-resolved X-ray scattering and absorption spectroscopy. A second focus is on imaging lateral spin textures in nanometer-scale magnetic materials in equilibrium and after excitation. The evaluation of new imaging techniques utilizing the light from coherent, highly brilliant soft-X-ray sources as well as the user operation of a laboratory-based X-ray microscope for the water window region are subjects of collaboration with partners from academia and industry.

2. Topics and collaborations

T1: Nanoscale imaging and spectroscopy with soft X-rays

The topic is centered around imaging, scattering and spectroscopy to investigate nanometer-scale structures with XUV and soft-X-ray radiation produced at synchrotron-radiation sources and free-electron lasers as well as by laser-driven laboratory sources. Part of the research in this topic is performed in the framework of the Berlin Laboratory for Innovative X-ray Technologies (BLiX) which is jointly operated by the TU Berlin and MBI (cf. Project 4.2).

Collaborations: F. Büttner (HZB, Berlin, Germany), G. S. D. Beach (MIT, USA), A. Madsen, L. Wei (European XFEL, Hamburg, Germany), J. Gräfe, G. Schütz (MPI-IS, Stuttgart, Germany), Y. Mokrousov, S. Blügel (FZ Jülich, Germany), C. M. Günther (ZELMI, TU Berlin, Germany), A. S. Johnson (ICFO, Barcelona, Spain), S. Wall (Aarhus University, Denmark), I. Mantouvalou (HZB, Berlin, Germany), T. Feigl (optiX fab GmbH, Jena, Germany), A. Erko (IAP eV. Berlin, Germany), T. Krist (NOB GmbH Berlin, Germany), K. Schadow (PREVAC GmbH Berlin, Germany), R. Kemmler (greateyes GmbH Berlin, Germany), H. Fiedorowicz (WAT, Warszawa, Poland)

T2: Femtosecond X-ray diffraction and absorption

Investigation of phase transitions and structural dynamics in solids, in close collaboration with projects 3.2 and 4.1.

3. Results in 2021

T1: Nanoscale imaging and spectroscopy with soft X-rays

Imaging mesoscopic charge and magnetization textures with soft X-rays

Real-space imaging with coherent radiation of nanometer-scale wavelength is one of the core activities in this topic. We particularly investigate mesoscopic emergent textures of magnetization and phase separation in materials characterized by correlations, utilizing the spectroscopic sensitivity endowed by core-resonant transition in the soft X-ray regime.

Regarding magnetization textures on the nanometer scale, we investigated the nucleation of isolated magnetic skyrmions in ferromagnetic multilayers mediated by an ultrashort laser pulse. Magnetic skyrmions are chiral topological spin textures with solitonic character. Due to their stability as confined, isolated textures with nanometer-scale dimensions at room temperature, the use of skyrmions has been discussed for data memory, storage, and processing applications. We have recently shown that skyrmion formation induced by a single sub-picosecond laser pulse proceeds via the formation of a high-temperature phase characterized by strong topological spin fluctuations, from which skyrmion nuclei freeze out [BPB21]. In a study focused on mapping out the parameter space for laser-induced skyrmion formation for applications [GPB21], we compare the effect in different multilayer systems with and without chiral interactions. As described in one of the highlights of this annual report, we observe the formation of stable skyrmions in both systems, with a density that can be controlled by the external magnetic field and a random spatial arrangement once a critical laser fluence is exceeded. Based on these findings, we proposed that laser-induced skyrmion nucleation may be used for the randomization of skyrmions-encoded bit patterns which is an important operation in probabilistic computing.

Focusing on the role of inhomogeneity on the nanometer-scale, we investigated the otherwise well-studied insulator-to-metal phase transition in the correlated material vanadium dioxide (VO_2) [JVV21]. Around the phase transition temperature of ≈65°C, thin vanadium-oxide films exhibit a coexistence of both phases spatially separated in mesoscopic patches. In our study carried out in collaboration with Aarhus University and ICFO, Barcelona, we use coherent diffractive imaging with multiple wavelengths of soft X-rays to image the spatial phase heterogeneity. To obtain contrast for the locally varying electronic structure connected to the different vanadium-oxide phases, the X-ray wavelengths are

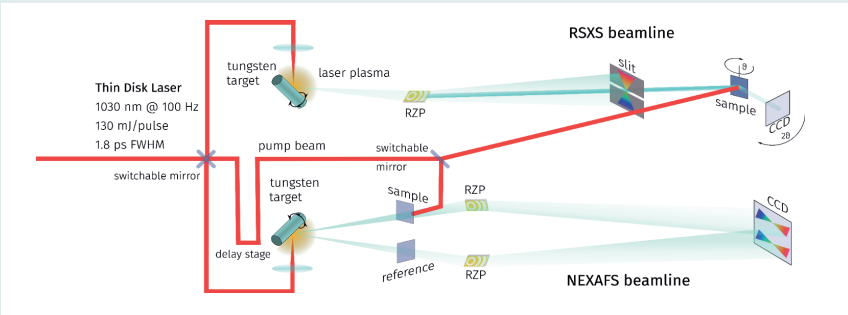

Fig. 1:
Setup of the ps-laser produced plasma source for time-resolved RSXS and NEXAFS investigations.

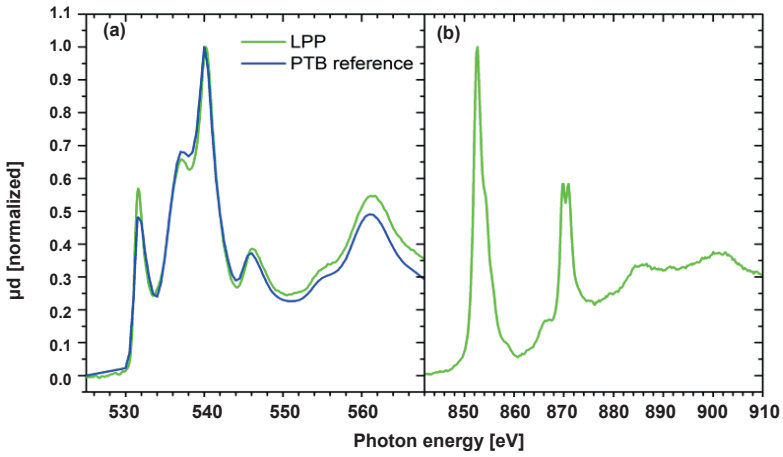

Fig. 2:
Oxygen K-edge (a) and Ni L-edge (b) NEXAFS spectra of a thin NiO film on Si_3N_4 recorded with an LPP source and a reflection zone plate spectrometer. For details cp. [SBJ21].

tuned through the electronic resonances of vanadium and oxygen. As a result, we are able to spatially map the presence of different vanadium oxides (VO_2 vs. V_2O_5) as well as the different phases of VO_2. In conjunction with time-resolved experiments which are currently under way, this is key information to understand how optically triggered phase transitions proceed in non-ideal solids containing heterogeneities.

Laser-driven resonant soft-x-ray scattering (RSXS) and near-edge X-ray absorption fine structure spectroscopy (NEXAFS)

In 2021, we commissioned a laser produced plasma source (LPP) based on a CPA thin disk pump laser system (1.5 ps, 100 Hz, 130 mJ). The plasma is generated by focusing the ultrashort laser pulse on a tungsten target. The tungsten plasma emits X-rays in a broad spectral range from 50 eV up to 2 keV. The photon flux of the source amounts to 5×10^{12} ph s^{-1} sr^{-1} in 0.1 % bw at 100 eV photon energy and 10^{11} ph s^{-1} sr^{-1} in 0.1 % bw at 1500 eV [SBT21]. The X-ray pulse duration has been estimated to <10 ps [SBB21]. For pump-probe measurements a delay line is implemented allowing time-resolved investigations with a delay between pump and probe pulse up to 6 ns. Two beamlines with independent target systems were implemented for RSXS and NEXAFS investigations (Fig. 1).

The NEXAFS setup consists of two reflection zone plates as dispersive elements and a CCD camera as a detector. First investigations to characterize the setup were focused on thin NiO films, recording NEXAFS at the oxygen *K*-edge and the nickel *L*-edges. In Fig. 2, the excellent quality of LPP-based NEXAFS measurements as compared to spectra recorded with synchrotron radiation is evident [SBJ21]. First pump–probe experiments are under way.

The RSXS setup employs a RZP to collect, focus, and disperse soft X-rays from the LPP towards the experimental chamber. A slit is used to monochromatize the X-rays prior to scattering off the sample, which is mounted on a ϑ–2ϑ goniometer. An in-vacuum CCD camera detects the scattered X-rays. First pump–probe scattering experiments investigating an antiferromagnetically coupled superlattice proved the feasibility of time-resolved resonant magnetic scattering in the soft-X-ray range at the laboratory scale [SBB21]. Details on these experiments are presented in one of the highlights of this annual report.

The availability of a closed-cycle cryostat and a rotatable in-vacuum magnet allows to study the ultrafast dynamics of a wide range of antiferromagnetic systems using resonant magnetic scattering. Other experimental techniques such as X-ray circular magnetic dichroism spectroscopy and magnetic small-angle X-ray scattering are currently evaluated and promise to investigate spin dynamics also in ferro- and ferrimagnetic systems with element-selectivity and the high magnetic sensitivity of soft X-rays with a table-top setup.

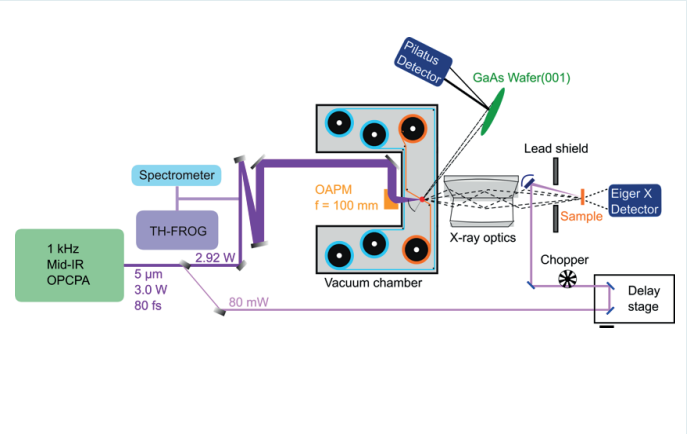

Fig. 3:
(a) Setup of the femtosecond X-ray diffractometer based on a midinfrared OPCPA driver providing 80-fs pulses at 5 µm with 3 mJ pulse energy and laser-target interaction chamber (OAPM, off-axis parabolic mirror). The Kα flux of the source and the alignment of the Montel optic (between source and sample) can be independently optimized in our femtosecond X-ray diffractometer using the (002) Bragg reflection from a GaAs wafer (green ellipse) and the Pilatus detector. The X-ray photons diffracted from the investigated sample are detected by the Eiger detector with a frame rate up to 3 KHz.

T2: Femtosecond X-ray diffraction and absorption

The analysis of the transient electron density $\rho(\mathbf{r},t)$ of solids allows for resolving atomic motion and/or relocation of electronic charge on atomic time and length scales. $\rho(\mathbf{r},t)$ is typically extracted from femtosecond X-ray diffraction measurements employing an optical-pump – X-ray-probe method, where changes of diffracted intensity $\Delta I/I$ on the order of 0.1 % have to be measured reliably. In 2021 we demonstrated such an unprecedented sensitivity in femtosecond X-ray diffraction measurements on cubic boron nitride [PGH] revealing a phonon-induced sharpening of the valence charge distribution in boron nitride. Details are discussed in one of the highlights of this annual report.

In order to measure even smaller $\Delta I/I$, and/or to conduct experiments in a faster fashion than up to now, femtosecond hard X-ray sources with a significantly higher photon flux and a detector technology with high frame rates are required. In 2021, we demonstrated a novel compact high-flux hard X-ray source which is driven by femtosecond mid-infrared pulses at a 1 kHz repetition rate [KHW21].

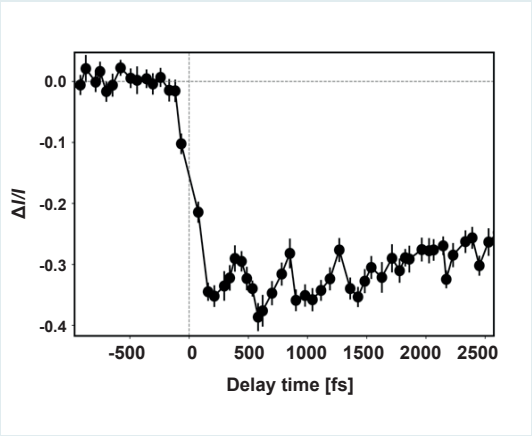

Fig. 4:
Transient intensity change $\Delta I/I$ of the (111) Bragg reflection after exciting a (111)-oriented thin bismuth film with 5-µm, 80-fs pump pulses with a fluence of 2 mJ cm^{-2}.

In parallel to the completion of the novel femtosecond X-ray source we implemented a new tool to monitor continuously the Kα flux of our new source. The experimental setup is shown in Fig. 3. Since the source emits both characteristic Kα radiation and bremsstrahlung, the emitted X-ray photons are diffracted off a single crystal-line GaAs wafer (orientation (001)), placed at a distance of 200 mm from the x-ray source. The wafer orientation is in accordance with the Bragg angle of the (002) reflection of 15.8°. An X-ray area detector (Pilatus) detects the (002) reflection from the GaAs wafer resulting in small sections of circular Debye-Scherrer rings resulting exclusively from the emitted Kα radiation. The distance of 100 mm between the GaAs wafer and the detector was selected such that both reflections of the individual Cu-Kα1 and Cu-Kα2 components (photon energies 8047 eV and 8027 eV) are well separated. Thus, the signal of this reference detector serves a direct monitor for the Kα flux of the femtosecond X-ray source. Consequently, the Kα flux of the source and the alignment of the Montel optic (between source and sample) can now be independently optimized in our femtosecond X-ray diffractometer.

Recently, we performed first femtosecond X-ray diffraction experiments with the new source. Fig. 4 shows the result of an (5 µm) pump – (X-ray) probe femtosecond diffraction experiment on a (111)-oriented thin bismuth film. Similar to earlier experiments reported in the literature and performed at shorter pump wavelengths, e.g., 800 nm, the transient intensity of the (111) Bragg reflection show a step-like decrease as a function of pump–probe delay superimposed by oscillations with a frequency of 2.6 THz. Thanks to the larger penetration depth of the femtosecond mid-infrared pump pulse the nonlinear signal has a much larger amplitude (i.e. $\Delta I/I$ = 0.4) for a distinctly smaller pump fluence (2 mJ cm^{-2}). This first time-resolved diffraction experiment gives an upper limit of the X-ray pulse duration of $\Delta t_{\text{x-ray}} < 200$ fs, in agreement with theoretical model calculations predicting a duration of 150 fs.

Moreover, besides the 30 times higher Kα flux of the X-ray source [KHW21] compared to sources with Ti:sapphire drivers, the new femtosecond X-ray diffractometer provides also mid-infrared pump pulses centered around 5 µm with a decent pulse energy (i.e., 80 µJ in

the present experiment). Such pump pulses open new opportunities for studying of photo-generated nonequilibrium states of condensed matter, among them, strong excitation of vibrational transitions in molecular crystals. This research direction will be pursued in 2022.

Own Publications 2021 ff

(for full titles and list of authors see appendix 1)

BPB21: F. Büttner *et al.*; Nat. Materials **20** (2021) 30-37

DKK21: V. Deinhart *et al.*; Beilstein J. Nanotechnol. **12** (2021) 304-318

GPB21: K. Gerlinger *et al.*; Appl. Phys. Lett. **118** (2021) 192403/1-7

JVV21: A. S. Johnson *et al.*; Sci. Adv. **7** (2021) eabf1386/1-9

JSK21: A. Jonas *et al.*; Rev. Sci. Instrum. **92** (2021) 023102/1-8

JWK21: A. Jonas *et al.*; SPIE Proc. **11886** (2021) 11886 11/1-8

KHW21: A. Koç *et al.*; Opt. Lett. **46** (2021) 210-213

PBü21: B. Pfau *et al.*; Physik in unserer Zeit **52** (2021) 6-7

SBB21: D. Schick *et al.*; Optica **8** (2021) 1237-1242

SBJ21: H. Stiel *et al.*; Int. J. Mol. Sci. **22** (2021) 13463/1-18

SBT21: H. Stiel *et al.*; SPIE Proc. **11886** (2021) 11886 12/1-9

SKB21: S. Staeck *et al.*; J. Instrum. **16** (2021) P03033/1-17

In press (as of Jan. 2022)

HWE: C. Hauf, M. Woerner, and T. Elsaesser; Femtosecond diffraction with laser-driven hard X-ray sources: Nuclear motions and transient charge densities; in *Structural Dynamics with X-ray and Electron Scattering*, K. Amini, A. Rouzée, and M. J. J. Vrakking, (eds.) (AIP)

Submitted

GKR: I. González Vallejo *et al.*; Underdamped longitudinal soft modes in ionic crystallites - lattice and charge motions observed by ultrafast x-ray diffraction; Struct. Dyn.

KBHa: C. Klose *et al.*; Photon correlation spectroscopy with heterodyne mixing based on soft-x-ray magnetic circular dichroism; Phys. Rev. B

KBHb: C. Klose *et al.*; Coherent Correlation Imaging: Resolving fluctuating states of matter; Nature

PGH: S. Priyadarshi *et al.*; Phonon-induced relocation of valence charge in boron nitride observed by ultrafast x-ray diffraction; Phys. Rev. Lett.

Invited Talks at International Conferences

(for full titles see appendix 2)

S. Eisebitt; EMA (The European Magnetism Association) - Plenary e-lecture (virtual, 2021-09)

S. Eisebitt; ALBA II - Workshop on Coherence and Time-resolved X-ray Science, Madrid, Spain (virtual, 2021-05)

S. Eisebitt; Photoinduced Phase Transitions and Cooperative Phenomena (PIPT7), Santa Fe, USA (virtual, 2021-11)

S. Eisebitt; sIMMposium, Institute for Molecules and Materials (IMM), Nijmegen, NL (hybrid, 2021-11)

S. Eisebitt; The 9th Int. Symposium on Surface Science (ISSS-9), Takamatsu, Japan, (virtual, 2021-11)

T. Elsaesser; CECAM: Second Discussion Meeting on Quantum Crystallography: Expectations & Reality (virtual, 2021-09)

C. Klose; INTERMAG 2021 (Lyon, France, 2021-04)

D. Schick; Optica, Advanced Solid State Lasers Conference - Laser Applications Conference (virtual, 2021-10)

M. Schneider; XFEL Users' Meeting, Hamburg, Germany (virtual 2021-01)

M. Schneider; XFEL workshop, Scientific Opportunities for the Spanish Community at XFELs, Hamburg, Germany (virtual, 2021-06)

M. Woerner; Discussion Workshop on Structural and Nuclear Dynamics (Universität Duisburg-Essen, Germany 2021-11)

4.1: Implementation of Lasers and Measuring Techniques

I. Will, F. Furch, U. Griebner (project coordinators)
and U. Bengs, F. Furch, L. von Grafenstein, C. Kleine, G. Klemz, M. Kretschmar, L. Lochner, T. Noll, M. Osolodkov, J. Tümmler, T. Nagy, T. Witting

1. Overview

The general goal of this project is the development of laser-based sources and optical measurement systems tailored to applications specific to the MBI or laboratories of collaboration partners.

Four unique OPCPA systems developed in the framework of this project during the past few years are currently being used in particular applications. One goal of this project is to further engineer these systems and optimize their characteristics to the needs of the particular applications in Program Areas 2 and 3.

2. Topics and collaborations

The project is organized in the following topics:

T1: Lasers for particle accelerators

This topic contributes to the development of Free Electron Lasers (FELs) and other advanced accelerator-based x-ray sources by providing highly specialized photo injector drive lasers and laser systems for application experiments. This work is carried out in cooperation with the Helmholtz-Zentrum Berlin für Materialien und Energie (HZB), the Helmholtz-Zentrum Dresden-Rossendorf (HZDR) and DESY.

T2: OPCPA engineering

Several OPCPA systems in the near- and mid-infrared have been developed in the last few years. The implementation of these OPCPA sources into particular experiments in Program Areas 2 and 3 require robust, reliable and reproducible day-to-day operation of these systems. Therefore, the constant improvement and engineering of these OPCPAs is the focus of this topic. The topic is divided in three subtopics:

Terawatt OPCPA

A high-energy OPCPA system that is pumped by a high-power thin-disk laser was developed and installed in the previous years. The system runs at a repetition rate of 100 Hz and is capable of delivering pulses with a peak power >4 TW, having a pulse energy of 40 mJ with < 9 fs duration. It is applied for the generation of high energy XUV beams through high-order harmonic generation.
Since 2019 the work on this OPCPA system is more and more reduced to maintenance and smaller upgrades. During 2021, 90 % of the laser beam time was allocated for experiments.

Near-IR high repetition rate OPCPAs

The development of high repetition-rate non-collinear OPCPA systems (repetition rate ≥100 kHz) is the goal of this topic. Two OPCPAs have been established. A 100 kHz OPCPA that delivers carrier-envelope phase stable sub-7 fs pulses with up to 190 µJ of energy and a 400 kHz OPCPA that delivers sub-8 fs pulses with up to 10 µJ of energy. The systems are intended for experiments in attosecond pump-probe spectroscopy with coincidence detection (project 2.1) and novel material processing applications (project 3.2).

Midwave-IR OPCPA driver for x-ray generation

This midwave-IR OPCPA system operates at 1 kHz repetition rate and delivers 80 fs pulses with up to 3.2 mJ of energy at a central idler wavelength of 5.0 µm. The system is pumped at 2.0 µm by a Ho:YLF CPA developed in-house. The application for this OPCPA is to serve as the driver laser for a Cu-K_α source utilized for time-resolved x-ray diffraction experiments (project 3.3).

T3: Implementation of experimental and measuring techniques

The topic is concerned with the improvement of particular technologies, experimental methods and measuring techniques and their implementation within the institute for the benefit of Program Areas 2 and 3.

3. Results in 2021

T1: Lasers for particle accelerators

This topic deals with the development and systematic improvement of photocathode lasers for linear accelerators (Linacs) of FELs, as well as with other lasers used at particle accelerators and storage rings.

In 2021, our work was focused on an extension of the MBI laser at the MAXYMUS scanning transmission x-ray microscope (STXM) at BESSY II, where the laser pulses are transported into the STXM to allow for pump-probe experiments in conjunction with raster-scan imaging. The initial version of this laser (see MBI annual report 2019) was built to generate pulses with 50 MHz repetition rate and with duration comparable to the length of the BESSY bunches and has been routinely used for experiments in this configuration. Novel experiments require shorter pulses (< 1 ps) with one order of magnitude higher energy than the initial setup. An additional margin in pulses energy is desired to speed up the alignment of the focussing system, in

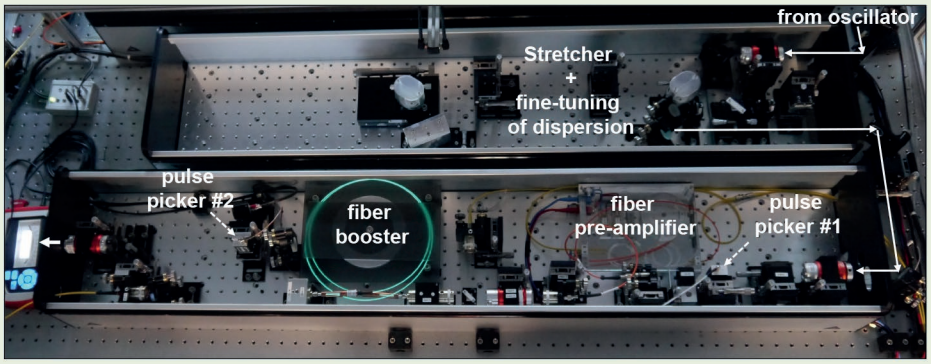

Fig. 1:
Pulse stretcher and two-stage amplifier producing pulses of several µJ for the laser at the MAXYMUS microscope.

order to compensate for reduced intensity due to the initially imperfect focussing of the laser beam.

To fit the increased demands on pulse energy, we have set up a new two-stage fiber amplifier that utilizes a photonic-crystal fiber of 40 µm core diameter in its second stage. The amplifier can deliver pulses of several µJ energy (Fig. 1).

Compression of the stretched pulses with increased energy to the sample is accomplished by an advanced pulse compressor. This compressor was built into the vacuum chamber as a compact optical unit that comprises also the focusing system (Fig. 2). A Chirped Volume Bragg Grating (VBG) is used as the compressing element. The total size of the main corpus of the "Mini Compressor" amounts to 13 x 23 x 49 mm, allowing it to fit into the very constrained space in the STXM vacuum chamber close to the sample.

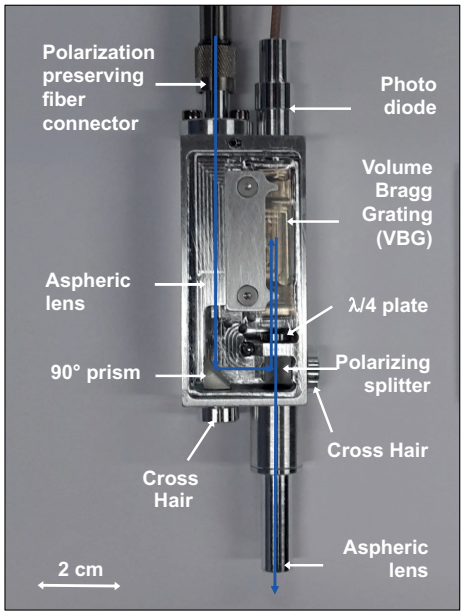

Fig. 2:
Miniature pulse compressor (cover removed) with focussing optics for the laser at the MAXYMUS magnetic microscope.

The pulses from the laser are delivered to the vacuum chamber by means of an 8 m long fiber. At present, the pulse energy at the sample is limited by nonlinear effects in this fiber. In order to operate with higher energy, in particular self-phase modulation in this fiber needs to be reduced significantly. Thus we are currently evaluating various hollow-core fibers to deliver pulses of up to 1 µJ to the vacuum chamber with minimum self-phase modulation.

The first experiments with the updated laser at the MAXYMUS microscope are scheduled in spring 2022.

T2: OPCPA engineering

Terawatt OPCPA system

As in the last year, the major goal of this topic is the operation and optimization of the Terawatt OPCPA system in order to supply few-fs TW-level driver pulses for high-order harmonic generation (HHG). The HHG source is capable of delivering XUV pulses centered at 25 eV with an energy >500 nJ (after generation) for the application in Project 2.1, topics T3 and T4:

- XUV-pump XUV-probe experiments investigating XUV-driven intensity autocorrelations to further understand the underlying multiphoton multi-electron dynamics
- time-resolved coherent diffractive imaging studies

In 2021, most of the beam time was used for the characterization of beamline properties, the preparation of experiments and, of course, for the above mentioned applications. In total the OPCPA system was applied for these tasks for more than 90 % of the working time.

The remaining time was used for improving the OPCPA system and its performance. This work was focused on the following topics:

- Installation of a chirp scan to optimize the pulse duration in the vacuum beam path.
- Further optimization of the beam pointing stabilization to ensure a better stability of the beam at the final position of the experiments.
- Maintenance

The mentioned chirp-scan measurement system was installed to allow for optimization of the pulse duration (Fig. 3). This system contains an ultra-thin BBO crystal of 5 µm thickness as the nonlinear element. A mirror on a motorized stage can be moved into the beam path and reflects the pulses towards this BBO crystal.

For optimization of the pulses, the spectrum of the emitted second harmonic in dependence on the chirp applied by the DAZZLER is measured and the parameters retrieved from its reconstruction routine are used to optimize the pulse duration.

The main advantage of this method compared to FROG is the very compact setup that can easily be installed in the vacuum chamber. Consequently, pulse optimization can be carried out without breaking the vacuum in the beam path, and perturbation of the pulse shape by air is avoided. Fig. 4 shows the measurement with the reconstructed pulse duration. A pulse duration of 8.6 fs was measured after optimization.

Near-IR high repetition rate OPCPAs

Two high repetition rate OPCPAs have been developed within this topic and in the last few years utilized for different applications related to projects 1.2, 2.2, 2.3 and 3.2. Both OPCPAs operate at a central wavelength of 800 nm, and are seeded by ultra-broadband Ti:Sapphire oscillators. In both systems, a small fraction of the oscillator spectrum around 1030 nm is also used to seed a chirped pulse amplification (CPA) system that provides the pump pulses for the OPCPA stages. In one OPCPA the pump pulses are provided by the second harmonic of a CPA based on a Yb:YAG thin-disk regenerative amplifier operating at 100 kHz. The second OPCPA is pumped by a fiber-CPA operating at 400 kHz.

In 2021, the 400 kHz system was commissioned for experiments in the corresponding SAW project linked to project 3.2. The system delivers sub-8 fs pulses with energy per pulse exceeding 8 µJ, and the output (spectral content, pulse duration, beam shape) has been tailored to the needs of the experiment.

The 100 kHz OPCPA continued to be commissioned for attosecond pump-probe experiments with electron-ion coincidence detection (see project 2.1). Towards the end of the year the beam quality and pulse duration were optimized in order to perform nonlinear post-compression of the OPCPA pulses in a gas-filled hollow-core fiber. Results on the pulse characterization are shown in the context of topic T3.

Midwave-IR OPCPA driver for x-ray generation

The large scale MWIR OPCPA system operating at 5-µm wavelength developed in project 1.2 was successfully implemented as driver for hard X-ray generation, its intended application in MBI's time-resolved X-ray diffraction research (see project 3.3). The system emits pulses with 1 kHz repetition rate at a central wavelength of 5 µm. The stability and reliability of the OPCPA system was continuously improved. As a consequence, the system was virtually uninterruptedly available as driver laser for the Cu-K_α source in 2021 which allows to setup the X-ray pump-probe line. The latter was tested successfully and is depicted in Fig. 5 (a).

The conceptual layout of the laser-driven hard X-ray source operating at a 1 kHz repetition rate is shown in Fig. 5 (a). Details of our four-stage midwave-IR OPCPA have been reported in [1]. The main components of the OPCPA are a three-color front-end based on fs Er:fiber sources, the ps Ho:YLF CPA at 2.05 µm as pump, and the OPA stages, all equipped with $ZnGeP_2$ crystals.

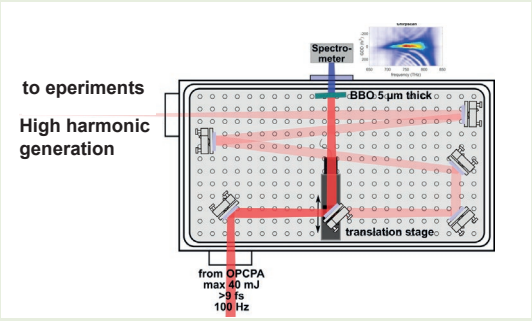

Fig. 3:
Setup of the chirp-scan device.

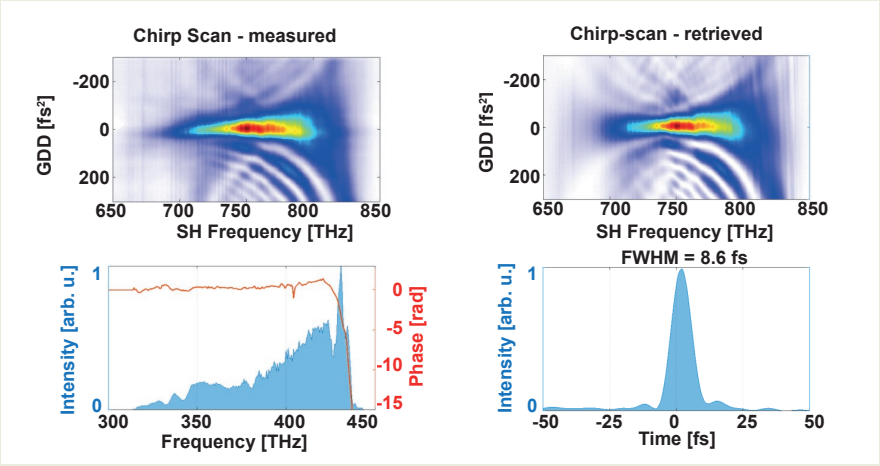

Fig. 4:
Pulse measurement after optimization utilizing a SHG chirp-scan.

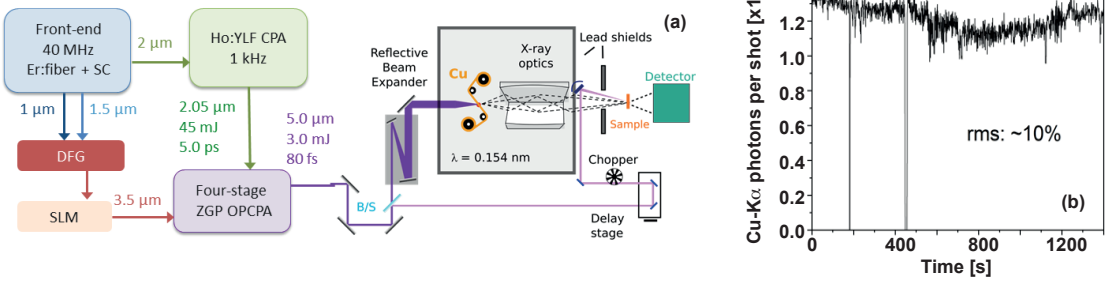

Fig. 5:
(a) Conceptual scheme of the 5-µm driver laser system and the setup for the generation and characterization of the X-ray pulses as well as the X-ray pump-probe line. (b) Long term stability measurement of the Cu-Kα flux emitted by the X-ray source.

The 2.05-µm pump delivers compressed pulses with 5 ps duration, adapted for the OPA stages, and 45 mJ energy at 1 kHz. Sub-30 fs signal pulses at 3.5 µm are generated via DFG and subsequently shaped spectrally by a spatial light modulator (SLM). For stretching of the signal and compression of the idler pulses different bulk materials are used. The output pulse energy of the idler after the four OPA stages amounts to 3.0 mJ. Its spectrum covers a wavelength range from 4.2 to 5.5 µm supporting a Fourier-transform limited pulse duration of ~60 fs. Successful re-compression is achieved in CaF_2 crystals resulting in linearly polarized pulses with a duration of 80 fs. The long-term power fluctuations are only 1.2 % and the beam quality is nearly diffraction limited with an $M^2 \leq 1.3$.

These exceptional output parameters qualify the 5-µm OPCPA as driver for ultrafast hard X-ray generation. The 5-µm beam is focused onto a 20-µm thick Cu target. An excellent agreement of the measured X-ray flux values with the theoretical prediction has to be emphasized. A maximum flux of 1.5×10^9 photons per pulse, corresponding to 1.5×10^{12} photons per second in the full solid angle, is retrieved. These numbers surpass the X-ray flux when using a Ti:sapphire laser driver at 0.8 µm by 30-times. The Fourier spectrum of the shot-to-shot Cu-Kα flux, measured for 25 minutes, is presented in Fig. 5 (b). It shows a remarkably stability with an rms-value of 10 %. For detailed results with respect to the hard X-ray generation see the project 3.3.

[1] L. von Grafenstein, M. Bock, D. Ueberschaer, A. Koç, E. Escoto, K. Zawilski, P. Schunemann, U. Griebner, and T. Elsaesser, “Multi-millijoule few-cycle 5 µm OPCPA at 1 kHz repetition rate,” Opt. Lett. **45**, 5998-6001 (2020).

T3: Implementation of experimental and measuring techniques

The temporal as well as the spatio-temporal structure of the laser pulses are crucial in most applications, including the employment of these laser pulses for driving secondary sources, e.g., attosecond pulse generation via high harmonic generation (HHG). Spatio-temporal distortions can occur frequently in non-collinear parametric amplifiers. This type of laser source is now becoming prevalent at MBI at various wavelengths. In previous years, the method known as spatially-encoded arrangement filter-based spectral phase interferometry for direct electric field reconstruction (SEA-F-SPIDER) has been adapted to work over a wide spectral region (from 800 nm to 2500 nm) and made available for the different lasers system in operation in the institute.

As an example of the role that this metrology tool plays in certain applications, in 2021 a careful analysis was performed of the spatio-spectral and spatio-temporal structure of few-cycle pulses from the 100 kHz OPCPA at 800 nm (see topic T2.2) in order to optimize the nonlinear pulse compression in a gas-filled hollow core fiber and push the pulse duration to the single-cycle limit. The OPCPA delivers sub-7 fs pulses with 190 µJ pulse energy. Fig. 6 shows the results of SEA-F-SPIDER measurements over two perpendicular spatial coordinates across the amplified beam. Fig. (a) and (b) show the retrieved spatio-spectral distributions, while Fig. 6 (c) and (d) show the corresponding spatially integrated spectra (red) and retrieved spectral phases (green). The different curves correspond to 10 different consecutive measurements taken over a time span of approximately 1 minute. The spectral phases shown were taken at the center of the corresponding spatial distributions. Fig. 6 (e) and (f) show the retrieved spatio-temporal distributions and Fig. 6 (g) and (h) show the spatially integrated pulse shapes. Once again, the result of 10 consecutive measurements are shown to illustrate the reproducibility of the measurement.

This detailed measurement of the spatio-temporal structure of the pulses allowed optimizing the OPCPA to minimize space-time couplings, which degrade the achievable peak intensity. In addition, the measured spectral phase was utilized to generate a phase mask in a 4f-pulse-shaper located before the OPA stages. In this way, the pulse compression can be optimized. Note that in the results shown in Fig. 6 the pulse compression has already been optimized achieving a pulse duration of approximately 6.5 fs.

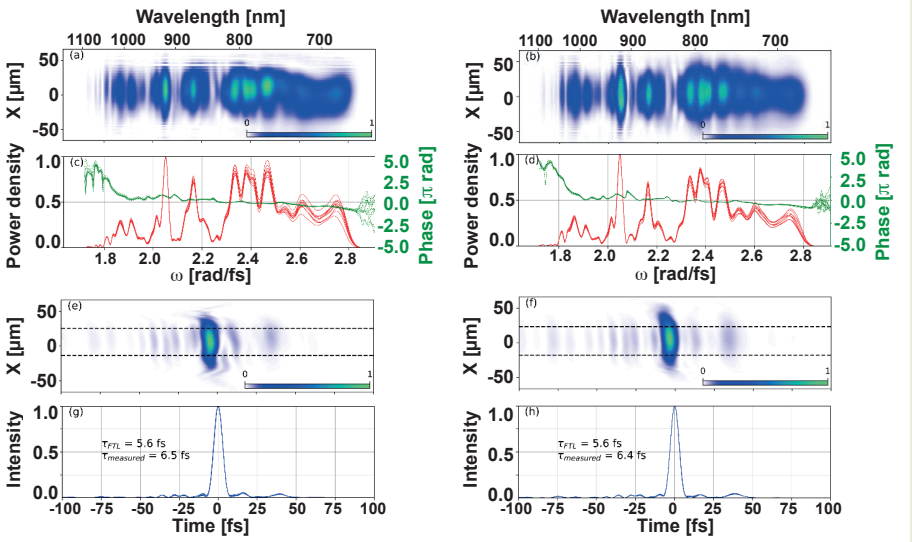

Fig. 6: *Characterization of the pulses emitted by the 100 kHz OPCPA at 800 nm. (a)-(b) Spatio-spectral distributions along two perpendicular directions across the amplified beam. (c)-(d) Integrated spectra from (a) and (b) and retrieved spectral phase. (e)-(f) Spatio-temporal reconstructions. (g)-(h) Integrated temporal pulse shape from (e) and (f).*

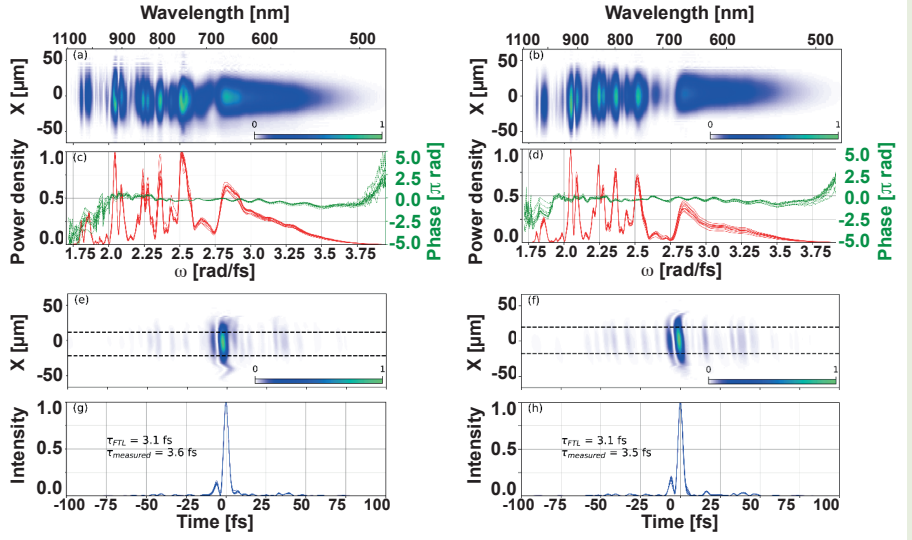

Fig. 7: *Characterization of the post-compressed pulses of the 100 kHz OPCPA at 800 nm by a HCF. (a)-(b) Spatio-spectral distributions along two perpendicular directions across the amplified beam. (c)-(d) Integrated spectra from (a) and (b) and retrieved spectral phase. (e)-(f) Spatio-temporal reconstructions. (g)-(h) Integrated temporal pulse shape from (e) and (f).*

The OPCPA pulses shown in Fig. 6 were post-compressed in a 1 m long hollow-core fiber filled with Ne gas at a pressure of 3 bars. After dispersion compensation with chirped mirrors and thin fused silica wedges, the compressed pulses were characterized once again with the SEA-F-SPIDER technique. The results are shown in Fig. 7. Note that during the experiment, a movable mirror allowed to quickly sent the OPCPA pulses or the pulse compressed pulses to the SEA-F-SPIDER device, in order to optimize the OPCPA pulses for the nonlinear compression. Fig. 7 (a) and (b) show the retrieved spatio-spectral distributions, while Fig. 7 (c) and (d) show the corresponding spatially integrated spectra (red) and retrieved spectral phases (green). Once again, the different curves correspond to 10 different consecutive measurements taken over a time span of approximately 1 minute. The spectral phases shown were taken at the center of the corresponding spatial distributions. Fig. 7 (e) and (f) show the retrieved spatio-temporal distributions and Fig. 7 (g) and (h) show the spatially integrated pulse shapes (results of 10 consecutive measurements). After the optimization of the OPCPA pulses, the post-compressed pulses had an approximate duration of 3.6 fs corresponding to 1.5 optical cycles.

Own Publications 2021

Publications which have emerged from work in this infrastructure project are listed under the relevant projects (1.2, 2.1, 2.2 and 3.2).

4.2: Application Laboratories and Technology Transfer

NanoMovie – Application Laboratory for nanoscopic spectroscopy and imaging

M. Schnürer (project coordinator)
and L. Ehrentraut, P. Friedrich, A. Heilmann, G. Kommol, M. van Mörbeck-Bock (until June 2021)

1. Overview

The NanoMovie project establishes a laboratory where soft X-rays in different photon energy ranges are used in application experiments. Of particular interest are studies of dynamic processes

- in the spectral region around 150 eV where the giant $N_{5,4}$-edge absorption resonances give access to the f-electrons in the lanthanides via magnetically dichroic transitions
- in systems with light elements (carbon, nitrogen, oxygen) which are of particular interest in biology and chemistry, where the 1 s core levels can be accessed in the so-called water window (284 eV-543 eV).
- in systems with 3d transition metals where the spin-orbit split L-edges exhibiting strong magnetic dichroism with photon energies beyond 450 eV are reached. Here, the ability to probe the d-electron system with element sensitivity is important e.g. in research of magnetic materials or of metal-organic compounds on an ultrafast timescale.

NanoMovie focuses both on applications and on establishing different soft X-ray technologies. The aim is to establish a reliable experiment and testing platform for internal and external users, including SMEs. Further aspects have been briefly highlighted in the past annual reports.

Femtosecond soft x-ray pulses are generated via High Harmonic Generation (HHG) with long-wavelength drivers. Towards this end, two high average power OPCPA systems with integration of cutting-edge commercial components are constructed. Both, the pump-lasers (500 W Thin Disk Laser (TDL) DIRA500 by *Trumpf Scientific GmbH*) and frontends (*Fastlite*) are "first of its kind" products. The infrared wavelengths of the two systems (2.1 µm and 3.1 µm) are chosen such that soft X-ray generation via HHG is enabled in spectral regions of 100 eV-600 eV and 500 eV-900 eV, respectively. The challenge, especially at higher photon energies, is the low photon flux of the HHG-sources. Therefore, IR-drivers with high flux are needed which perform at high stability, in conjunction with efficient soft x-ray optics. Towards this end, system design and further development is carried out with the support of projects 1.2 and 4.1 and optimization of the HHG process is aided by numerical simulations within project 1.1.

The 2.1 µm OPCPA system with 10 kHz pulse repetition rate is in operation. Standard parameters are 28 W to drive the HHG for the probe beam and additional 2 W for the pump beam. The pulse duration is about 26 fs. (Absolute best values are 33 W and 22 fs at OPCPA output without further pulse manipulation.) First pump-probe experiments probing magnetization dynamics in $Gd_{24}Fe_{76}$ thin film sample at the magnetically dichroic Gd $N_{4,5}$ absorption resonance in the spectral region around 150 eV were completed successfully (see Project 3.2). Systematic HHG source characterization, especially with respect to design considerations for the MOSFER spectrometer (cf. below) was carried out.

The design of the second OPCPA system operating at 3.1 µm was completed and amplification tests with different crystals delivered 5 W with the first power amplification stage as a milestone.

In 2021, a significant amount of in-house technical work was necessary to keep the performance of the pump-lasers (DIRA 500) as well as the frontends (Fastlite), mainly due to the Covid pandemic situation hindering service work from companies.

Until June 2021 NanoMovie was cofounded through the European Regional Development Fund (ERDF).

2. Results in 2021

The NanoMovie 2.1 µm and 3.1 µm systems feature a monolithic concept, deriving the seed and the pump beam for the OPCPA stages from the same pump laser. This compact approach, techniques and key parameter have been described in detail within the last annual reports, publication and conference papers (cf. references in 1.2).

Laboratory layout

Fig.1 depicts the final layout of the NanoMovie laboratory. The 2.1 µm OPCPA system is in operation and delivers pump and probe beams to the "Bunker" lab

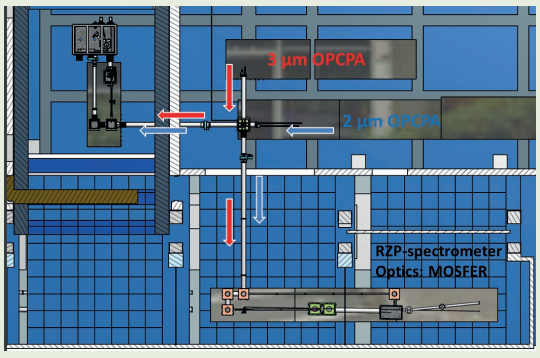

Fig. 1:
Layout of NanoMovie in the XPL

where a complete pump-probe endstation is available. The power OPA-stages of the 3.1 µm OPCPA system are currently under construction. In 2021, the laboratory rooms to set up the spectroscopy-beamline in the context of the MOSFER project were equipped with a concrete floor to enable stable operation on the optical table. A beam switching chamber located in the laser hall enables the use of both the 2.1 µm and 3.1 µm-driven HHG beam in both beamlines.

Frontend modifications with respect to CEP-stability

The super continuum generation (SCG) used in the frontend offers a passively stabilized carrier phase envelope. CEP-stabilization becomes important for the shot-to-shot stability of the soft X-ray output if pulses with only few cycles are used to drive HHG-bursts at attosecond timescale. So far, sufficient CEP-stability for such applications is achieved for the 3.1 µm frontend but not for the 2.1 µm case. Implementation of a specifically designed telescope aiming for reduction of the input beam pointing at the super continuum generation (SCG) crystal did not solve the problem. Ongoing discussions with MBI-experts (project 1.2), international partners (University Ottawa) and companies (Fastlite, TSL) show a strong interest in solving this problem. In addition to pump laser stability also other phenomena influencing CEP-stability of pulses derived from SCG are studied in an on-going effort.

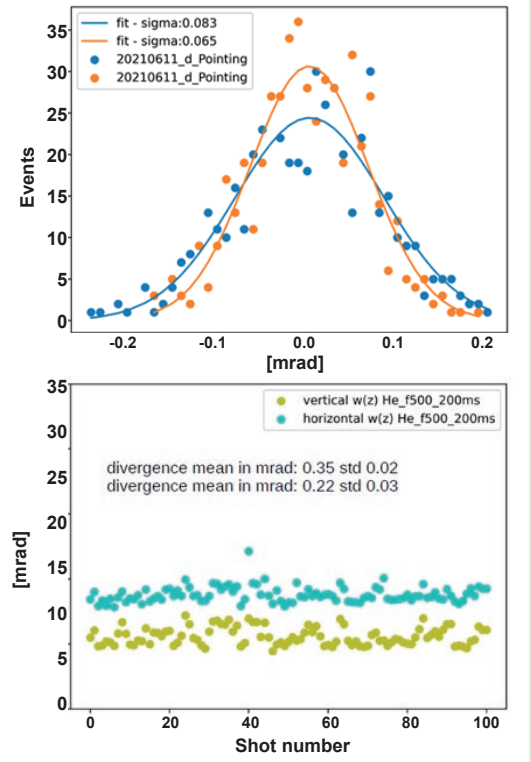

Fig. 2:
HHG-beam pointing and divergence stability: The beam footprint has been recorded with a CCD (downstream of Al-filters with 200 nm cumulated thickness and 200 ms acquisition time for each point) at about 3 m distance downstream from the source.

Characterization of the High Harmonic Source

Optimizing the soft X-ray photon flux in spectroscopic setups requires slit-less approaches. Thus beam pointing and divergence stability are important for the achievable resolution in imaging-type spectrometers as realized with the MOSFER design.

Fig. 2 shows the result of HHG beam pointing and divergence characterization when focusing (f = 500 mm) the 2.1 µm beam into a 3 mm long He-gas cell. Width and stability of the Gaussian distribution are crucial input parameters for the design of a spectrometer working with this input beam. For spectral calibration a thin film multilayer target (SiN 200 nm + Ti 30 nm + Cr 30 nm + Cu 20 nm + Fe 30 nm) grown in project 4.3 has been employed.

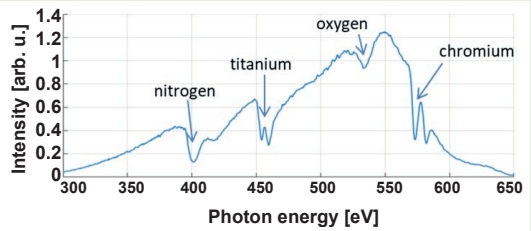

Fig. 3:
Spectrum and absorption edges of a multilayer calibration target (cf. text).

The resulting transmission spectrum featuring the respective absorption edges is depicted in Fig. 3. Furthermore, we cross-checked again the source photon flux (in $eV^{-1}s^{-1}$) which we can realize: O: K-edge ~ 5 x 10^5, Ti: L-edge ~ 10^6, C: K-edge ~ 6 x 10^6, Gd: N-edge ~ 10^9 [MFH21]. Here we rely on a CCD-camera and a grating assembly with absolute sensitivity calibration by the German metrology institute PTB.

Experiments and activities in context with other MBI-projects

A complete IR-pump – (150 +/- 50) eV probe setup in transverse magneto-optical Kerr effect (TMOKE) geometry with variable angle of incidence was completed and used for application experiments. Results are discussed in the context of project 3.2. Furthermore, young researcher projects have been carried out by A. Heilmann (Elliptically polarized HHG) and M. v. Mörbeck-Bock (Two cycle pulse generation at ~ 2 µm); results are presented in the context of project 1.2.

MOSFER

The ProFIT-funded project „Modular Spectrometer with Femtosecond Resolution for soft X-ray radiation" (MOSFER) aims at the design and construction of an efficient and modular soft X-ray spectrometer for use with laboratory sources. The design is aiming for commercialization, taking requirements of ultrafast time-resolved spectroscopy into account. Two demonstrators, one optimized for the NanoMovie HHG-source (cf. Fig. 4) and one optimized for a laser-produced plasma (LPP)

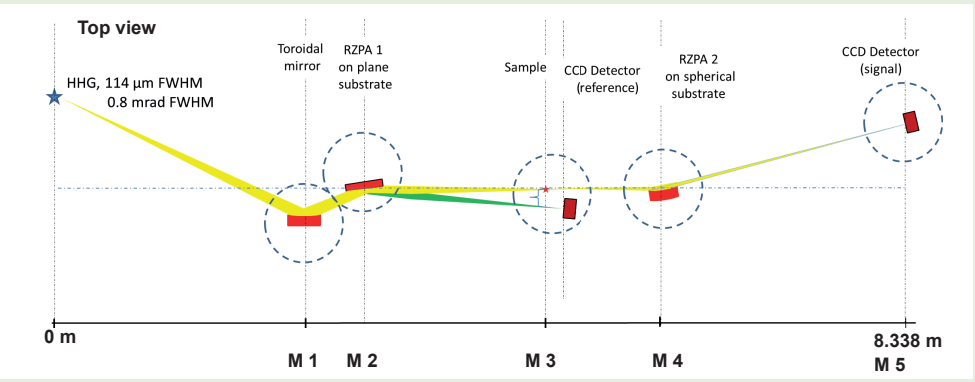

Fig. 3: *Schematic of the MOSFER spectrometer optimized for a HHG source covering the spectral range 100-900 eV.).*

source (cf. 3.2) will be set-up at MBI. The innovative optical design relies on the development and production of highly efficient reflection zone plates on bent substrates as dispersive elements. The work is organized in the framework of an industrial research project between MBI, PREVAC GmbH, IAP eV. and nob GmbH.

Own Publications 2021 ff

The infrastructure is currently under construction.

A publication on ultrafast element- and depth-resolved magnetization dynamics has been submitted in the context of project 3.2

Publication is referenced in project 1.2.

Berlin Laboratory for innovative X-ray Technologies (BLiX)

H. Stiel (project coordinator)

1. Overview

The Berlin Laboratory for innovative X-ray Technologies (BLiX) is jointly operated by the Institut für Optik und Atomare Physik (IOAP) of the Technische Universität Berlin and the Max-Born-Institut (MBI). BLiX is the „Leibniz-Applikationslabor“ of MBI.

BliX operates at the interface of scientific research and industrial application with the goal to transfer research results into instrument prototypes, with a focus on instruments and techniques that can be used in a laboratory environment without the need for large scale facilities. BLiX is supposed to be a place of collaborative technology development in the knowledge triangle of research – innovation – education.

In 2021, the joint research group SyncLab between the Helmholtz-Zentrum Berlin and BLiX was established. This joint research group will identify and promote the advantages of combining the laboratory methods developed at BLiX with the capabilities offered by large scale facilities like BESSY. The research group is funded with a permanent position for the deputy research group leader and a PhD position.

The main fields of activity in BLiX are:

- Soft X-ray imaging using laboratory X-ray microscopy
- Confocal micro X-ray fluorescence analysis
- Detection of chemical species
- X-ray absorption spectroscopy in the laboratory
- Customer inspired development of hard and soft X-ray spectrometers based on advanced X-ray optics

MBI contributes to BLiX predominantly via:

- The support of development and operation of a soft X-ray absorption spectroscopy beamline based on a laser produced plasma X-ray source and novel X-ray optics
- The upgrade of a full field laboratory transmission X-ray microscope (LTXM) capable of tomographic nanoscale imaging and support of LTXM user operation
- The transfer of know-how concerning the development and application of laser based sources, optics and detectors for the soft X-ray region.

Near-edge X-ray absorption fine structure spectroscopy in the laboratory

A laser produced plasma (LPP) source based on long time experience of MBI in laser plasma dynamics has been implemented at BLiX in collaboration between IOAP/TU Berlin and BESTEC GmbH. The pump laser is a high average power commercial Yb:YAG – thin disk laser system (TRUMPF Laser Technology) which is modified with a variable pulse length seed-diode (AMPHOS, 0.5 ns- 30 ns) in order to adapt the pulse duration to the experimental needs. In standard operation mode the system delivers 1 ns laser pulses with 100 Hz repetition rate, up to 250 mJ single pulse energy and an $M^2 < 1.2$. The laser pulses are focused onto a rotating and translating metal cylinder, forming a small hot dense plasma, which emits the desired soft X-rays. The target material can be exchanged with Cu and W the standard materials for line emission or quasi-continuous spectra, respectively. A real-time feedback system ensures source position stability, while the laser and the emission intensity are monitored during measurements. Two beamlines offer the possibility of two simultaneous experiments. The LPP source delivers soft X-ray pulses in the photon energy range between 200 and 1200 eV at a maximum average brightness in selected emission lines of up to 10^{11} ph/s*mm^2*mrad^2.

For investigations of samples relevant for users from life and environmental sciences an X-ray absorption beamline has been implemented. It is equipped with a novel two-channel reflection zone-plate (RZP) spectrometer combining a probe and a reference channel (collaboration with HZB and nob GmbH, Berlin) for near edge X-ray absorption fine structure (NEXAFS) spectroscopy investigations with a spectral resolution up to $E/\Delta E$ = 1000 at the carbon, nitrogen and oxygen K-edges as well as on L-edges of transition metal compounds. A beam splitter inserted in the laser beamline in conjunction with a delay line allows for pump-probe experiments with a sub-ns resolution.

Currently a project „Modular Spectrometer with Femtosecond Resolution for soft X-ray radiation (MOSFER)“ in the framework of the MBI on-demand application laboratories has been started. MOSFER is a joint research activity by MBI, IAP eV, Nano Optics Berlin GmbH and Prevac GmbH. The project aims at the conception and construction a soft X-ray spectrometer in a modular design on an optical table in spite of the vacuum requirements, allowing for easy customization by combining standardized units. Furthermore, the development and production of highly efficient reflection zone plates on bent substrates as dispersive elements is part of the project. After commissioning of a prototype spectrometer the demonstration of its performance will be pursued in application expe

Laboratory X-ray microscopy

The full field laboratory transmission X-ray microscope (LTXM) operated at BLiX enables the detection of high quality nanoscopic images at 500 eV with a magnification up to 1000 in a field of view of about 30 µm, a spatial resolution of 30 nm and a typical data accumulation time of less than one minute.

The soft X-ray radiation of the LTXM is provided by a laser-generated plasma. A high average power laser beam is focused onto a nitrogen cryo-jet. Line emission from the resulting hot dense plasma is collected by a multilayer condenser mirror (Optixfab GmbH, Jena), monochromatized and focused on the sample. Behind the sample, a zone plate objective, projects the image onto a cooled back illuminated X-ray CCD-camera Roper Scientific, 2048x2048 pixels).

The LTXM is equipped with a high-precision cryo-stage for the sample which allows tomographic measurements.

2. Results in 2021

Results with direct participation of MBI personnel

Pump-probe NEXAFS spectroscopy in the photon energy range 200 – 1000 eV

In order to make pump-probe NEXAFS spectroscopy with sub-ns resolution available to a community mainly interested in investigations on organic molecules, the work on pump-probe experiments on thin layers of porphyrins prepared on thin foil Si_3N_4 and Al substrates has been continued in 2021. Major improvements in data acquisition using sCMOS detectors has been made (cp. [B2-P-2020.11] and [B2-P-2021.07]).

Reflection zone plates (RZP) on curved substrates as novel high resolution dispersive optics for lab based NEXAFS

In the framework of the MOSFER project (see above) prototype RZPs on curved substrates provided by the industrial partner Nano Optics Berlin GmbH have been evaluated using the MBI laser produced plasma source (see also Project 3.3). In contrast to a RZP on a planar substrate, the new design allows a high spectral resolution of up to $\Delta E/E = 1000$ on the detector for a wide spectral range (design-energy ± 150 eV) without an energy dependent spatial and spectral limited focusing. This enables to record a spectrum with retaining one dimension for spatial imaging, similar to spectrometers based on Varied Line-Spaced (VLS) gratings. In contrast to a VLS, a RZP on a curved substrate offers a high efficiency up to 25 % in a large spectral range. As an example, figure 1 shows the detector image if the RZP on a curved substrate has been illuminated by soft X-rays from our ps-laser produced plasma (LPP) source.

Nanoscale imaging in the water window

In order to increase the stability of the laser-produced plasma source of the LTXM a thin disk laser system developed at MBI has been implemented. The setup of the new compact LTXM together with the “custom-developed” thin disk laser is shown in Fig. 2.

The Collaborative Research Center 1340 (Sonderforschungsbereich SFB 1340) “Matrix in Vision” is dedicated to systematically exploring the interaction of magnetic nanoparticles with glycosamino-glycans (GAGs) as a basis for non-invasive imaging of inflammatory diseases such as atherosclerosis. X-ray microscopy in the water window could help to understand these processes on a cellular or even sub-cellular level. Work in 2021 has concentrated on investigations on imaging of THP1-cells in the context of CRC 1340 research. A special sample

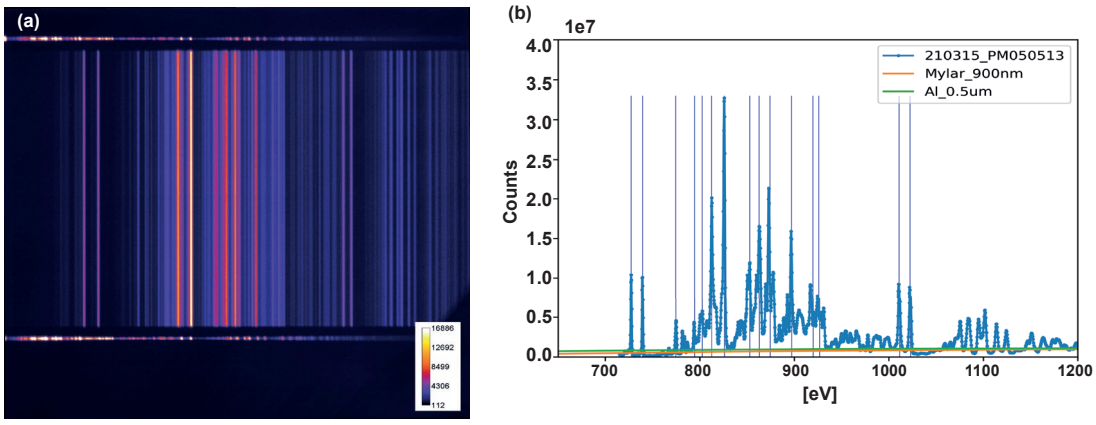

Fig. 1:
(a) CCD detector image of an iron target spectrum taken with the prototype RZP (design energy 780 eV) using the ps-LPP @ MBI.
(b) Lineout of the image. The emission spectrum of the ion plasma shows a cascade of emission lines well resolved over the entire *photon energy range. In contrast, for RZPs on flat substrates, highest resolution can only be obtained in the immediate vicinity of the design photon energy. For details see [B2-P-2021.08]*

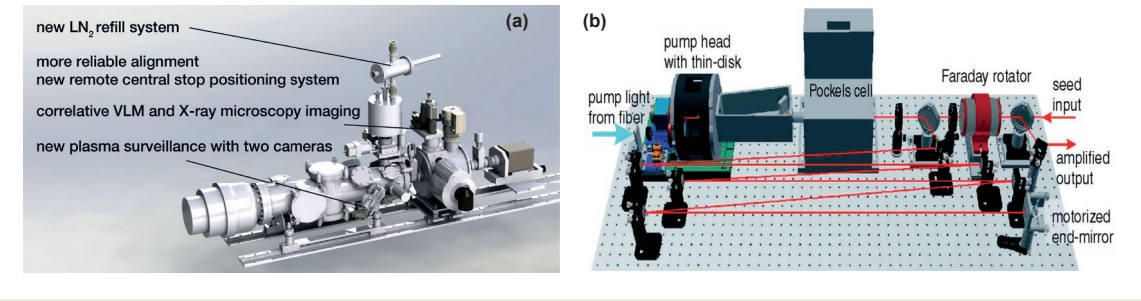

Fig. 2:
(a)Setup of the upgraded Laboratory X-ray Transmission Microscope (LTXM), (b) Scheme of the custom developed thin disk pump laser (60 mJ @500 Hz, 500 ps) for the LTXM.

preparation protocol and surveillance system has been developed.

LTXM and synchrotron TXM (3D tilt series) at BESSY II (Berlin, Germany) were successfully utilized to resolve the glycocalyx of THP-1 cells at 25 nm resolution in collaboration with the Royal Institute of Technology (KTH) in Sweden [B2-P-2020.05]

Results by TU Berlin personnel, without participation of MBI scientists.

In the following, results by non-MBI staff within BLiX are briefly summarized to allow for a complete picture of the BLiX activities.

The instrumentation for X-ray spectroscopy and microscopy developed in BLiX has reached a state, where it can be used in applications. The development of three X-ray absorption spectrometers for the Max-Planck Institute for Chemical Energy Conversion was continued. Two instruments are operating in the hard X-ray region and are optimized for XANES and EXAFS respectively. The third instrument employs a laser-plasma source for the soft X-ray range below 1 keV. During 2021 the application experiments at BLiX shifted increasingly from demonstration measurements to research applications. Interdisciplinary collaborations in the fields of chemistry, material science and medical science continued to be an important focus.

X-ray absorption spectroscopy (XANES, EXAFS)

The BLiX spectrometer is capable of producing XANES spectra with moderate energy resolution and excellent EXAFS spectra within reasonable acquisition times. Application projects are carried out with various partners:

- Catalysis within the Cluster of Excellence ‘Unifying Systems in Catalysis’, UniSysCat (XANES and EXAFS)
- Environmental Chemistry Removal of toxic chromium from water
- Materials research: Cement
- Quantitative analysis of species mixtures

First steps towards the application of laboratory XANES for in-situ experiments were made. Together with the group of Prof. Aleksander Gurlo (TU Berlin), changes of the chenical state of catalytic active nano-particles with changing temperature and during the reaction with gases shall be investigated.

Confocal micro-X-ray fluorescence spectroscopy (XRF)

A dedicated laboratory for micro-XRF and confocal micro-XRF is operated within BLiX. In 2021, the main focus was on biomedical samples. Ongoing application projects focus on:

- Mineral exchange between host plant and cuscuta parasite
- Interface dynamics in teeth close to restauration
- Metal distribution in cacao beans
- Zn localization and speciation in honey bees and larvae

In the framework of the DFG Forschungsgruppe InterDent, a second project was approved and started utilizing BLiX facilities within the Synclab cooperation.

Angle-resolved X-ray fluorescence spectroscopy (XRF)

Three different setups for angle-resolved XRF are operational, in part with custom hardware solutions developed at BLiX. While the main focus is still on the improvement of the setups, a first application project is in progress:

- inter- and intra-layer diffusion processes in water window multilayer optics
- Compositional gradients in CIGSe solar cells.

The long term cooperation with the X-ray Spectrometry group at PTB was continued. In joint experiments with PTB, Bruker Nano and BLiX, laboratory methods were evaluated and validated using calibrated instrumentation at the PTB laboratory at BESSY II.

Dsign of X-ray optics

The BMBF-funded joint research project Optiecs4Xi with the University of Hamburg was continued. It aims at the design and application of highly annealed pyrolytic graphite (HAPG) based X-ray optics for X-ray flu-

orescence imaging at high photon energies for medical applications. An optic for beam shaping at a PETRA IV high energy beamline was successfully tested.

People: Johannes Tümmler (MBI), Julia Bränzel (MBI), Oliver Reichel (MBI), Christian Seim (TUB), Aurélie Dehlinger (TUB), Maria Meitinger (TUB), Ioanna Mantouvalou (HZB), Adrian Jonas (TUB), Daniel Grötzsch (TUB), Christopher Schlesiger (TUB), Wolfgang Malzer (TUB), Birgit Kanngießer (TUB), Leona Bauer (HZB), Richard Gnewkow (HZB), Frank Förste (TUB)

Users & Collaborations: Charité Berlin / The Arctic University of Norway, Tromsö / Institutes of TU Berlin: Chemistry, Food Technology, Environment Protection, Construction Engineering / MPI for Chemical Energy Conversion, Mühlheim / Leibniz Institut für Gewässerökologie und Binnenfischerei, Berlin / TU Bergakademie Freiberg / Forschungszentrum Jülich / FhG-ILT, Aachen / optixFab GmbH, Jena / greateyes GmbH, Berlin / HZB/BESSY, Berlin / PTB, Berlin / KTH, Stockholm, Sweden / BESTEC GmbH, Berlin / PREVAC GmbH, Berlin / Institut für angewandte Photonik eV, Berlin / Nano Optics Berlin GmbH, Berlin / Excillum Ltd, Kista, Sweden / Helmut Fischer GmbH, Berlin/Sindelfingen Optigraph GmbH / Université P. & M. Curie, Paris, France / Hamburg University / Leibniz Universität Hannover

Own Publications 2021 ff

All publications involving MBI scientists which have emerged from work in BLiX and MOSFER are listed under the relevant research projects (cp. Project 3.3).

Publications related exclusively to TU Berlin personnel, without contribution of MBI scientists:

L. Bauer *et al.*; J. Anal. At. Spectrom. **36** (2021) 2519
T. Priemel *et al.*; Science **374** (2021) 206

H. Oguztürk *et al.*; Part. Part. Syst. Charact. **38** (2021) 2000328

J. Baumann *et al.*; Spectroch. Acta B **181** (2021) 106216

F. Maged *et al.*; ACS Catal. **11** (2021) 43

W. Malzer *et al.*; Spectrochim. Acta B **177** (2021) 106101

Publication is referenced in project 1.2.

4.3: Nanoscale Samples and Optics

W. D. Engel (project coordinator)
and D. Sommer, M. Schneider

1. Overview

The Laboratory for Nanoscale Samples and Optics supports experiments in different scientific projects of the MBI. We develop and produce thin-film sample systems on various substrates with the focus on magnetic multilayers, alloys and metal foils using magnetron sputtering and thermal evaporation. The close integration of deposition, structuring and characterization of these systems with experiments promotes fast feedback on sample performance and rapid development cycles. We collaborate closely with several MBI projects as well as with external cooperation partners to provide custom sample-related services.

To enable new experimental techniques as for example Spin Hall Effect measurements and skyrmion nucleation via high current density pulses, a UV-lithography system is used to create masks, which enables necessary structuring and lift-off processes. Topographic and magnetic characterization is carried out via atomic and magnetic force microscopy (AFM/MFM), electron microscopy (SEM, EDX), X-ray reflectivity and diffraction, Kerr-magnetometry and Kerr-microscopy.

In close cooperation with the central facility for electron microscopy (ZELMI) at the TU Berlin the 3D patterning on a few-micrometer and nanometer scale via electron beam lithography (EBL) and focused ion beam milling (FIB) is carried out.

Main external collaborations: ZELMI (TU Berlin), F. Kronast (Helmholtz-Zentrum Berlin, HZB), R. Ernstorfer (TU Berlin), A. Scherz (XFEL), G.S.D. Beach (Massachusetts Institute of Technology, MIT), S. Bonetti (Stockholm University), C. Gutt (Siegen University), S. Wall (ICFO), K. Höflich (Ferdinand-Braun-Institut, FBH), T. Kampfrath (FU Berlin).

2. Results in 2021

In the last year, we have focused on the fabrication of oxide- and nitride-based layer systems, ferri-/antiferro- and ferromagnetic layer systems and filter/calibration systems, both on different substrates and free-standing - depending on the requirements of the experiments.

Example: Polarization filter

We produced special thin film filters, used as polarizers and analysers for soft x-rays for experiments in the NanoMovie project and for ultrafast x-ray diffraction using a table-top laser-driven plasma source setup. The filters consist of a 50 nm thick $Gd_{24}Fe_{76}$ film deposited with our electron-beam evaporation system (Telemark) on Si_3N_4-membranes.

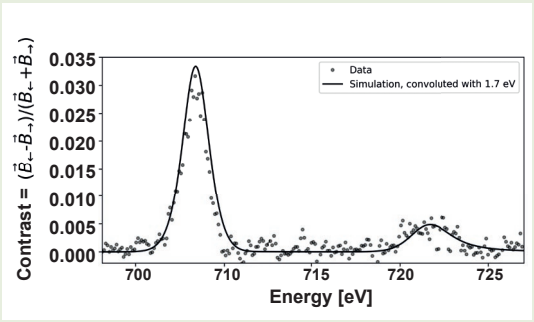

Fig. 1:
Magnetic dichroic transmission signal at the L_2 and L_3 edge of Fe demonstrating the functionality of the GdFe polarization filter.

These ferrimagnetic thin film filters are out-of-plane magnetized in remanence and show no domain pattern, allowing for easy use without an external magnetic field. With this type of filter, e.g., the unpolarized light of the plasma source can be elliptically polarized, enabling XMCD measurements (see Fig.1: First results for this kind of magnetic dichroic experiments).

Example: Synthetic antiferromagnets

We have fabricated laterally patterned synthetic antiferromagnet layers for joint experiments with the group of F. Kronast (HZB). Synthetic antiferromagnets consist of nm-thin ferromagnetic layers that couple antiferromagnetically across a non-magnetic spacer layer via RKKY-interaction. The samples were fabricated on a polished transparent MgO substrate by

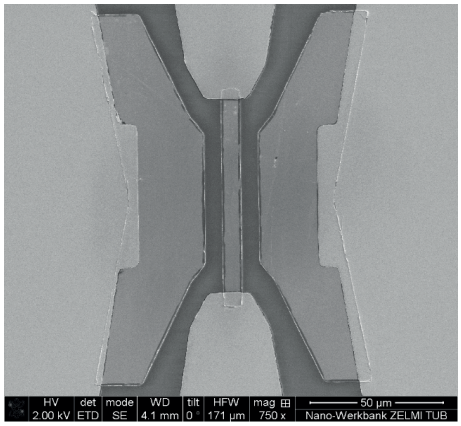

Fig. 2:
SAF sample on MgO with 8 µm strip line and 8 µm gaps to the Au contacts and ground.

magnetron sputtering at room temperature. This allows the magnetization to be changed by a fs laser pulse from the MgO substrate side and a subsequent measurement of the change in magnetic domains can be carried out from the top side with surface sensitive photoemission electron microscopy. The magnetic properties of SAF can be tuned by varying the layer thickness and the type of materials to control, for example, the size and stability of magnetic skyrmions, which is an advantage over pure antiferromagnets.

Example: Workflow multifunctional chip

Another main task in 2021 was the establishment of a workflow for the production of multifunctional chips, which are used in a variety of experiments. We optimized the mask fabrication process from technical drawing to exposure with the existing UV lithography system and adapted it to a special PMMA resist as mask material. In a multi-step process, the different structures are generated and different functional materials (magnetic thin films and gold contacts) are deposited in intermediate steps. This enables us to produce customized samples for the respective experiments and the correspondingly required specific substrates in short development and manufacturing times. As an example for such a chip design, an enlargement of the membrane area (dark vertical stripe), the gold contacts and the Hall-bars is shown in Fig. 3.

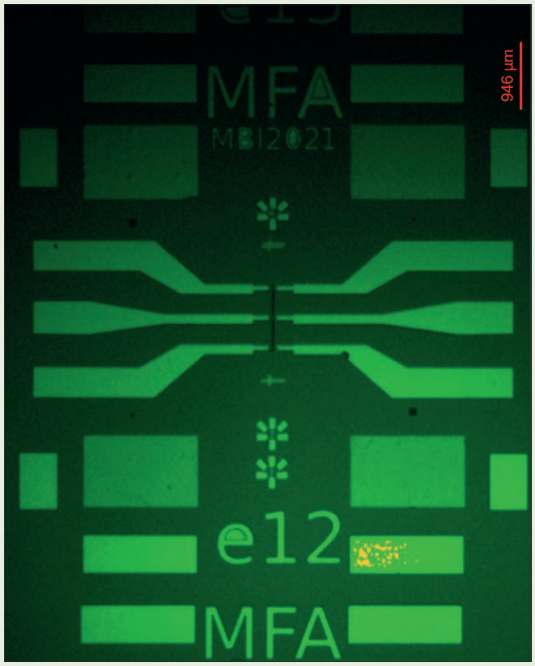

Fig. 3:
Partial view of the Si_3N_4-chip with Hall-bars, strip-lines and Au contacts produced by UV-lithography, magnetron sputtering and e-beam evaporation.

Own Publications 2021 ff

(for full titles and list of authors see appendix 1)

ZJW21: D. Zahn et al.; Phys. Rev. Research 3 (2021) 023032/1-14

Other publications which have emerged from this work in context of projects 3.2 and 3.3 are listed there.

Appendices

Appendix 1

Publications

AAA21: F. Allum, K. Amini, M. Ashfold, D. Bansal, R. J. F. Berger, M. Centurion, G. Dixit, D. Durham, E. Fasshauer, J. P. F. Nunes, I. Fischer, G. Grell, M. Y. Ivanov, A. Kirrander, O. Kornilov, C. Kuttner, K. Lopata, L. Ma, V. Makhija, A. Maxwell, A. M. Carrascosa, A. Natan, D. Neumark, S. Pratt, A. Röder, D. Rolles, J. M. Rost, T. Sekikawa, M. Simmermacher, A. Stolow, E. Titov, J. C. Tremblay, P. M. Weber, H. Yong, and L. Young; Time-resolved diffraction: general discussion; Faraday Discuss. **228** (2021) 161-190

AAB21: R. Arkhipov, M. Arkhipov, I. Babushkin, A. Pakhomov, and N. Rosanov; Coherent propagation of a half-cycle unipolar attosecond pulse in a resonant two-level medium; J. Opt. Soc. Am. B **38** (2021) 2004-2011

AAD21: K. Acheson, F. Allum, R. Das, G. Dixit, H. Doan, E. Fasshauer, L. Ge, G. Grell, M. Y. Ivanov, O. Kornilov, J. Küpper, C. Kuttner, F. Martín, A. Maxwell, N. Mayer, A. Palacios, S. Pratt, A. Röder, N. Rohringer, A. Rouzée, T. Suzuki, E. Titov, J. C. Tremblay, H. Yong, and L. Young; Strong-field physics: general discussion; Faraday Discuss. **228** (2021) 470-487

AAn21: I. A. Aleksandrov and A. A. Andreev; Pair production seeded by electrons in noble gases as a method for laser intensity diagnostics; Phys. Rev. A **104** (2021) 052801/1-12

ACC21: F. Allum, F. Calegari, S. M. Cavaletto, M. Centurion, G. Dixit, E. Fasshauer, I. Fischer, R. Forbes, G. Grell, M. Y. Ivanov, A. Kirrander, O. Kornilov, J. Küpper, C. Kuttner, J. Marangos, S. Matsika, A. Maxwell, R. S. Minns, A. M. Carrascosa, A. Natan, D. Neumark, A. Odate, A. Oyarzún, A. Palacios, T. Pfeifer, A. Röder, J. M. Rost, A. Rouzée, A. Stolow, E. Titov, P. M. Weber, and T. Wolf; Ultrafast X-ray science: general discussion; Faraday Discuss. **228** (2021) 597-621

ACE21: K. Amini, A. Chacón, S. Eckart, B. Fetić, and M. Kübel; Quantum interference and imaging using intense laser fields; Eur. Phys. J. D **75** (2021) 275/1-22

ACF21: M. Ashfold, M. Chergui, I. Fischer, L. Ge, G. Grell, M. Y. Ivanov, A. Kirrander, O. Kornilov, S. R. Krishnan, J. Küpper, C. Kuttner, V. Makhija, F. Martín, S. Matsika, R. S. Minns, A. Natan, D. M. Neumark, A. Palacios, S. Pratt, A. Röder, J. M. Rost, M. Ruberti, A. Stolow, E. Titov, and L. Young; Time-resolved ultrafast spectroscopy: general discussion; Faraday Discuss. **228** (2021) 329-348

AHR21: R. M. Abrudan, M. Hennecke, F. Radu, T. Kachel, K. Holldack, R. Mitzner, A. Donges, S. Khmelevskyi, A. Deak, L. Szunyogh, U. Nowak, S. Eisebitt, and I. Radu; Element-specific magnetization damping in ferrimagnetic DyCo5 alloys revealed by ultrafast X-ray measurements; Phys. Status Solidi-R **15** (2021) 2100047/1-15

AJM21: D. R. Austin, A. S. Johnson, F. McGrath, D. Wood, L. Miseikis, T. Siegel, P. Hawkins, A. Harvey, Z. Mašín, S. Patchkovskii, M. Vacher, J. P. Malhado, M. Y. Ivanov, O. Smirnova, and J. P. Marangos; Extracting sub-cycle electronic and nuclear dynamics from high harmonic spectra; Sci. Rep. **11** (2021) 2485/1-8

AKB21: D. Azoury, M. Krüger, B. D. Bruner, O. Smirnova, and N. Dudovich; Direct measurement of Coulomb-laser coupling; Sci. Rep. **11** (2021) 495/1-9

AKL21: G. S. J. Armstrong, M. A. Khokhlova, M. Labeye, A. S. Maxwell, E. Pisanty, and M. Ruberti; Dialogue on analytical and ab initio methods in attoscience; Eur. Phys. J. D **75** (2021) 209/1-31

AOD21: D. Ayuso, A. Ordoñez, P. Decleva, M. Y. Ivanov, and O. Smirnova; Enantio-sensitive unidirectional light bending; Nat. Commun. **12** (2021) 3951/1-9

AOI21: D. Ayuso, A. Ordoñez, M. Y. Ivanov, and O. Smirnova; Ultrafast optical rotation in chiral molecules with ultrashort and tightly focused beams; Optica **8** (2021) 1243-1246

APA21: R. Arkhipov, A. Pakhomov, M. Arkhipov, I. Babushkin, A. Demircan, U. Morgner, and N. Rosanov; Population difference gratings created on vibrational transitions by nonoverlapping subcycle THz pulses; Sci. Rep. **11** (2021) 1961/1-12

APL21a: A. Andreev, K. Platonov, Z. Lécz, and N. Hafz; Generation and collective interaction of giant magnetic dipoles in laser cluster plasma; Sci. Rep. **11** (2021) 15971/1-9

APL21b: A. Alles, Z. Pan, P. Loiko, J. M. Serres, S. Slimi, S. Yingming, K. Tang, Y. Wang, Y. Zhao, E. Dunina, A. Kornienko, P. Camy, W. Chen, L. Wang, U. Griebner, V. Petrov, R. M. Solé, M. Aguiló, F. Díaz, and X. Mateos; Tm^{3+}-doped calcium lithium tantalum gallium garnet (Tm:CLTGG): novel laser crystal; Opt. Mater. Express **11** (2021) 2938-2951

ARB21: S. Amiranashvili, M. Radziunas, U. Bandelow, K. Busch, and R. Ciegis; Additive splitting methods for parallel solutions of evolution problems; J. Comput. Phys. **436** (2021) 110320

ASU21: L. Alber, V. Scalera, V. Unikandanunni, D. Schick, and S. Bonetti; NTMpy: An open source package for solving coupled parabolic differential equations in the framework of the three-temperature model; Comput. Phys. Commun. **265** (2021) 107990/1-7

AZP21: J. A. Anaya-Contreras, A. Zúñiga-Segundo, A. Perez-Leija, R. d. J. León-Montiel, and H. M. Moya-Cessa; Multiphoton processes via conditional measurements in the two-field interaction; J. Opt. **23** (2021) 095201/1-9

BBA21: L. Beichert, Y. Binhammer, J. R. C. Andrade, R. Mevert, A.-K. Kniggendorf, B. Roth, and U. Morgner; Real-time stimulated Raman spectroscopy with a non-collinear optical parametric oscillator; Opt. Express **29** (2021) 31499-31507

BCD21: J. Biegert, F. Calegari, N. Dudovich, F. Quéré, and M. J. J. Vrakking; Attosecond technology(ies) and science; J. Phys. B **54** (2021) 070201/1-14

BHL21: M. R. Bionta, E. Haddad, A. Leblanc, V. Gruson, P. Lassonde, H. Ibrahim, J. Chaillou, N. Émond, M. R. Otto, Á. Jiménez-Galán, R. E. F. Silva, M. Y. Ivanov, B. J. Siwick, M. Chaker, and F. Légaré; Tracking ultrafast solid-state dynamics using high harmonic spectroscopy; Phys. Rev. Res. **3** (2021) 023250/1-12

BLJ21: L. Basyrova, P. Loiko, W. Jing, Y. Wang, H. Huang, E. Dunina, A. Kornienko, L. Fomicheva, B. Viana, U. Griebner, V. Petrov, M. Aguiló, F. Díaz, X. Mateos, and P. Camy; Spectroscopy and efficient laser operation around 2.8 μm of Er:$(Lu,Sc)_2O_3$ sesquioxide ceramics; J. Lumin. **240** (2021) 118373/1-11

BLM21: L. Basyrova, P. Loiko, R. Maksimov, V. Shitov, J. M. Serres, U. Griebner, V. Petrov, M. Aguiló, F. Díaz, and X. Mateos; Comparative study of Yb:$Lu_3Al_5O_{12}$ and Yb:Lu_2O_3 laser ceramics produced from laser-ablated nanopowders; Ceramics Int. **47** (2021) 6633-6642

BPB21: F. Büttner, B. Pfau, M. Böttcher, M. Schneider, G. Mercurio, C. M. Günther, P. Hessing, C. Klose, A. Wittmann, K. Gerlinger, L.-M. Kern, C. Strüber, C. von Korff Schmising, J. Fuchs, D. Engel, A. Churikova, S. Huang, D. Suzuki, I. Lemesh, M. Huang, L. Caretta, D. Weder, J. H. Gaida, M. Möller, T. R. Harvey, S. Zayko, K. Bagschik, R. Carley, L. Mercadier, J. Schlappa, A. Yaroslavtsev, L. L. Guyarder, N. Gerasimova, A. Scherz, C. Deiter, R. Gort, D. Hickin, J. Zhu, M. Turcato, D. Lomidze, F. Erdinger, A. Castoldi, S. Maffessanti, M. Porro, A. Samartsev, J. Sinova, C. Ropers, J. H. Mentink, B. Dupé, G. S. D. Beach, and S. Eisebitt; Observation of fluctuation-mediated picosecond nucleation of a topological phase; Nat. Materials **20** (2021) 30–37

BZh21: U. Bengs and N. Zhavoronkov; Elliptically polarized high-harmonic radiation for production of isolated attosecond pulses; Sci. Rep. **11** (2021) 9570/1-9

CHJ21: V. Chardonne, M. Hennes, R. Jarrier, R. Delaunay, N. Jaouen, M. Kuhlmann, N. Ekanayake, C. Léveillé, C. von Korff Schmising, D. Schick, K. Yao, X. Liu, G. S. Chiuzbăian, J. Lüning, B. Vodungbo, and E. Jal; Toward ultrafast magnetic depth profiling using time-resolved x-ray resonant magnetic reflectivity; Struct. Dyn. **8** (2021) 034305/1-10

CNK21: H. Cao, R. S. Nagymihaly, N. Khodakovskiy, V. Pajer, J. Bohus, R. Lopez-Martens, A. Borzsonyi, and M. Kalashnikov; Sub-7 fs radially-polarized pulses by post-compression in thin fused silica plates; Opt. Express **29** (2021) 5915-5922

CWB21: M.-A. Codescu, M. Weiß, M. Brehm, O. Kornilov, D. Sebastiani, and E. T. J. Nibbering; Switching between proton vacancy and excess proton transfer pathways in the reaction between 7-hydroxyquinoline and formate; J. Phys. Chem. A **125** (2021) 1845-1859

DDM21: F. R. Díaz, H.-G. Duan, R. J. D. Miller, and M. Thorwart; Ultrafast charge transfer and relaxation at a donor-acceptor interface; J. Phys. Chem. B **125** (2021) 8869-8875

DKK21: V. Deinhart, L.-M. Kern, J. N. Kirchhof, S. Juergensen, J. Sturm, E. Krauss, T. Feichtner, S. Kovalchuk, M. Schneider, D. Engel, B. Pfau, B. Hecht, K. I. Bolotin, S. Reich, and K. Höflich; The patterning toolbox FIB-o-mat: Exploiting the full potential of focused helium ions for nanofabrication; Beilstein J. Nanotechnol. **12** (2021) 304-318

DKW21: L. Drescher, O. Kornilov, T. Witting, V. Shokeen, M. J. J. Vrakking, and B. Schütte; Extreme-ultraviolet spectral compression by four-wave mixing; Nat. Photonics **15** (2021) 263-266

DSE21: J. K. Dewhurst, S. Shallcross, P. Elliott, S. Eisebitt, C. von Korff Schmising, and S. Sharma; Angular momentum redistribution in laser-induced demagnetization; Phys. Rev. B **104** (2021) 054438/1-5

EDS21: E. Escoto, A. Demircan, and G. Steinmeyer; Cage Solitons; IEEE J. Quantum Electron. **57** (2021) 1300106/1-6

EEM21: R. Y. Engel, M. Ekimova, P. S. Miedema, C. Kleine, J. Ludwig, M. Ochmann, B. Grimm-Lebsanft, R. Ma, M. Teubner, S. Dziarzhytski, G. Brenner, M.-K. Czwalinna, B. Rösner, T. K. Kim, C. David, S. Herres-Pawlis, M. Rübhausen, E. T. J. Nibbering, N. Huse, and M. Beye; Shot noise limited soft x-ray absorption spectroscopy in solution at a SASE-FEL using a transmission grating beam splitter; Struct. Dyn. **8** (2021) 014303/1-10

EMV21: U. Elu, L. Maidment, L. Vamos, F. Tani, D. Novoa, M. H. Frosz, V. Badikov, D. Badikov, V. Petrov, P. S. J. Russell, and J. Biegert; Seven-octave high-brightness and carrier-envelope-phase-stable light source; Nat. Photonics **15** (2021) 277-281

ESK21: T. Elsaesser, J. Schauss, A. Kundu, and B. P. Fingerhut; Phosphate vibrations probe electric fields in hydrated biomolecules: spectroscopy, dynamics, and interactions; J. Phys. Chem. B **125** (2021) 3899-3908

FGU21: P. Fuertjes, L. v. Grafenstein, D. Ueberschaer, C. Mei, U. Griebner, and T. Elsaesser; Compact OPCPA system seeded by a Cr:ZnS laser for generating tunable femtosecond pulses in the MWIR; Opt. Lett. **46** (2021) 1704-1707

Fin21: B. P. Fingerhut; The mutual interactions of RNA, counterions and water - quantifying the electrostatics at the phosphate-water interface; Chem. Commun. **57** (2021) 12880-12897

FSK21: B. P. Fingerhut, J. Schauss, A. Kundu, and T. Elsaesser; Contact pairs of RNA with magnesium ions - electrostatics beyond the Poisson-Boltzmann equation; Biophys. J. **120** (2021) 5322–5332

GDC21: M. de Goede, M. Dijkstra, L. Chang, N. Acharyya, G. Kozyreff, R. Obregón, E. Martínez, and S. M. García-Blanco; Mode-splitting in a microring resonator for self-referenced biosensing; Opt. Express **29** (2021) 346-358

GFR21: A. Ghalgaoui, B. P. Fingerhut, K. Reimann, T. Elsaesser, and M. Woerner; Terahertz polaron oscillations of electrons solvated in liquid water; Phys. Rev. Lett. **126** (2021) 097401/1-5

GKG21: E. Golias, I. Kumberg, I. Gelen, S. Thakur, J. Gördes, R. Hosseinifar, Q. Guillet, J. K. Dewhurst, S. Sharma, C. Schüßler-Langeheine, N. Pontius, and W. Kuch; Ultrafast optically induced ferromagnetic state in an elemental antiferromagnet; Phys. Rev. Lett. **126** (2021) 107202/1-6

GPB21: K. Gerlinger, B. Pfau, F. Büttner, M. Schneider, L.-M. Kern, J. Fuchs, D. Engel, C. M. Günther, M. Huang, I. Lemesh, L. Caretta, A. Churikova, P. Hessing, C. Klose, C. Strüber, C. von Korff Schmising, S. Huang, A. Wittmann, K. Lizius, D. Metternich, R. Battistelli, K. Bagschik, A. Sadovnikov, G. S. D. Beach, and S. Eisebitt; Application concepts for ultrafast laser-induced skyrmion creation and annihilation; Appl. Phys. Lett. **118** (2021) 192403/1-7

GPi21: R. Gutiérrez-Cuevas and E. Pisanty; Optical polarization skyrmionic fields in free space; J. Opt. **23** (2021) 024004/1-9

GRB21: P. Grychtol, D. E. Rivas, T. M. Baumann, R. Boll, A. D. Fanis, B. Erk, M. Ilchen, J. Liu, T. Mazza, J. Montaño, J. Müller, V. Music, Y. Ovcharenko, N. Rennhack, A. Rouzée, P. Schmidt, S. Schulz, S. Usenko, R. Wagner, P. Ziołkowski, H. Schlarb, J. Grünert, N. Kabachnik, and M. Meyer; Timing and x-ray pulse characterization at the Small Quantum Systems instrument of the European X-ray Free Electron Laser; Opt. Express **29** (2021) 37429-37442

GRE21: M. Génévriez, C. Rosen, and U. Eichmann; Structure and electron dynamics of planetary states of Sr below the $Sr^{+}7_{d}$ and 8_{p} thresholds; Phys. Rev. A **104** (2021) 012812/1-12

HBM21a: D. Habibović, W. Becker, and D. B. Milošević; High-order harmonic generation by aligned heteronuclear diatomic molecules in an orthogonally polarized two-color field; Eur. Phys. J. D **75** (2021) 122/1-15

HBM21b: D. Habibović, W. Becker, and D. B. Milošević; High-order harmonic generation by planar polyatomic molecules exposed to an orthogonally polarized two-color laser field; J. Phys. B **24** (2021) 134004/1-15

HBMc21: D. Habibović, W. Becker, and D. B. Milošević; Attosecond-pulse-train generation using an orthogonally polarized two-color field; J. Opt. Soc. Am. B **38** (2021) 3367-3377

HBMd21: D. Habibović, W. Becker, and D. B. Milošević; Symmetries and selection rules of the spectra of photoelectrons and high-order harmonics generated by field-driven atoms and molecules; Symmetry (Special Issue Time and Symmetry in Quantum Mechanics) **13** (2021) 1566/1-27

HDJ21: M. Hempel, S. Dadgostar, J. Jiménez, R. Kernke, A. Gollhardt, and J. W. Tomm; Catastrophic optical damage in semiconductor lasers: Physics and new results on InGaN high-power diode lasers; Phys. Status Solidi-R **16** (2021) 2100527/1-12

HDK21: O. Hort, A. Dubrouil, M. A. Khokhlova, D. Descamps, S. Petit, F. Burgy, E. Mével, E. Constant, and V. V. Strelkov; High-order parametric generation of coherent XUV radiation; Opt. Express **29** (2021) 5982-5992

HPM21: Z. Heiner, V. Petrov, and M. Mero; Few-cycle, µJ-level pulses beyond 5 µm from 1-µm-pumped OPA's based on non-oxide nonlinear crystals; SPIE Proc. **11670** (2021) 116700W/1-8

HWH21: J. Hong, H. Wen, J. He, J. Liu, Y. Dan, J. W. Tomm, F. Yue, J. Chu, and C. Duan; Stimulated emission at 1.54 µm from erbium/oxygen-doped silicon-based light-emitting diodes; Photonics Res. **9** (2021) 714-721

Iva21: M. Y. Ivanov; Concluding remarks: The age of molecular movies; Faraday Discuss. **228** (2021) 622-629

Jas21: M. Jasiulek; Solving nonlinear integral equations for laser pulse retrieval with Newton's method; Phys. Rev. E **103** (2021) 053306/1-15

JLB21: W. Jing, P. Loiko, L. Basyrova, Y. Wang, H. Huang, P. Camy, U. Griebner, V. Petrov, J. M. Serres, R. M. Solé, M. Aguiló, F. Díaz, and X. Mateos; Spectroscopy and laser operation of highly-doped 10 at. % Yb:$(Lu,Sc)_2O_3$ ceramics; Opt. Mater. **117** (2021) 111128/1-7

JSK21: A. Jonas, S. Staeck, B. Kanngießer, H. Stiel, and I. Mantouvalou; Laboratory quick near edge x-ray absorption fine structure spectroscopy in the soft x-ray range with 100 Hz frame rate using CMOS technology; Rev. Sci. Instrum. **92** (2021) 023102/1-8

JSS21: Á. Jiménez-Galán, R. E. F. Silva, O. Smirnova, and M. Y. Ivanov; Sub-cycle valleytronics: control of valley polarization using few-cycle linearly polarized pulses; Optica **8** (2021) 277-280

JVV21: A. S. Johnson, J. Valls-Conesa, L. Vidas, D. Perez-Salinas, C. M. Günther, B. Pfau, K. A. Hallman, R. F. Haglund Jr, S. Eisebitt, and S. Wall; Quantitative hyperspectral coherent diffractive imaging spectroscopy of a solid-state phase transition in vanadium dioxide; Sci. Adv. **7** (2021) eabf1386/1-9

JWK21: A. Jonas, K. Witte, B. Kanngießer, H. Stiel, and I. Mantouvalou; Transient laboratory X-ray absorption fine structure spectroscopy on thin films demonstrated with F8BT; SPIE Proc. **11886** (2021) 11886 11/1-8

KAB21: M. Kuster, K. Ahmed, K.-E. Ballak, C. Danilevski, M. Ekmedžić, B. Fernandes, P. Gessler, R. Hartmann, S. Hauf, P. Holl, M. Meye, J. Montaño, A. Münnich, Y. Ovcharenko, N. Rennhack, T. Rüter, D. Rupp, D. Schlosser, K. Setoodehnia, R. Schmitt, L. Strüder, R. M. P. Tanyag, A. Ulmer, and H. Yousef; The 1-Megapixel pnCCD detector for the Small Quantum Systems Instrument at the European XFEL: system and operation aspects; J. Synchrot. Radiat. **28** (2021) 576-587

KBM21: K. Kato, V. V. Badikov, K. Miyata, and V. Petrov; Refined Sellmeier equations for $BaGa_4S_7$; Appl. Opt. **60** (2021) 6600-6603

KER21: M. A. Khokhlova, M. Y. Emelin, M. Y. Ryabikin, and V. V. Strelkov; Polarization control of quasimonochromatic XUV light produced via resonant high-order harmonic generation; Phys. Rev. A **103** (2021) 043114/1-8

KEW21: C. Kleine, M. Ekimova, M.-O. Winghart, S. Eckert, O. Reichel, H. Löchel, J. Probst, C. Braig, C. Seifert, A. Erko, A. Sokolov, M. J. J. Vrakking, E. T. J. Nibbering, and A. Rouzée; Highly efficient soft x-ray spectrometer for transient absorption spectroscopy with broadband table-top high harmonic sources; Struct. Dyn. **8** (2021) 034302/1-6

KHW21: A. Koç, C. Hauf, M. Woerner, L. v. Grafenstein, D. Ueberschaer, M. Bock, U. Griebner, and T. Elsaesser; Compact high-flux hard X-ray source driven by femtosecond mid-infrared pulses at a 1 kHz repetition rate; Opt. Lett. **46** (2021) 210-213

KKK21: M. Kliem, T. Kiel, M. Kück, S. Meister, A. Mischok, H. Fröb, K. Busch, and K. Leo; Defect-State lasing in photonic lattices of metal–organic microcavities; Adv. Photonics Res. **2** (2021) 2000116/1-8

KLR21: E. Kifle, P. Loiko, C. Romero, J. Rodríguez Vázquez de Aldana, V. Zakharov, Y. Gurova, A. Veniaminov, V. Petrov, U. Griebner, R. Thouroude, M. Laroche, P. Camy, M. Aguiló, F. Díaz, and X. Mateos; Tm^{3+} and Ho^{3+} colasing in in-band pumped waveguides fabricated by femtosecond laser writing; Opt. Lett. **46** (2021) 122-125

KMP21: K. Kato, K. Miyata, and V. Petrov; Refined Sellmeier equations for $AgGaSe_2$ up to 18 μm; Appl. Opt. **60** (2021) 805-808

Kor21: O. Kornilov; A quantum vortex made of atoms; Science **373** (2021) 1084-1084

KPC21: Y. Kang, E. Pisanty, M. Ciappina, M. Lewenstein, C. Figuera de Morisson Faria, and A. S. Maxwell; Conservation laws for electron vortices in strong-field ionisation; Eur. Phys. J. D **75** (2021) 199/1-10

KPM21: K. Kato, V. Petrov, and K. Miyata; Accurate Sellmeier equations for $AgGaS_2$ in the 0.565-10.6321 μm spectral range; SPIE Proc. **11670** (2021) 116701K/1-5

KSP21: E. Kozari, M. Sigalov, D. Pines, B. P. Fingerhut, and E. Pines; Infrared and NMR spectroscopic fingerprints of the asymmetric $H_7^+O_3$ complex in solution; ChemPhysChem **22** (2021) 053306/1-15

KSZ21: M. Kowalczyk, Ł. Sterczewski, X. Zhang, V. Petrov, Z. Wang, and J. Sotor; Dual-comb femtosecond solid-state laser with inherent polarization-multiplexing; Laser Photon. Rev. **15** (2021) 2000441/1-10

KVB21: T. Kiel, P. Varytis, B. Beverungen, and K. Busch; Enhanced Faraday rotation by dielectric metasurfaces with Bayesian shape-optimized scatterers; Opt. Lett. **46** (2021) 1720-1723

KVS21: M. Kretschmar, M. J. J. Vrakking, and B. Schütte; Intense XUV pulses from a compact HHG setup using a single harmonic; J. Phys. B **54** (2021) 20LT01/1-6

KYP21: E. T. Karamatskos, S. Yarlagadda, S. Patchkovskii, M. J. J. Vrakking, R. Welsch, J. Küpper, and A. Rouzée; Time-resolving the UV-initiated photodissociation dynamics of OCS; Faraday Discuss. **228** (2021) 413-431

KYS21: A. Kumar, D. Yagodkin, N. Stetzuhn, S. Kovalchuk, A. Melnikov, P. Elliott, S. Sharma, C. Gahl, and K. I. Bolotin; Spin/Valley coupled dynamics of electrons and holes at the MoS_2–$MoSe_2$ interface; Nano Lett. **21** (2021) 7123-7130

KZK21: T. Kang, J. Zhang, A. Kundu, K. Reimann, M. Woerner, T. Elsaesser, B. Gil, G. Cassabois, C. Flytzanis, G. Fugallo, M. Lazzeri, R. Page, and D. Jena; Ultrafast nonlinear phonon response of few-layer hexagonal boron nitride; Phys. Rev. B **104** (2021) L140302/1-6

LAK21: Z. Lécz, A. Andreev, C. Kamperidis, and N. Hafz; Generation of high-quality GeV-class electron beams utilizing attosecond ionization injection; New J. Phys. **23** (2021) 043016/1-10

LCP21: M. Lewenstein, M. F. Ciappina, E. Pisanty, J. Rivera-Dean, P. Stammer, T. Lamprou, and P. Tzallas; Generation of optical Schrödinger cat states in intense laser–matter interactions; Nat. Phys. **17** (2021) 1104-1108

LDW21: J. Liu, J. Dong, Y. Wang, J. Guo, Y. Xue, J. Xu, Y. Zhao, X. Xu, H. Yu, Z. Wang, X. Xu, W. Chen, and V. Petrov; Tm:YAG single-crystal fiber laser; Opt. Lett. **46** (2021) 4454-4457

LED21: Q. Z. Li, P. Elliott, J. K. Dewhurst, S. Sharma, and S. Shallcross; Ab initio study of ultrafast charge dynamics in graphene; Phys. Rev. B **103** (2021) L081102/1-6

LKG21: P. Loiko, E. Kifle, L. Guillemot, J.-L. Doualan, F. Starecki, A. Braud, M. Aguiló, F. Díaz, V. Petrov, X. Mateos, and P. Camy; Highly efficient 2.3 µm thulium lasers based on a high-phonon-energy crystal: evidence of vibronic-assisted emissions; J. Opt. Soc. Am. B **38** (2021) 482-495

LLH21: T. Lamprou, R. Lopez-Martens, S. Haessler, I. Liontos, S. Kahaly, J. Rivera-Dean, P. Stammer, E. Pisanty, M. F. Ciappina, M. Lewenstein, and P. Tzallas; Quantum-optical spectrometry in relativistic laser–plasma interactions using the high-harmonic generation process: a proposal; Photonics **8** (2021) 192/1-12

LMJ21: X. Liu, A. Merhe, E. Jal, R. Delaunay, R. Jarrier, V. Chardonnet, M. Hennes, S. G. Chiuzbaian, K. Légaré, M. Hennecke, I. Radu, C. von Korff Schmising, S. Grunewald, M. Kuhlmann, J. Lüning, and B. Vodungbo; Sub-15-fs X-ray pump and X-ray probe experiment for the study of ultrafast magnetization dynamics in ferromagnetic alloys; Opt. Express **29** (2021) 32388-32403

LOP21: J. Lloyd-Hughes, P. Oppeneer, T. Pereira dos Santos, A. Schleife, S. Meng, M. A. Sentef, M. Ruggenthaler, A. Rubio, I. Radu, M. Murnane, X. Shi, H. Kapteyn, B. Stadtmüller, K. M. Dani, F. d. Jornada, E. Prinz, M. Aeschlimann, R. Milot, M. Burdanova, J. Boland, T. L. Cocker, and F. A. Hegmann; The 2021 ultrafast spectroscopic probes of condensed matter road map; J. Phys.-Condens. Mat. **33** (2021) 353001/1-15

LPS21: P. Loiko, A. Pavlyuk, S. Slimi, R. M. Solé, E. B. Salem, E. Dunina, A. Kornienko, P. Camy, U. Griebner, V. Petrov, F. Díaz, M. Aguiló, and X. Mateos; Growth, spectroscopy and laser operation of monoclinic Nd:CsGd$(MoO_4)_2$ crystal with a layered structure; J. Lumin. **231** (2021) 117793/1-10

LSA21: Z. Lécz, A. Sharma, A. Andreev, J. Fülöp, and C. Kamperidis; Sliding-wave acceleration of ions in high-density gas jet targets; Phys. Rev. E **103** (2021) 053210/1-5

LTB21: M. Liebmann, A. Treffer, M. Bock, M. Jurke, U. Wallrabe, and R. Grunwald; Tailored spectral rotation of vortex pulses by non-uniform spiral phase gratings; SPIE Proc. **11701** (2021) 11701V/1-7

LXH21: M. Liu, S. Xu, S. Hu, W. Becker, W. Quan, X. Liu, and J. Chen; Electron dynamics in laser-driven atoms near the continuum threshold; Optica **8** (2021) 765/1-6

LZZ21: Z.-L. Lin, H.-J. Zeng, G. Zhang, W.-Z. Xue, Z. Pan, H. Lin, P. Loiko, H.-C. Liang, V. Petrov, X. Mateos, L. Wang, and W. Chen; Kerr-lens mode-locked Yb:$SrLaAlO_4$ laser; Opt. Express **29** (2021) 42837-42843

MBL21: L. Mertenskötter, K. Busch, and R. d. J. León-Montiel; Entangled two-photon absorption spectroscopy with varying pump wavelengths; J. Opt. Soc. Am. B **38** (2021) C63-C68

MFH21: M. van Mörbeck-Bock, T. Feng, A. Heilmann, L. Ehrentraut, H. Stiel, M. Hennecke, T. Sidiropoulos, C. von Korff Schmising, S. Eisebitt, and M. Schnürer; High average power OPCPA MIR-systems for coherent soft x-ray generation accessing inner-shell absorption edges of metals; SPIE Proc. **11777** (2021) 117770C/1

MGK21: B. Major, O. Ghafur, K. Kovács, K. Varjú, V. Tosa, M. J. J. Vrakking, and B. Schütte; Compact intense extreme-ultraviolet source; Optica **8** (2021) 960-965

MJI21: M. S. Mrudul, Á. Jiménez-Galán, M. Y. Ivanov, and G. Dixit; Light-induced valleytronics in pristine graphene; Optica **8** (2021) 422-427

MRO21: F. Morales, M. Richter, V. Olvo, and A. Husakou; Propagator operator for pulse propagation in resonant media; Opt. Express **29** (2021) 29128

MRP21: M. L. Murillo-Sanchez, G. Reitsma, S. M. Poullain, P. Fernández-Milán, J. Gonzalez-Vázquez, R. d. Nalda, F. Martín, M. J. J. Vrakking, O. Kornilov, and L. Banares; Femtosecond XUV-IR induced photodynamics in the methyl iodide cation; New J. Phys. **23** (2021) 073023/1-12

MSt21: C. Mei and G. Steinmeyer; Space-time focusing and coherence properties of supercontinua in multipass cells; Phys. Rev. Res. **3** (2021) 013259/1-12

NGU21: T. Nagy, L. v. Grafenstein, D. Ueberschaer, and U. Griebner; Femtosecond multi-10-mJ pulses at 2 µm wavelength by compression in a hollow-core fiber; Opt. Lett. **42** (2021) 3033-3036

NLM21a: Z. Nie, F. Li, F. Morales, S. Patchkovskii, O. Smirnova, W. An, N. Nambu, D. Matteo, K. A. Marsh, F. Tsung, W. B. Mori, and C. Joshi; In situ generation of high-energy spin-polarized electrons in a beam-driven plasma wakefield accelerator; Phys. Rev. Lett. **126** (2021) 054801/1-6

NLM21b: Z. Nie, F. Li, F. Morales, S. Patchkovskii, O. Smirnova, W. An, N. Nambu, D. Matteo, K. A. Marsh, F. Tsung, W. B. Mori, and C. Joshi; Erratum: In situ generation of high-energy spin-polarized electrons in a beam-driven plasma wakefield accelerator; Phys. Rev. Lett. **127** (2021) 269901

NSV21: T. Nagy, P. Simon, and L. Veisz; High-energy few-cycle pulses: post-compression techniques; Adv. Phys. X **6** (2021) 1845795/1-42

NVP21: E. G. Neyra, P. Vaveliuk, E. Pisanty, A. S. Maxwell, M. Lewenstein, and M. F. Ciappina; Principal frequency of an ultrashort laser pulse; Phys. Rev. A **103** (2021) 053124/1-11

OFi21: M. Osswald and B. Fingerhut; Electron transfer induced active site structural relaxation in 64-photolyase of drosophila melanogaster; J. Phys. Chem. B **125** (2021) 8690–8702

OSm21: A. F. Ordoñez and O. Smirnova; Inducing enantiosensitive permanent multipoles in isotropic samples with two-color fields; in *Molecular Beams in Physics and Chemistry: From Otto Stern's Pioneering Exploits to Present-Day Feats*, Bretislav Friedrich and Horst Schmidt-Böcking ed. (Springer, Heidelberg, 2021) 335-352

PBB21: V. Petrov, V. V. Badikov, D. V. Badikov, K. Kato, G. S. Shevyrdyaeva, K. Miyata, M. Mero, L. Wang, Z. Heiner, and V. L. Panyutin; Barium nonlinear optical crystals for the mid-IR: characterization and some applications; J. Opt. Soc. Am. B **38** (2021) B46-B58

PBü21: B. Pfau and F. Büttner; Ultraschnelle Erzeugung von Skyrmionen; Physik in unserer Zeit **52** (2021) 6-7

Pis21: E. Pisanty; Knotted topologies in the polarization state of bichromatic light; SPIE Proc. **11818** (2021) 1181809 /1-9

PKa21: V. Pajer and M. Kalashnikov; High temporal contrast ultrashort pulses generated by nonlinear ellipse rotation in multipass cells; Laser Phys. Lett. **18** (2021) 065401/1-6

PKI21: M. Prämassing, T. Kiel, S. Irsen, K. Busch, and S. Linden; Electron energy loss spectroscopy on free-standing perforated gold films; Phys. Rev. B **103** (2021) 115403/1-7

PLW21: Z. Pan, P. Loiko, Y. Wang, Y. Zhao, H. Yuan, K. Tang, X. Dai, H. Cai, J. M. Serres, S. Slimi, E. B. Salem, E. Dunina, A. Kornienko, L. Fomicheva, J.-L. Doualan, P. Camy, W. Chen, U. Griebner, V. Petrov, M. Aguiló, F. Díaz, R. M. Solé, and X. Mateos; Disordered Tm^{3+},Ho^{3+}-codoped CNGG garnet crystal: Towards efficient laser materials for ultrashort pulse generation at ~2 µm; J. Alloy. Compd. **853** (2021) 157100/1-15

PSY21: S. Pal, N. Strkalj, C.-J. Yang, M. C. Weber, M. Trassin, M. Woerner, and M. Fiebig; Origin of terahertz soft-mode nonlinearities in ferroelectric perovskites; Phys. Rev. X **11** (2021) 021023/1-13

PWB21: Z. Pan, L. Wang, J. E. Bae, F. Rotermund, Y. Wang, Y. Zhao, P. Loiko, X. Mateos, U. Griebner, V. Petrov, and W. Chen; SWCNT-SA mode-locked Tm,Ho:LCLNGG laser; Opt. Express **29** (2021) 40323-40332

RAA21: N. N. Rosanov, I. A. Aleksandrov, M. V. Arkhipov, R. M. Arkhipov, I. Babushkin, N. A. Veretenov, A. V. Dadeko, D. A. Tumakov, and S. V. Fedorov; Dissipative aspects of extreme nonlinear optics; Quantum Electron. **51** (2021) 959-969

RCL21: R. Román-Ancheyta, B. Çakmak, R. d. J. León-Montiel, and A. Perez-Leija; Quantum transport in non-Markovian dynamically disordered photonic lattices; Phys. Rev. A **103** (2021) 033520/1-11

Rei21: H. R. Reiss; No light at the end of the tunnel; Eur. Phys. J. D **75** (2021) 158/1-6

RKB21: M. Runge, T. Kang, K. Biermann, K. Reimann, M. Woerner, and T. Elsaesser; Mono-cycle terahertz pulses from intersubband shift currents in asymmetric semiconductor quantum wells; Optica **8** (2021) 1638-1641

RPD21: G. Reitsma, S. Patchkovskii, J. Dura, L. Drescher, J. Mikosch, M. J. J. Vrakking, and O. Kornilov; Vibrational relaxation of XUV-induced hot ground state cations of naphthalene; J. Phys. Chem. A **125** (2021) 8549-8556

RSP21: J. Rivera-Dean, P. Stammer, E. Pisanty, T. Lamprou, P. Tzallas, M. Lewenstein, and M. F. Ciappina; New schemes for creating large optical Schrödinger cat states using strong laser fields; J. Comput. Electron. **51** (2021) 2111-2123

RVW21: P. Rueda, F. Videla, T. Witting, G. A. Torchia, and F. J. Furch; 8 fs laser pulses from a compact gas-filled multi-pass cell; Opt. Express **29** (2021) 27004-27013

RWE21: K. Reimann, M. Woerner, and T. Elsaesser; Two-dimensional terahertz spectroscopy of condensed-phase molecular systems; J. Chem. Phys. **154** (2021) 120901/1-14

RZB21: M. Rothammer, C. Zollfrank, K. Busch, and G. v. Freymann; Tailored disorder in photonics: Learning from nature; Adv. Opt. Mater. **9** (2021) 2100787/1-18

SBB21: D. Schick, M. Borchert, J. Braenzel, H. Stiel, J. Tümmler, D. E. Bürgler, A. Firsov, C. von Korff Schmising, B. Pfau, and S. Eisebitt; Laser-driven resonant magnetic soft-x-ray scattering for probing ultrafast antiferromagnetic and structural dynamics; Optica **8** (2021) 1237-1242

SBE21: J. Stamm, J. Benel, E. Escoto, G. Steinmeyer, and M. Dantus; Milliradian precision ultrafast pulse control for spectral phase metrology; Opt. Express **29** (2021) 14314-14325

SBH21: L. Shi, I. Babushkin, A. Husakou, O. Melchert, B. Frank, J. Yi, G. Wetzel, A. Demircan, C. Lienau, H. Giessen, M. Y. Ivanov, U. Morgner, and M. Kovacev; Femtosecond field-driven on-chip unidirectional electronic currents in nonadiabatic tunneling regime; Laser Photon. Rev. **15** (2021) 2000475/1-9

SBJ21: H. Stiel, J. Braenzel, A. Jonas, R. Gnewkow, L. T. Glöggler, D. Sommer, T. Krist, A. Erko, J. Tümmler, and I. Mantouvalou; Towards understanding excited-state properties of organic molecules using time-resolved soft X-ray absorption spectroscopy; Int. J. Mol. Sci. **22** (2021) 13463/1-18

SBK21: E. Spreafico, G. Benedek, O. Kornilov, and J. P. Toennies; Magic numbers in boson ^{4}He clusters: The auger evaporation mechanism; Molecules **26** (2021) 6244/1-8

SBT21: H. Stiel, J. Braenzel, J. Tuemmler, A. Jonas, I. Mantouvalou, A. Erko, A. Heilmann, M. Moerbeck-Bock, and M. Schnürer; Ultrafast NEXAFS spectroscopy in the lab using laser-based sources and advanced X-ray optics; SPIE Proc. **11886** (2021) 11886 12/1-9

Sch21: D. Schick; udkm1Dsim – a Python toolbox for simulating 1D ultrafast dynamics in condensed matter; Comput. Phys. Commun. **266** (2021) 108031

SED21: N. Singh, P. Elliott, J. K. Dewhurst, and S. Sharma; Manipulating magnons via ultrafast magnetization modulation; Phys. Rev. B **103** (2021) 134402/1-6

SHW21: E. Shestaev, S. Haedrich, N. Walther, T. Nagy, P. Simon, A. Blumenstein, A. Klenke, R. Klas, J. Buldt, H. Stark, M. Gebhardt, S. Breitkopf, C. Gaida, P. Jójárt, I. Seres, Z. Várallyay, Á. Börzsöny, T. Eidam, and J. Limpert; CEO-stable pulses from a 1kW fiber CPA; SPIE Proceedings **116760** (2021) 116760K/1

SIE21: G. G. Scott, G. F. H. Indorf, M. A. Ennen, P. Forestier-Colleoni, S. J. Hawkes, L. Scaife, M. Sedov, D. R. Symes, C. Thornton, F. Beg, T. Ma, P. McKenna, A. A. Andreev, U. Teubner, and D. Neely; Kinematics of femtosecond laser-generated plasma expansion: Determination of sub-micron density gradient and collisionality evolution of over-critical laser plasmas; Phys. Plasmas **28** (2021) 093109/1-10

SKB21: S. Staeck, Y. Kayser, J. Baumann, A. Jonas, I. Mantouvalou, R. Hartmann, B. Kanngießer, and H. Stiel; Towards soft x-ray fluorescence measurements in the laboratory using a laser-produced plasma source and a complementary metal-oxide semiconductor detector; J. Instrum. **16** (2021) P03033/1-17

SKF21: J. Schauss, A. Kundu, B. P. Fingerhut, and T. Elsaesser; Magnesium contact ions stabilize the tertiary structure of transfer RNA: electrostatics mapped by two-dimensional infrared spectra and theoretical simulations; J. Phys. Chem. B **125** (2021) 740-747

SKM21: G. P. Szekeres, S. Krekic, R. L. Miller, M. Mero, K. Pagel, and Z. Heiner; The interaction of chondroitin sulfate with a lipid monolayer observed by using nonlinear vibrational spectroscopy; Phys. Chem. Chem. Phys. **23** (2021) 13389-13395

SKT21: M. Szymański, A. Kozłowska, J. Tomm, R. Huk, A. Maląg, and M. Rusek; From two- to three-dimensional model of heat flow in edge-emitting laser: theory, experiment and numerical tools; Energies **14** (2021) 7006/1-14

SMR21: T. S. Seifert, U. Martens, F. Radu, M. Ribow, M. Berritta, L. Nádvorník, R. Starke, T. Jungwirth, M. Wolf, I. Radu, M. Münzenberg, P. M. Oppeneer, G. Woltersdorf, and T. Kampfrath; Frequency-independent terahertz anomalous Hall effect in $DyCo_5$, $Co_{32}Fe_{68}$, and $Gd_{27}Fe_{73}$ thin films from DC to 40 THz; Adv. Mater. **33** (2021) 2007398/1-10

SPR21: T. P. H. Sidiropoulos, N. D. Palo, D. E. Rivas, S. Severino, M. Reduzzi, B. Nandy, B. Bauerhenne, S. Krylow, T. Vasileiadis, T. Danz, P. Elliott, S. Sharma, K. Dewhurst, C. Ropers, Y. Joly, K. M. E. Garcia, M. Wolf, R. Ernstorfer, and J. Biegert; Probing the energy conversion pathways between light, carriers, and lattice in real time with attosecond core-level spectroscopy; Phys. Rev. X **11** (2021) 0410601-15

SSK21: F. Steinbach, D. Schick, C. von Korff Schmising, K. Yao, M. Borchert, W. D. Engel, and S. Eisebitt; Wide-field magneto-optical microscope to access quantitative magnetization dynamics with femtosecond temporal and sub-micrometer spatial resolution; J. Appl. Phys. **130** (2021) 083905/1-9

SSM21a: J. Schötz, L. Seiffert, A. Maliakkal, J. Blöchl, D. Zimin, P. Rosenberger, B. Bergues, P. Hommelhoff, F. Krausz, T. Fennel, and M. F. Kling; Onset of charge interaction in strong-field photoemission from nanometric needle tips; Nanophotonics **10** (2021) 3769-3775

SSM21b: P. Scheid, S. Sharma, G. Malinowski, S. Mangin, and S. Lebèguey; Ab initio study of helicity-dependent light-induced demagnetization: from the optical regime to the extreme ultraviolet regime; Nano Lett. **21** (2021) 1943-1947

SSN21: D. Schick, F. Steinbach, T. Noll, C. Strüber, W. D. Engel, C. von Korff Schmising, B. Pfau, and S. Eisebitt; High-speed spatial encoding of modulated pump-probe signals with slow area detectors; Meas. Sci. Technol. **32** (2021) 025901/1-7

TAC21: J. Teichert, A. Arnold, G. Ciovati, J.-C. Deinert, P. Evtushenko, M. Justus, J. M. Klopf, P. Kneisel, S. Kovalev, M. Kuntzsch, U. Lehnert, P. Lu, S. Ma, P. Murcek, P. Michel, A. Ryzhov, J. Schaber, C. Schneider, R. Schurig, R. Steinbrück, H. Vennekate, I. Will, and R. Xiang; Successful user operation of a superconducting radio-frequency photoelectron gun with Mg cathodes; Phys. Rev. Accel. Beams **24** (2021) 033401/1-16

TFG21: S. Theil, M. Fleischmann, R. Gupta, F. Rost, F. Wullschläger, S. Sharma, B. Meyer, and S. Shallcross; General relation between stacking order and Chern index: A topological map of minimally twisted bilayer graphene; Phys. Rev. B **104** (2021) 125412/1-12

TFI21: K. Tschernig, R. L. Franco, M. Y. Ivanov, M. A. Bandres, K. Busch, and A. Perez-Leija; Topological protection of highly entangled non-Gaussian two-photon states; Mater. Quantum. Technol. **1** (2021) 035001/1-10

THI21: E. Titov, H. Hummert, E. Ikonnikov, R. Mitrić, and O. Kornilov; Electronic relaxation of aqueous aminoazobenzenes studied by time-resolved photoelectron spectroscopy and surface hopping TDDFT dynamics calculations; Faraday Discuss. **228** (2021) 226-241

TJC21: K. Tschernig, Á. Jiménez-Galán, D. N. Christodoulides, M. Y. Ivanov, K. Busch, M. A. Bandres, and A. Pérez-Leija; Topological protection versus degree of entanglement of two-photon light in photonic topological insulators; Nat. Commun. **12** (2021) 1974/1-7

TJP21: R. Trebino, R. Jafari, P. Piksarv, P. Bowlan, H. Valtna-Lukner, P. Saari, Z. Guang, and G. Steinmeyer; The measurement of ultrashort laser pulses; in *Handbook of Laser Technology and Applications*, C. Guo, and S. C. Singh (eds.) (CRC Press, New York, NY, USA, 2021) 487-535

TMS21: K. Tschernig, C. Müller, M. Smoor, T. Kroh, J. Wolters, O. Benson, K. Busch, and A. Perez-Leija; Direct observation of the particle exchange phase of photons; Nat. Photonics **15** (2021) 1-5

TRG21: J. Tomm, J. Ruschel, J. Glaab, F. Mahler, T. Kolbe, and S. Einfeldt; On the carrier kinetics in Al(In) GaN quantum wells stressed by high current densities; SPIE Proc. **11705** (2021) 117050E/1-6

VDL21: A. Volokitina, S. P. David, P. Loiko, K. Subbotin, A. Titov, D. Lis, R. M. Solé, V. Jambunathan, A. Lucianetti, T. Mocek, P. Camy, W. Chen, U. Griebner, V. Petrov, M. Aguiló, F. Díaz, and X. Mateos; Monoclinic zinc monotungstate Yb^{3+},Li^{+}:$ZnWO_4$: Part II. Polarized spectroscopy and laser operation; J. Lumin. **231** (2021) 117811/1-12

Vra21: M. J. J. Vrakking; Control of attosecond entanglement and coherence; Phys. Rev. Lett. **126** (2021) 113203/1-5

WCP21: L. Wang, W. Chen, Z. Pan, P. Loiko, J. E. Bae, F. Rotermund, X. Mateos, U. Griebner, and V. Petrov; Sub-100 fs mode-locked Tm:CLTGG laser; Opt. Express **29** (2021) 31137-31144

WCS21: L. Wang, W. Chen, P. Schunemann, A. Schirrmacher, E. Büttner, A. A. Boyko, N. Ye, G. Zhang, Y. Zhao, and V. Petrov; Nanosecond optical parametric oscillator with midinfrared intracavity difference-frequency mixing in orientation-patterned GaAs; Opt. Lett. **46** (2021) 332-335

WCZ21a: L. Wang, W. Chen, Y. Zhao, P. Schunemann, A. Schirrmacher, E. Büttner, A. A. Boyko, N. Ye, G. Zhang, and V. Petrov; Mid-IR difference-frequency generation in OP-GaAs inside the cavity of a narrow-band nanosecond PPLN optical parametric oscillator; SPIE Proc. **11670** (2021) 1167011/1-6

WCZ21b: L. Wang, W. Chen, Y. Zhao, P. Loiko, X. Mateos, M. Guina, Z. Pan, M. Mero, U. Griebner, and V. Petrov; Sub-50 fs pulse generation from a SESAM mode-locked Tm,Ho-codoped calcium aluminate laser; Opt. Lett. **46** (2021) 2642-2645

WCZ21c: L. Wang, W. Chen, Y. Zhao, H. Yang, W. Jing, Z. Pan, H. Huang, J. Liu, J. E. Bae, F. Rotermund, P. Loiko, X. Mateos, Z. Wang, X. Xu, U. Griebner, and V. Petrov; Power-scalable sub-100-fs Tm laser at 2.08 µm; High Power Laser Sci. Eng. **9** (2021) e50/1-5

WGR21: M. Woerner, A. Ghalgaoui, K. Reimann, and T. Elsaesser; Two-color two-dimensional terahertz spectroscopy: A new approach for exploring even-order nonlinearities in the nonperturbative regime; J. Chem. Phys. **154** (2021) 154203/1-9

WLP21: A. P. Wozniak, M. Lesiuk, M. Przybytek, D. K. Efimov, J. S. Prauzner-Bechcicki, M. Mandrysz, M. Ciappina, E. Pisanty, J. Zakrzewski, M. Lewenstein, and R. Moszynski; A systematic construction of Gaussian basis sets for the description of laser field ionization and high-harmonic generation; J. Chem. Phys **154** (2021) 094111/1-19

ZJW21: D. Zahn, F. Jakobs, Y. W. Windsor, H. Seiler, T. Vasileiadis, T. A. Butcher, Y. Qi, D. Engel, U. Atxitia, J. Vorberger, and R. Ernstorfer; Lattice dynamics and ultrafast energy flow between electrons, spins, and phonons in a 3d ferromagnet; Phys. Rev. Res. **3** (2021) 023032/1-14

ZLL21: H. Zeng, H. Lin, Z. Lin, L. Zhang, Z. Lin, G. Zhang, V. Petrov, P. Loiko, X. Mateos, L. Wang, and W. Chen; Diode-pumped sub-50-fs Kerr-lens mode-locked Yb:GdYCOB laser; Opt. Express **29** (2021) 13496-13503

ZLX21a: H.-J. Zeng, Z.-L. Lin, W.-Z. Xue, G. Zhang, Z. Pan, H. Lin, P. Loiko, X. Mateos, V. Petrov, L. Wang, and W. Chen; SESAM Mode-Locked Yb:$Ca_3Gd_2(BO_3)_4$ femtosecond laser; Appl. Sci. **11** (2021) 9464/1-8

ZLX21b: H.-J. Zeng, Z.-L. Lin, W.-Z. Xue, G. Zhang, Z. Pan, H. Lin, P. Loiko, X. Mateos, V. Petrov, L. Wang, and W. Chen; SESAM mode-locked Yb:$SrLaAlO_4$ laser; Opt. Express **29** (2021) 43820-43826

ZOP21: Y. Zhou, R. Ovcharenko, B. Paulus, Y. Dedkov, and E. Voloshina; Modification of the magnetic and electronic properties of the graphene-Ni(111) interface via halogens intercalation; Adv. Theory Simul. **5** (2021) 2100319/1-7

ZWC21a: Y. Zhao, L. Wang, W. Chen, P. Loiko, X. Mateos, X. Xu, Y. Liu, D. Shen, Z. Wang, X. Xu, U. Griebner, and V. Petrov; Structured laser beams: toward 2-µm femtosecond laser vortices; Photonics Res. **9** (2021) 357-363

ZWC21b: Y. Zhao, L. Wang, W. Chen, P. Loiko, Y. Wang, Z. Pan, H. Yang, W. Jing, H. Huang, J. Liu, X. Mateos, Z. Wang, X. Xu, U. Griebner, and V. Petrov; Kerr-lens mode-locked Tm-doped sesquioxide ceramic laser; Opt. Lett. **46** (2021) 3428-3431

in press

AOD: D. Ayuso, A. F. Ordonez, P. Decleva, M. Y. Ivanov, and O. Smirnova; Strong chiral response in non-collinear high harmonic generation driven by purely electric-dipole interactions; Opt. Express

DWK: L. Drescher, T. Witting, O. Kornilov, and M. J. J. Vrakking; Phase dependence of resonant and antiresonant two-photon excitations; Phys. Rev. A

FGM: P. Fuertjes, L. v. Grafenstein, C. Mei, M. Bock, U. Griebner, and T. Elsaesser; Cr:ZnS-based soliton self-frequency shifted signal generation for a tunable sub-100 fs MWIR OPCPA; Opt. Express

GJM: R. Grunwald, M. Jurke, M. van Moerbeck-Bock, M. Liebmann, B. P. Bruno, H. Gowda, and U. Wallrabe; High-flexibility control of structured light with combined adaptive optical systems; Photonics

GBS: F. Guo, E. Boursier, P. Segonds, A. Pena, J. Debray, V. Badikov, V. Panyutin, D. Badikov, V. Petrov, and B. Boulanger; Second-order nonlinear optical coefficients of the monoclinic crystal $BaGa_4Se_7$; Opt. Lett.

HWE: C. Hauf, M. Woerner, and T. Elsaesser; Femtosecond diffraction with laser-driven hard x-ray sources: Nuclear motions and transient charge densities; in *Structural Dynamics with X-ray and Electron Scattering*, K. Amini, A. Rouzée, and M. J. J. Vrakking (eds.)

JLK: P. Juergens, B. Liewehr, B. Kruse, C. Peltz, T. Witting, A. Husakou, A. Rouzee, M. Y. Ivanov, T. Fennel, M. J. J. Vrakking, and A. Mermillod-Blondin; Characterization of laser-induced ionization dynamics in solid dielectrics; ACS Photonics

KLA: H. Köckert, J. Lee, F. Allum; UV-induced dissociation of CH2BrI probed by intense femtosecond XUV pulses; J. Phys. B

KMD: L.-M. Koll, L. Maikowski, L. Drescher, T. Witting, and M. J. J. Vrakking; Experimental control of quantum-mechanical entanglement in an attosecond pump-probe experiment; Phys. Rev. Letters

KTW: D. Kühn, A. Treffer, F. Wyrowski, and R. Grunwald; Simultaneous spatio-temporal focusing with pulse front symmetrization; Opt. Lett.

MBN: C. Mei, I. Babushkin, T. Nagy, and G. Steinmeyer; Spatial cage solitons - taming light bullets; Photonics Res.

MSY: C. Mei, G. Steinmeyer, J. Yuan, X. Zhou, and K. Long; Intermodal synchronization effects in multimode fibers with noninstantaneous nonlinearity; Phys. Rev. A

PGH: S. Priyadarshi, I. González Vallejo, C. Hauf, K. Reimann, M. Woerner, and T. Elsaesser; Phonon-induced relocation of valence charge in boron nitride observed by ultrafast x-ray diffraction; Phys. Rev. Lett.

SLD: S. Shallcross, Q. Li, J. K. Dewhurst, S. Sharma, and P. Elliott; Ultrafast optical control over spin and momentum in solids; Appl. Phys. Lett.

SSE: S. Sharma, S. Shallcross, P. Elliott, S. Eisebitt, C. von Korff Schmising, and J. K. Dewhurst; Computational analysis of transient XMCD sum rules for laser pumped systems: When do they fail?; Appl. Phys. Lett.

WOS: T. Witting, M. Osolodkov, F. Schell, F. Morales, S. Patchkovskii, P. Šušnjar, F. H. M. Cavalcante, C. S. Menoni, C. P. Schulz, F. J. Furch, and M. J. J. Vrakking; Generation and characterisation of isolated attosecond pulses at 100 kHz repetition rate; Optica

ZJS: D. Zahn, F. Jakobs, H. Seiler, T. A. Butcher, D. Engel, J. Vorberger, U. Atxitia, Y. W. Windsor, and R. Ernstorfer; Intrinsic energy flow in laser-excited 3d ferromagnets; Phys. Rev. Res.

Submitted

ARF: N. Acharyya, M. Richter, and B. P. Fingerhut; Coherent dynamics of the off-diagonal Spin-Boson model in the ultra-strong coupling regime; Phys. Rev. Res.

BKS: M. Borchert, C. von Korff Schmising, D. Schick, D. Engel, S. Sharma, and S. Eisebitt; Manipulation of ultrafast demagnetization dynamics by optically induced intersite spin transfer in magnetic compounds with distinct density of states; Appl. Phys. Lett.

BMi: W. Becker and D. B. Milošević; Elliptic dichroism in strong-field ionization of atoms subjected to tailored laser fields; Phys. Chem. Chem. Phys.

BPI: U. Bengs, S. Patchkovskii, M. Ivanov, and N. Zhavoronkov, All-optical Stückelberg spectroscopy of strongly driven Rydberg states; Phys. Rev. Lett.

EKL: M. Ekimova, C. Kleine, J. Ludwig, M. Ochmann, T. E. G. Agrenius, E. Kozari, E. Pines, N. Huse, P. Wernet, M. Odelius, and E. T. J. Nibbering; Covalent nature and hydration of the Zundel cation in solution; Angew. Chem. Int. Edit.

EWK: S. Eckert, M.-O. Winghart, C. Kleine, A. Banerjee, M. Ekimova, J. Ludwig, J. Harich, M. Fondell, R. Mitzner, E. Pines, N. Huse, P. Wernet, M. Odelius, and E. T. J. Nibbering; Revealing the transient electronic structure changes along the photoacid Förster cycle with picosecond nitrogen K-edge x-ray absorption spectroscopy; Angew. Chem. Int. Edit.

FTG: P. Fuertjes, J. W. Tomm, U. Griebner, G. Steinmeyer, S. S. Balabanov, E. M. Gavrishchuk, and T. Elsaesser; Kinetics of excitation transfer from Cr^{2+} to Fe^{2+} ions in co-doped ZnSe; Opt. Lett.

GKR: I. González Vallejo, A. Koç, K. Reimann, M. Woerner, and T. Elsaesser; Underdamped longitudinal soft modes in ionic crystallites - lattice and charge motions observed by ultrafast x-ray diffraction; Struct. Dyn.

GRe: A. Ghalgaoui and K. Reimann; Excitation of tunable plasmons in silicon using microwave transmission through a metallic aperture; Appl. Phys. Lett.

HSS: M. Hennecke, D. Schick, T. Sidiropoulos, F. Willems, A. Heilmann, M. van Moerbeck-Bock, L. Ehrentraut, D. Engel, P. Hessing, B. Pfau, M. Schmidbauer, A. Furchner, M. Schnuerer, C. von Korff Schmising, and S. Eisebitt; Ultrafast element- and depth-resolved magnetization dynamics probed by transverse magneto-optical Kerr effect spectroscopy in the soft x-ray range; Phys. Rev. Lett.

KBHa: C. Klose, F. Büttner, W. Hu, C. Mazzoli, G. S. D. Beach, S. Eisebitt, and B. Pfau; Photon correlation spectroscopy with heterodyne mixing based on soft-x-ray magnetic circular dichroism; Phys. Rev. B

KBHb: C. Klose, F. Büttner, W. Hu, C. Mazzoli, K. Litzius, I. Lemesh, J. M. Bartell, M. Huang, C. M. Günther, M. Schneider, A. Barbour, S. B. Wilkins, G. S. D. Beach, S. Eisebitt, and B. Pfau; Coherent Correlation Imaging: Resolving fluctuating states of matter; Nature

MBe: D. B. Milošević and W. Becker; Negative-travel-time quantum orbits in strong-field ionization by an elliptically polarized laser field; Phys. Rev. A

MKW: T. Mullins, E. T. Karamatskos, J. Wiese, J. Onvlee, A. Rouzée, A. Yachmenev, S. Trippel, and J. Küpper; Picosecond pulse shaping for strong three-dimensional field-free alignment of generic asymmetric top molecules; Nat. Commun.

OSma: A. F. Ordoñez and O. Smirnova; Disentangling enantiosensitivity from dichroism using bichromatic fields; Phys. Rev. A

OSmb: A. F. Ordoñez and O. Smirnova; On the molecular information revealed by photoelectron angular distributions of isotropic samples; Phys. Rev. A

PPA: M. Pancaldi, C. E. Pedersoli, D. D. Angelis, I. P. Nikolov, M. Manfredda, L. Foglia, S. Yulin, C. Spezzani, M. Sacchi, S. Eisebitt, C. von Korff Schmising, and F. Capotondi; The COMIX polarimeter as a compact device for XUV polarization analysis; J. Synchrot. Radiat.

RES: H. Rottke, R. Y. Engel, D. Schick, J. O. Schunck, P. S. Miedema, M. C. Borchert, M. Kuhlmann, N. Ekanayake, S. Dziarzhytski, G. Brenner, U. Eichmann, C. von Korff Schmising, M. Beye, and S. Eisebitt; Probing electron and hole co-localization by resonant four-wave mixing spectroscopy in the extreme-ultraviolet; Sci. Adv.

SSE: F. Steinbach, N. Stetzuhn, D. Engel, C. von Korff Schmising, and S. Eisebitt; Accelerating double pulse all-optical write/erase cycles in metallic ferrimagnets; Appl. Phys. Lett.

WFE: M. Woerner, B. P. Fingerhut, and T. Elsaesser; Field-induced electron generation in water: solvation dynamics and many-body interactions; J. Phys. Chem. B

WLZ: Y. Wang, P. Loiko, Y. Zhao, Z. Pan, W. Chen, M. Mero, X. Xu, J. Xu, X. Mateos, A. Major, M. Guina, V. Petrov, and U. Griebner; Polarized spectroscopy and SESAM mode-locking of Tm,Ho:CALGO; Opt. Express

Master and PhD Theses

Master Theses

Cha21: F. Chahrour; *Numerical analysis of thermalization effects in multimode nonlinear optical systems* (Supervisors: A. Perez-Leija and K. Busch), Humboldt-Universität zu Berlin

Klo21: C. Klose; *Coherent correlation imaging* (Supervisor: S. Eisebitt), Technische Universität Berlin

Mai21: L. Maikowski; *Fourier transform spectroscopy with XUV pulses* (Supervisors: M. J. J. Vrakking and T. Witting), Freie Universität Berlin

PhD theses

Hes21: P. Hessing; *Interference-based spectroscopy with XUV radiation* (Supervisor: S. Eisebitt), Technische Universität Berlin

Lan21: B. Langbehn; *Imaging the shapes and dynamics of superfluid helium nanodroplets* (Supervisors: D. Rupp, T. Möller, and K.-H. Meiwes-Broer), Technische Universität Berlin

Mah21: F. Mahler; *Ultraschnelle Ladungsträger- und Gitterdynamik in GaN- und GaAs-basierten Übergittern* (Supervisor: T. Elsaesser), Humboldt-Universität zu Berlin

Rei21: D. Reiche; *Long-time correlations in nonequilibrium dispersion forces* (Supervisors: F. Intravaia and K. Busch), Humboldt-Universität zu Berlin

Zim21a: J. Zimmermann; *Probing ultrafast electron dynamics in helium nanodroplets with deep learning assisted diffraction imaging* (Supervisors: T. Möller, D. Rupp, and S. Eisebitt), Technische Universität Berlin

Zim21b: H. Zimmermann; *Strong-field excitation of neutral atoms in the tunneling and multiphoton regime and the role of nondipole effects* (Supervisor: U. Eichmann), Technische Universität Berlin

Appendix 2

External Talks, Teaching

Invited talks at conferences

D. Ayuso; Lund Attoscience Symposium 2021 (Lund, Sweden, virtual, 2021-06): *Ultrafast and highly enantio-sensitive imaging of molecular chirality via HHG spectroscopy*

D. Ayuso; 32nd Int. Conference on Photonic, Electronic and Atomic Collisions (IPEAC) (Canada, virtual, 2021-07): *Ultrafast, all-optical, and highly enantio-sensitive imaging of molecular chirality*

D. Ayuso; 11th Int. Conference on Metamaterials, Photonic Crystals and Plasmonics (META 2021) (Warsaw, Poland, virtual, 2021-07): *Synthetic chiral light for efficient control of chiral light matter interaction*

D. Ayuso; DPG-Tagung der Sektion Atome, Moleküle, Quantenoptik und Plasmen SAMOP, special symposium chirality meets ultrafast (Hanover, Germany, virtual, 2021-09): *Synthetic chiral light for efficient laser-controlled chiral discrimination*

U. Eichmann; XFEL Users' Meeting (Hamburg, Germany, virtual, 2021-01): *Photon-recoil imaging: A new route to study nonlinear x-ray physics*

U. Eichmann; 52nd Annual Meeting of the APS Division of Atomic, Molecular and Optical Physics, DAMOP (virtual, 2021-06): *Photon-recoil imaging: A new route to study nonlinear x-ray physics*

S. Eisebitt; ALBA II - Workshop on Coherence and Time-resolved X-ray Science (Madrid, Spain, virtual, 2021-05): *Coherent correlation imaging: a new tool for high-resolution imaging of Stochastic Dynamics*

S. Eisebitt; EMA (The European Magnetism Association) - Plenary e-lecture (virtual, 2021-09): *Manipulating magnetization and magnetic order with light pulses*

S. Eisebitt; Photoinduced Phase Transitions and Cooperative Phenomena (PIPT7) (Santa Fe, USA, virtual, 2021-11): *Optical generation of magnetic skyrmions via a fluctuation driven, topology-sensitive mechanism*

S. Eisebitt; sIMMposium (Institute for Molecules and Materials (IMM), Nijmegen, The Netherlands, hybrid, 2021-11): *Mesoscale magnetization dynamics*

S. Eisebitt; The 9th Int. Symposium on Surface Science (ISSS-9) (Takamatsu, Japan, virtual, 2021-11): *Ultrafast optical generation and control of magnetic skyrmions*

T. Elsaesser; Max Water Workshop on Hydration (Max-Planck-Institute for Polymer Research, Mainz, Germany, virtual, 2021-01): *Structure and dynamics of hydrated RNA - femtosecond vibrational spectroscopy and theoretical simulations*

T. Elsaesser; Int. Conference on Time-Resolved Vibrational Spectroscopy (TRVS 2021) (virtual, 2021-06): *Electric interactions and structure of hydrated RNA: 2D-IR spectroscopy and theoretical simulations*

T. Elsaesser; CECAM Workshop "Nonequilibrium dynamical solvent effects on excited states: From spectroscopy to photoreactivity" (Nancy, France, virtual, 2021-06): *Electrons and contact ions solvated in water: Ultrafast dynamics and electric interactions*

T. Elsaesser; Vibrational Dynamics Workshop (Telluride, CO, USA, virtual, 2021-07): *Electric interactions of hydrated RNA: 3D-IR sprectroscopy and theoretical simulations*

T. Elsaesser; Summer School 2021 for the International Max Planck Research School for Many Particle Systems in Structured Environments (Dresden, Germany, 2021-09): *Ultrafast many-body charge dynamics in hydrated molecular systems (2 lectures)*

T. Elsaesser; CECAM: Second Discussion Meeting on Quantum Crystallography: Expectations & Reality (virtual, 2021-09): *Real-time charge and polarization dynamics mapped by femtosecond x-ray diffraction*

T. Elsaesser *together with* J. Schauss, A. Kundu, and B. P. Fingerhut; Pacifichem 2021 (virtual, 2021-12): *Electric interactions of hydrated RNA and DNA probed by femtosecond infrared spectroscopy*

B. P. Fingerhut; Symposium Physikalische und Theoretische Chemie (Technische Universität München (TUM), virtual, 2021-04): *From structure to function: towards the numerically exact transfer dynamics in photoactive proteins*

B. P. Fingerhut; Int. Conference on Time-Resolved Vibrational Spectroscopy (TRVS 2021) (virtual, 2021-06): *Contact pairs of dsRNA with magnesium ions - electrostatics beyond the Poisson-Boltzmann equation*

B. P. Fingerhut; Int. Symposium on Molecular Spectroscopy (ISMS) (Urbana-Champaign, USA, virtual, 2021-06): *Invited hydrated DNA and RNA mapped by 2D-IR spectroscopy*

B. P. Fingerhut; Symposium Theoretische Chemie (Ludwig-Maximilians-Universität München (LMU), virtual, 2021-07): *From structure to function: towards the numerically exact transfer dynamics in photoactive proteins*

U. Griebner *together with* L. von Grafenstein, M. Bock, T. Nagy, and T. Elsaesser; Photonics Days Berlin Brandenburg 2021 (Berlin, Adlershof, Germany, 2021-10): *Picosecond Ho:YLF chirped pulse amplifier system at 2.05 µm wavelength with 52 mJ pulse energy at a 1 kHz repetition rate*

A. Heilmann; Optica, Advanced Solid State Lasers Conference - Laser Applications Conference (virtual, 2021-10): *High power OPCPA systems generating high harmonic radiation at the oxygen K-edge and beyond*

M. Y. Ivanov; Faraday Discussions, (virtual, 2021-02): *Time-resolved imaging of photo-induced dynamics*

M. Y. Ivanov *together with* A. Jiménez-Galán, R. E. F. Silva, and O. Smirnova; Laser Physics 2021, (virtual, 2021-07): *Lightwave control of topological properties in 2D materials*

M. Y. Ivanov; Int. Quantum Optics X conference (Torun, Poland, 2021-09): *Towards PHz lightwave electronics*

C. Klose; INTERMAG 2021 (Lyon, France, 2021-04): *Coherent correlation imaging: High-resolution imaging of stochastic dynamics*

E. T. J. Nibbering *together with* M.-A. Codescu, M. Weiß, M. Brehm, O. Kornilov, and D. Sebastiani; Int. Conference on Time-Resolved Vibrational Spectroscopy (TRVS 2021) (virtual, 2021-06): *Switching between proton vacancy and excess proton transfer pathways*

E. T. J. Nibbering *together with* S. Eckert, M.-O. Winghart, A. Banerjee, C. Kleine, J. Ludwig, M. Ekimova, J. Harrich, R. Mitzner, E. Pines, N. Huse, Ph. Wernet, and M. Odelius; Int. Conference on Photochemistry - 30th Edition ICP2021 (virtual, 2021-07): *Photoacid charge distribution changes along the Förster cycle determined with ultrafast nitrogen K-edge absorption spectroscopy*

E. T. J. Nibbering *together with* S. Eckert, M.-O. Winghart, M. Ekimova, C. Kleine, J. Ludwig, M. Ochmann, T. A. E. Agrenius, A. Banerjee, E. Kozari, J. Harich, R. Mitzner, E. Pines, N. Huse, Ph. Wernet, and M. Odelius; Ultrafast Dynamic Imaging of Matter 2021 (UFDIM 21) (Potsdam, Germany, virtual, 2021-09): *Photoacid charge distribution changes along the Förster cycle determined with ultrafast nitrogen K-edge absorption spectroscopy*

E. T. J. Nibbering; Solid State Proton Conductors SSPC-21 (virtual, 2021-09): *Probing elementary steps of proton transport pathways with ultrafast infrared and soft-X-ray spectroscopy (keynote talk)*

E. T. J. Nibbering *together with* M. Ekimova, C. Kleine, J. Ludwig, M.-A. Codescu, S. Eckert, M.-O. Winghart, F. Hoffmann, G. Bekçioğlu-Neff, M. Weiß, M. Ochmann, A. Rafferty, A. Banerjee, T. E. G. Agrenius, E. Kozari, J. Harich, M. Brehm, O. Kornilov, R. Mitzner, E. Pines, N. Huse, Ph. Wernet, M. Odelius, and D. Sebastiani; 7th Theme Meeting on Ultrafast Science – 2021 (UFS-2021) (virtual, 2021-11): *Ultrafast structural dynamics of elementary steps of proton transport pathways with time-resolved infrared and soft-X-ray spectroscopy*

A. Ordoñez; Molecular quantum dynamics beyond bound states Workshop (Rostock, Germany, virtual, 2021-03): *Recent advances in ionization of chiral molecules*

A. Ordoñez, Seminar (ICFO, Barcelona, Spain, virtual, 2021-05): *Enantio-specific unidirectional harmonic emission: The chiral double slit experiment*

A. Ordoñez; Int. Laser Physics Workshop (LPHYS'21) (Lyon, France, virtual, 2021-07): *Structuring light's chirality to induce enantio-sensitive light bending*

A. Ordoñez; MD-GAS COST Action: 2nd Annual Meeting (UK, virtual, 2021-10): *Enantio-sensitive unidirectional light bending*

A. Perez-Leija; METANANO 2021, (virtual, 2021-09): *Two-photon edge states in photonic topological insulators: topological protection versus degree of entanglement*

V. Petrov *together with* Z. Heiner, and M. Mero; Photonics West'21: LASE 2021 (San Francisco, USA, virtual, 2021-03): *Few-cycle, µJ-level pulses beyond 5 µm from 1-µm-pumped OPA's based on non-oxide nonlinear crystals*

V. Petrov *together with* Z. Heiner, S. Krekic, and M. Mero; CLEO'21, (virtual, 2021-05): *Multi-branch, 1-µm-pumped, few-cycle mid-IR OPA system for nonlinear vibrational spectroscopy*

V. Petrov *together with* Y. Zhao, L. Wang, W. Chen, Z. Pan, Y. Wang, and U. Griebner; The 16th National Conference on Laser Technology and Optoelectronics, LTO 2021, (Shanghai, China, virtual, 2021-06): *Research progress of 2-micron ultrafast solid-state lasers*

V. Petrov *together with* A. Sennaroglu, Y. Morova, E. N. Kamun, and M. Tonelli; 28th Annual Int. Conference on Advanced Laser Technologies, ALT'21, (Moscow, Russia, virtual, 2021-09): *Upconversion pumping of continuous-wave tunable Tm^3+-doped KY_3F_{10} lasers near 2 and 2.3 µm*

V. Petrov *together with* M. Kowalczyk, Ł. Sterczewski, X. Zhang, Z. Wang, and J. Sotor; 28th Annual Int. Conference on Advanced Laser Technologies, ALT'21, (Moscow, Russia, virtual, 2021-09): *Dual-comb mode-locked lasers based on intrinsic polarization-multiplexing*

V. Petrov *together with* U. Elu, L. Maidment, L. Vamos, F. Tani, D. Novoa, M. H. Frosz, V. Badikov, D. Badikov, P. St. J. Russell, and J. Biegert; 2021 IEEE Photonics Conference, (virtual, 2021-10): *340-40,000 nm coherent light source*

E. Pisanty *together with* M. F. Ciappina, and M. Lewenstein; 32nd Int. Conference on Electronic and Atomic Collisions ViCPEAC, (virtual, 2021-07): *The imaginary part of the high-order harmonic cutoff*

E. Pisanty; Laser Beam Shaping XXI, (virtual, 2021-08): *Knotted topologies in the polarization state of bichromatic light*

M. Richter *together with* M. Lytova, F. Morales, S. Haessler, O. Smirnova, M. Spanner, and M. Y. Ivanov; CLEO/Europe-EQEC 2021, (virtual, 2021-06): *Rotational quantum beat lasing without inversion*

D. Rupp; Attosecond to Few-Femtosecond Ultrafast Science at Future FELs (EuXFEL, Schenefeld, Germany, 2021-06): *Imaging electron dynamics in isolated nanoscale particles*

D. Rupp; ICPEAC 21, (virtual, 2021-07): *Time-resolved imaging of light-induced dynamics in isolated nanoparticles*

D. Rupp; AttoChem Annual Meeting, (DESY, Hamburg, Germany, virtual, 2021-10): *Ultrafast dynamics in clusters followed with coherent diffraction imaging*

D. Rupp; MAX IV satellite workshop on Ultrafast x-ray science using SXL at MAX IV, (virtual, 2021-10): *Towards attosecond imaging of electron dynamics in nanoscale matter*

D. Schick; Optica, Advanced Solid State Lasers Conference - Laser Applications Conference (virtual, 2021-10): *Laser-driven resonant magnetic soft-X-ray scattering*

M. Schneider; XFEL Users' Meeting (Hamburg, Germany, virtual, 2021-01): *Mechanism of optically induced skyrmion nucleation*

M. Schneider; XFEL workshop, Scientific Opportunities for the Spanish Community at XFELs (Hamburg, Germany, virtual, 2021-06): *Following skyrmion nucleation in reciprocal and real space using soft x-rays*

B. Schütte; DPG-Tagung der Sektion Atome, Moleküle, Quantenoptik und Plasmen (virtual, 2021-09): *Highly nonlinear ionization of atoms induced by intense HHG pulses*

S. Shallcross; Int. Psi-K Workshop, Correlated synthetic quantum matter: Theory meets experiment (Bremen, Germany, 2021-02): *Twist and stacking faults in graphene like systems*

S. Shallcross and S. Sharma; Int. Psi-K Workshop, Correlated synthetic quantum matter: Theory meets experiment (Bremen Center for Computational Materials Science (BCCMS), Germany, 2021-02): *Twists and other stacking faults in the graphene bilayer*

S. Sharma; 736. WE-Heraeus-Seminar, Magnetism at the Nanoscale: Imaging – Fabrication – Physics (Bad Honnef, Germany, virtual, 2021-01): *Ultrafast spin dynamics: ab-initio description*

S. Sharma, On-line SPICE-SPIN+X Seminar (Johannes Gutenberg-Universität Mainz, Germany, virtual, 2021-06): *Ultrafast coupled charge, spin and nuclear dynamics: ab-initio description*

S. Sharma, Joint School on Spin Physics/SFB/TRR173 (Apolda, Thuringia, Germany, 2021-10): *Condensed matter theory - Ultrafast spin and charge dynamics*

S. Sharma; 25. Physikerinnentagung (Universität Duisburg-Essen, Germany, 2021-11): *Ultrafast spin dynamics: ab-initio description*

S. Sharma; 13th BESSY@HZB User Meeting (Berlin, Germany, virtual, 2021-12): *Ultrafast response functions*

O. Smirnova; Second advisory meeting for AMO science cases in Shanghai soft XFEL-II (Shanghai, China, virtual, 2021-04): *Geometric magnetism and new enantio-sensitive observables in non-linear photoionization*

O. Smirnova; CLEO'21, Conference on Lasers and Electro-Optics (USA, virtual, 2021-05): *Chiral Young's double slit experiment and polarization of chirality*

O. Smirnova; Int. Nobel Symposium on chirality (Stockholm, Sweden, 2021-06): *Geometric magnetism and new enantio-sensitive observables in photoionization of chiral molecules*

O. Smirnova; 6th Int. Symposium on Intense Field, Short Wavelength Atomic and Molecular Processes (ISWAMP) 2021, Satellite conference of the Int. Conference on Electronic, Atomic and Photonic Collisions (ICPEAC) (Ottawa, Canada, virtual, 2021-07): *Geometric magnetism and new enantio-sensitive observables in photoionization of chiral molecules*

O. Smirnova; 57th Symposium on Theoretical Chemistry (Würzburg, Germany, virtual, 2021-09): *Geometric magnetism and new enantio-sensitive observables in photoionization of chiral molecules*

O. Smirnova; Student Conference on Optics and Photonics (SCOP) (Ahmedabad, India, 2021-11): *Ultrafast chirality: twisting light to twist electron*

O. Smirnova; AKP-80 Workshop (2021-12): *Geometric fields and new enantio-sensitive observables in photoionization of chiral molecules*

O. Smirnova; Pacifichem 2021 (Honolulu, Hawaii, USA, virtual, 2021-12): *Geometric fields and new enantio-sensitive observables in photoionization of chiral molecules*

G. Steinmeyer; URSI GASS (Rome, Italy, virtual, 2021-09): *Pseudo combs - the liquid state of mode-locking*

M. J. J. Vrakking; The European Research Council (ERC) – Webinar for Starting and Consolidator Grants (EU Office of Charité, Berlin, 2021-11): *Testimonial of an ERC panel member*

L. Wang *together with* W. Chen, and V. Petrov; 28th Annual Int. Conference on Advanced Laser Technologies, ALT'21, (Moscow, Russia, virtual, 2021-09): *Non-resonant PPLN optical parametric oscillator in the narrow-band regime*

M.-O. Winghart *together with* C. Kleine, Z.-Y. Zhang, M. Ekimova, S. Eckert, M. J. J. Vrakking, E. T. J. Nibbering, and A. Rouzée; 2nd Annual Workshop of the COST Action AttoChem (virtual, 2021-10): *Soft X-ray absorption spectroscopy of aqueous solutions using a table-top femtosecond soft X-ray source*

M. Woerner; Discussion Workshop on Structural and Nuclear Dynamics (Universität Duisburg-Essen, Germany, 2021-11): *Phonon-induced relocation of valence charge in semiconductors and ferroelectrics*

Invited external talks at seminars and colloquia

D. Ayuso, Attochem Webinar Series (virtual, 2021-06): *Ultrafast, all-optical, and highly enantio-sensitive imaging of molecular chirality*

D. Ayuso, Atto Fridays Seminar Series (University College London, UK, virtual, 2021-07): *Ultrafast, all-optical, and highly enantio-sensitive imaging of molecular chirality*

D. Ayuso, Seminar (KTH Royal Institute of Technology, Stockholm, Sweden, 2021-12): *Ultrafast, all-optical, and highly enantio-sensitive imaging of molecular chirality*

T. Elsaesser, LPA seminar (Salamanca, Spain, virtual, 2021-02): *Laser-driven hard x-ray sources for femtosecond Bragg diffraction experiments*

M. Hennecke; EMA (The European Magnetism Association) - Early-Career Seminar (virtual, 2021-09): *Ultrafast spin dynamics of a ferrimagnet revealed by femtosecond soft X-ray and XUV radiation*

M. Y. Ivanov; Int. Zaragoza School on Attosecond Physics (virtual, 2021-03): *Analytical strong field methods in intense laser fields*

M. Y. Ivanov; Atto Fridays Seminar Series (UCL, London, UK, virtual, 2021-10): *Air Lasing: How does it work?*

M. Y. Ivanov; Int. Workshop and School on Laser Filamentation (Shanghai, virtual, 2021-10): *Lasing without inversion in the air*

M. Y. Ivanov; Int. Workshop and School on Laser Filamentation (Shanghai, virtual, 2021-10): *Not so free, free electron lasing*

M. Y. Ivanov; Colloquium (University of Kassel, 2021-11): *Towards PHz lightwave electronics*

P. Juergens; ARCNL Kolloquium (Amsterdam, Netherlands, virtual, 2021-11): *Linking harmonic generation in solids to strong-field-induced plasma dynamics*

L. M. Kern, Seminar (Helmholtz-Zentrum Berlin (HZB), virtual, 2021-09): *Linking harmonic generation in solids to strong-field-induced plasma dynamics*

O. Kornilov, Laserlab Europe user training workshop on data analysis in time-resolved imaging and spectroscopy (Int. Laser Centre, Slovak Centre of Scientific and Technical Information, Slovakia, virtual, 2021-05): *Time-resolved photoelectron spectroscopy*

J. Mikosch; Physikalisches Kolloquium (Universität Kassel, virtuell, 2021-02): *Structural molecular dynamics studied with intense laser fields and XUV pulses*

J. Mikosch; Interview application for professorship (Technische Universität Graz, Institute for Experimental Physics, Graz, Austria, 2021-07): *Structural molecular dynamics studied with intense laser fields and XUV pulses*

J. Mikosch; Interview application for professorship (Technische Universität Graz, Institute for Experimental Physics, Graz, Austria, 2021-10): *Der elektrische Schwingkreis*

E. T. J. Nibbering, Seminar (Imperial College, London, UK, virtual, 2021-07): *Ultrafast structural dynamics of elementary water-mediated proton transfer processes*

E. T. J. Nibbering, Department Seminar, (G. Meijer), Fritz Haber Institute of the Max Planck Society, Berlin, Germany (virtual, 2021-10): *Ultrafast structural dynamics of elementary water-mediated proton transfer processes*

B. Pfau, Seminar der AG Nanostrukturierte Materialien und des IZM (Martin-Luther-Universität Halle-Wittenberg, Institut für Physik, Germany, 2021-02): *Laser-driven resonant magnetic soft-X-ray scattering*

D. Rupp; Smart-X Marie-Curie Network virtual symposium (2021-04): *Imaging ultrafast dynamics in isolated nanoparticles*

D. Schick, Virtual weekly seminar (HZB, Germany, 2021-): *Tracing magnetic and structural dynamics in artificial magnetic nanostructures utilizing ultrafast resonant soft X-ray scattering*

B. Schütte; Seminar (Max-Planck-Institut für Quantenoptik, Garching, virtual, 2021-07): *From XUV refractive optics to attosecond nonlinear optics*

B. Schütte; Seminar (ELI Beamlines, Prague, Czech Republic, virtual, 2021-11): *From XUV refractive optics to attosecond nonlinear optics*

S. Sharma; Atto Fridays Seminar Series (UCL, London, UK, virtual, 2021-05): Ultrafast spin, charge and nuclear dynamics

S. Sharma, Colloquia, "transient response functions" (Duisburg-Essen University, group of Prof. Bovensiepen, virtual, 2021-05): *Ultrafast spin, charge and nuclear dynamics*

S. Sharma, Colloquia (Center for Hybrid, Active, & Responsive Materials, University of Delaware, virtual, 2021-12): *Ultrafast spin, charge and nuclear dynamics*

O. Smirnova, Ultrafast from coast to coast, Webinar series (Montreal, Canada, virtual, 2021-05): *Ultrafast chirality: twisting light to twist electrons*

O. Smirnova, Ultrafast from coast to coast, Webinar Series (Max-Planck Institute for Chemical Physics of Solids, virtual, 2021-07): *Ultrafast chirality: twisting light to twist electrons*

O. Smirnova, Ultrafast from coast to coast, Webinar Series (Max-Planck Institute for Chemical Physics of Solids, virtual, 2021-09): *On subtle difference between left and right: controlling and probing ultrafast chiral dynamics*

O. Smirnova, COST (European Cooperation in Science and Technology), 2nd round of AttoChem Webinar Series 2021 (virtual, 2021-09): *Ultrafast chirality: twisting light to twist electrons*

O. Smirnova, Ohio University Webinar (Ohio, USA, virtual, 2021-09): *Ultrafast chirality: twisting light to twist electrons*

O. Smirnova, Atto Fridays Seminar Series (University College London, UK, virtual, 2021-11): *Ultrafast chirality: twisting light to twist electrons*

O. Smirnova, Kassel University Colloquium (Kassel, Germany, virtual, 2021-11): *Geometric magnetism and new enantio-sensitive observables in photoionization of chiral molecules*

O. Smirnova, Seminar on 2e-ARPES (University of British Columbia, Canada, virtual, 2021-011): *Attosecond measurements of correlated processes without attosecond pulses*

G. Steinmeyer, Seminar (Cornell University, Ithaca, NY, USA, virtual, 2021-03): *Cage solitons*

G. Steinmeyer, PhoenixD Colloquium (Leibniz-Universität Hannover, Germany, 2021-06): *Time-resolved spectroscopy on quantum heterostructures*

M. J. J. Vrakking; Virtual colloquium at Imperial College “Frontiers of Ultrafast Measurement” network (2021-02): *Attosecond Science and “spooky action at a distance”*

M. J. J. Vrakking; Virtual colloquium at AMOLF (Amsterdam, Netherlands, 2021-06): *Attosecond Science and “spooky action at a distance”*

M. Woerner, Seminar (Hamburg, Germany, 2021-11): 2-dimensional THz spectroscopy on ferroelectrics, semiconductors, and liquids

Academic Teaching

K. Busch *together with* F. Intravaia, and D.-N. Huynh; Vorlesungen und Übungen, 10 SWS (Humboldt-Universität zu Berlin/virtuell, WS 2020/21): *Theoretische Physik IV: Fortgeschrittene Quantenmechanik/Fortgeschrittene Quantentheorie*

K. Busch, Tutorium, 2 SWS (Humboldt-Universität zu Berlin/virtuell, WS 2020/21): *Theoretische Physik IV: Fortgeschrittene Quantenmechanik/Fortgeschrittene Quantentheorie*

K. Busch *together with* O. Benson, A. Peters, A. Saenz, S. Ramelow, F. Intravaia, and M. Krutzik; Seminar, 2 SWS (Humboldt-Universität zu Berlin, SS 2021): *Optik/ Photonik: Projekt und Seminar*

K. Busch *together with* T. Kiel; Vorlesung und Übungen, 6 SWS (Humboldt-Universität zu Berlin, SS 2021): *Computerorientierte Photonik*

K. Busch *together with* D. Reiche, and V. Bender; Vorlesung und Übungen, 10 SWS (Humboldt-Universität zu Berlin, SS 2021): *Quantenmechanik*

K. Busch *together with* F. Intravaia, G. Wegner, and B. Grützner; Vorlesung und Übungen, 8 SWS (Humboldt-Universität zu Berlin, SS 2021): *Theoretische Physik V Thermodynamik*

K. Busch *together with* A. Perez-Leija, and K. Tschernig; Vorlesung und Übungen, 4 SWS (Humboldt-Universität zu Berlin, WS 2021/22): *Diskrete Quantenoptik*

K. Busch *together with* F. Intravaia, and K. Höflich; Vorlesung und Übungen, 8 SWS (Humboldt-Universität zu Berlin, WS 2021/22): *Fundamentals of optical sciences*

K. Busch *together with* O. Benson, A. Peters, A. Saenz, S. Ramelow, F. Intravaia, M. Krutzik, J. Volz, and P. Schneeweiß; Seminar, 2 SWS (Humboldt-Universität zu Berlin, WS 2021/22): *Optik/ Photonik: Projekt und Seminar*

S. Eichmann, Vorlesung, 2 SWS (Technische Universität Berlin, WS 2020/21): *Höhere Atomphysik*

S. Eisebitt, Ringvorlesung „Aktuelle Methoden der Physik“ (Technische Universität Berlin, Institut für Optik und Atomare Physik, WS 2020/21): *Zeitaufgelöste (Röntgen-) Mikroskopie und Spektroskopie zum Studium magnetischer Dynamik*

S. Eisebitt *together with* B. Kanngießer, and T. Möller; Vorlesung und Übungen, 4 SWS (Technische Universität Berlin, Institut für Optik und Atomare Physik, WS 2020/21): *Röntgenphysik I*

S. Eisebitt *together with* B. Kanngießer; Vorlesung und Übungen, 4 SWS (Technische Universität Berlin, Institut für Optik und Atomare Physik, SS 2021): *Röntgenphysik II*

T. Elsaesser and A. Saenz, Vorlesung, 4 SWS (Humboldt-Universität zu Berlin, WS 2020/21): *Laserphysik*

T. Elsaesser and G. Steinmeyer, Vorlesung, 4 SWS (Humboldt-Universität zu Berlin, SS 2021): *Physik ultraschneller Prozesse (Kurzzeitspektroskopie)*

T. Elsaesser and K. Busch, Vorlesung, 4 SWS (Humboldt-Universität zu Berlin, WS 2021/22): *Laserphysik*

I. V. Hertel, Seminar, 2 SWS (Humboldt-Universität zu Berlin/virtuell, WS 2020/21): *Forschungspraktikum mit Seminar*

F. Intravaia and M. Woerner, Übung, 4 SWS (Humboldt-Universität zu Berlin, WS 2021/22): *Laserphysik*

M. Y. Ivanov *together with* T. Bredtmann; Vorlesungen und Übungen, 4 SWS (Humboldt-Universität zu Berlin, virtuell, WS 2020/21): *Nichtlineare Optik*

M. Y. Ivanov *together with* T. Bredtmann; Vorlesung und Übungen, 4 SWS (Humboldt-Universität zu Berlin, WS 2021/22): *Nichtlineare Optik*

A. Perez-Leija *together with* K. Busch, and K. Tschernig; Vorlesungen und Übungen, 4 SWS (Humboldt-Universität zu Berlin, virtuell, WS 2020/21): *Diskrete Quantenoptik*

O. Smirnova *together with* U. Woggon; Vorlesung und Übungen, 8 SWS (Technische Universität Berlin, Institut für Optik und Atomare Physik, SS 2021): *Attosecond Physics*

G. Steinmeyer, Vorlesung und Übung, 4 SWS (Humboldt-Universität zu Berlin, WS 2020/21): *Physik III Optik*

M. J. J. Vrakking, Vorlesungen und Übungen, 4 SWS (Freie Universität Berlin, virtuell, WS 2020/21): *Ultrafast Laserphysics*

M. Woerner, Übung, 2 SWS (Humboldt-Universität zu Berlin, WS 2020/21): *Laserphysik*

General talks (popular, science politics etc.)

T. Elsaesser, BBAW Schulvortrag: Was ist Quantentechnologie? Die physikalische Sicht
Alexander-von-Humboldt-Gymnasium, Eberswalde, 28.01.2021
Freies Gymnasium Joachimsthal, Joachimsthal, 18.11.2021
Goethe-Schiller-Gymnasium, Jüterbog, 02.12.2021

T. Elsaesser, BBAW Schulvortrag: Licht und Materie - kann man Atome sichtbar machen?
Oberstufenzentrum Johanna Just, Potsdam, 02.03.2021
Marie-Curie-Gymnasium, Ludwigsfelde, 11.11.2021

T. Elsaesser, BBAW Schulvortrag: Die Messung der Zeit - eine physikalische Herausforderung
Gymnasium Aktive Naturschule, Templin, 09.12.2021
Friedrich-Anton-von-Heinitz-Gymnasium, Rüdersdorf, 14.12.2021

Appendix 3

Ongoing Master, and PhD theses

Bachelor theses

L. Tran; Tempern von FeGd-Dünnschichten zur gezielten Beeinflussung der magnetischen Eigenschaften (Supervisor: S. Eisebitt), Technische Universität Berlin

B. Weinmann; *Transportmessungen der laser-induzierten Nukleation von Skyrmionen* (Supervisor: S. Eisebitt), Technische Universität Berlin

Master theses

M. Anus; *Optimization of XUV intensity using a novel compact HHG scheme* (Supervisors: C. Saraceno and M. J. J. Vrakking), Ruhr Universität Bochum

V. Deinhart; *Ion-patterning of ferrimagnetic FeGd films* (Supervisor: S. Eisebitt), Technische Universität Berlin

L. Glöggler; *First pump-probe NEXAFS experiments using a laser-based plasma source* (Supervisor: B. Kangießer, H. Stiel), Technische Universität Berlin

X. Li; *Measurement of the saturation fluence of semiconductor saturable absorbers* (Supervisor: G. Steinmeyer), Humboldt-Universität zu Berlin

A. Molodtsova; *Time- and angle-resolved scattering of magnetic nanostructures in the extreme ultraviolet spectral range* (Supervisor: S. Eisebitt), Technische Universität Berlin

P. Smaliukas; *Setup of a frontend for a chirped-pulse optical parametric amplifier* (Supervisor: G. Steinmeyer), Humboldt-Universität zu Berlin

PhD theses

N. Abdurakhimov; *Development and characterisation of an EUV/soft X-ray single-photon sensitive sCMOS Camera* (Supervisors: M. J. J. Vrakking and T. Kampfrath), Freie Universität Berlin and SMART-X network

V. Bender; *Modeling of non-linear and active material in interaction with plasmonic nanostructres* (Supervisors: K. Busch and A. Perez-Leija), Humboldt-Universität zu Berlin

U. Bengs; *Generation of isolated attosecond pulses with circular polarization* (Supervisors: M. Y. Ivanov and N. Zhavaronkov), Humboldt-Universität zu Berlin

M. Borchert; *Ultrafast magnetic spectroscopy in the extreme ultraviolet spectral range* (Supervisor: S. Eisebitt), Technische Universität Berlin

F. Branchi; *Ultrafast structural dynamics in molecules by time-resolved photoelectron holography* (Supervisors: J. Mikosch and M. J. J. Vrakking), Freie Universität Berlin

M.-A. Codescu; *Ultraschnelle Dynamik von photoinduzierten Prozessen* (Supervisor: T. Elsaesser), Humboldt-Universität zu Berlin

F. A. R. Diaz; *Development of a high-repetition rate, short pulse ultrafast electron diffraction set-up for time-resolved structural dynamics* (Supervisors: M. J. J. Vrakking and M. Weinelt), Freie Universität Berlin

P. J. Fuertjes; *Generation and application of ultrashort mid-infrared pulses* (Supervisor: T. Elsaesser), Humboldt-Universität zu Berlin

K. Gerlinger; *X-ray imaging of optically induced spin textures* (Supervisor: S. Eisebitt), Technische Universität Berlin

M. O. S. Guzman; *Ultrafast charge carrier dynamics in oxide semiconductors by time-resolved soft x-ray absorption spectroscopy* (Supervisors: M. J. J. Vrakking and M. Weinelt), Freie Universität Berlin

E. Ikonnikov; *Time-resolved photoelectron spectroscopy of solvated molecules with phase-locked pulse pairs* (Supervisors: M. J. J. Vrakking and K. Heyne), Freie Universität Berlin

T. K. Kalousdian; *Strongfield dissociation of state-selected H_2^+ (v,J)* (Supervisors: M. J. J. Vrakking and H.-J. Freund), Freie Universität Berlin

L.-M. Kern; *Laser-driven magnetic switching at inhomogeneities and nanostructures* (Supervisor: S. Eisebitt), Technische Universität Berlin

C. Kleine; *Ultraschnelle Spektroskopie von Ladungstransferprozessen untersucht mit weichen Röntgenimpulsen* (Supervisor: T. Elsaesser), Humboldt-Universität zu Berlin

N. Klimkin; *Attosecond electron dynamics in light-driven solids* (Supervisor: M. Y. Ivanov, Humboldt-Universität zu Berlin

C. Klose; *Mesoscale Magnetization Dynamics* (Supervisor: S. Eisebitt), Technische Universität Berlin

L.-M. Koll; *2D XUV Spectroscopy* (Supervisors: M. J. J. Vrakking and T. Witting), Freie Universität Berlin

J. Lebendig-Kuhla; *Role of delocalized states for the excited state dynamics of nucleotide oligomers* (Supervisors: M. J. J. Vrakking and A. Lübcke), Freie Universität Berlin

Q. Li; *Ultra long range effects in ultra fast spin dynamics* (Supervisors: P. Brouwer and S. Sharma), Freie Universität Berlin

F. Loth; *Light path engineering in disordered waveguide structures* (Supervisor: K. Busch), Humboldt-Universität zu Berlin

N. Mayer; *Generation, characterization, and application of chiral attosecond pulses* (Supervisors: M. Y: Ivanov and O. Kornilov), Humboldt-Universität zu Berlin

M. Osolodkov; *Attosecond IR pump probe measurements of small molecules using 3D momentum spectroscopy* (Supervisors: M. J. J. Vrakking and T. Witting), Freie Universität Berlin

M. Osswald; *Theoretical description and simulation of non-linear spectroscopic signals of the light induced primary processes in (6-4) photolyase* (Supervisors: K. Busch and B. P. Fingerhut), Humboldt-Universität zu Berlin

L. Rammelt; *Direct laser writing of photonic chips for applicators in the classical and quantum regime* (Supervisors: M. J. J. Vrakking and T. Kampfrath), Freie Universität Berlin

M. Runge; *Nonlinear terahertz spectroscopy of biomolecules* (Supervisor: T. Elsaesser), Humboldt-Universität zu Berlin

J. Schauss; *Ultrakurzzeitdynamik der Wechselwirkung zwischen Ionen und Biomolekülen* (Supervisor: T. Elsaesser), Humboldt-Universität zu Berlin

B. Senfftleben; *Time resolved diffractive imaging with intense attosecond pulses* (Supervisors: S. Eisebitt and D. Rupp), Technische Universität Berlin

P. Singh; *Ultrafast vibrational probes of electric fields in hydrated molecular systems* (Supervisors: J. Kneipp and T. Elsaesser), Humboldt-Universität zu Berlin

F. Steinbach; *All optical switching in complex magnetic structures* (Supervisor: S. Eisebitt), Technische Universität Berlin

N. Stetzuhn; *Ultrafast Magnetization Dynamics in van der Waals Ferromagnets* (Supervisors: K. Bolotin, S. Eisebitt), Freie Universität Berlin

E. Svirplys; *Entwicklung einer Attosekunden-Plasmalinse* (Supervisor: M. J. J. Vrakking), Freie Universität Berlin

K. Tschernig; *Tailoring non-classical states of light for applications in quantum information processing* (Supervisors: K. Busch and A. Perez-Leija), Humboldt-Universität zu Berlin

K. Yao; *Ultrafast spin dynamics in heterogeneous magnetic systems* (Supervisor: S. Eisebitt), Technische Universität Berlin

Z. Zhang; *Soft X-ray spectroscopy of investigating charge transfer processes in push-pull chromophores* (Supervisor: M. J. J. Vrakking), Freie Universität Berlin

Appendix 4

Guest Lectures at the MBI

A. Leitenstorfer, University of Konstanz, Germany (virtual, 2021-01-13): *Electrons and photons under elementary spatio-temporal confinement*

J. Biegert, ICFO - The Institute of Photonics Sciences, Barcelona, Spain (virtual, 2021-02-17): *Lightwave-driven quantum dynamics: Molecular "selfie" to electron-phonon scattering*

P. Saliéres, Université Paris-Saclay, Paris, France (virtual, 2021-03-10): *Revealing photoionization dynamics using attosecond spectroscopy*

T. Weinacht, Stony Brook University, New York, USA (virtual, 2021-03-24): *Multi-modal probes of excited state dynamics in molecules: Getting the full story*

W. Kühn, Zeiss Oberkochen, Germany (virtual, 2021-04-07): *EUV lithography – An European success story*

L. Gallmann, ETH Zürich, Switzerland (virtual, 2021-04-21): *Attosecond spectroscopy of optical-field-driven dynamics in solids*

N. Dudovich, Weizmann Institute of Science, Israel (virtual, 2021-05-05): *Attosecond interferometry*

M. Chergui, Laboratoire de Spectroscopie Ultrarapide and Lausanne Centre for Ultrafast Science, ISIC, Lausanne, Switzerland (virtual, 2021-05-19): *Charge carrier dynamics in perovskites and transition metal oxides*

A. L'Huillier, Lund University, Lund, Sweden (virtual, 2021-06-02): *Attosecond pulses for capturing electron dynamics*

P. Gambardella, ETH Zurich, Switzerland (virtual, 2021-06-16): *Time- and spatially-resolved magnetization dynamics induced by charge-spin conversion phenomena*

D. Rupp, ETH Zurich, Switzerland (virtual, 2021-07-14): *Visualizing ultrafast dynamics in nanoparticles with coherent diffraction imaging*

T. Pfeifer, Max Planck-Institut für Kernphysik, Heidelberg, Germany (virtual, 2021-09-22): *Modifying the electronic response with lasers: From double excitation in He and two-electron entanglement in H2 to multi-electron exchange interaction in SF6*

B. Jones, University of Virginia, Charlottesville, USA (2021-10-20): *Probing electronic binding potentials with attosecond photoelectron wavepackets*

A. Kimel, Radboud University, Nijmegen, The Netherlands (virtual, 2021-11-17): *Ultrafast emergence of ferromagnetism in antiferromagnetic FeRh*

R. van der Veen, Helmholtz Zentrum Berlin and University of Illinois Urbana-Champaign, USA (virtual, 2021-12-01): *Fast electrons and hard X-rays for unraveling charge carrier dynamics*

Appendix 5

Grants and Contracts

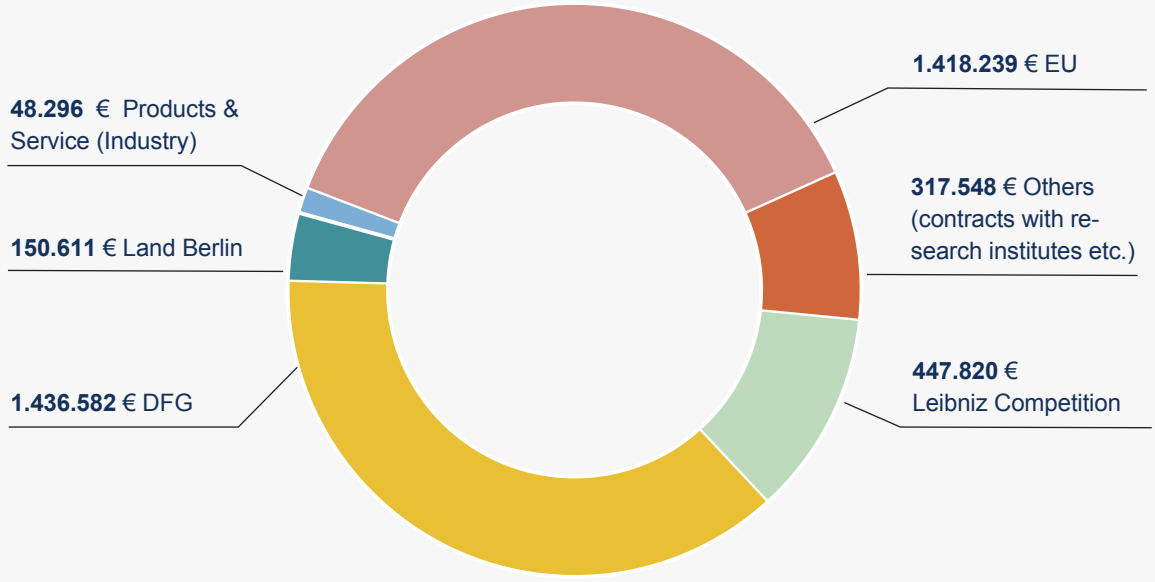

Total amount spent in 2021: 3.819.096 €

Appendix 6

Activities in Scientific Organizations

W. Becker

Member, Editorial Board Laser Physics Letters

Member, Editorial Board, Applied Sciences

Member, Editorial Board, Science open

Member, Advisory and Program Committee, 29th Int. Laser Physics Workshop - LPHYS'21, virtual format, Lyon, France

Co-chair Seminar 2, Strong Field & Attosecond Physics of the 29th Int. Laser Physics Workshop - LPHYS'21, virtual format, Lyon, France

K. Busch

Editor-in-chief, Journal of the Optical Society of America B

S. Eisebitt

Member, Komitee für Forschung mit Synchrotronstrahlung (KFS)

Member, Scientific Advisory Committee (SAC) of the European XFEL

Member, DESY Photon Science Comittee

Member, Scientific Advisory Council Elettra-Sincrotrone Trieste, Italy

Chair, Scientific Advisory Council Elettra-Sincrotrone Trieste, Italy

Designierter Vorsitzender der PGzB (Physikalischen Gesellschaft zu Berlin)

T. Elsaesser

Secretary of the Mathematics and Science Class, Berlin Brandenburg Academy of Sciences

Chair, TELOTA steering group, Berlin Brandenburg Academy of Sciences

Conference Chair, Program Committee, 15th Femtochemistry Conference (FEMTO 15)

Member, IRIS Adlershof, Humboldt-Universität zu Berlin

Member, Kuratorium of the Max Planck Institute for Quantum Optics, Garching

Member, Standing Committee for the Evaluation of International Max Planck Centers, Max Planck Society, Munich

Member, Editorial Board, Chem. Phys. Lett.

Member, Proposal Review Panel for the LCLS X-ray FEL facility, SLAC, Menlo Park, CA, USA

Associate Editor, Struct. Dyn., AIP

Member, Science Policy Committee, SLAC, Menlo Park; CA, USA

Member, FXE Proposal, Review Panel, Schenefeld, European XFEL

Chair, Physics Group, Gesellschaft Deutscher Naturforscher und Ärzte (GdNÄ)

Member, Advisory Board, Int. Conference on Coherent Multidimensional Spectroscopy

Member, Advisory Board, Conference Series on Time Resolved Vibrational Spectroscopy

B. P. Fingerhut

Member, Coblentz Award Committee of the Coblentz Society

Member, Advisory Board, Conference Series on Time Resolved Vibrational Spectroscopy

R. Grunwald

Member, SPIE Fellows Committee 2021

Member, Editorial Board, Applied Sciences (MDPI)

Associate Editor, Opt. Express

E. T. J. Nibbering

Member, Advisory Board, Conference Series on Time Resolved Vibrational Spectroscopy

Member, Scientific Selection Panel, Helmholtz-Zentrum Berlin - BESSY II

Member, Editorial Board, Journal of Photochemistry and Photobiology A

V. Petrov

Chair, Laser Sources Section, 28th Annual International Conference on Advanced Laser Technologies, ALT' 2021, Virtual Conference (Moscow, Russia)

Member, Program Committee, Nonlinear Frequency Generation and Conversion: Materials and Devices XX, SPIE Conference 11670, Part of LASE symposium at Photonics West (San Francisco, USA)

A. Rouzée

Editor, Advances in Physics X

O. Smirnova

Member, dynaMENT Mentoring for Women in Natural Sciences, University of Hamburg and DESY

Member, Advisory Board of the Max Planck School of Photonics

Member, Scientific Committee International Conference on on Attosecond Science and Technology, ATTO

Member, Scientific Committee International Conference on Photonic, Electronic and Atomic Collisions, ICPEAC

S. Sharma

Member, Executive Organising Committee SPIE Photonics Europe, Advances in Ultrafast Condensed Phase Physics II (Strasbourg, France)

G. Steinmeyer

Subcommittee Chair, Nonlinear Photonics 2022 (Maastricht, Netherlands)

Associate Editor, Optica

Member, Editorial Board, Phys. Lett. A

Member, Program Committee, Ultrafast Optics 2023, Bariloche, Argentina

H. Stiel

Member, Scientific Committee International Conference on X-ray Lasers, EMPA, Dübendorf, Switzerland

Member, Advisory board of Institute of Applied Photonics (IAP) eV, Berlin

J. W. Tomm

Permanent Member, Int. Steering Committee, Int. Conference on Defects - Recognition, Imaging and Physics of Semiconductors, DRIP (Yokohama, Japan)

Member Editorial Board, Journal of Electronic Materials (JEMS)

Member Editorial Board, Communications in Physics (CIP)

Member, Programm Committee, ESREF 2021, 32th European Symposium on Reliability of Electron Devices, Failure Physics and Analysis, Bordeaux, France

M. J. J. Vrakking

Chairman, SAC of the Advanced Research Centre for Nanolithography, Amsterdam, The Netherlands

Editor-in-chief, Journal of Physics B

Member Supervisory board, SMART-X training network

Member UED proposal review panel at LCLS, Stanford University

Member Proposal review panel, FLASH FEL, Hamburg, Germany

Chairman *together with* S. Techert, VUVX, International Scientific Committee

Chairman, ERC Advanced Grant Panel PE2, 2020-2021, Brussels, Belgium, remote meeting

Member, DFG review panel on CRC 1319

Member Management Board, Laserlab Europe V AISBL

Honors and awards

M.-A. Codescu: Switching between proton vacancy and excess proton transport pathways, Poster Award - Solid State Proton Conductors (SSPC-20)

L. Drescher: Carl-Ramsauer-Preis 2021, Physikalische Gesellschaft zu Berlin, Regionalverband Berlin/Brandenburg

Á. Jiménez-Galán: QUMATTO Grant, EU HORIZON 2020, Marie Curie Individual Fellowship

D. Reiche: Lise-Meitner-Preis 2021, Vereinigung der Freunde und Förderer des Institutes für Physik der Humboldt-Universität zu Berlin e.V.

M. Schneider: The European XFEL Young Scientist Award, European XFEL

Max-Born-Institut (MBI)
für Nichtlineare Optik und Kurzzeitspektroskopie
im Forschungsverbund Berlin e. V.

Mail Address: Max-Born-Institut
Max-Born-Straße 2 A
12489 Berlin
Germany

Phone: (++49 30) 6392 1505
Fax: (++49 30) 6392 1519
mbi@mbi-berlin.de
www.mbi-berlin.de

The Divisions of the Max-Born-Institut

Division A: Attosecond Physics
Prof. Dr. M. J. J. Vrakking

Division B: Transient Electronic Structure and Nanoscience
Prof. Dr. S. Eisebitt

Division C: Nonlinear Processes in Condensed Matter
Prof. Dr. T. Elsaesser

City district: Berlin Treptow-Koepenick
Subdistrict: Berlin-Adlershof

Site: Berlin-Adlershof
Street: Max-Born-Straße 2 A

S-Bahn: S45, S46, S85, S8, and S9
Station: Berlin-Adlershof
from there:
Bus 162, 164 to Magnusstraße
Tram: 61, 63 to Karl-Ziegler-Straße

Subway: U7
Station: Rudow
from there:
Bus 162 to Magnusstraße

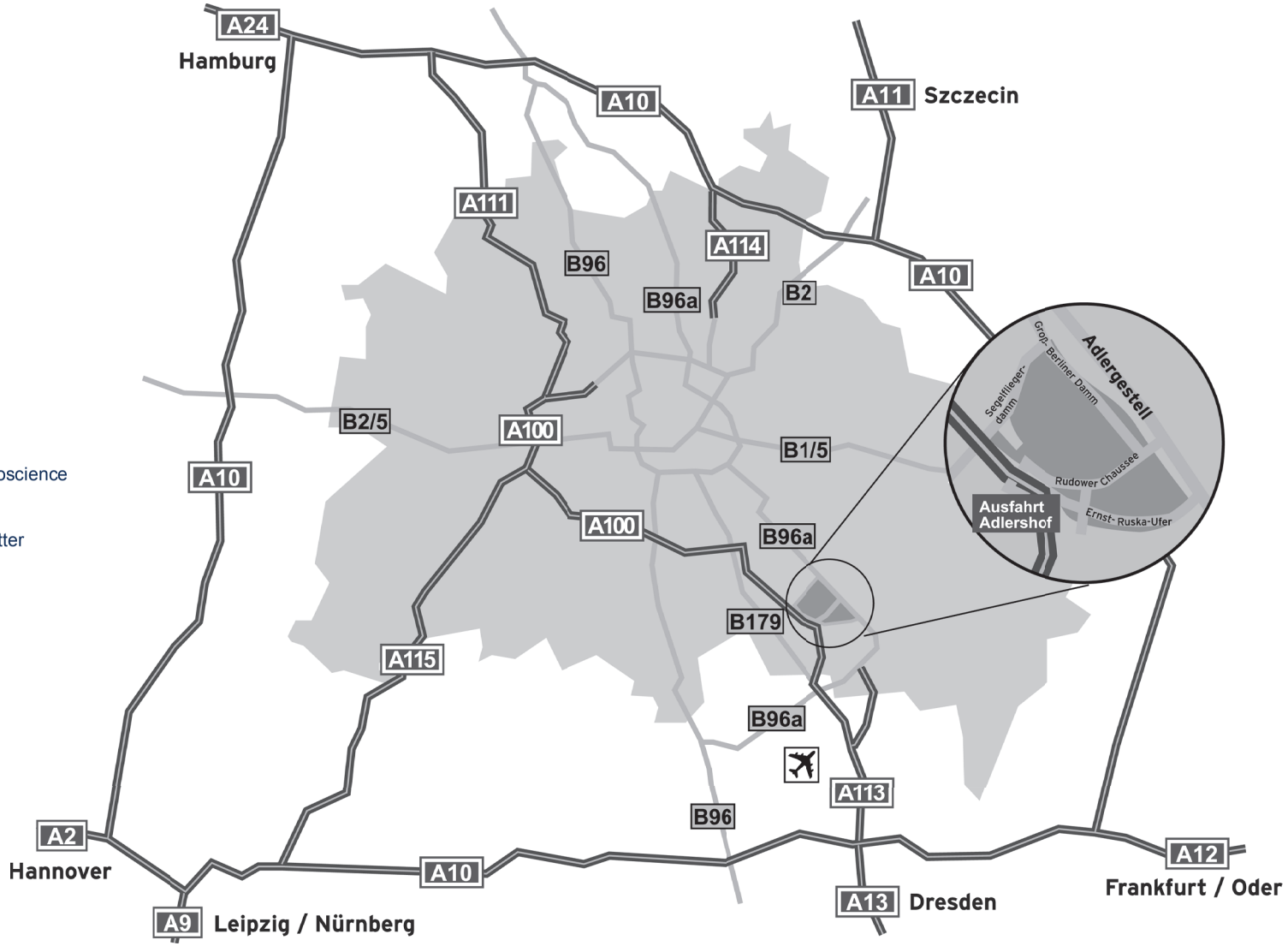

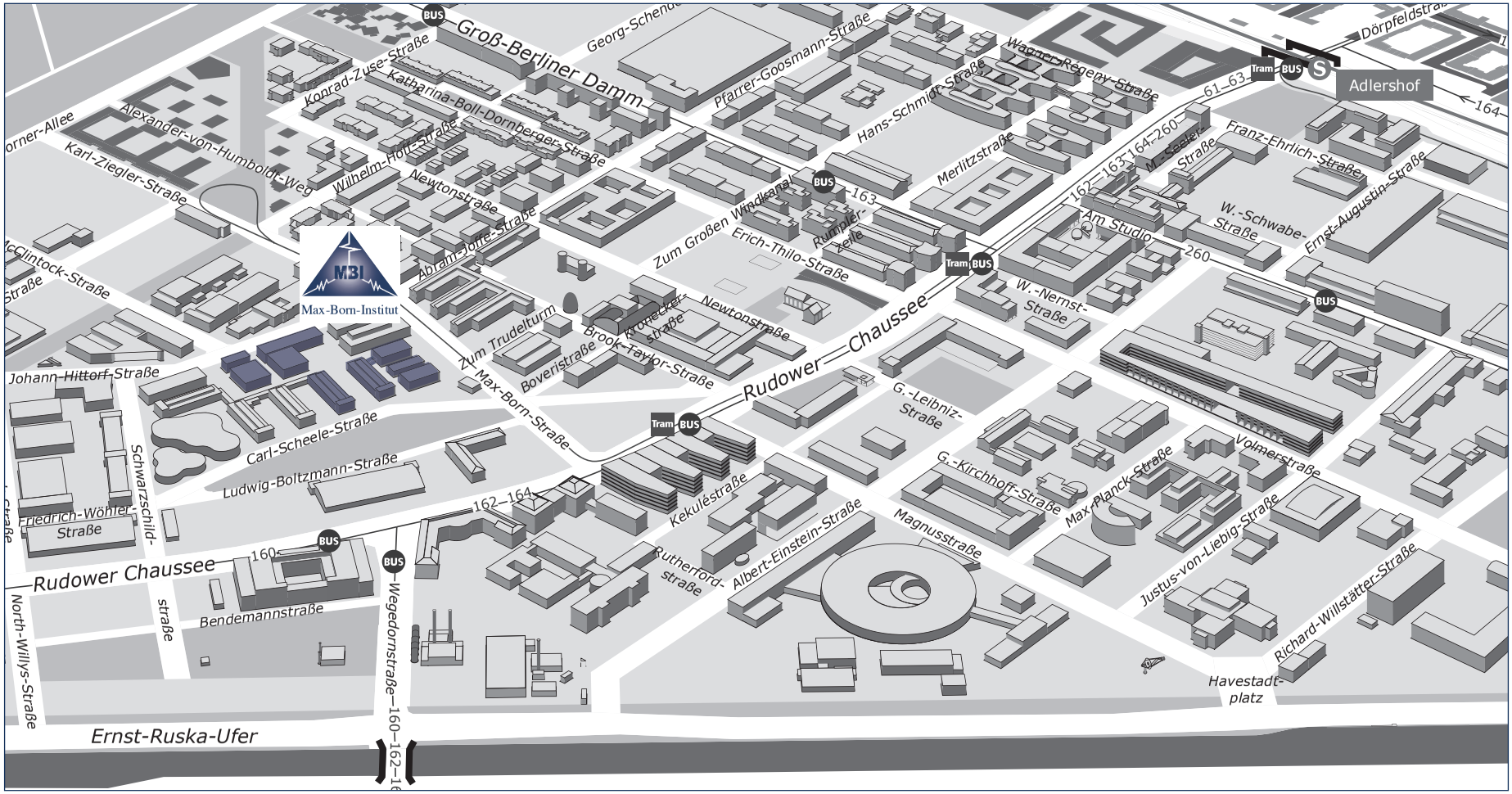
Groß-Berliner Damm
Georg-Schenu
Konrad-Zuse-Straße
Katharina-Boll-Dornberger-Straße
Pfarrer-Goosmann-Straße
Hans-Schmidt-Straße
Wagner-Régeny-Straße
Dörpfeldstra
Adlershof
Alexander-von-Humboldt-Weg
Karl-Ziegler-Straße
Wilhelm-Hoff-Straße
Newtonstraße
Merlitzstraße
Franz-Ehrlich-Straße
W.-Seeler-Straße
W.-Schwabe-Straße
Ernst-Augustin-Straße
Am Studio
Zum Großen Windkanal
Rumpler-Teile
Erich-Thilo-Straße
Abram-Joffe-Straße
MBI
Max-Born-Institut
Johann-Hittorf-Straße
Zum Trudelturm
Boveristraße
Brook-Taylor-Straße
Rotherstraße
Newtonstraße
W.-Nernst-Straße
Rudower Chaussee
G.-Leibniz-Straße
Max-Born-Straße
Carl-Scheele-Straße
Ludwig-Boltzmann-Straße
Schwarzschild-straße
Friedrich-Wöhler-Straße
Kekuléstraße
G.-Kirchhoff-Straße
Max-Planck-Straße
Volmerstraße
Justus-von-Liebig-Straße
Magnusstraße
Albert-Einstein-Straße
Rutherford-straße
Rudower Chaussee
Bendemannstraße
Wegedornstraße
North-Willys-Straße
straße
Richard-Willstätter-Straße
Havestadt-platz
Ernst-Ruska-Ufer